GEMP-190g
(INFORMAL)

213p

FACILITY FORM 602

N64-29790	
(ACCESSION NUMBER)	(THRU)
213	1
(PAGES)	(CODE)
CR-52955	23
(NASA CR OR TMX OR AD NUMBER)	(CATEGORY)

Nuclear Materials & Propulsion Operation

INTRODUCTION TO NUCLEAR PROPULSION

Lectures 11 and 12 - MECHANICAL DESIGN

O. G. Woike

[redacted]

FLIGHT PROPULSION LABORATORY DEPARTMENT
GENERAL ELECTRIC

SqT-10563g

GEMP-190g
(INFORMAL)

INTRODUCTION TO NUCLEAR PROPULSION

Lectures 11 and 12 - MECHANICAL DESIGN

Otto G. Woike

[redacted]

April 9, 10, and 11, 1963

Prepared for the George C. Marshall
Space Flight Center of the National
Aeronautics and Space Administration

Contract No. NAS8-5215

CONTENTS

Page

1. Introduction . . . 1
2. Major Considerations . . . 3
  - 2.1 Structural Design Criteria . . . 3
  - 2.2 Material Considerations in Structures . . . 9
3. High Temperature Design and Thermal Stress . . . 14
  - 3.1 Unrestrained Thermal Expansions . . . 14
  - 3.2 Thermal Stresses . . . 19
  - 3.3 Transient Conditions . . . 27
  - 3.4 Material Thermal Stress Resistance . . . 31
4. Ceramic Reactors . . . 34
  - 4.1 Introduction . . . 34
  - 4.2 Description . . . 35
  - 4.3 Significant Design Factors . . . 37
    - 4.3.1 Configuration Considerations . . . 37
    - 4.3.2 Design Principles of the Slab and Tube Concept 40
    - 4.3.3 Tube Bundle Considerations . . . 53
  - 4.4 Mechanical Design Principles of the Tube Bundle . . . 58
    - 4.4.1 Introduction . . . 58
    - 4.4.2 H[redacted]es of Radial Support . . . 61
    - 4.4.3 S ial Support . . . 65
    - 4.4.4 Integrated Principles of Radial Support . . . 75
    - 4.4.5 Comparison of the Radial Support System Principles . . . 81
    - 4.4.6 Tube Bundle Vibration . . . 84
    - 4.4.7 Three-Tier Mockup Testing . . . 88
    - 4.4.8 Pressure Magnification in the Tube Bundle . . . 95
    - 4.4.9 Effects of Core Liner Fit on Tube Bundle Pressure Distribution . . . 97
    - 4.4.10 Dimension Stackup of the Tube Bundle . . . 98
    - 4.4.11 Displacements of the Tube Bundle . . . 101
    - 4.4.12 Longitudinal Pressure Between Tubes . . . 101
  - 4.5 Mechanical Design Details of Components in the Tube Bundle . . . 102
    - 4.5.1 Introduction . . . 103
    - 4.5.2 Mechanical Stresses in Fuel Elements . . . 103
    - 4.5.3 Thermal Stresses in Fuel Elements . . . 110
    - 4.5.4 Combined Total Stresses in Fuel Tubes . . . 138
    - 4.5.5 Other Components . . . 139

Page

4.6 Design Details of Components in the Radial Support System.......... 147
  4.6.1 Design Parameters.......... 147
  4.6.2 Spring Design.......... 149
  4.6.3 Structural Shell.......... 159
  4.6.4 Pressure Pads.......... 160
  4.6.5 Spring Retractors and Adjustors.......... 160
4.7 Design Details of Components in the Axial Support System.......... 160
  4.7.1 Significant Design Parameters.......... 160
  4.7.2 Modified Tube Sheet.......... 161
  4.7.3 Small Retainer Plates Individually Supported by Axial Tension Rods.......... 167
  4.7.4 Dome, or Roman Arch, Structures in Compression.......... 171
4.8 General Comments on Techniques of Reactor Handling.......... 174

Appendix A
Elastic Thermal Stress Analysis.......... 178

Appendix B
Linearized Thermal Expansion Approach.......... 198

Appendix C
Viscoelastic Behavior.......... 202

Appendix D
Sample Problem.......... 214

Acknowledgements

To J.E.McConnelee who contributed Sections 3.3, 3.4 and the Appendix and to B.A.Chandler who contributed Section 4.5.3.

1.0 INTRODUCTION

A discussion of the mechanical design of gas-cooled high-temperature nuclear reactors is presented. Design problems peculiar to this application are stressed. GE-ANPD reactor designs, described in the first lecture, will be used to illustrate the mechanical design aspects. Emphasis is placed on the ceramic reactor design.

It is probable that the listener cannot use these specific designs, instead he will be able to discern the underlying principles that guided the designs and apply them to his own problems.

The required attributes of a nuclear reactor in a development cycle are: performance, reliability, timing, cost and weight. To achieve these the mechanical engineer reviews input guidance from various sources. The customer supplies the design requirements (in conjunction with the monies). The thermal analyst provides temperature distributions relative to time. The nuclear analyst provides reactor and shield analyses including component heat generation, reactor safety evaluation,etc. The materials engineer assures material stability through proper material choice and where property data is lacking, conducts material tests. The test engineer provides product confidence limits. The fabricator provides economical processes in accordance with schedule and quality requirements. The final output of the mechanical designer is structural analyses, drawings and product specifications. These assure leaving a minimum of variables to chance.

The evolution of the final design of a nuclear reactor does not permit a clear separation of the major design areas. Throughout the design period, constant integration and coordination of the input data from each of these areas is required to achieve the design objectives. For this reason, a project, or team, approach is frequently used to expedite the design process. The mechanical design contribution to this team effort is a core configuration incorporating practical component designs that satisfy the nuclear, thermal, and mechanical requirements. The mechanical designer must insure that each component remains dimensionally stable and retains its structural integrity and ability to function under anticipated loadings and environmental conditions for the design life.

The usual approach to the mechanical design of reactor components starts by establishing the design specifications and developing a configuration that satisfies the requirements. This is followed by a complete stress analysis and material evaluation. The stress analysis involves: (1) a definition of the loads imposed on the component, (2) a detailed analytical stress analysis supported by experimental stress analysis where necessary, and (3) establishing the failure criteria. The materials evaluation involves: (1) the determination of the required material properties, (2) an analysis of the material properties for the intended use, and (3) fabrication development and component testing. Figure 1 illustrates these steps. It can be seen that failure of the structural design will result if any of the steps are missing or if there is a weak link in the design process.

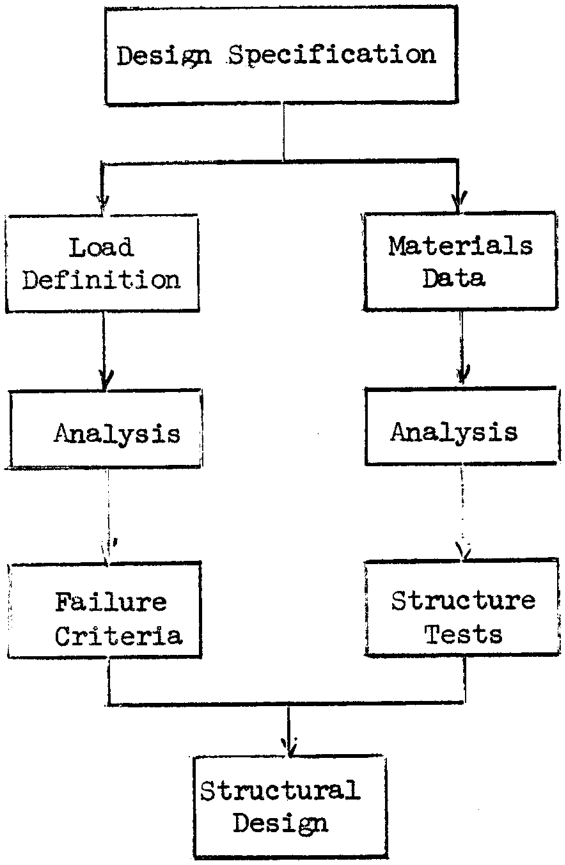
Design Specification
Load Definition
Materials Data
Analysis
Analysis
Failure Criteria
Structure Tests
Structural Design

Fig. 1 - Structural Design Process

2.0 MAJOR MECHANICAL DESIGN CONSIDERATIONS

The major mechanical design considerations of gas cooled reactors include material considerations; remote maintenance; quality control; component testing; structural design methods and criteria, and thermal stresses. The first two subjects are covered in detail in subsequent lectures. The third is well covered in the literature and will not be included here. Component testing of ceramic fuel elements is illustrated in Section 4.5.3.

2.1 STRUCTURAL DESIGN CRITERIA

Establishment of consistent criteria governing the structural design of mechanical components in load-carrying systems is an essential prerequisite to successful design. In a power-generating system, the working cycle and the required thermodynamic characteristics can be established independently of the mechanical aspects of the components by merely assuming that the necessary components exist in the required form. However, in a nuclear system complicated interrelationships exist between the nuclear parameters and the poisoning effects of the structural elements of the reactor that severely influence the nuclear characteristics and the economics of designing a nuclear power plant. Since nuclear safety is dependent on the structural reliability to a considerable extent, safety requirements permit no compromise with the structural reliability of the components or of the total power plant. Economical utilization of the nuclear-power plant requires uninterrupted operation free from breakdowns and malfunctioning of components. On the other hand, the nuclear performance and the economics of building a reactor are adversely effected if excessive conservatism in the interest of reliability and safety governs the mechanical design. Therefore, reasonable, but adequate, criteria must be established during the initial stages of a new reactor design to guide the mechanical designer in his task of providing minimum weight and cost consistent with component functional and structural reliability.

Utilization of design criteria is an important step in the achievement of consistent reliability. Criteria provide the guide lines for the design process but they do not guarantee that complex problems are accurately analyzed, or that a completely valid analytical model is practical. Hence, the utilization of logical design criteria is undoubtedly the basic step toward achievement of a consistent degree of reliability, but component and material testing and past experience are elements absolutely essential in the attainment of a high degree of reliability.

Design criteria constitute an essential aid to the designer; they have evolved in the past from the need to insure consistency in the conditions governing the design of various categories of engineering structures and machines, thus, insuring standards of material quality and public safety.

The ASME Pressure Vessel Codes are a prime example where the public safety is served. These codes specify the analytical methods to be applied when estimating the strength of all types of pressure vessels; they also specify the material properties, quality and methods of fabrication that influence strength and serviceability. These criteria are widely applicable to ground-based and marine-type nuclear power plants, but are unsuitable for aircraft and space-flight components.

Design criteria may be provided in whole or in part by a requirement to adhere to existing codes, such as the pressure vessel codes. However, there is a need for the formulation of a set of consistent design criteria that specifically apply to gas-cooled high-temperature reactors. Design criteria and design practice in the aircraft industry essentially provided the starting point for the set of design criteria that evolved during the GE-ANPD program. Some of these criteria are repeated here in a somewhat generalized form as an indication of the current philosophy pertaining to the logical identification of the design criteria. Criteria such as these are based upon accepted and practical analytical methods and on the success of past practices and past experience with materials and their practical applications.

At the time that design work was begun on the flight prototype GE-ANPD system, structural design criteria applicable to such a system did not exist. Design guides developed for submarine reactors were combined with strength requirements for aircraft turbojets and aircraft structures to arrive at the following structural design criteria. For additional information reference 16 is recommended.

Limit Loading Criteria

Limit loads are the most severe loads that the reactor could reasonably be expected to sustain during its service life and still function in accordance with design requirements. Accordingly, the design is such that neither failure nor excessive deformation of components results from subjecting the reactor to the specified limit loads required during the service life.

The reactor and its supports are designed to withstand the following limit loads, each acting separately or in any combination that can produce the most severe stress condition, without failure or permanent deformation.

1. Operational endurance loads
   a. Loads due to direct design pressure
   b. Loads due to a vertical downward load factor of 1. 0, i. e., normal weight loads
   c. Loads due to aerodynamic forces (including pressure drop)
   d. Loads due to anticipated thermal gradients, either transient or steady state
2. Operational inertial loads
   a. Loads due to direct design pressure
   b. Loads due to inertial load factors determined by the mode of operation of the power plant that contains the reactor (See Figure 2-1)
   c. Loads due to aerodynamic forces (including pressure drop)
   d. Loads due to anticipated thermal gradients, either transient or steady state
3. Ground operation in aircraft (landing, taxi, and takeoff operations)
   a. Loads due to direct design pressure
   b. Loads due to inertial load factors set forth in Figure 2-1, under caption "ground operation in aircraft"
   c. Loads due to aerodynamic forces (including pressure drop)
   d. Loads due to anticipated thermal gradients, either transient or steady state
4. Ground handling
   a. Loads due to direct design pressure, if applicable
   b. Loads due to inertial load factors determined by the conditions under which the reactor or power plant will be transported or handled (See Figure 2-1 for aircraft.)
   c. Loads due to aerodynamic forces, if applicable
   d. Loads due to anticipated thermal gradients, if applicable

Ultimate Loading Criteria

Ultimate loads are defined as being equivalent to 1. 5 times the limit loads, or the absolute maximum loads that the reactor could be subjected to during its service life. Subsequent to such loading the reactor would not be required to remain functional, as ultimate loads cause malfunction due to excessive and permanent deformation of components. Accordingly, the reactor and its supports are designed to withstand, without failure because of rupture, ultimate loads equivalent to 1. 5 times the limit loads specified above. "Failure" is interpreted as including detrimental changes in the systems charac-

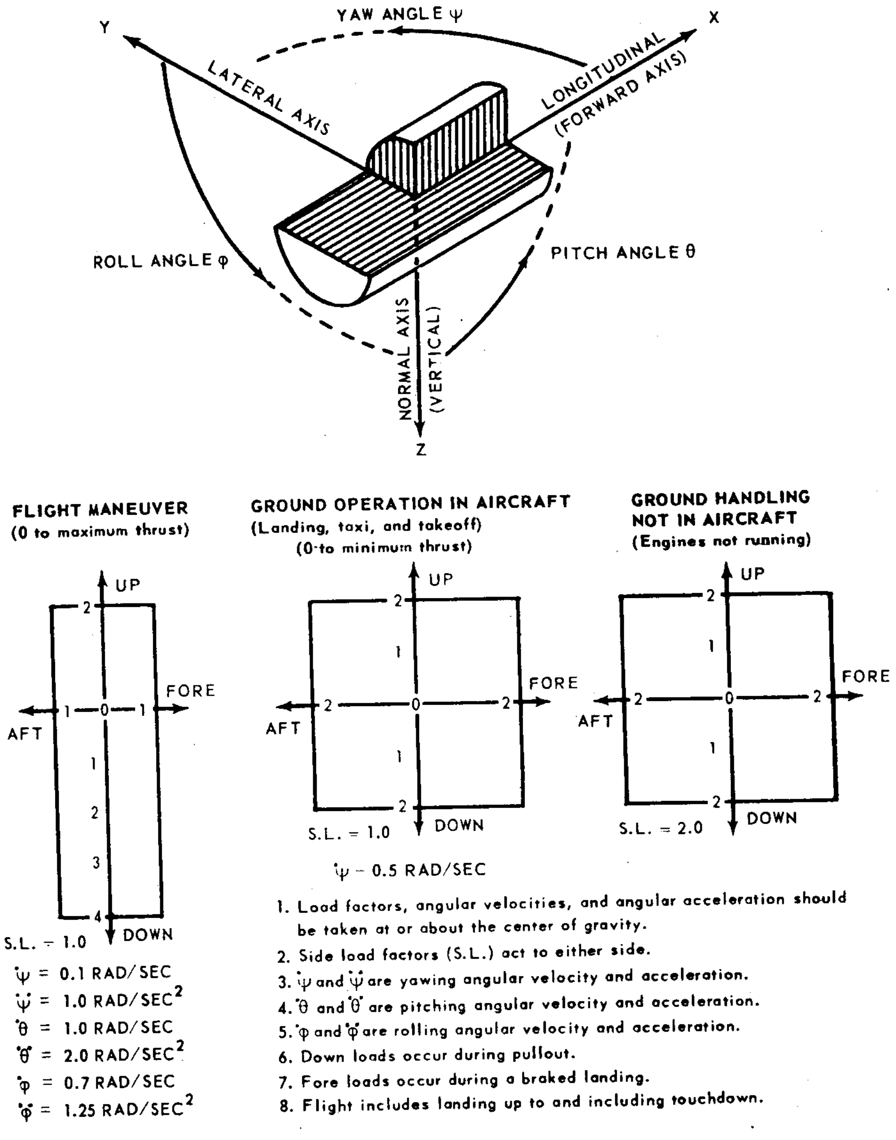
Y
YAW ANGLE ψ
X
LATERAL AXIS
LONGITUDINAL (FORWARD AXIS)
ROLL ANGLE φ
PITCH ANGLE θ
NORMAL AXIS (VERTICAL)
Z
FLIGHT MANEUVER
(0 to maximum thrust)
GROUND OPERATION IN AIRCRAFT
(Landing, taxi, and takeoff)
(0 to minimum thrust)
GROUND HANDLING NOT IN AIRCRAFT
(Engines not running)
UP
DOWN
FORE
AFT
2
1
0
1
2
3
4
S.L. = 1.0
S.L. = 1.0
S.L. = 2.0

$\dot{\psi}$ = 0.1 RAD/SEC
$\ddot{\psi}$ = 1.0 RAD/SEC^2
$\dot{\theta}$ = 1.0 RAD/SEC
$\ddot{\theta}$ = 2.0 RAD/SEC^2
$\dot{\varphi}$ = 0.7 RAD/SEC
$\ddot{\varphi}$ = 1.25 RAD/SEC^2

$\dot{\psi}$ - 0.5 RAD/SEC

1. Load factors, angular velocities, and angular acceleration should be taken at or about the center of gravity.
2. Side load factors (S.L.) act to either side.
3. $\dot{\psi}$ and $\ddot{\psi}$ are yawing angular velocity and acceleration.
4. $\dot{\theta}$ and $\ddot{\theta}$ are pitching angular velocity and acceleration.
5. $\dot{\varphi}$ and $\ddot{\varphi}$ are rolling angular velocity and acceleration.
6. Down loads occur during pullout.
7. Fore loads occur during a braked landing.
8. Flight includes landing up to and including touchdown.

Fig. 2-1 – Example of power plant design limit load factors for aircraft

teristics as a result of permanent deflections, or a malfunction within the time required to complete the mission.

If the reactor operates in an aircraft, or other vehicle, the reactor and its supports must be designed to withstand crash loads, which act separately or in any combination to produce the most severe stress conditions, without causing separation of the major components from the reactor assembly or failure of the reactor supports. Typical conditions are:

1. Loads due to direct design pressure
2. Loads due to inertial load factors acting forward, down, up, or to either side, each inertial load factor acting independently, i. e., for aircraft, loads are 8 G forward, 4.5 G down, 2 G up, and 1.5 G to the side.
3. Loads due to aerodynamic forces (including pressure drop)
4. Loads due to anticipated thermal gradients, either transient or steady state

The reactor is not required to function after being subjected to crash loads.

Thermal and Mechanical Stress Combination

The combinations of thermally and mechanically induced stresses are evaluated according to the straight line hypothesis graphically presented in Figure 2-2 . The second and fourth quadrants of the diagram are rectangular, indicating that the assumption is made that mechanical and thermal stresses of opposite sign do not alleviate each other, i. e., it is presumed that conditions will generally exist in which each might act separately. A point is drawn on this diagram representing the calculated combination of mechanical (σ_m) and thermal stresses (σ_t) for the given design conditions. If the point falls inside the diagram, the structures are considered to have adequate structural strength. In the triangular region a radial line drawn from the origin through the point representing the state of stress and intersecting the allowable stress line is used to indicate the margin of safety.

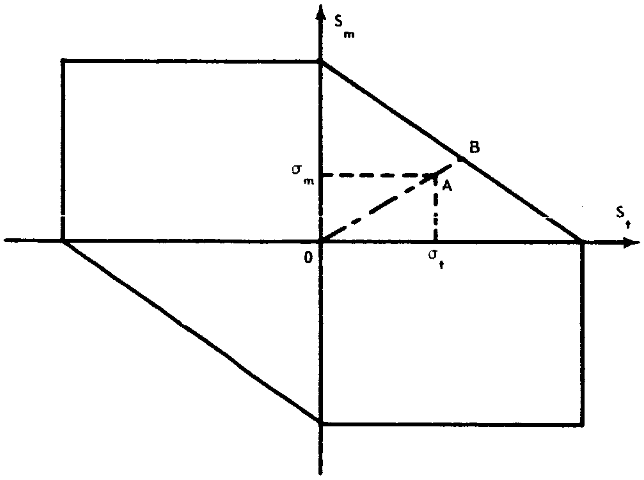

Fig. 2-2 – Combination stress diagram – thermal and mechanical

In those instances where vibratory stresses are of interest, the combination of mechanical and thermal stresses are combined with the vibratory stresses in a manner similar to that described above. This is done using the graphical procedure illustrated in Figure 2-3 . In this straight line relationship S_v represents the allowable alternating stress, e. g., endurance limit, or fatigue strength for a specified number of cycles, and the points OA and OB are taken from the nonvibratory stress diagram of Figure 2-2 . In those cases where sufficient experimental data are available for the material under consideration, the proper nonlinear relationship is substituted for the straight-line relationship of Figure 2-3 .

The margin of safety is computed for the combined mechanical and thermal stresses by the equation

$$\text{M. S.} = \frac{OB}{OA} - 1 \qquad (1)$$

The zero margin of safety line is defined by the line

$$\frac{\sigma_m}{S_m} + \frac{\sigma_t}{S_t} = 1 \qquad (2)$$

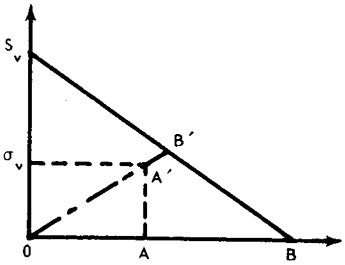

Fig. 2-3 – Combination stress diagram – vibratory, thermal, and mechanical

and the

$$\text{M. S.} = \frac{1}{\frac{\sigma_m}{S_m} + \frac{\sigma_t}{S_t}} - 1 = \frac{S_m S_t}{\sigma_m S_t + \sigma_t S_m} - 1 \tag{3}$$

S_m = allowable mechanical stress, psi
S_t = allowable thermal stress, psi
S_v = allowable vibratory stress, psi
OB = value of OB in Figure 2-2
OA = value of OA in Figure 2-2
σ_m = applied mechanical stress, psi
σ_t = applied thermal stress, psi
σ_v = applied vibratory stress, psi

The margin of safety for stress combinations occurring in the second and fourth quadrants is used as the minimum margin of safety computed for either the mechanical or thermal stress condition alone.

Composite Service Life Requirements

In the cases where the structural integrity of a component is based on the creep strength or stress-rupture strength of the material, a method is available for examining the integrity of the component when the total life is governed by a composite mode of operation. The composite mode of operation is defined as one where the stress and/or temperature in the component is constant for only one phase of its total life, and is different for each of the other phases of the component life. In the method used for examining the structural integrity of the component which undergoes the composite mode of operation, it is assumed that the various phases can occur in any order and that the integrity of the component is independent of the order in which the stress and temperatures of the various phases are applied.

In analyzing composite modes of operation, the expected life of each phase is determined from stress-rupture or creep-strength curves which are calculated from the Larson-Miller parameter described in reference 18, where

$$P = (T + 460)(C + \log_{10} t) \times 10^{-3} \tag{4}$$

T = temperature, ^{o}F
t = time, hours
C = a constant dependent upon the particular material or class of material. If sufficient material test data are unavailable to determine the constant, a value of C = 20, in general, gives good correlation for most high temperature metallic alloys in use.

To apply this criterion in a consistent manner it is necessary to know the ratio σ/S (the used-up mechanical stress) in order to combine it with the stress used up under conditions of thermal or vibratory stress. Therefore, the various phases are transformed into equivalent phases having the same stress and temperature levels and an appropriate equivalent life for that phase. This is done using the relationships given in reference 19. The calculation of an equivalent composite operational phase time is dependent upon the ability to trade "time for temperature" and "time for stress."

The relationships used to determine the equivalent life of each phase of the mission are as follows:

$$t_n^{T\sigma} = t_n^{T} \left(\frac{\sigma}{\sigma_n}\right)^m \qquad (5)$$

where

$$\log_{10} t_n^{T} = \frac{(T_n + 460)}{(T_o + 460)} (C + \log_{10} t_n) - C \qquad (6)$$

and

$$m = \frac{(P_o - P_n) \times 10^3}{(T_o + 460)(\log_{10} \sigma_o - \log_{10} \sigma_n)} \qquad (7)$$

$t_n^{T\sigma}$ = equivalent time of the nth phase
o = stress and temperature of the base phase
n = stresses, temperatures, and time of the nth phase being examined
P_o and P_n = Larson-Miller parameters which are found from the 80 percent strength line, for the corresponding stress, of the stress-rupture or creep-strength curves for the material
C = Larson-Miller constant

Sample Composite Life

The application of Equation (5) is illustrated by analyzing a sample composite mode using the stress-rupture data shown in Figure 2-4. The mission analyzed consists of two phases having the following values for stress, temperature, and required life:

Base Phase Data	Secondary Phase Data
σ_o = 20,000 psi	σ_1 = 7000 psi
T_o = 1000°F	T_1 = 1200°F
t_o = 1500 hours	t_1 = 1000 hours

The equivalent time corresponding to a uniform base phase temperature can be found from the following relationship:

$$\log_{10} t_1^{T} = \frac{T_1 - 460}{T_o + 460} (20 + \log_{10} t_1) - 20 \qquad (8)$$

so that

$$t_1^{T} = 1.415 \times 10^6 \text{ hours} \qquad (9)$$

Using the data curve of Figure 2-4, the two parameters, P_o and P_1, corresponding to 20,000 psi and 7000 psi respectively, are found to be

$$P_o = 35.2, \quad P_1 = 40.2$$

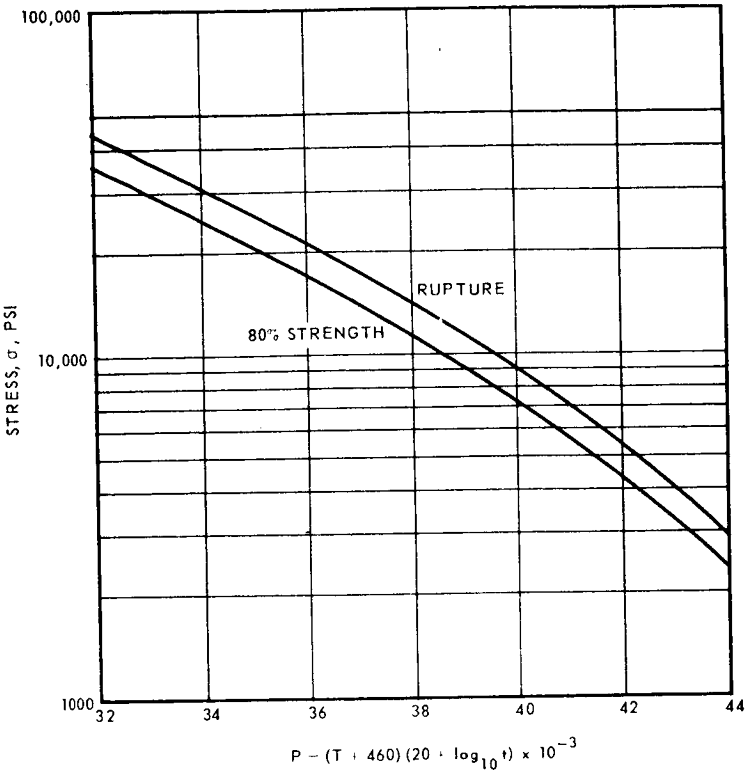

Fig. 2-4 – AISI 321 SST wrought-annealed, rupture and 80 percent stress-rupture curves

The index m can be found from the equation

$$m = \frac{(P_o - P_1) \times 10^3}{(T_o + 460)(\log_{10} \sigma_o - \log_{10} \sigma_1)} \tag{10}$$

or

$$m = \frac{(35.2 - 40.2) \times 10^3}{(1460)(4.3010 - 3.38451)} = -7.51$$

The equivalent time can then be found from the equation

$$t_1^{T\sigma} = t_1^{T} \left(\frac{\sigma_o}{\sigma_1}\right)^m \tag{11}$$

or

$$t_1^{T\sigma} = (1.415 \times 10^6)(0.35)^{7.51} = 537 \text{ hours}$$

The final combined equivalent phase is

$\sigma_o = 20,000$ psi
$T_o = 1000^oF$
$t_{eq} = t_o + t_1 = 2037$ hours.

Entering the curve of Figure 2-5 at a temperature of 1000°F, and extrapolating between a life of 1000 hours and 5000 hours to obtain a point for 2037-hours life, the corresponding value of P is found to be approximately 34. In Figure 2-4, reading up from

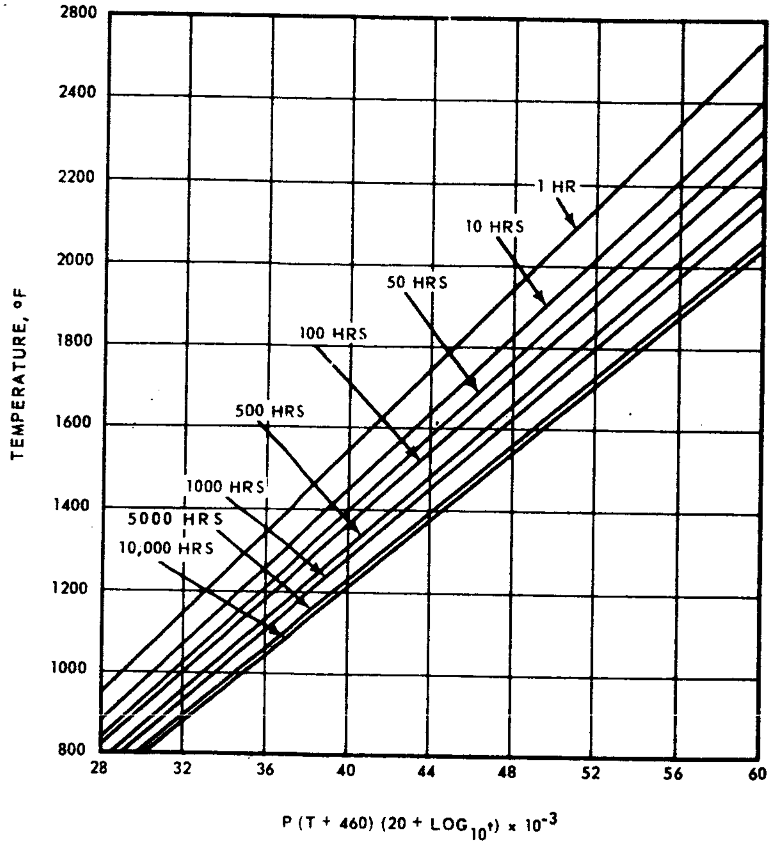

Fig. 2-5 – Larson-Miller parameter

a value of $P = 34$ to the 80 percent strength line, the allowable stress is seen to be 25,000 psi. Then, the ratio

$$\frac{\sigma}{S} = \frac{20,000}{25,000} = 0.8 \tag{12}$$

Thus, the margin of safety is

$$\text{M.S.} = \frac{S}{\sigma} - 1 = +0.25 \tag{13}$$

2.2 MATERIAL CONSIDERATIONS IN STRUCTURES

The design considerations for the reactor support structure are comparable to those for a conventional heat exchanger operating at the same temperature and pressure. However, the nuclear environment of the reactor necessitates additional considerations with respect to the selection of the structural materials and with respect to the maintenance requirements. One of the aspects of material selection is the absorption of neutrons. Neutron economy is an important consideration inside the reactor core. Neutron absorbers either shorten the useful life of the reactor or increase the amount of nuclear fuel needed for a given power output since they remove neutrons that could contribute to the fission process. A structural material should have a low neutron absorption cross section. Although the bulk of the neutrons that cause fission in hydrogen-moderated reactors are at, or near, thermal energies, the structural material cannot be based on thermal cross section comparison. Certain materials, such as molybdenum, for example, have relatively low thermal cross sections with large resonance capture cross sections at higher neutron energies. Therefore, these elements are less desirable than a material like nickel, which has a higher thermal cross section, but a lower cross section when integrated over the whole spectrum of the reactor. The volume and location of the structural material may also be an important consideration in the structural design.

The effect of reactor radiations upon the structural materials must also be considered. Dimensional stability and changes in material properties are the main concerns. The degree to which the material properties change is a function of the material composition, temperature of irradiation, and the quantity and energy of the radiation. Generally, the tensile and yield strengths of structural materials increase with increasing neutron irradiation. This offers little, if any, benefit to the designer as the allowable stresses are normally based on unirradiated properties.

The designer is most concerned with the extent to which radiation reduces the ductility and raises the temperature of the transition from ductile to brittle fracture under impact loading. A rapid change in reactor power may cause a thermal transient that can have an effect similar to a sudden impact. This makes prevention of brittle failure an essential consideration on the design of the structure. Appreciable changes in the transition temperature may occur with increasing dosage at irradiation temperatures below 500°F. Irradiation at temperatures above 500°F usually results in less damage of this type than irradiation at lower temperatures, presumably because of concurrent thermal annealing of the material. Therefore, structural materials with a low transition temperature in the unirradiated condition such as austenitic stainless steels are the most desirable. Radiation damage in structural materials is discussed in a subsequent lecture.

In addition to the nuclear and thermal material properties discussed above, the mechanical properties, such as tensile strength, impact strength, and creep strength, must be adequate for the operating conditions. The reactor structural material should have adequate corrosion and oxidation resistance in the selected coolant or other environmental fluid. It also must be possible to fabricate the structural material in the required shapes and to make joints or welds that are needed. Compatibility of contacting materials must also be assured at elevated temperatures. Anisotropic properties must be considered in design and proper material orientation assured throughout fabrication. Toxicity and pyrophoric qualities also must receive prime attention during handling. Material considerations for reactor components are of prime importance to the designer and are therefore covered in separate lectures.

3.0 HIGH TEMPERATURE DESIGN AND THERMAL STRESSES

Among the recurring design problems in a compact gas cooled reactor are those associated with high temperature levels, the component transients (temperature-time relation), and the internal heat generated. The latter varies over a wide range depending upon the material, reactor power level, and the location within the reactor assembly. Much design time is consumed in defining design conditions. A well knit team approach is required to properly evaluate these complex effects on the design. It is especially important that "worst cases" or "limiting design cases" be identified during the preliminary design phases.

In this section are discussed unrestrained thermal expansions, stresses arising from restrained thermal expansions, transient design problems, and material thermal stress resistance. Actual designs are used to illustrate the problems.

3.1 Unrestrained Thermal Expansions

Materials normally expand as they are heated. The change in length per unit length (strain) is

$$\epsilon_{th} = \frac{\Delta 1}{1} = \alpha \, \Delta T \qquad (1)$$

where α is the linear coefficient of thermal expansion and ΔT is the temperature change. This thermal expansion can be used to advantage. For example a tight jar lid can be loosened readily after the metal lid has been heated a few seconds by hot water. In a reactor the differential thermal expansions between components must be allowed for to prevent binding. A 30 inch metallic fuel cartridge may grow in length 0.3 inch more than the structural tube in which it is contained. Thus, pitot tubes and thermocouples must be initially spaced away from the cartridge end.

When a linear temperature distribution exists in a plate, the plate will expand as shown in Figure 3.1-1. No stresses will be set up unless the expansion is restrained. A typical GE-ANPD air cooled control rod was assembled from short length segments by semi-flexible straps to prevent bowing and possible seizure due to unequal heating across the diameter, see Figure 3.1-2. Eccentricity within its guide tube (see Figure 3.1-3), non-uniform material distribution, and variation in heat flux density across the rod could contribute to the unequal heating. A typical limiting case temperature differential across the rod was estimated to be 330°F and the resulting

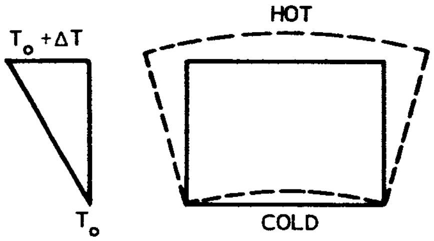
HOT
$T_o + \Delta T$
T_o
COLD

Fig. 3.1-1 – Plate with linear temperature distribution

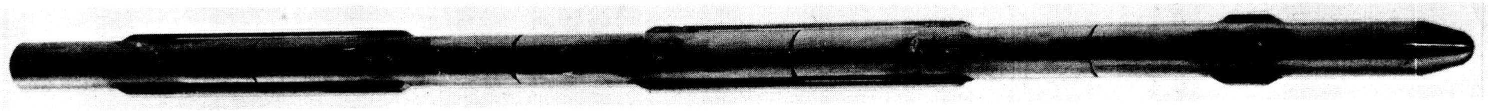

Fig. 3.1-2 – Typical GE-ANP control rod (Neg. U38803B)

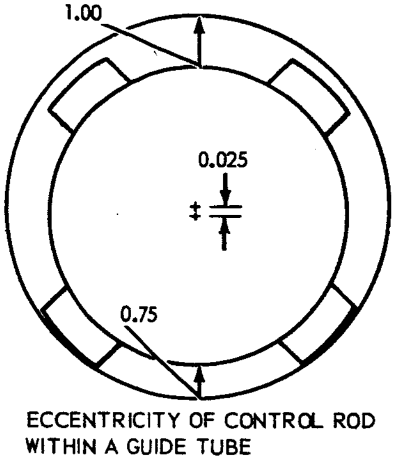
1.00
0.025
0.75
ECCENTRICITY OF CONTROL ROD
WITHIN A GUIDE TUBE

Fig. 3.1-3 – Two extreme cases of eccentricity of a control rod within a guide tube

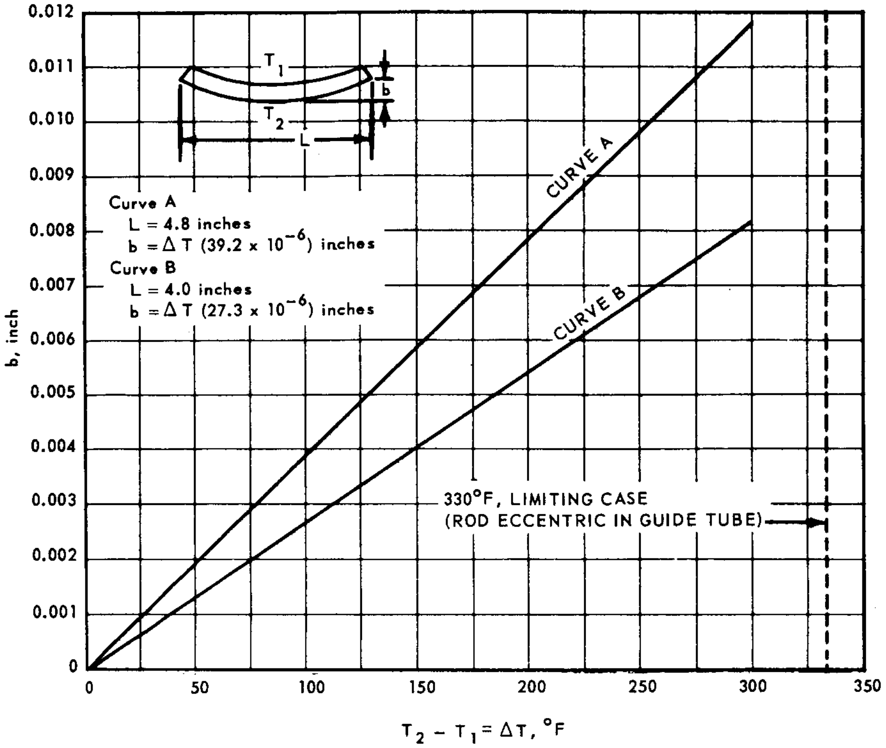

Fig. 3.1-4 – Control rod segment thermal bowing due to temperature differential between sides

camber of a single segment is shown in Fig. 3.1-4. Thermal camber is discussed further in Section 4.5.2.2 and equations are given.

3.2 Thermal Stresses

When the free thermal expansions of an element are restricted, stresses are set up so that each element will have dimensions compatible with neighboring elements. If a plate is heated along the centerline and cooled at the edges as shown in Fig. 3.2-1, stresses result. If the plate were cut along the hot centerline, two plates similar to that shown in "b" result. In order to join the halves into a single plate again, tensile forces must be applied at the edges and compressive forces at the center. These forces in an uncut plate represent the temperature stresses due to internal restraint.[12]

In the elastic range of a material, the strain is proportional to stress, σ. The strain in the x direction due to forces in the "x" direction is:

$$\epsilon_x = \frac{\sigma_x}{E} \qquad (2)$$

where E is the modulus of elasticity. If additional forces exist in the "y" direction, these cause a dimension change, also in the "x" direction, according to:

$$\epsilon_x = \frac{-\nu\sigma_y}{E} \qquad (3)$$

where ν is the poisson's ratio. Forces in the "z" direction similarly produce a strain in the "x" direction:

$$\epsilon_x = \frac{-\nu\sigma_z}{E} \qquad (4)$$

Thus, the cumulative effect of these mechanical stresses results in a strain

$$\epsilon_x = \frac{1}{E} \left[\sigma_x - v\,(\sigma_y + \sigma_z)\right] \qquad (5)$$

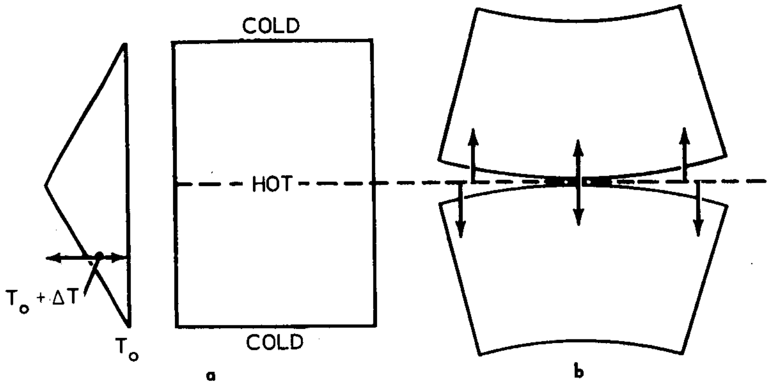
COLD
HOT
COLD
$T_o + \Delta T$
T_o
a
b

Fig. 3.2-1 – Plate heated along the centerline and cooled at the edge

Equation (5) is Hooke's law for a homogeneous and isotropic material. Poisson's ratio for an isotropic material ranges between 0 and 0.5. When both thermal and mechanical strains exist, the total strain in the x direction is:

$$\epsilon_x = \frac{1}{E} [\sigma_x - \nu(\sigma_y + \sigma_z)] + \alpha \Delta T \qquad (6)$$

similarly in the y and z direction:

$$\epsilon_y = \frac{1}{E} [\sigma_y - \nu(\sigma_x + \sigma_z)] + \alpha \Delta T \qquad (7)$$

$$\epsilon_z = \frac{1}{E} [\sigma_z - \nu(\sigma_x + \sigma_y)] + \alpha \Delta T \qquad (8)$$

Several cases of external restraint of thermal expansions will be considered. Case I: A uniform bar rigidly fixed at the ends is heated. Since the bar is prevented from expanding, $\epsilon_x = 0$. If lateral forces do not exist, i.e. $\sigma_y = \sigma_z = 0$, equation (6) yields;

$$\sigma_x = - \alpha E \Delta T$$

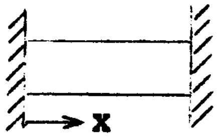

The negative sign indicates compressive stresses.

Case II: If the bar is heated and rigidly restrained in both the x and y directions but free to expand in the z direction:

$$\epsilon_x = 0, \quad \epsilon_y = 0, \quad \sigma_z = 0$$

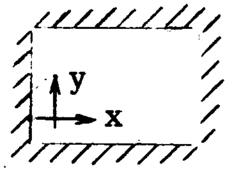

from equation (6)

$$\sigma_x - \nu \sigma_y = - \alpha E \Delta T$$

from equation (7)

$$\sigma_y - \nu \sigma_x = - \alpha E \Delta T$$

combining these yields

$$\sigma_x = \sigma_y = - \frac{\alpha E \Delta T}{1 - \nu} \tag{9}$$

The strain in the free direction is found from equation

$$\epsilon_z = - \frac{\nu}{E} \left(\sigma_x + \sigma_y \right) + \alpha \Delta T$$

Combining the last two equations gives

$$\epsilon_z = \left[\frac{1 + \nu}{1 - \nu} \right] \alpha \Delta T \tag{10}$$

Case III: If the bar is heated but restrained in all three directions, the three strains are zero and the stresses are

$$\sigma_x = \sigma_y = \sigma_z = - \frac{\alpha E \Delta T}{1 - 2\nu} \tag{11}$$

A perfectly rigid mounting is physically non-existent. However, the three cases are useful reference points when comparing various materials or shapes subject to temperature changes. A useful parameter (single restraint) is

$$\gamma = \frac{\sigma}{\alpha E \Delta T}$$

where γ is a factor dependent on the geometry of the physical system and a measure of its rigidity. A free expansion is denoted by $\gamma = 0$ while $\gamma = 1$ denotes complete restraint in one dimension. ($\gamma = \frac{1}{1 - (N-1)\nu}$ for complete restraint in N-dimensions: N = 1, 2, 3).

Case IV: Partial Restraint

The struts a, b and c join two "rigid" blocks. Struts a and c are of equal area, A and temperature T_0. Strut b has an area $\frac{A}{2}$ and a temperature $T_0 + \Delta T$. The struts are of a common material. Find the thermal stress in b and the amount of restraint.

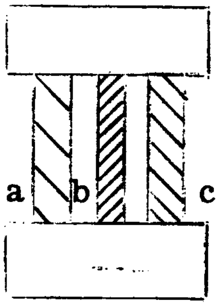

Assume sufficient section in the strut to prevent buckling. Since no external mechanical loads are present, the loads in the three struts must be "self-equilibrating", this condition is common to all thermal stress problems in which there are no external constraints.

The change in strut lengths is equal, thus

$$\epsilon_a = \epsilon_b = \epsilon_c \tag{12}$$

Since equilibrium exists, the net force is zero, i.e.:

$$\Sigma F = 0$$

$$A \cdot \sigma_a + \frac{A}{2} \sigma_b + A\sigma_c = 0$$

and the stress in strut b is:

$$\sigma_b = -4\sigma_a \tag{13}$$

From equation (12),

$$\epsilon_a = \left(\alpha T_0 + \frac{\sigma a}{E} \right) = \epsilon_b = \left(\alpha T_0 + \alpha \Delta T + \frac{\sigma b}{E} \right) \tag{14}$$

Therefore

$$\sigma_a - \sigma_b = E \alpha \Delta T \tag{15}$$

Substituting (8) into (10) yields

$$\sigma_a = \frac{1}{5} E \alpha \Delta T \tag{16}$$

and

$$\sigma_b = -\frac{4}{5}\alpha E\,\Delta T \tag{17}$$

Therefore the degree of restraint on strut b is

$$\gamma = -0.8$$

It should be noted that any change in material (α and E properties), strut cross sectional area ratio, or the temperature difference will change the stress level. Case IV is analogous to the differential thermal expansion problem for a cladding bonded to the surface of a fuel element. This problem is discussed in greater detail in the appendix.

A common misconception with regard to the factor γ, is that it cannot exceed the value $\gamma = 1/1-(N-1)\nu$. Consider a problem identical to Case IV except that narrow slits have been added to bar b as illustrated.

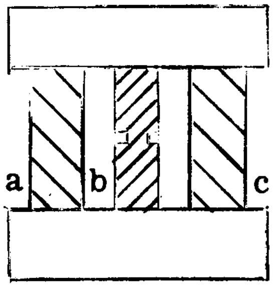

The slits are so narrow that the overall stiffness of bar b is essentially unaltered in the elastic range. Therefore the load in bar b will still be

$$P_b = -\left(\frac{A}{2}\right)\left(\frac{4}{5}\right)\alpha E\,\Delta T \tag{18}$$

Denoting the cross-sectional area of the bar at the slits by A_s, the nominal stress on this section will be

$$\sigma_{bs} = \frac{P_b}{A_s} = -\left(\frac{2}{5}\right)\left(\frac{A}{A_s}\right)\alpha E\,\Delta T \tag{19}$$

In addition, there will be a stress concentration at the root of these slits. Denoting the stress concentration factor by K, the maximum stress in bar b is

$$\sigma_{bmax} = -\frac{2}{5}K\left(\frac{A}{A_s}\right)\alpha E\,\Delta T \tag{20}$$

Therefore

$$|\gamma| = \frac{2}{5} K \left(\frac{A}{A_s}\right) \tag{21}$$

The stress concentration factor can easily be as high as 5 if the radius at the root of the slits is small, and the area ratio can be almost any value greater than unity. Suppose both K and the area ratio are 5.0 then

$$|\gamma| = (2/5)\ (5)\ (5) = 10 \tag{22}$$

A stress raiser of this nature can produce premature failure in brittle materials or a serious strain concentration in ductile materials which will greatly reduce the cyclic life of the component. A stress raiser of this nature in a design would be representative of very poor design practice. It is the type of thing referred to by Thompson and Rogers'[17] statement "An ingenious design to eliminate thermal stresses is preferable to an ingenious calculation of an inferior design."

Case V: Internal Restraint

The case of a plate subject to a temperature distribution symmetric about the mid-plane as illustrated is an example of internal or "self" restraint. Away from the edges of the plate, the maximum thermal stress for this case occurs at the surfaces and has the value

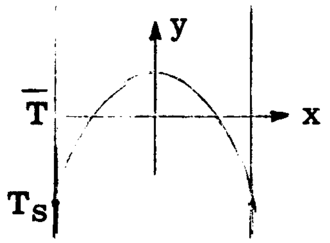

$$\sigma_{max} = \sigma_{ys} = \frac{E\alpha}{1-\nu} (\bar{T} - T_s) \tag{23}$$

where $\bar{T}$ = Average temperature
T_s = Surface temperature

In general, the maximum stresses will occur at a surface, and for bodies with one or more degrees of symmetry the equation for calculating the maximum stress can be put in a form analogous to (23) but utilizing the factor γ.

This form is

$$\sigma_{max} = \gamma E \alpha \Delta T$$

where

$$\Delta T = \overline{T} - T_s$$

The following table gives values of γ for several simple shapes.

Shape	Representative Temperature Profile	γ
Thin Plate (1)	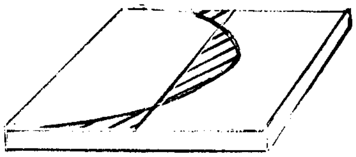	1.0
(2)	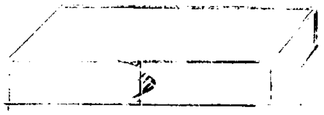	$\left(\frac{1}{1-\nu}\right)$
Thin Circular Disk	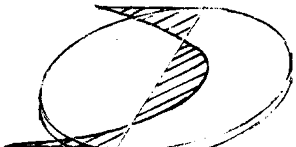	1.0
Long Solid Cylinder	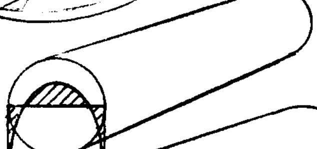	$\left(\frac{1}{1-\nu}\right)$
Long Hollow Cylinder	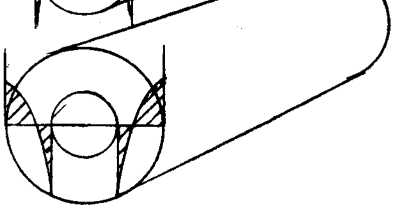	$\left(\frac{1}{1-\nu}\right)$

The temperature distributions used in these calculations are obtained independently of the stress solutions, i.e., the thermoelastic equations are uncoupled. (Boley and Weiner[20] discuss the coupled thermoelastic equations but show that for the vast majority of engineering problems the coupling effect need not be considered.) Therefore, the stress solution is quasi-static in the sense that it is the static stress solution for the transient (or steady) temperature distribution at a given instant of time.

Boley and Weiner also discuss the problem of dynamic coupling, i.e., inertia effects in thermal shock problems. Again the conclusion reached is that rarely if ever is it necessary to include these effects in practical engineering problems.

The ANPD ceramic fuel element was basically a long cylindrical tube. The details of the stress analysis of this element are discussed in the appendix.

3.3 Transient Conditions

As noted in the previous section, the thermal stress calculations are essentially static. Transient thermal stress levels can be significantly improved through the use of good design practice. This can be accomplished by several means (1) reducing the degree of internal restraint by reducing the size of the pieces involved, (2) reducing and/or delaying the maximum temperature gradients through the use of insulation or controlled coolant flow and (3) changing materials. The latter is frequently not possible due to the nuclear requirements of the system.

The 140E forward reflector illustrates the use of insulation to reduce temperature differences occurring during reactor scram conditions. The beryllium reflector consisted of twelve 30° sectors arranged to form a perforated circular plate just forward of the ceramic tube bundle. It served as a neutron reflector and restrained the ceramics during forward inertia loads. The perforations permitted coolant flow to the active core and side reflector regions.

Thermal stresses in the plate during steady-state conditions were negligible when compared to those for transient conditions. Immediately after shutdown when the inlet air temperature dropped rapidly, the plate temperature ahead of the side reflector lagged that of the active core region due to the larger heat removal capability in the latter region (an order of magnitude). Insulation placed in the perforation in the form of a thin walled tube in the area ahead of the active core provided a sufficient temperature lag, thus minimizing the temperature difference. The lower curve of Fig. 3.3-1 shows the margin of safety in the beryllium plate for the uncorrected condition. The upper curve illustrates the design fix..

Suddenly Cooled Flat Plate

As another example of transient solutions consider the problem of a flat plate initially at a uniform temperature $T = T_0$. If the lateral surfaces of the plate are suddenly exposed to a coolant with temperature, T_a, and film heat transfer coefficient, h, at time zero, the resulting "thermal shock" will produce a transient thermal stress condition. The maximum stress level and also the time of occurrence of the maximum stress will depend on the value of Biot's modulus, $\beta = hL/k$, where L = one-half the plate thickness and k = the conductivity of the plate material. Figure 3.3-2 is a non-dimensional plot of maximum stress and time of maximum stress versus Biot's modulus.

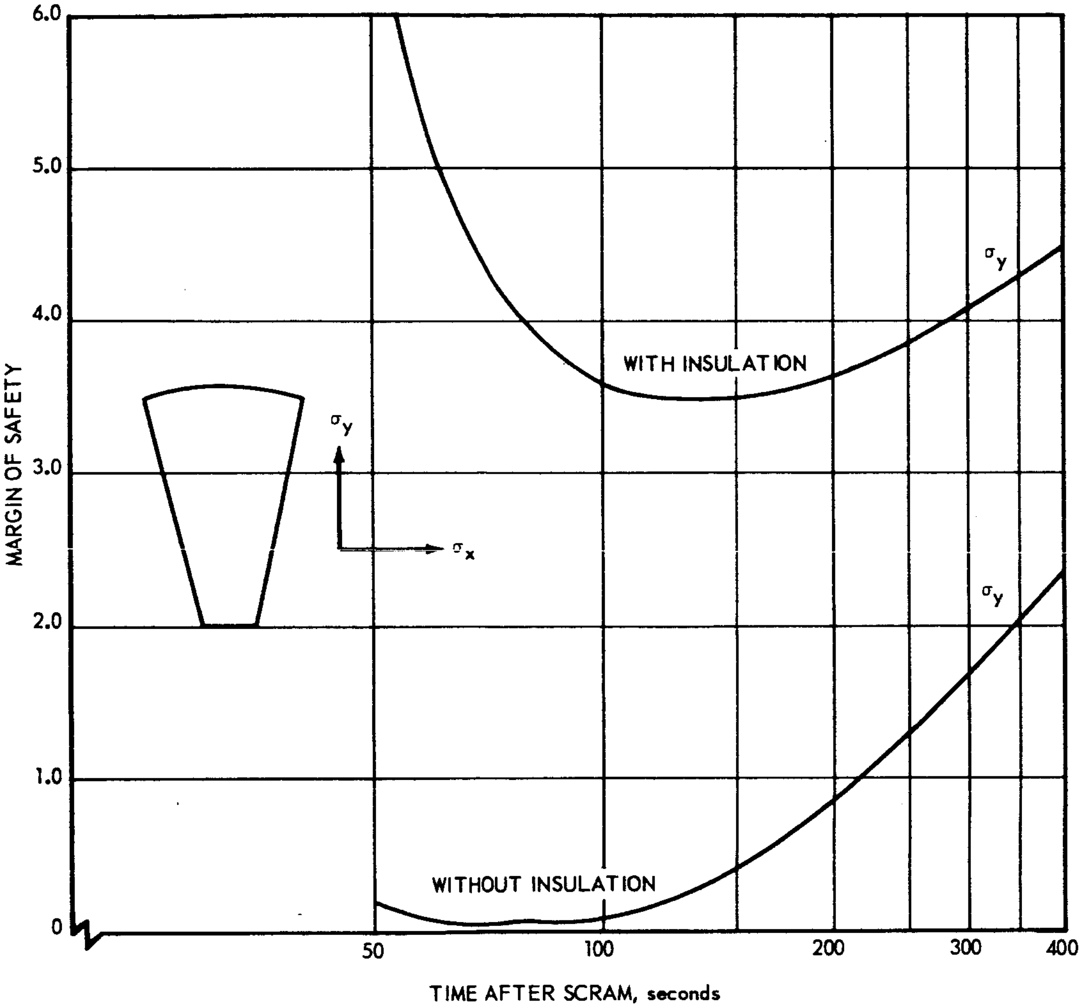

Fig. 3.3-1 – Forward reflector thermal stress safety margins

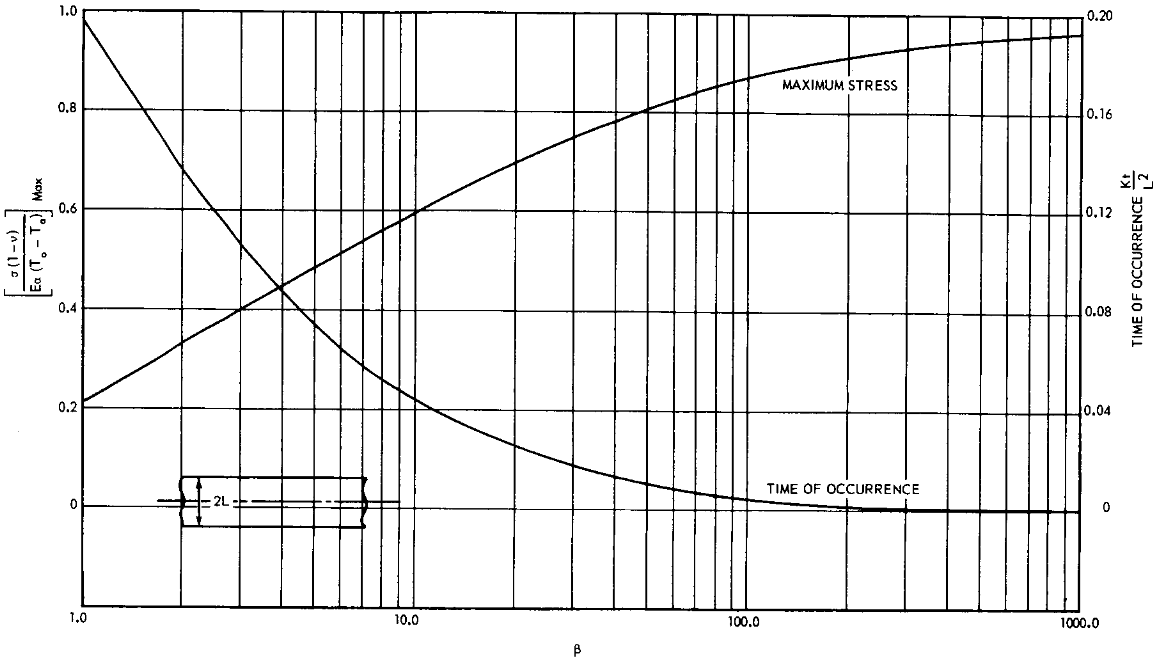

Fig. 3.3-2 – Maximum stress level and time of occurrence versus Biot's modulus

3.4 SPECIAL MATERIALS CONSIDERATIONS

The thermal stress problems discussed so far have assumed that the material is (1) homogenous - i.e., has the same properties at every point of the body, (2) isotropic - i.e., that the properties of the material at a point are the same in all directions and (3) the materials properties (locally) are not temperature dependent.

The first assumption is generally quite good for most engineering materials provided the process quality control is good.

The assumption of isotropy is not always valid. Some forms of graphite are highly anisotropic. The following discussion should give some idea of the added complexity in thermal stress analysis arising from anisotropy. For the completely isotropic material considered so far, there are only two basic material constants (E, v) required to define the elastic response (stress strain-relations). For a completely anisotropic material, there are in general 36 elastic constants[21] required to define the elastic response plus 6 thermal expansion coefficients. Fortunately it has been shown from basic thermodynamic considerations that only 21 of the 36 elastic constants are independent, but even this does not make the problem tenable. No general thermal stress solutions are available for the completely anisotropic material. Most materials exhibit some degree of isotropy. A special case of interest is the orthotropic material which has three planes of elastic symmetry and requires 9 elastic constants to define its elastic response.

Some of the graphites - notably pyrolytic graphite - are representative of another class of orthotropic materials referred to as monotropic materials which exhibit elastic symmetry about a plane and also about an axis normal to this plane. These materials require 5 elastic constants to define their elastic response. Garber[22] gives a very good discussion of thermal stresses in heat shields of pyrolytic graphite. Generally, as in the case of pyrolytic graphite, there will be anisotropy of other properties also, e.g., conductivity, associated with the elastic anisotropy, which adds additional complications to the analysis. For a single significant thermal cycle, e.g., as in the case of the heat shield, the added complications of analysis are easily justified since the associated anisotropy of the conductivity is extremely beneficial in the heat shield problem. However, in problems involving high cyclic thermal strains, the presence of elastic anisotropy is generally undesirable since it greatly reduces the life of the component.

The final assumption of local independence of material properties on temperature is valid provided the local temperature variations from the mean are small (of the order of 100°F or less). However each problem should be evaluated on its own merits to determine the validity of this assumption.

Flow and Failure Criterion

Frequently engineers confuse failure criterion with inelastic flow criterion. The latter defines the boundary between the elastic and inelastic domains of a state of stress in a body. The VonMises-Hencky or Tresca conditions are the generally accepted criteria for the initiation of inelastic deformations. The Tresca condition is simpler to apply in hand calculations since it is expressed in terms of a limiting value of the maximum shear stress while the VonMises-Hencky condition is expressed in terms of the second invariant of the deviatoric stress tensor, which is an unfamiliar quantity to most practicing engineers. When computer solutions are used however, there is little difference in the calculation time for the two methods and therefore the VonMises-Hencky condition is generally used since it is in closer agreement with experimental results.

The failure criterion for materials is not nearly as well defined as the flow criterion. For brittle materials, the maximum principle stress failure criterion is generally used due to its simplicity. The other more common failure theories for brittle materials are (1) Mohr's theory of strength which includes the effect of mean stress on failure. Nadai[23] gives a very complete discussion of Mohr's theory of failure, (2) Griffith crack propogation criteria and (3) Weibell's statistical approach. In general, the last two are very difficult to apply in practice and are not recommended for most engineering applications.

Failure of ductile materials is extremely difficult to predict with any degree of accuracy except in the very simplest of problems. As a result, the approach taken is to place a limit on the total inelastic deformation in a single cycle or a limit on the maximum plastic strain per cycle for multiple cycles.

In the event of multiple cycles of varying amplitude, a "cumulative damage" criterion is used to account of the fraction of the structures useful life which is expended by the number of cycles associated with each particular amplitude.

The most commonly used cumulative damage criterion is that due to Minor which states that

$$\sum_{i=1}^{m} \frac{n_i}{N_i} \leq k$$

where:

n_i is the number of cycles associated with the i-th amplitude.

N_i is the allowable cyclic life if only cycles of the i-th amplitude are involved.

k is a constant associated with the specific material. Generally $k \leq 1.0$ but for some materials may be as high as 3.0. However a value greater than 1.0 should not be used unless a very large amount of experimental evidence is available in support of the higher value.

m is the number of different significant amplitude values.

4.0 CERAMIC REACTORS

4.1 INTRODUCTION

Because of their great thermal stability and refractory nature, ceramic materials appear to be especially suited for use in reactors operating at elevated temperature approaching and even exceeding the melting point of the high temperature-alloys.

The ceramic reactors considered herein are beryllium moderated (the beryllium is in the form of BeO) and fueled with fully enriched uranium (the uranium is in the form of UO_2). Fuel elements are in the shape of small tubes fabricated from a basic ceramic matrix of UO_2 uniformly dispersed in BeO. Various additives and cladding are used to perform specific functions.

The technology described herein is based upon the development of ceramic reactors to be used in direct air cycle nuclear turbojets, and these reactors are used to illustrate the design principles being described. The principles, however, are applicable to generalized gas cooled, high temperature reactors, requiring only the usage of the proper physical, chemical, and nuclear properties of the gas coolant.

A number of ceramic materials were recognized as having potential value as fuel-carrying materials due to their inherent refractory properties and good strength at the desired temperature levels. Thus, feasibility studies toward a ceramic fuel element began in 1953 with the nuclear ramjet missile as an initial application. During this time research studies were conducted on silicon carbide (SiC), molybdenum disilicide ($MoSi_2$), beryllia (BeO), magnesium oxide (MgO), zirconia (ZrO_2), and alumina (Al_2O_3).

Engineering investigations conducted concurrently with the material studies identified a number of requirements and system characteristics. To minimize the fuel inventory, an epithermal neutron spectrum was chosen and a good neutron moderator became a material requirement. A nearly homogeneous fuel element was obtained by dispersing the fuel in a ceramic moderator. Uranium dioxide, UO_2, converts to a more volatile oxide in the presence of oxygen at the desired operating temperatures and fuel loss was greatly reduced by the addition of a stabilizer to the fuel. Fully enriched uranium was necessary to assure a compact reactor. A low thermal neutron absorption cross section of the ceramic material, and high retention of fission products and fuel to 3000°F when using air as the coolant were added objectives. An adherent coating to protect beryllia against water-vapor corrosion is desired when beryllia temperatures exceed 2100°F and long time operation in air is required. The principal effect of water vapor corrosion is to increase the roughness of the surface and thereby reduce the airflow in the affected tubes.

Void fractions for airflow of between 40 and 50 percent were indicated. A multitude of small cooling passages parallel to the core axis appeared natural, and a large heat transfer surface was necessary to lower the wall temperature. Small diameter tubes were required to minimize heat removal thermal stresses.

In addition to their many desirable characteristics, ceramic materials exhibit several undesirable characteristics that must be mitigated by careful engineering design. They are weak in tension (compared to the compressive strength), have poor resistance to mechanical shock and thermal stress, and are relatively expensive to fabricate into component shapes if hot pressing and final machining are required. To take advantage of the desirable properties of the ceramic while minimizing the undesirable characteristics, the following design philosophy was adopted:

1. The fueled components must be small simple shapes to minimize thermal stress and thermal shock conditions.
2. The shapes must lend themselves to rapid and automatic manufacturing processes to minimize production costs.
3. The design configuration should assure that mechanical and aerodynamic loads produce primarily compressive stresses in the ceramic parts while air-cooled metallic parts take the tensile loads.

Beryllia is the most desirable available material. A small tubular shape is chosen for the fuel element, to be fabricated by the extrusion process. A single, rather than multiple, passage unit fuel element is selected to assure a higher yield through more effective process control; this is an especially pertinent factor when cladding is used in the coolant passage. To minimize capture of thermal neutrons and to assure a more uniform radial temperature through the core, metallic cells or containment structure within the core are eliminated. Small ceramic pieces, per se, require many parts; this in turn increases the probability of failure and requires a configuration in which the load paths are redundant.

Structural failures of ceramic materials may occur as breaks or cracks. The configuration should provide redistribution of load around the failed member while assuring containment and, if possible, alignment of the pieces. Thus, the small ceramic parts should be snugly assembled and maintained as a unit through external compression by cooler metallic supports.

4.2 DESCRIPTION

Two configurations were explored in detail. The first was a network of beryllia slabs forming triangular cells in which loose hexagonal or round fueled tubes were placed, see Fig. 4.2-1. Compression from the periphery of the cylindrical bundle maintained the cellular structure. The slabs represented approximately one half of the moderator fraction - the

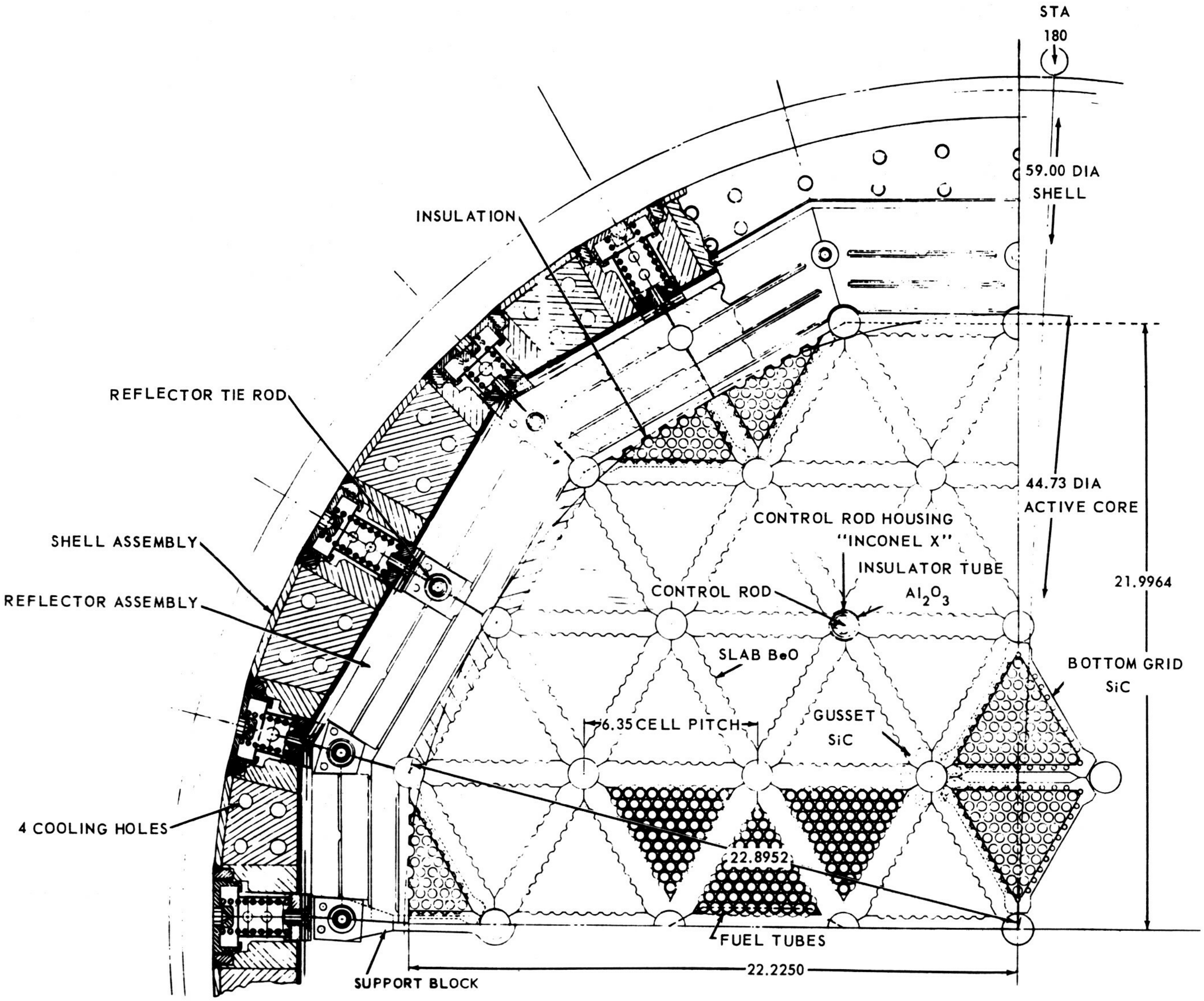
STA
180
59.00 DIA
SHELL
INSULATION
REFLECTOR TIE ROD
44.73 DIA
ACTIVE CORE
CONTROL ROD HOUSING
"INCONEL X"
INSULATOR TUBE
Al_2O_3
SHELL ASSEMBLY
REFLECTOR ASSEMBLY
CONTROL ROD
21.9964
SLAB BeO
BOTTOM GRID
SiC
6.35 CELL PITCH
GUSSET
SiC
4 COOLING HOLES
22.8952
FUEL TUBES
SUPPORT BLOCK
22.2250

Fig. 4.2-1 - D101E ceramic reactor

fuel tubes the other half. Air-cooled metallic tubes, penetrating the slab system at each apex to the triangle, served as axial support structure. The reactor pressure drop load was carried by these tubes to the forward shield plug.

A second configuration, the D141A-1 reactor, used hexagonal ceramic tubes as unit building blocks. The portion of the reactor constituting the active core contained fueled tubes in which the ceramic matrix acted as both moderator and fuel carrier. The unit building block concept was used also in an outer annular region comprising the outer reflector. The tube bundle was contained in, and supported by external metallic radial and axial support systems. As in the D101E reactor, cooling air was channeled through circular bores in the tubes. The D141A-1 is shown in Figures 4.2-2 and 4.2-3.

4.3 SIGNIFICANT DESIGN FACTORS

Mechanical design restraints are implicit in any reactor application. A cladding on a beryllia-base fuel element would be superfluous in a closed cycle system with an inert gas coolant. A short-life core may not need built-in maintainability, and a long-life reactor requiring large fuel inventory for burnup allowances may permit a metallic structure within the reactor to assure easy fuel reloading. Therefore, the requirements assumed in this text are the narrow restraints of the GE-ANPD objectives. Other applications may follow different, and possibly less stringent, paths. The general design criteria of section 2.1 are used and axial, or straight-through, airflow through the reactor is assumed.

4.3.1 Configuration Considerations

When minimizing the core diameter to assure a minimum shield weight, fuel element surface temperatures are pushed to the maximum allowable levels and flattened axially as much as is practical or feasible. Temperature-limited metallic structure is avoided as much as possible.

A ceramic moderated, straight-through flow reactor approximates a large cylinder pierced with many small coolant passages parallel to its axis. If hole spacing is varied, the radial power flattening may be readily accomplished. If the overall diameter is in the order of several feet, fabrication as a unit is not likely. Another extreme is an assembly of small fuel elements having a single flow passage such as employed in the design. This permits fabrication control, but greatly complicates the mechanical design of supporting devices.

A dominant factor in configuration considerations is that failure of some of the multitude of ceramic elements is inevitable. Recognition of this fact is paramount. Ceramics are highly sensitive to flaws, stress concentrations, and fabrication inconsistencies. The strength of the

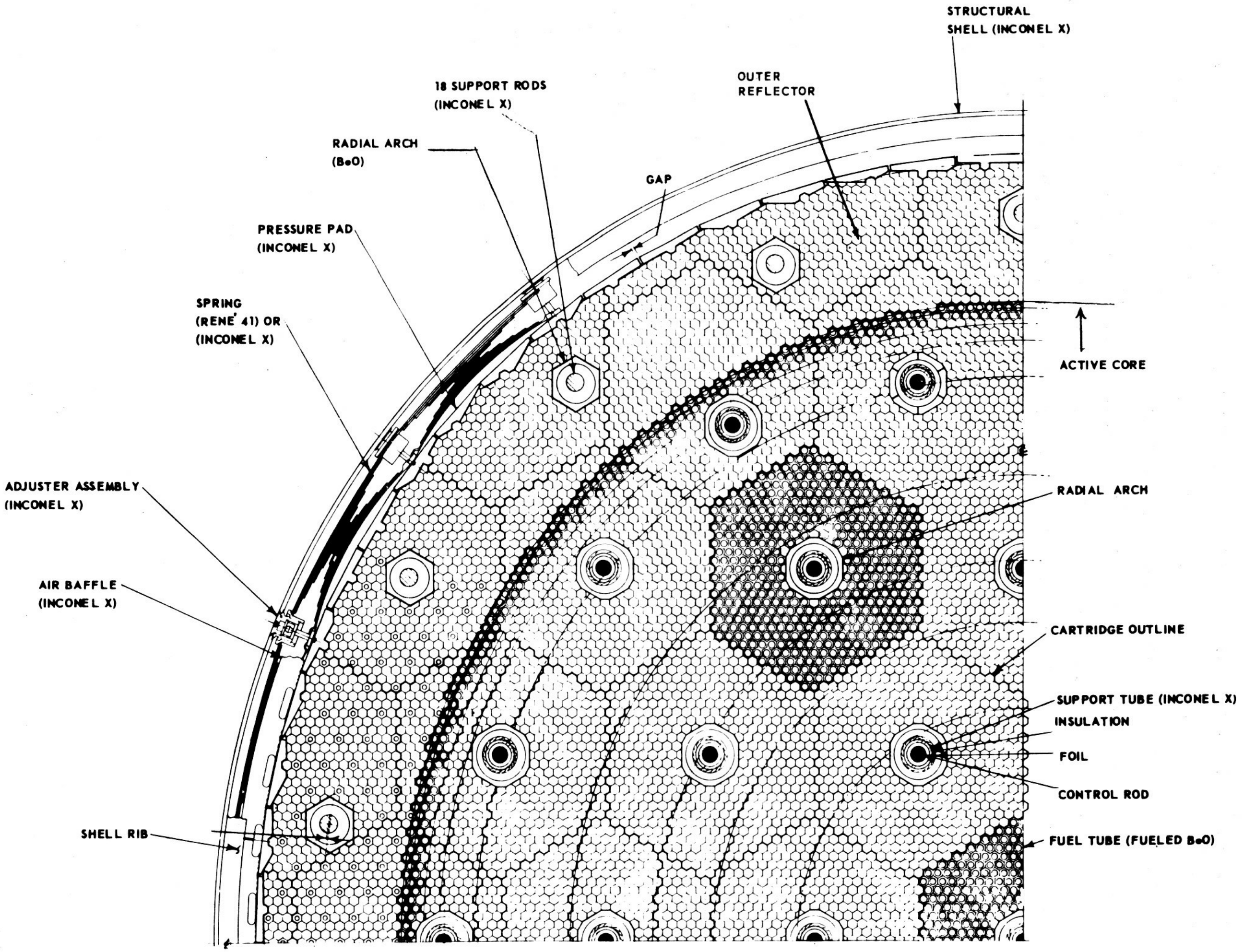
STRUCTURAL SHELL (INCONEL X)
OUTER REFLECTOR
18 SUPPORT RODS (INCONEL X)
RADIAL ARCH (BeO)
GAP
PRESSURE PAD (INCONEL X)
SPRING (RENÉ 41) OR (INCONEL X)
ACTIVE CORE
ADJUSTER ASSEMBLY (INCONEL X)
RADIAL ARCH
AIR BAFFLE (INCONEL X)
CARTRIDGE OUTLINE
SUPPORT TUBE (INCONEL X)
INSULATION
FOIL
CONTROL ROD
SHELL RIB
FUEL TUBE (FUELED BeO)

Fig. 4.2-2 - D141A-1 reactor

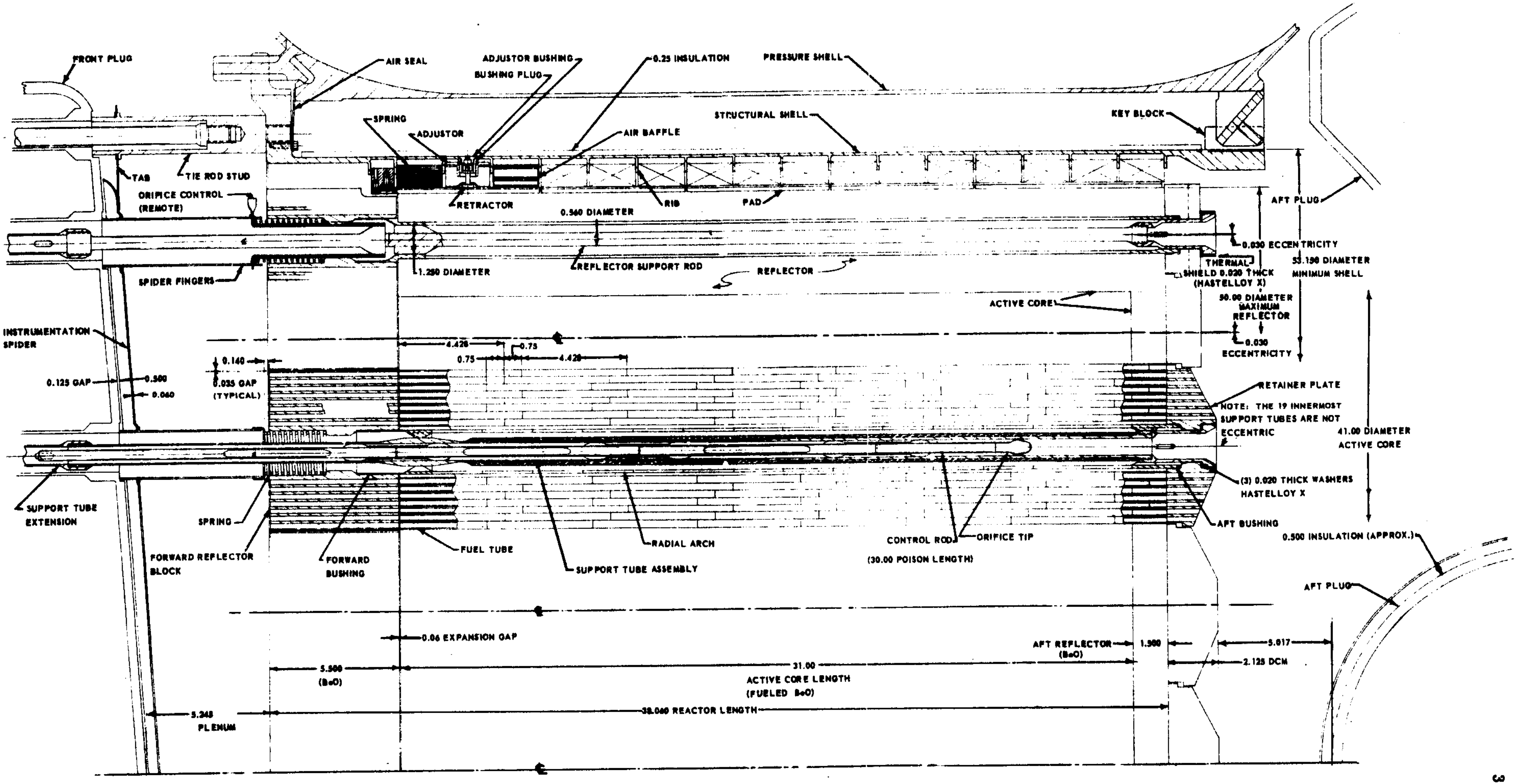
FRONT PLUG
AIR SEAL
ADJUSTOR BUSHING
BUSHING PLUG
0.25 INSULATION
PRESSURE SHELL
SPRING
ADJUSTOR
AIR BAFFLE
STRUCTURAL SHELL
KEY BLOCK
TAB
TIE ROD STUD
ORIFICE CONTROL (REMOTE)
RETRACTOR
0.560 DIAMETER
RIB
PAD
AFT PLUG
0.030 ECCENTRICITY
53.150 DIAMETER MINIMUM SHELL
THERMAL SHIELD 0.020 THICK (HASTELLOY X)
SPIDER FINGERS
1.250 DIAMETER
REFLECTOR SUPPORT ROD
REFLECTOR
ACTIVE CORE
50.00 DIAMETER MAXIMUM REFLECTOR
0.030 ECCENTRICITY
INSTRUMENTATION SPIDER
4.426
0.75
0.75
4.426
0.140
0.035 GAP (TYPICAL)
0.125 GAP
0.500
0.060
RETAINER PLATE
NOTE: THE 19 INNERMOST SUPPORT TUBES ARE NOT ECCENTRIC
41.00 DIAMETER ACTIVE CORE
(3) 0.020 THICK WASHERS HASTELLOY X
SUPPORT TUBE EXTENSION
SPRING
FORWARD REFLECTOR BLOCK
FORWARD BUSHING
FUEL TUBE
SUPPORT TUBE ASSEMBLY
RADIAL ARCH
CONTROL ROD (30.00 POISON LENGTH)
ORIFICE TIP
AFT BUSHING
0.500 INSULATION (APPROX.)
AFT PLUG
0.06 EXPANSION GAP
AFT REFLECTOR (BeO)
1.500
5.017
2.125 DCM
5.500 (BeO)
31.00 ACTIVE CORE LENGTH (FUELED BeO)
5.248 PLENUM
38.060 REACTOR LENGTH

NOTE: Dimensions in inches

Fig. 4.2-3 - Longitudinal cross section of D141A-1 reactor

material follows a different distribution curve from that of the unit stresses at various locations. Both distributions exhibit scatter above and below their average values, and a finite probability of obtaining low strengths combined with high stresses exists. This is visualized qualitatively in Figure 4.3.1-1. The fraction of elements in the cross-hatched areas have unit stresses in excess of their internal strength and fracture of the ceramic material is likely to occur. To reduce the overlap (and fractures), the spread between the average strength and average stress must be increased and the variability in strength and stress decreased. Fractures are normally classed in three categories; (1) transverse breaks, (2) splitting along the axis, and (3) spalling or flaking, especially at the ends.

Occasional fractures are not catastropic or even harmful if the configuration supplies external restraints to confine the pieces and provides for redistribution of load around the failed piece or pieces. Confinement implies maintaining the pieces in their original position to assure alignment while simultaneously preventing channel blockage. This load redistribution is best accomplished by a redundant structure.

Designs wherein unfueled ceramics serve as radial structure have been used. Larger pieces, which can be fitted into cells for containing the fuel element, are permitted because of their lower thermal stresses, but failure of these pieces must not impair reliability. When the fueled ceramic and the unfueled structure both serve as moderator, their volume fraction ratios can be adjusted to obtain significant changes in thermal stresses.

4.3.2 Design Principles of the Slab and Tube Concept

If some of the moderator is removed from the fuel element matrix without changing the net fuel loading or the heat transfer geometry, the volume of fueled matrix is reduced and thinner fuel element walls result. The fuel concentration necessarily increases, and is a limiting materials factor in the overall design. Thermal stresses are proportional to the volumetric coefficient of heat generation and the square of the wall thickness. Since the coefficient of heat generation is inversely proportional to the wall thickness, it is apparent that the net result of decreasing the wall thickness and increasing the fuel concentration is a reduction in thermal stresses.

4.3.2.1 Thermal Stress Considerations

The major design problem in a slab and tube reactor is the thermal stress problem in the relatively large structure-moderator slabs. This problem is not due solely to the normal temperature gradient resulting from internal heat generation, but is due also to gradients which result from variations in the heating rate throughout the slab and variations in

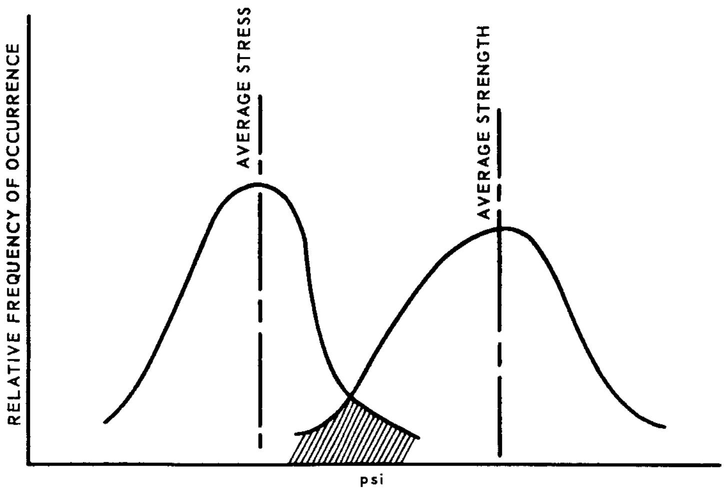

Fig. 4.3.1-1 – Distribution curves of material strengths and stresses

the heat removal conditions over the surfaces of the slabs. The gross effects of the latter conditions on thermal stresses are difficult to predict but probably are far more serious than the basic thermal stresses due to internal heat generation.

Any large core component has widely varying temperature distributions and it is advisable to eliminate these components whenever this can be done without penalizing the integrity of the mechanical structure. Basically, this is the design philosophy that leads to the tube bundle concept.

Assuming the same design requirements for a slab and tube reactor and a tube bundle reactor, several characteristics would be approximately the same in each reactor. These characteristics are as follows:

Dimensional

Overall size
Void volume
Moderator volume
Number of coolant passages
Hydraulic diameter of coolant passages
Heat transfer surface area

Thermal

Total power
Surface heat flux

If the ratio of wall thickness to diameter is small for a tube with internal heat generation, the maximum tensile thermal stress in the tube, based on elastic theory, is given by the following equation:

$$\sigma = \left[\frac{\alpha E}{3k(1 - \nu)} \right] q''' t^2 \qquad (1)$$

where:

σ = Thermal stress
α = Coefficient of thermal expansion
E = Modulus of elasticity
k = Thermal conductivity
ν = Poisson's ratio
q''' = Volumetric coefficient of heat generation
t = Wall thickness

The bracketed term in the Equation (1) contains as variables only materials properties and may be treated as a single materials factor, M, which can be evaluated as a function of temperature. Assuming heat transfer from one side only, the surface heat flux, q'', is the product of the power density and the wall thickness, and the stress equation can be rewritten as $\sigma = Mq''t$. This expression shows that the thermal stress is directly proportional to the wall thickness for a given surface heat flux.

The 101E reactor studies led to geometries wherein the fuel elements comprised approximately one-half the total moderator volume. Since in a tube bundle reactor almost all of the BeO is fueled, the wall thicknesses of the fuel element are approximately twice as great as those in the 101E design to retain the same moderator volume. Therefore, the thermal stress in the slab and tube reactor fuel element is approximately one-half that in a tube bundle design. This may become a significant factor depending upon the actual stress limitations and the possible consequences of fuel element rupture due to thermal stress.

4.3.2.2 Structural Integrity of the Slab Cellular Walls

Boundary conditions of the slab cellular walls are established by the spring rate of the radial support system. Internal loads at each apex are calculated by a unit analysis condition and most of the apexes are identical, with difference occurring only at the half slabs. Most of the slab members are equal in length and cross section, thereby allowing use of actual loads rather than displacements. The specific load paths are determined by the following steps in a numerical relaxation technique:

1. Loads in the various members are assumed. These assumed loads are based on previously calculated outer member loads.
2. Internal loads are applied to the apexes and the summation of horizontal and vertical force is made equal to zero. Unbalanced forces are balanced by equal and opposite forces at the apexes, and referred to as residual forces.
3. The residual forces are distributed to adjacent apexes until they become zero or approach a permissible error. This iteration alters individual slab loads until exact slab loads are obtained.
4. The summations of forces at each apex are checked for accuracy. Errors are eliminated by repeating the relaxation procedure until the permissible refinement is obtained.

Specific loads and load paths in the 101E slab structure are shown in Figure 4.3.2.2-1 for a 4G vertical and a 1G horizontal dynamic load. For the 90 cell arrangement, loads are introduced at the 24 peripheral junctions through a hydrostatic-type radial support system which assures that no peripheral shear stresses on the matrix are required.

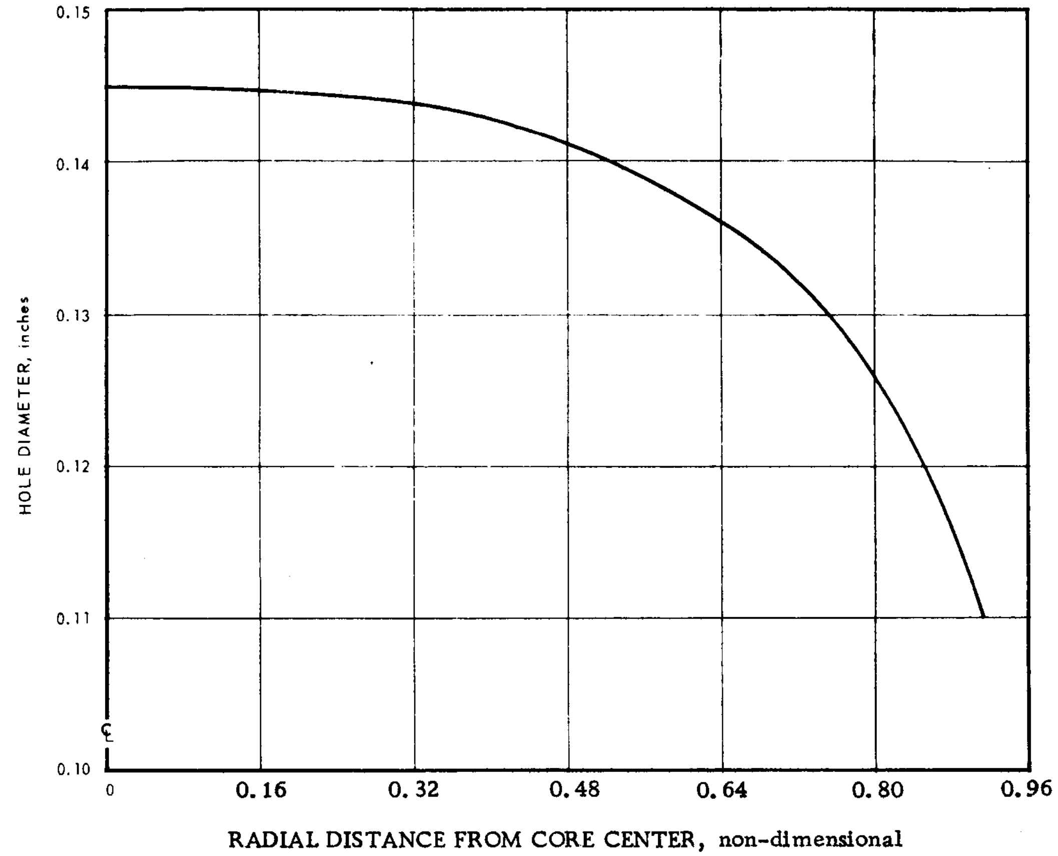

Fig. 4.3.2.3-1 - Moderator coolant hole diameter as a function of location in core

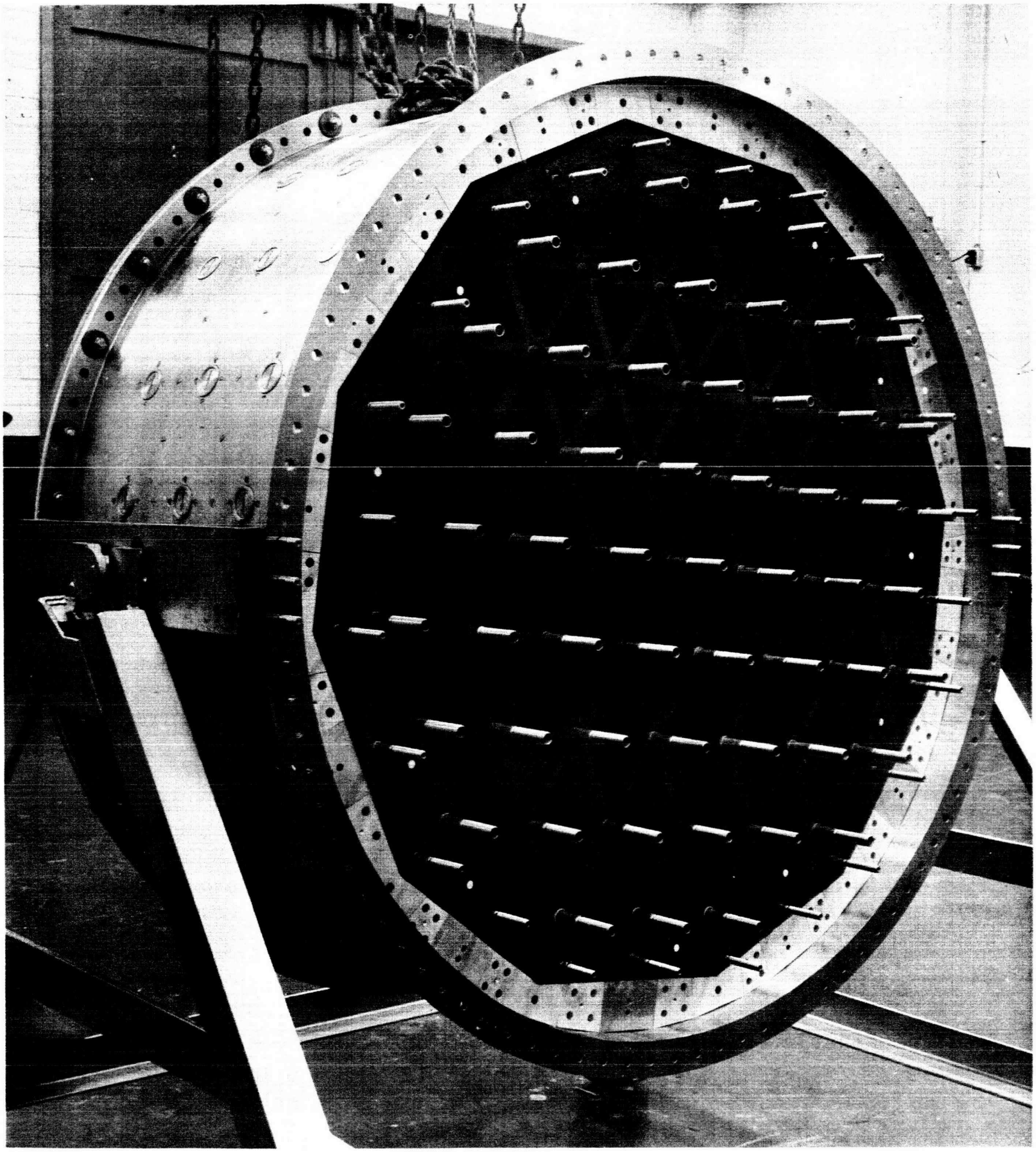

Fig. 4.3.2.2-2 – Three-tier mockup of D101E structure (Neg. C-20629)

Preload is set to allow the load of the least-loaded spring to approach zero at the time of the maximum deflection due to acceleration forces. These external loads are identified as the outer member loads.

The short term compressive and bearing stresses in the maximum loaded slab, 628.5 pounds in Figure 4.3.2.2-1, are 275 psi in compression and 400 psi in load bearing at the 60-degree bevel at the apex. Mechanical stresses in the slabs are not excessive.

Tests of the structural integrity of the slab assembly included vibration, thermal cycling to 1000°F, simulated differential expansion among slabs, simulated broken slabs, various radial pressures, removal of radial loads locally, load distribution, and variation in cell dimensions. The three tier mockup is shown in Figure 4.3.2.2-2. The tests revealed a tendency for failures to develop in the walls of the half cells. Ceramic gussets similar to a short hexagonal tube were placed at the apex to limit displacements with flat rather than beveled load-bearing edges. (This is the only required function of the gusset.) The apex at one half-cell, with its gusset removed, became distorted due to the wedging action of the 60-degree beveled edges of the slabs.

The longitudinal structure consists of small triangular retainer plates held axially by tension tubes which pass through the apexes of the moderator slabs. Considerable alleviation in the temperature distributions on the face of the slabs is achievable by repositioning the tension members at the center of every other cell. A hexagonal retainer plate pattern, for example, would be satisfactory. A reliability feature may be incorporated with the triangular plate supported on the three edges so that, even when cracked into two pieces, its original function is retained. Edge support may be effected by setting the plate into small slots within the aft-most tier of moderator slabs, or resting on ribs beneath the slabs. A reduction in thermal stresses, especially during transients, may be achieved by routing slab cooling-air between retainer plates rather than through them. This is readily achieved with edge-supported triangular plates in combination with internally cooled moderator slabs.

4.3.2.3 Moderator Slab Cooling Characteristics

The moderator secondary heating rates varied by a factor of two along the radius of the core. The initial implications of a large radial variation is that, unless some means is provided for selectively cooling each slab, a similar variation will exist in slab temperatures.

Adjacent fuel tubes exerted a strong dampening influence when moderator temperatures tend to differ from tube temperatures, and mitigates large variations. However, it is desirable to provide reductions in radial temperature variations since these variations are undesirable from the following standpoints:

1. Core performance. The moderator coolant would be appreciably cooler on the outer radius of the active core and lead to a lower mixed exit-air temperature.
2. Core distortion. Differential expansion of components within the core due to variation in temperature may lead to misalignment, flow restrictions, local hot spots, and excessive stresses in structural components.
3. Additional internal temperature gradients. Excessive nonlinear temperature gradients in some of the ceramic components may cause mechanical failure (cracking) of these components.

Since a criterion in moderator design is achievement of a relatively flat radial temperature profile through the core, slab temperatures should approximately equal the fuel tube temperatures. To compensate for the gross radial variation in moderator heating, the cooling holes should be sized so that similar moderator-surface and bulk-air temperature profiles are obtained at any radial position. Figure 4.3.2.3-1 shows the variation in hole size required as a function of core radius to give maximum surface temperatures equal to the maximum inner surface temperature of the average tube.

However, it is more desirable from a manufacturing and assembling point of view to maintain a constant size for each cooling hole within a single slab and to limit the number of such variations as much as possible. Accordingly, the 101E core was divided into three regions and one hole size specified for all slabs lying within each region. If further temperature flattening had been desired in those slabs which were not situated at the average position for a region, it would have been accomplished by preferentially restricting the flow through the holes in each slab within an orifice plate.

4.3.2.4 Thermal Stress in Slabs

Thermal stresses in the moderator slabs are caused by two temperature gradients, those varying laterally across the face of the slabs and those varying transversely through the thickness of the slabs.

Internal thermal stresses in an unrestrained slab are a function of the magnitude of the maximum deviations from a linear internal temperature profile. One profitable design change was splitting the slab in half as shown in Figure 4.3.2.4-1. This not only permitted better control of the moderator cooling air but also provided a reduction in thermal stresses by a factor of four. Figure 4.3.2.4-2 shows typical internal temperature profiles through a slab thickness and indicates this deviation to be reduced by a factor of four when the slab is split in half. This

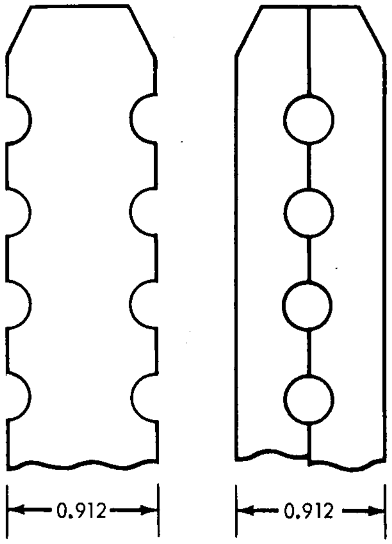

Fig. 4.3.2.4-1 – D101E split moderator slab

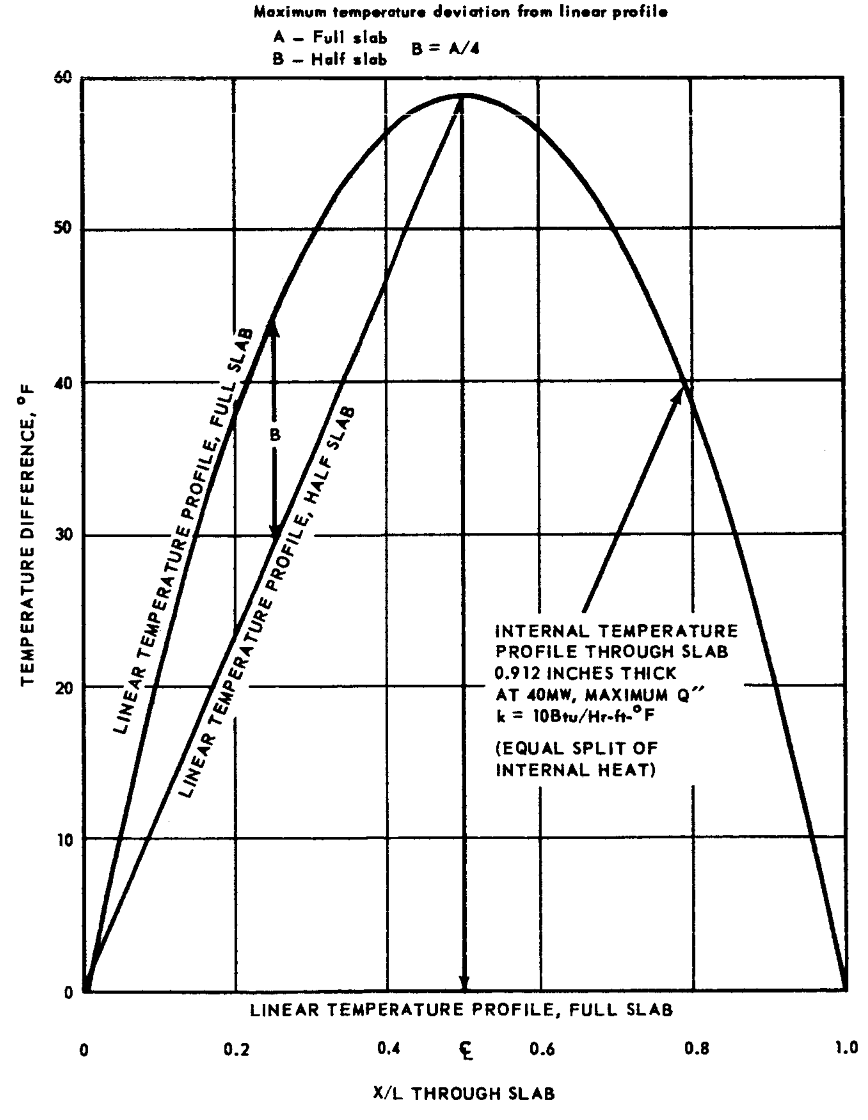

Fig. 4.3.2.4-2 – Internal temperature profile through a moderator slab

relationship still holds even if the profile is not symmetrical as shown therein. Since the split slabs are cooled by air flowing through holes, the exact internal temperature profiles can not be obtained by a simple slab analysis wherein cooling exists over one complete surface. Figure 4.3.2.4-3 shows the configuration which was considered for the 101E reactor and the internal temperature profiles for this configuration. A comparison of Figures 4.3.2.4-2 and 4.3.2.4-3 shows the difference for one situation to be 59°F versus 63°F for the other. The more exact temperature profiles of the latter geometry was obtained through the use of a 28 nodal point solution. Cooling was shifted to the interior surface in preference to the exterior to permit the slabs to bow in an unrestrained manner.

An analysis was made to determine the lateral temperature profiles across the vertical face of the slab between two parallel control rod and guide tube assemblies. These profiles vary for every position in the core and an exact solution must take into account many factors which complicate the analysis to the point where it is impossible to get a solution for even one specific core location without expending an unreasonable amount of time and effort. Some of these are as follows:

1. Variation in internal heating rates longitudinally, radially, and locally because of the presence or absence of a control rod.
2. Variation in coolant flow and temperature in each cooling channel.
3. Influence of adjacent fuel tubes which may differ in temperature and internal heat generation, and do not have the same longitudinal variation in heating rates.
4. Influence of heat losses to control rod cooling air.
5. Longitudinal and lateral conduction within a slab.
6. Variations from nominal mechanical configurations.

The analysis consisted of a 49 nodal point solution for one horizontal plane through a slab, assuming the following conditions:

1. Uniform heat generation rates.
2. Uniform cooling flow rates and temperatures in all holes.
3. Adjacent fuel tubes had no influence on slab temperatures.
4. All nominal dimensions.
5. Lateral heat conduction.

Figure 4.3.2.4-4 shows the results of this analysis on a dimensionless parameter basis and for a point of maximum internal heat generation within the core. For simplicity, only, one of the four lateral profiles is shown. (The three profiles not shown occurred at different locations within the slab.) It is seen here that the case of 4 percent of the moderator heat going to the control rod and guide tube coolant gives a fairly flat temperature profile. Deviations from the flat temperature profile assume a general parabolic shape; allowing for the various assumptions made in

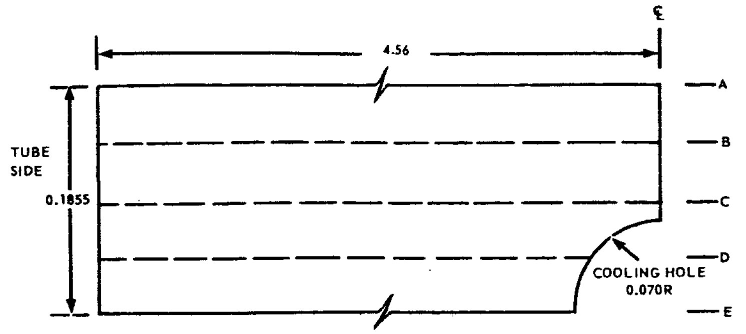
℄
4.56
TUBE SIDE
0.1855
A
B
C
D
E
COOLING HOLE
0.070R

TYPICAL SECTION OF MODERATOR SLAB

Note:

$$T = 0.5085 \frac{k(T_X - To)}{Q'' A_n}$$

$T_x - T_o$ = Temperature above reference
k = Thermal conductivity
Q'' = Internal heat generation rate
A_n = Areal of node (0.0042 in.^{2})

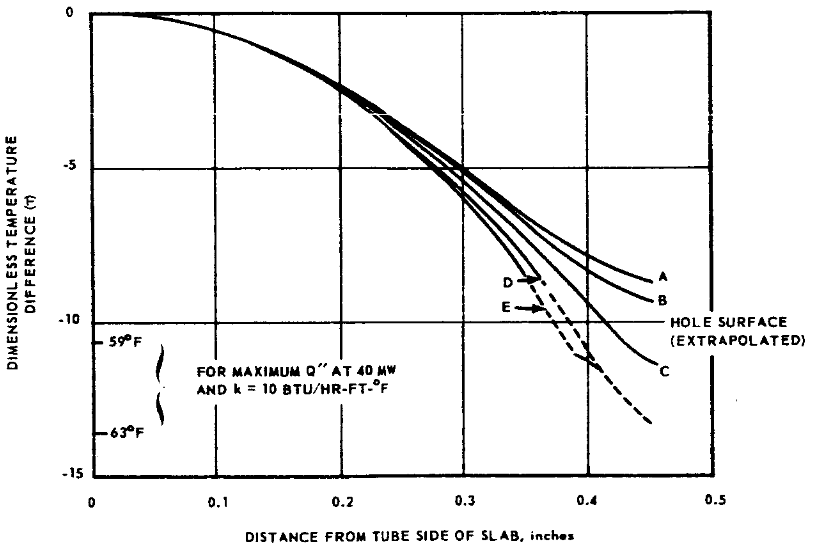

Fig. 4.3.2.4-3 – Internal temperature profile through a moderator slab with all heat being transferred to the cooling hole

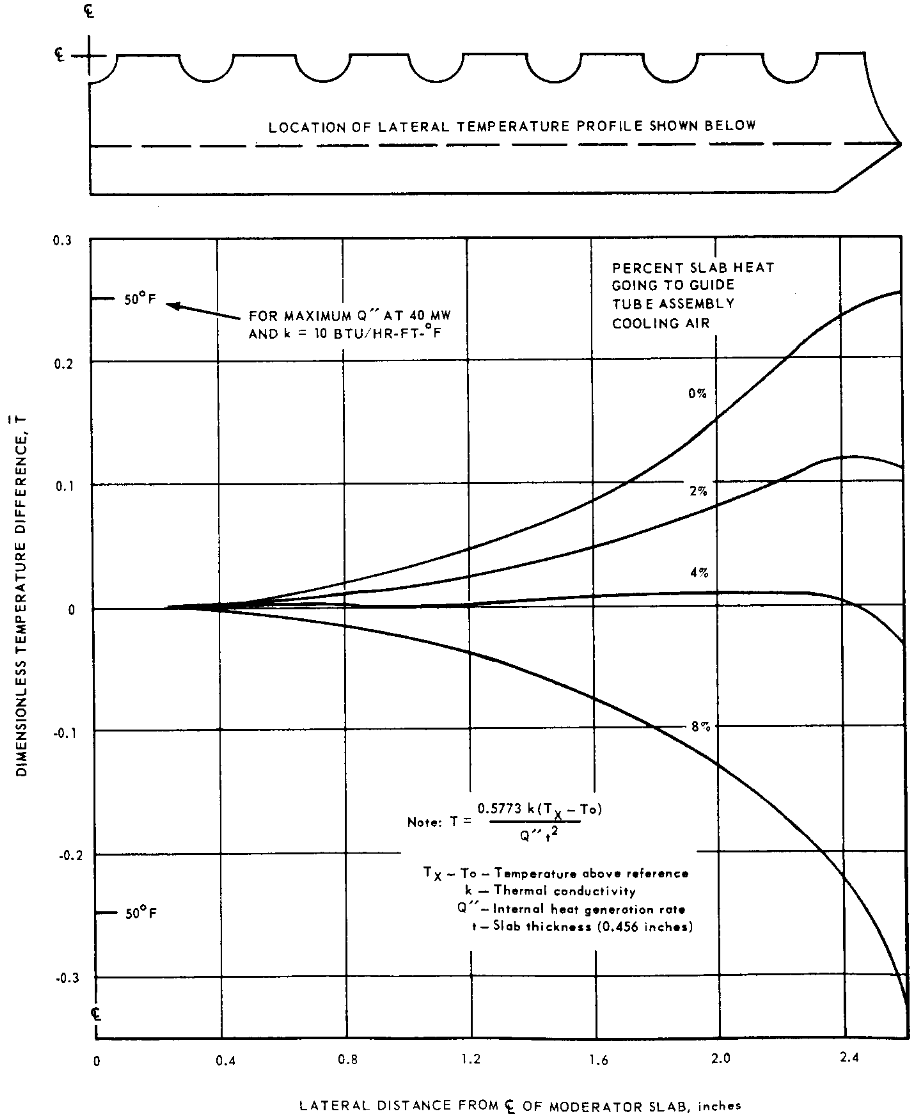

Fig. 4.3.2.4-4 – Lateral temperature profiles in a moderator slab

this analysis, it seems realistic to expect maximum temperature variations in the order of 150°F in actual reactor operation.

Basic solutions exist for slabs of infinite length, i.e., solutions which are valid only at distances far removed from the ends and edges of the slab. The end effects of the finite length on thermal stress distributions are difficult to derive because the basic differential equations are two-dimensional rather than one-dimensional. Dimensions and the coordinate system used in the analysis are shown in Figure 4.3.2.4-5. Thermal stresses were determined for the three temperature gradients shown in Figure 4.3.2.4-6. Temperature gradients are shown for a parabolic temperature distribution, a distribution identified as T_{716}, and a distorted temperature distribution. The T_{716} gradient is the same as a temperature distribution which was used in a thermal stress development test to crack a moderator slab. The T_{dist} gradient represents a typical distorted temperature profile in the slab that may result from causes such as perturbed cooling along the edges of the slab, or by the presence of control rods at the apex of each triangle.

Several methods were used in the analysis to include the effect of finite length on the stress distribution in the slabs. The most effective method was developed by Ross.(12) It was extremely simple but exact in the case of parabolic temperature gradients. This method makes use of an analogy between thermal stresses in slabs and the stresses developed in thin flat plates clamped along their edges and surface loaded by a pressure distribution determined by the temperature distribution of the original thermal stress problem. For the particular case in which the temperature is parabolic in one direction, i.e., parabolic in one direction and constant or linearly varying in the other direction, the thermal stresses are found from analogy with a thin plate clamped at the edges and loaded by a uniform surface pressure. Although the solution is complicated, a great deal of work has been done in developing and tabulating the results of these solutions for clamped-plate bending.

4.3.3 Tube Bundle Considerations

The tightly packed bundle of hexagonal fuel-moderator pieces satisfied requirements for reliability. As shown in numerous tests, confinement of fractured elements is complete. Load redistribution is achieved, even to the extent of bridging around large voids or cavities up to 30 times the across-flats dimension of one tube. Load concentration due to such bridging has been shown to be low. The development of this structural configuration is a significant advancement in ceramic reactor technology.

Design principles, details, and supporting development testing of the

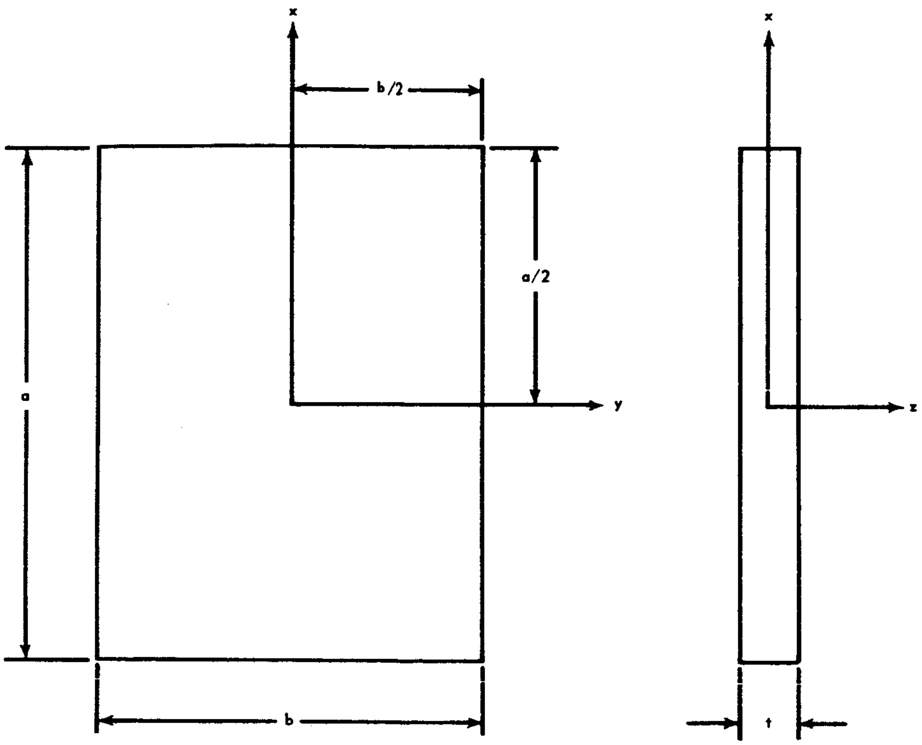

Fig. 4.3.2.4-5 - Dimensions and coordinate system used in moderator slab analysis

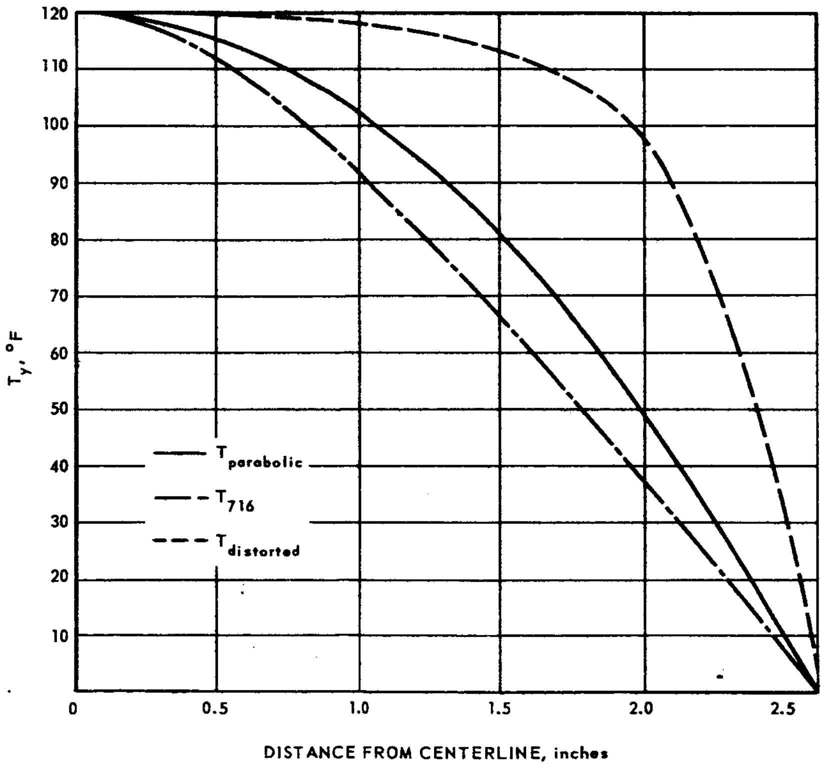

Fig. 4.3.2.4-6 - Temperature gradients used in moderator slab analysis

tube bundle is emphasized in the following text. The material presented includes the obvious tolerance stackup problems as well as the not so obvious load distributions occurring within the bundle during lateral accelerations. To prevent undue loads on the fuel tubes, it is necessary to determine the minimum pressure to maintain the bundle as an integral cylinder. Thermal expansion clearances are not provided locally for the fuel element, and these displacements accumulate at the outer boundaries of the bundle where relatively large differential motions are experienced that impose design restraints on the external structure. Maximum loads on the tubes are not easily established in the redundant structure; limiting cases rather than exact analyses are employed.

Mechanical stresses in fuel tubes within the bundle are primarily determined by the solid fraction in the core and are independent of size, i. e., dimension across flats. The thermal stresses are dependent on wall thickness. Therefore, to minimize the combined stresses a small, thin-wall tube is used. Increased pressure drop as well as possible clogging and misalignment are considerations in fixing the minimum size passage. The external tube size should be held as large as feasible to reduce the mechanical stresses greatly as well as the number of pieces in the tube bundle, thereby minimizing fabrication and handling costs. Furthermore, with extremely small sizes, twisting or turning of the elements may occur especially near the cooler outer reflector region.

At high temperatures combined stresses in the fuel element may be relieved through creep or relaxation. However, upon return to room temperature the fuel element may experience a stress greater than the initial operating stress because of the high temperature yielding, and the stresses may be reversed. Fracture may occur during the shutdown cycle rather than during operation. Also, the modulus of rupture of the beryllia-base fuel element may be less at room temperature than at operating temperature.

Peripheral compression is maintained on the tube bundle by the radial support system to assure a unit assembly. Further, the external support limits the eccentricity of the bundle, including that due to lateral acceleration forces. The system utilized springs to compress the bundle by reacting against a large cylindrical shell. Since the spring is the critical component of the system, many are provided to assure a redundant system in which the malfunction of a few parts will not impair the system usefulness.

The reactor discharge-air temperature and local temperature profiles are the principal limits in choosing the type of axial support system. Three basic support types are discussed in the text. One consists of small retainer plates held in position axially by tension members which pierce the tube bundle. For high discharge-air temperatures, internal cooling may be necessary for the retainer plates. A second system is discussed wherein 12 circular sectors provide support for the aft face of the bundle. These have external insulation for isolation from the high temperature environment and are internally cooled. A third type employs a refractory material built up into a dome, or Roman arch, configuration. Although requiring more axial space, the dome provides an all-ceramic growth version.

Local deviations from the average air temperature leaving the reactor may cause rather severe thermal stresses in the aft structure, and present a significant design consideration.

4.4 MECHANICAL DESIGN PRINCIPLES OF THE TUBE BUNDLE STRUCTURAL CONCEPT

4.4.1 INTRODUCTION

The low tensile strength of ceramic materials, together with the high thermal and mechanical stresses imposed on the ceramic components dictates the use of small, simple shapes wherever possible. The design approach utilized in the tube bundle concept is to nest these basic building blocks together to form a large circular cylinder. The overall reactor integrity is assured by maintaining compressive forces externally on the cylinder. To establish the integrity of the small ceramic pieces, however, it is necessary to carefully evaluate the mechanical (as well as thermal) loads acting on them. Mechanical design of the concept is greatly concerned with internal pressure forces in the ceramic bundle and the shift in these internal forces required to enable it to act as a solid during various external loading conditions.

Although the tube bundle is geometrically simple, its analysis is complex and is approached through limiting cases rather than through rigorous solutions. Emphasis is placed on defining the maximum loads that can safely be carried by the hexagonal tube. The maximum forces are developed during short-term, vertical inertial loading conditions and the method of radial support is a key design consideration. Extensive design principles have been derived for hydrostatic, shear, and an integrated radial support system. Each has its proper place. In addition to the internal pressure distribution in the tube bundle, the supporting systems prevent its distortion, permit dimensional deviations due to stack-up, and handle displacements of the reactor due to inertial loading.

Some of the variables frequently referred to in the analysis are as follows:

δ_a - The allowable bundle displacement relative to the reactor structural shell, inch
S - The peripheral spring rate, evaluated in pounds/inch of deflection per square inch of supported tube bundle surface

Δ - The dimensional change in the radial direction in the tube bundle and radial structure, inch

n - Inertia load factor

n_o - Design inertia load factor in the lateral direction

P_{min} - The least radial pressure necessary to maintain the tube bundle as a unit while preventing internal distortions, psi

P_{auto} - The autoclaving pressure due to radial mismatch of gas pressures at the periphery of the bundle, psi

X_R - The combined force acting in the tube bundle in a radial direction, psi

X_T - The force acting in the tube bundle in a tangential direction, psi

τ - The shear forces due to inertia forces which tend to cause separations within the tube bundle, psi

Allowable displacement, δ_a - This design parameter is established by the limiting control rod alignment, cooling channel misalignments, displacement of hot gas seals, etc. By dividing this deflection into the weight supported, a system spring rate is found which remains an invariant in the design. As shown later, if δ_a is arbitrarily chosen too small, it can cause large increases in bundle pressure and, consequently, fuel element unit stresses. As herein defined, the allowable displacement represents the farthest movement of the tube bundle relative to the reactor structural shell.

Spring rate, S - This parameter of the radial structure is defined as pounds per inch of bundle deflection per square inch of supported tube bundle surface, or

$$S = \frac{k_S}{A_S} = \frac{\text{spring rate of a spring}}{\text{bundle area covered by a spring}} = \frac{\text{lb}}{\text{inch-inch}^2} \quad (1)$$

The simplification permits a ready comparison among support systems. The subscripts R and T describe radial and tangential directions, respectively, in which the spring rate acts.

Differential radial motion, Δ - This dimensional change is measured in the radial direction and between the tube bundle and the radial support system. It is perhaps the most obvious design variable. Differential thermal expansions, assembly tolerances, component relaxations, and/or growth all contribute to Δ. Since the radial structure must maintain a minimum pressure throughout the range between $\Delta = 0$ to $\Delta = \max$, the extremes of the four variables must be added. For simplicity, it is assumed that Δ does not go negative; negative Δ provides load relief on the tube bundle.

Outer expansion of the tube bundle closely follows the shape of the fuel element average channel axial temperature profile shown in Figure 4. 4-1. A radial differential expansion extreme occurs during the condition of maximum fuel temperature and an associated minimum radial structure temperature; this condition translates to the maximum structure and fuel tube mechanical stresses. The other temperature expansion extreme occurs when the tube bundle and metallic radial structure are at a common temperature. The larger average coefficient of thermal expansion of the metals then causes the structure to expand away from the tube bundle. The maximum gap occurs at the highest temperature that the support system and the tube bundle have in common.

Tolerances have the same detrimental effect as thermal expansions. In a tube bundle made up of thousands of small parts, accurate prediction of the stackup is essential. Thus, minimum radial structure radius and maximum tube bundle size define one tolerance extreme while the reverse defines the other. Tolerance effects can, by design, be minimized by providing adjusting devices to be set during final assembly.

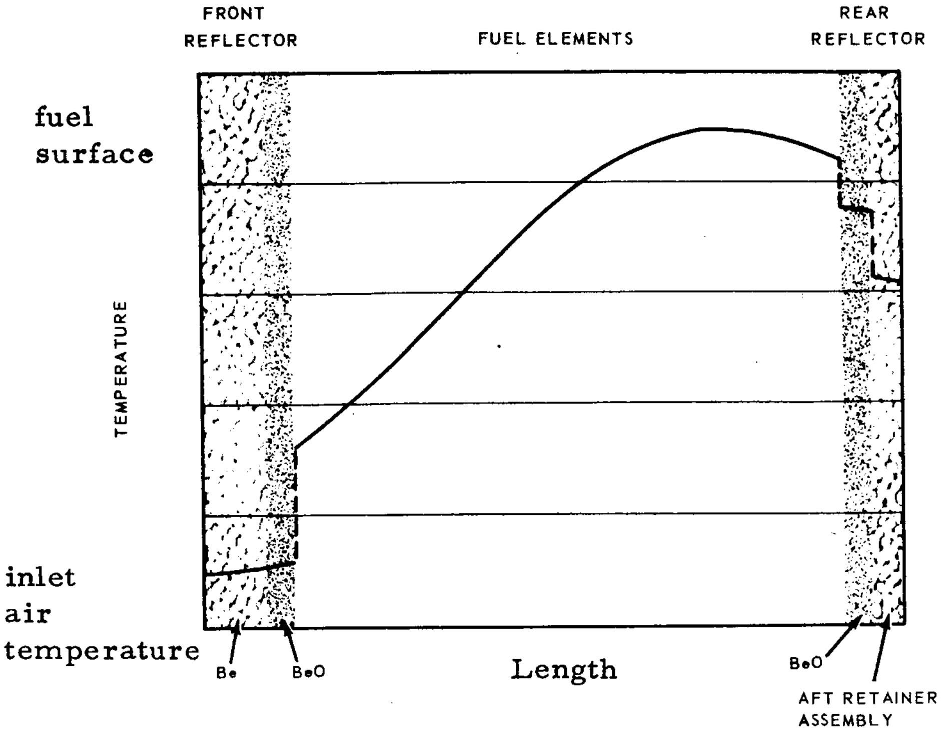

Fig. 4.4-1 – Longitudinal temperature distribution, average channel

Component relaxation and growth also increase Δ. Permanent relaxation of the radial structure and the fuel elements due to high temperature creep may cause a lessening of available radial pressure. Some of ceramic materials have at times exhibited a permanent growth rather than relaxation. If an allowance for this is necessary, an increase in the effective tube bundle diameter results. It should be noted that the time for each event to occur may be considerably different and that, for a reactor of long life, growth and relaxation allowances may be additive and result in a larger Δ.

Inertial load factor, n - This factor is considered as acting vertically when the reactor axis is horizontal. The design inertial load factor, n_o, represents the limiting case, and is used to establish the design radial pressure. See section 2.1.

Minimum radial pressure, P_{min} - The value of this parameter is that value required to prevent permanent distortions in the tube bundle when inertial loads are applied. Since the value of P_{min} varies dependent on how vertical loads are transferred to the structural shell, a dimensionless factor, C_1, is used to serve as a design comparison. The C_1 factor is applied as follows:

$$P_{min} = C_1 R \rho n_o$$

where R = the outer radius of the tube bundle

$$\rho = \text{apparent density} = \frac{\text{suspended weight}}{\text{suspended volume}} \qquad (2)$$

Autoclaving pressure, P_{auto} - This pressure is the additional peripheral load, in psi, on the tube bundle caused by mismatch of static pressure axially within the tube bundle and external to it within the radial structure. Autoclaving is discussed in a later section.

Tube loading pressure, X - This parameter denotes an internal force within the bundle, as differentiated from a peripheral external force. The latter force could be caused by spring forces or autoclaving. The internal pressure is considered to act in two directions, radial, X_R, and tangential, X_T.

Shear force, τ - This parameter is a force acting between tubes to cause slippage, and is similar to the shear stress in a beam. The forces appear only in the shear concept of radial support.

4. 4. 2 HYDROSTATIC PRINCIPLES OF RADIAL SUPPORT

The design principles of hydrostatically effecting radial support are shown in Figure 4. 4-2. With this method of radial support, when the tube bundle is displaced bodily the radial pressure from the springs follows hydrostatic distribution. There is no shear stress anywhere within the tube bundle and the tube bundle has no tendency to deform internally. From the standpoint of shock loads, hydrostatic radial suspension using a spring rate just high enough to limit deflection to the permissible amount appears ideal. Unfortunately, large differential motions often require spring rates such that the resulting internal pressure introduces severe fuel element mechanical stresses.

4. 4. 2. 1 External Support

When a rigid body is supported by a multiple spring system, it is necessary to compute and integrate the spring rate of the individual springs in terms of the system deflection. An approximate solution assumes that the spring suspension is continuous at the periphery and a deflection, δ , is imposed on the bundle relative to a cylindrical shell. General expressions are written for the radial components of the deflection at a point as shown in [illegible] then converted to forces by means of the linear radial spring rate, S_R. The vertical components of the radial forces are then integrated

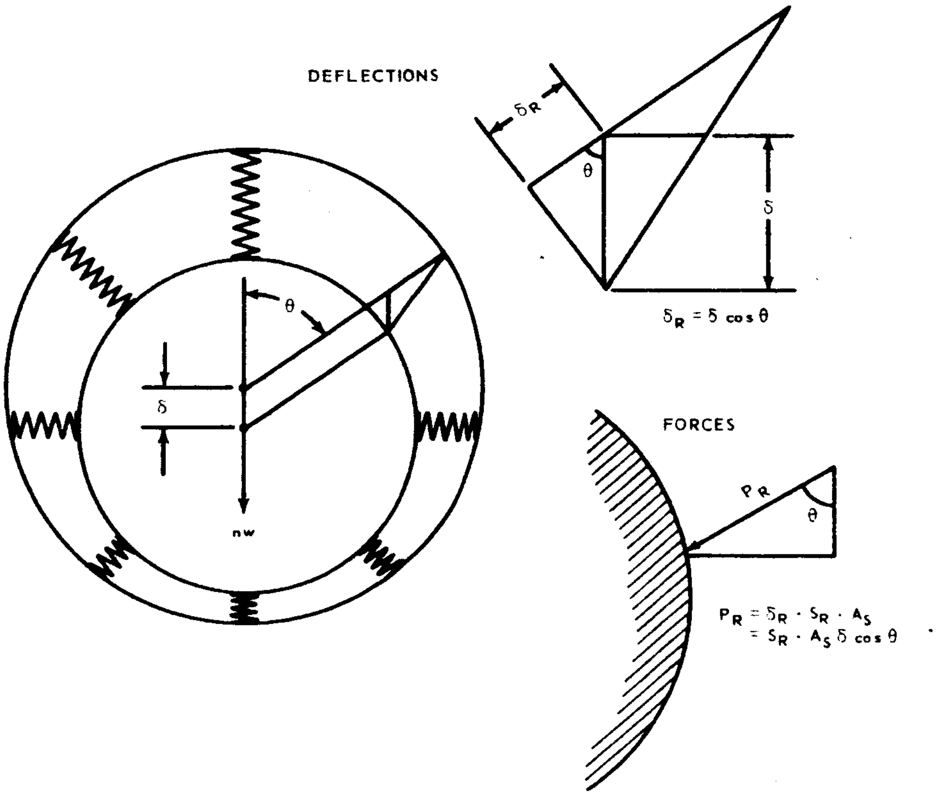
DEFLECTIONS
δ_R
θ
δ
$\delta_R = \delta \cos\theta$
θ
δ
nw
FORCES
P_R
θ
$P_R = \delta_R \cdot S_R \cdot A_S$
$= S_R \cdot A_S\, \delta \cos\theta$

Fig. 4. 4-2 – Hydrostatic principles of radial suspension around the perimeter and equated to the weight to derive an equation containing deflection as the only unknown. The method is as follows:

$$
\begin{aligned}
n\,W &= \sum_0^{2\pi} \text{ vertical components of the radial forces} \\
&= \sum_0^{2\pi} P_R \cos\theta \\
&= \sum_0^{2\pi} S_R\, A_S\, (\delta \cos\theta) \cos\theta \\
&= \sum_0^{2\pi} S_R\, \delta \cos^2\theta \; R\, (d\theta)\, L \qquad (3)
\end{aligned}
$$

$$\frac{n\,W}{L} = R S_R\, \delta \int_0^{2\pi} \cos^2\theta \; (d\theta)$$

$$\frac{n\,W}{L} = \pi\, R\, S_R\, \delta$$

where

n = inertia load factor
W = suspended weight
R = outer radius of bundle
L = length of bundle

The springs are preloaded by a minimum load fixed so that the force in the top springs approach zero under maximum vertical loading. Any further reduction in preload may endanger the system integrity since the structural shell can deflect out of round as the fluid distribution is altered. As shown later, the deflection limit, δ_a, cannot be maintained if the top springs lose contact with the bundle.

The minimum external pressure for the rigid body is derived from Equation (3) as follows:

$$
\begin{aligned}
P_{min} &= S_R\, \delta \\
&= \frac{n\,W}{\pi L R} \qquad (4) \\
&= R \rho n \text{ (psi)}
\end{aligned}
$$

External load variations on a typical tube bundle under inertial forces up to 4.13G with values of Δ equal to zero and maximum are shown in Figure 4.4-3. With maximum G forces and $\Delta = 0$, the top spring force equals zero, the side force remains unchanged, and the bottom force doubles. The analysis of the tube bundle used in this example assumed that the pressure exerted on the tube bundle was distributed around the periphery in 5-degree increments as shown in the figure.

When the tube bundle is displaced relative to the structural shell, the radial pressure from the springs follows a hydrostatic distribution. The springs act in pairs to accelerate a vertical strip of the tube bundle as shown in Figure 4.4-4. The strip is parallel to the direction of acceleration forces and sees only compressive stresses; the resulting pressure distribution within the bundle is purely hydrostatic. The weight of the control strip

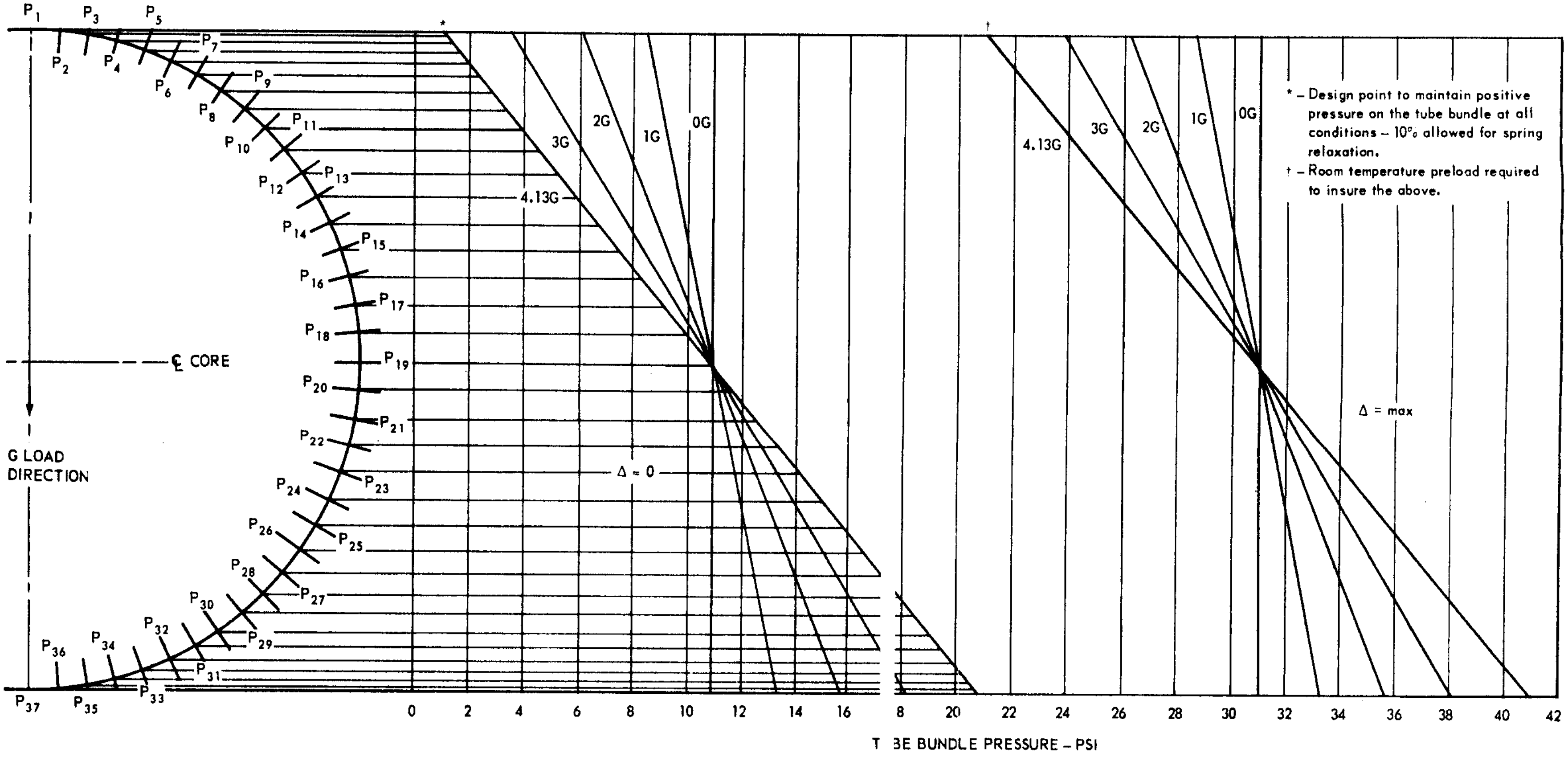

Fig. 4.4-3 - External load variations due to arying inertial forces

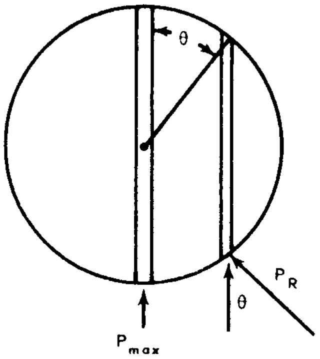

Fig. 4.4-4 – Paired spring reactions

is 2R ρn for a unit length in the direction of loading. The minimum preload is given by the following equation:

$$P_{min} = R\rho\, n \tag{5}$$

This preload is sufficient for bundle integrity. The tube bundle does not tend to deform internally since there is no shear stress anywhere in the tube bundle. The derivation is as follows:

$$\begin{aligned} W_{strip} &= 2R\,\rho\, n = P_{max} \\ P_R &= P_{max}\cos\theta \\ P_V &= P_{max}\cos^2\theta \\ &= 2R\rho n \cos^2\theta \end{aligned} \tag{6}$$

4.4.2.2 Internal Pressure Distribution

As previously shown, the radial spring rate is established by the permissible core deflection. For given values of the linear spring rate, spring relaxation during reactor lifetime, and the total differential radial motion (Δ) the highest tube loading pressure, X, is fixed. The highest pressure is due to the sum of the minimum radial pressure, the load due to differential radial motion, and is given by the following equation:

$$X_R = X_T = P_{min} + \Delta S_R \pm P_{auto} \pm \left(\frac{h}{R}\right) R\rho n \tag{7}$$

where h is a function of the vertical location with the axis as zero, i.e., no change in pressure is felt at the axis due to G forces.

A useful dimensionless expression for pressure variation in the tube bundle is as follows:

$$\frac{X_R}{R\rho n} = \frac{X_T}{R\rho n} = 1 + \frac{\Delta}{\delta_a} \pm \frac{P_{auto}}{R\rho n} \pm \left(\frac{h}{R}\right) \tag{8}$$

The maximum dimensionless pressure experienced by a hexagonal tube, at the bottom, is then readily determined from the following expression:

$$\frac{X}{R\rho n} = 2 + \frac{\Delta}{\delta_a} \pm \frac{P_{auto}}{R\rho n} \tag{9}$$

This parameter is shown in Figure4. 4-5as curve A. The pressures acting on the tube bundle are shown in Figure4. 4-6.These factors are useful in later comparisons of the support systems.

In the discussion, Δ has been assumed as positive, i.e., the spring gap decreases. Design pressures would be significantly decreased if a negative Δ existed, and Equation (3) would still apply. Autoclaving, when predictable and reproducible, can also alleviate the bundle maximum pressures. Since all springs must remain in contact with the bundle to maintain the design system spring rate and deflection limit, the GE-ANPD practice is to design for zero autoclaving.

4. 4. 3 SHEAR PRINCIPLES OF RADIAL SUPPORT

The pure hydrostatic support system normally represents a compromise between tube bundle deflection and fuel element stresses. An alternative design approach is to support the tube bundle during inertial loads at its periphery by a shear distribution to the structural shell. The tube bundle allowable deflection, now independent of the radial spring rate, no longer dominates the fuel element stresses. Again, sufficient radial pressure must be maintained externally and transmitted through the tube bundle to insure that it behaves as a rigid body under inertia loads.

Three methods of achieving such a shear support are illustrated in Figure 4. 4-7 High lateral bearing pressures on side keys, possibly leading to galling and seizing at high temperatures, limit the use of methods A and B. This limitation is avoided in method C since the elliptical spring acts as a flexible key.

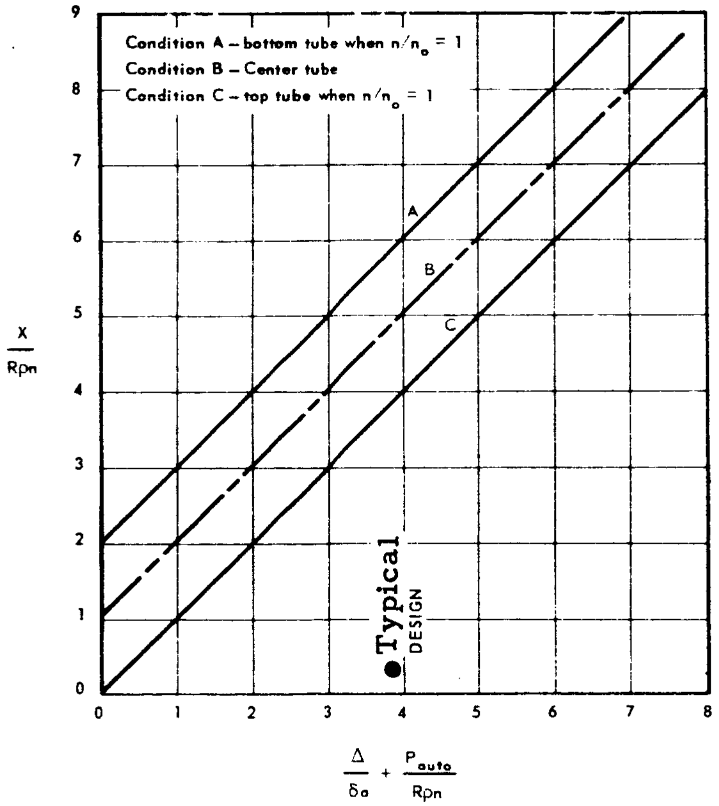

Fig. 4. 4-5 – Internal pressure for hydrostatic radial support

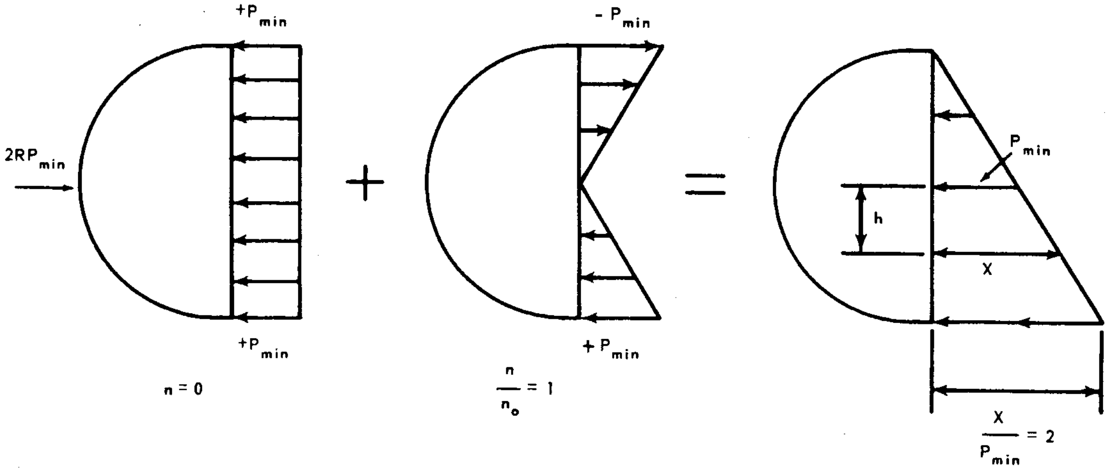
+P min
- P min
2RP min
+
=
P min
h
X
+P min
+ P min
n = 0
n / n₀ = 1
X / P min = 2

Fig. 4. 4-6 – The minimum radial pressure case, hydrostatic radial support

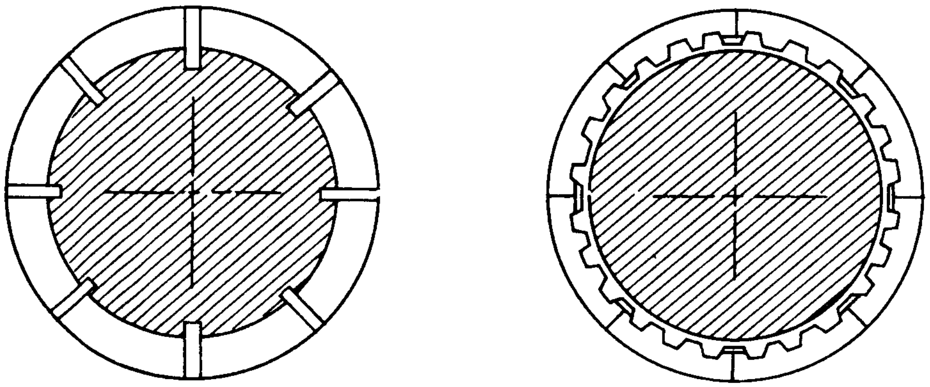

A. DIRECT PINS OR KEYS BETWEEN
PRESSURE PADS AND SHELL

B. CORRUGATED RADIAL SPRINGS
MESHING WITH KEYS ATTACHED
TO SHELL

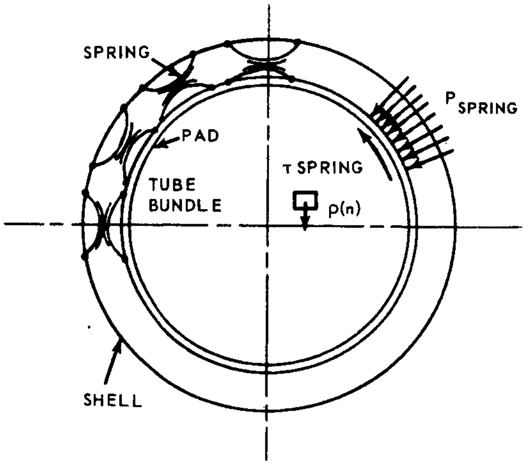
SPRING
PAD
TUBE BUNDLE
τ SPRING
p(n)
P SPRING
SHELL

C. AN ELLIPTICAL (BUGGY) OR OTHER
SPRING WITH A VERY LOW RADIAL
SPRING RATE AND A HIGH TANGENTIAL
(LATERAL) STIFFNESS

Fig. 4. 4-7 – Methods of achieving shear radial support

In pure shear suspension, with the bundle displaced bodily, the outer surface is loaded in shear, and the highest shear stress is developed at the diameter perpendicular to the direction of displacement. Internal shear strength is required to hold the shape of the bundle, and a minimum radial pressure equal to 1.3 times the maximum shear stress is desirable. From the standpoint of shock loads, pure shear suspension at times may be the poorest possible solution. It has the advantage, though, that large stresses are not induced by thermal expansion of the reactor.

4.4.3.1 External Support

The shear-system spring rate is developed similar to the method used in the pure hydrostatic system by equating the weight with the summation of vertical components of the tangential forces. The resulting equation is as follows:

$$\frac{nW}{L} = \pi R S_T \delta \qquad (10)$$

The development of peripheral shear stresses is shown in Figure 4.4-9.The circumferential shear distribution shown is valid if the tube bundle itself is rigid with respect to the surrounding tangential support, i.e., if it undergoes small internal deformations with respect to spring tangential deflections.

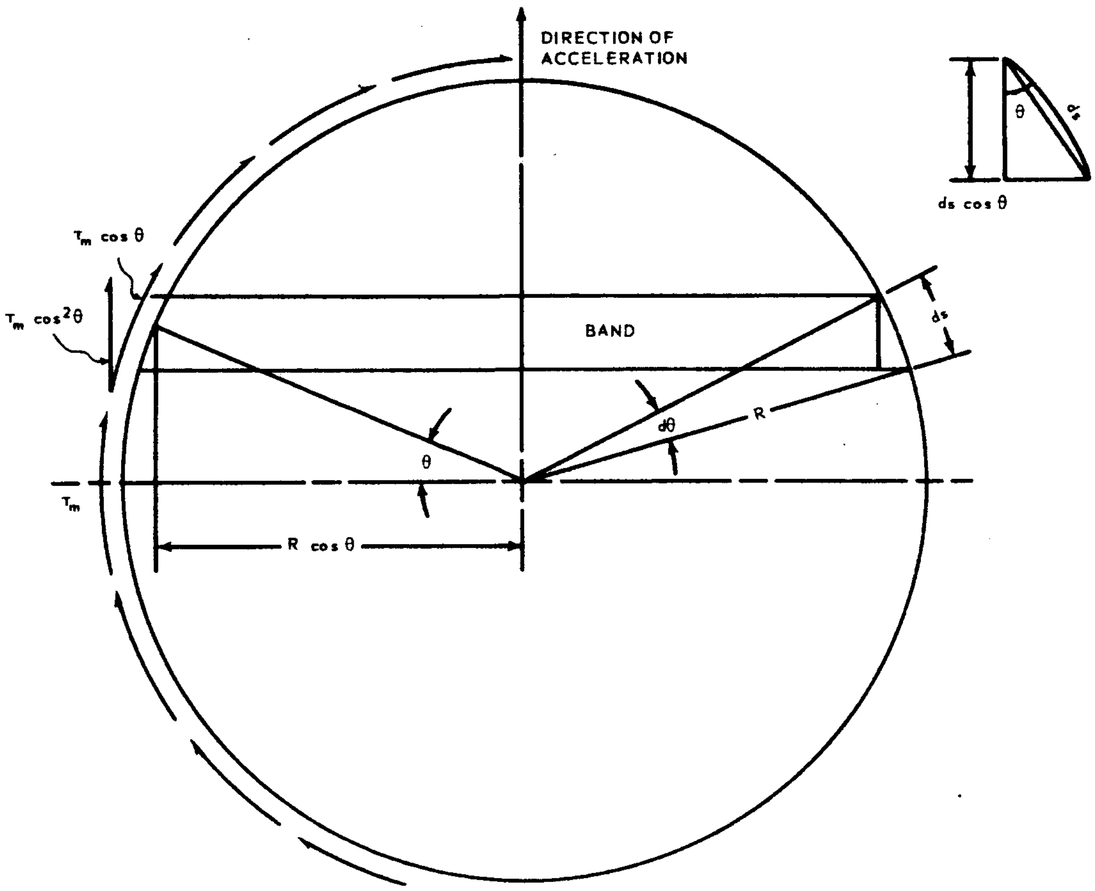

Fig. 4.4-9 – Peripheral shear stresses

If the effective transverse acceleration is n times gravity, the average gross density of the reactor is ρ, and the reactor radius is R, the maximum tangential shear stress is given by the expression

$$\tau_{max} = \rho n R \tag{11}$$

and occurs at the angle $\theta = 0$, where θ is measured from the horizontal. It is readily seen that any band perpendicular to the direction of transverse acceleration requires only those shear forces acting along its peripheral boundaries for transmission of the acceleration forces corresponding to its mass. Referring to Figure 4. 4-9, the area of the band is

$$\begin{aligned} A &= (2R\cos\theta)\cdot(Rd\,\theta\cos\theta) \\ &= 2R^2\cos^2\theta\, d\theta \end{aligned} \tag{12}$$

and the weight of the band per unit axial length is

$$\begin{aligned} dW &= n\rho\cdot A \\ &= 2n\rho R^2\cos^2\theta\, d\theta \end{aligned} \tag{13}$$

The incremental vertical shear component at the band boundary is a force given by the following expression:

$$dV = 2\tau_m R\cos^2\theta\, d\theta \tag{14}$$

The resultant of these shear forces for the whole reactor is as follows:

$$\begin{aligned} V &= 2\tau_m R\int_0^{2\pi}\cos^2\theta\, d\theta \\ &= \pi R\tau_m \end{aligned} \tag{15}$$

The shell supports the bundle by supplying a shear reaction through a device such as keys. This is consistent with the ability of a thin shell (membrane) to furnish a shear reaction (VQ/I distribution) without an out-of-round distortion resulting.

Shear ties as typically illustrated in Figure 4. 4-8 cause shear stresses within the tube bundle. In order to reduce gross distortion or crack formation due to these shear stresses, minimum radial pressure is applied as required to bring about a radial compression that, under the most unfavorable conditions, prevents gross deformation under the maximum acceleration.

This minimum radial pressure is considered from several viewpoints; pure frictional case, nested hexagonal elements without friction, and the tube bundle acting as a beam with suppressed tensile stresses.

Pure frictional case - If the tube bundle were made of noninterlocking pieces, such as aligned square or triangular cross sections, transverse slippage could occur between planes and be opposed only by friction. There being no change in bundle volume, radial pressure would not provide stiffness. Since the radial spring gradient is low, it does not provide an appreciable restoring force.

In the case of pure frictional resistance, the conditions require, on any plane that the product of the normal pressure, P, and frictional coefficient, μ, exceed the shear stress, τ. The minimum ratio of radial pressure to maximum shear stress can be calculated from Mohr's circle theory. The conditions are shown in Figure 4. 4-10. From the simi-

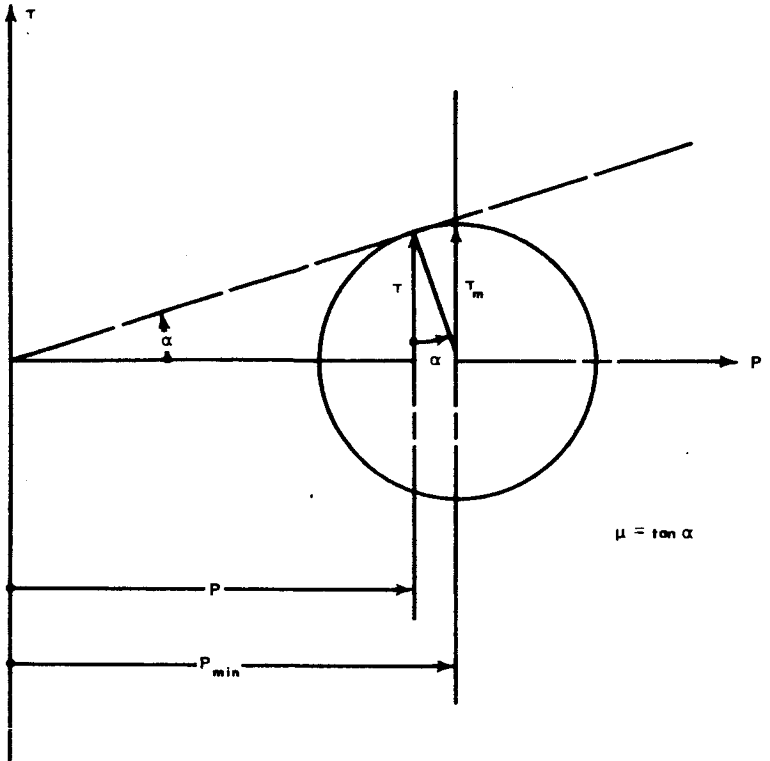

Fig. 4.4-10 - Mohr's circle for case of pure friction

larity of triangles, the minimum value of the radial pressure is given by the following equation:

$$P_{min} \geqq \tau_m \frac{1 + \mu^2}{\mu} \qquad (16)$$

The maximum shear force, τ_m, was shown in Equation (11) to equal $R\rho n$.

The ratio of minimum radial pressure to maximum shear stress is plotted versus the frictional coefficient, μ, in the upper curve of Figure 4. 4-11. However, the factor applies only where planes can be drawn through the fuel element geometry. A minimum value of 0.2 may be assumed for most ceramics of interest, and requires that

$$P_{min} \geqq 5.2\, \tau_m \qquad (17)$$

Hexagonal elements with zero friction - If the pieces have a hexagonal cross section, transverse slippage between adjacent layers always entails an increase in tube bundle volume because of the void between tubes. This increase in volume is opposed by the radial pressure. During the process of slippage, energy is stored in the radial springs and equals the product of the volume increase times the radial pressure. The work produced by the shear forces is equal to the product of the shear force and the displacement in the direction of the shear force. By equating the stored energy with the work produced, the minimum radial pressure that is required to prevent slippage can be found. The geometric model is shown in Figure 4. 4-12

Using the nomenclature of Figure 4. 4-12, the energy stored equals the work done by shear forces. This means that the product of the radial pressure and the change in volume is equal to the force multiplied by the displacement, in other words

$$P_{min} \times 0.8666 \times a = (\tau_m \times 1.73\, a)\ (0.8666) \qquad (18)$$

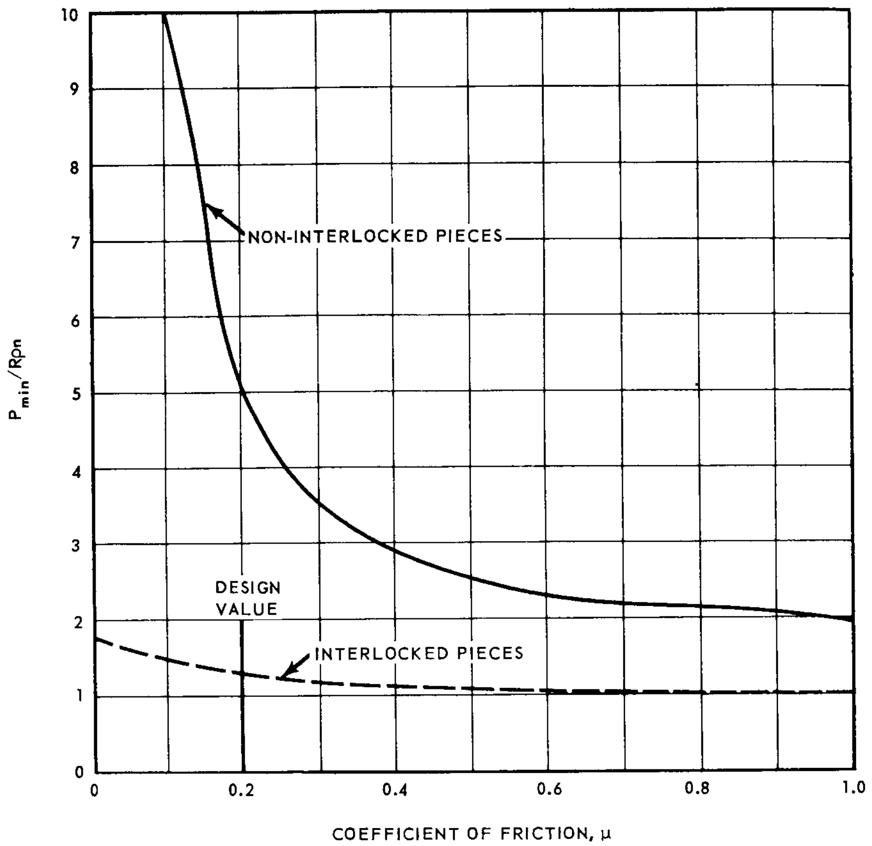

Fig. 4.4-11–Ratio of minimum radial pressure and maximum shear stress versus coefficient of friction

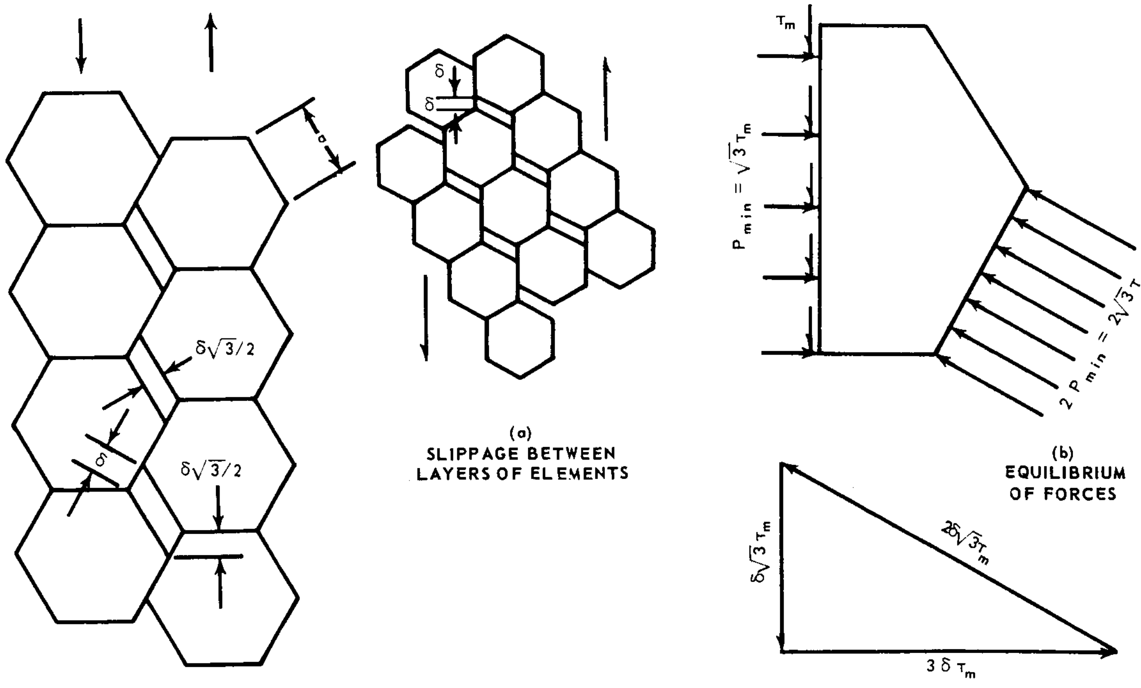
a
δ
δ
$\delta\sqrt{3}/2$
$\delta\sqrt{3}/2$
δ
τ_m
$P_{min} = \sqrt{3}\tau_m$
$2P_{min} = 2\sqrt{3}\tau_m$
$\delta\sqrt{3}\tau_m$
$2\delta\sqrt{3}\tau_m$
$3\delta\tau_m$

(a) SLIPPAGE BETWEEN LAYERS OF ELEMENTS

(b) EQUILIBRIUM OF FORCES

Fig. 4.4-12–Geometric model of slippage between hexagonal tubes

To prevent slippage,

$$P_{min} \geqq 1.73\tau_{max} \tag{19}$$

As shown in Figure 4. 4-12, the half-element with shear stress acting along its dividing line is in equilibrium for the extreme case of zero friction. It is estimated that if friction were included in the calculation, the ratio of minimum radial pressure to maximum shear stress for the nested hexagonals would appear as shown by the lower dashed curve of Figure 4. 4-11. Choosing the conservative frictional coefficient of 0.2, the minimum desired radial pressure is equal

$$P_{min} \geqq 1.3\ \tau_m \tag{20}$$

Tube bundle as a beam - The distribution of transverse forces within the tube bundle is rather complicated. However, conditions can be established, based on somewhat conservative assumptions, that estimate the magnitude of theoretical tensile stresses. The tube bundle is visualized as a beam of variable depth loaded by body forces proportional to the depth and supported by shear reactions around the periphery. Inertial loads cause a distorting couple tending to cause separation along the diameter parallel to the force. A restoring couple equal to or greater than the distorting moment is caused by the resultant of the radial pressure acting at a distance d_1. The geometric model is shown in Figure 4. 4-13.

The location of the resultant of the shear forces is determined by dividing the moment of the shear forces on half of the reactor by the resultant of the shear forces. The moment equals

$$\int_{\frac{\pi}{2}}^{\frac{\pi}{2}} R\ \tau_m \cos\theta\ R\ d\theta = 2\ R^2\ \tau_m \tag{21}$$

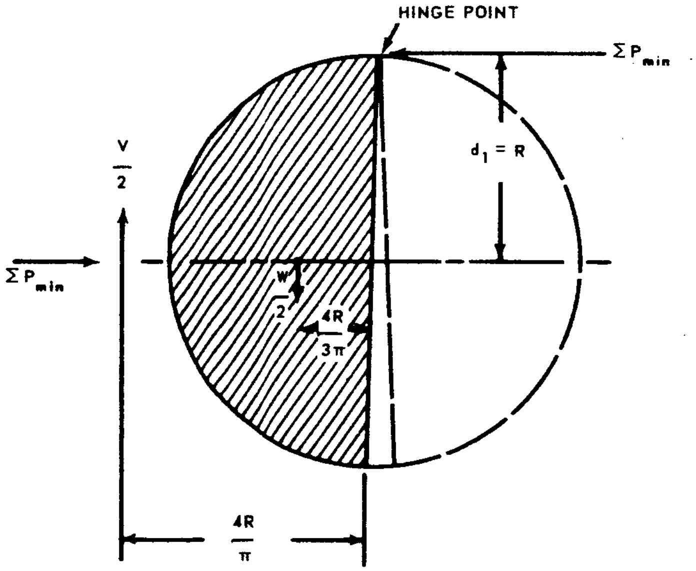

Fig. 4. 4-13 – Model of tube bundle acting as a beam

and the resultant of these same shear forces, Equation (15), is

$$\int_{-\frac{\pi}{2}}^{\frac{\pi}{2}} R\, \tau_m \cos^2\theta \, d\theta = \frac{\pi R \tau_m}{2} \tag{22}$$

The location of the resultant is then equal to

$$\frac{2R^2 \tau_m}{\pi R \tau_m} = \frac{4R}{\pi} \tag{23}$$

Note that the resultant falls outside of the tube bundle as shown in Figure 4. 4-13.

The couples are evaluated as follows:

Distorting couple = restoring couple

$$\frac{W}{2}\left(\frac{4R}{\pi} - \frac{4R}{3\pi}\right) = d_1 \times \Sigma P_{min}$$

Since Equation (15) demands that

$$\frac{4R^3 \rho n}{3} = d_1 \; (2R\, P_{min})$$

stability, therefore, requires the following equation:

$$P_{min} \geqq \frac{2R^2 \rho n}{3d_1} = \frac{2R\, \tau_m}{3d_1} \tag{24}$$

Stability requires that the moment arm, d_1, must vary between zero and R. In the limit, when $d_1 = R$, the equation reduces to

$$P_{min} \geqq \frac{2}{3} \tau_m \tag{25}$$

The resultant of the shear forces acts to cleave the reactor about the hinge point and a permanent distortion of the tube bundle may occur. It is shown later that extremely high local pressures would act on the hexagonal tubes near the hinge if cleavage occurs. Further, it must be remembered that the expression

$$P_{min} \geqq \tau_m \tag{26}$$

must be satisfied, or separation occurs at the location of τ_m (the end of the horizontal diameter). This is similar to the case of pure shear in a beam where the maximum diagonal tensile stress equals the shear stress.

Figure 4. 4-13 shows that the moment arm, d_1, is a function of the pressure distribution occurring during inertial loads along the vertical diameter. Assuming a triangular pressure distribution in the beam as shown in Figure 4. 4-14, the moment arm, d_1, is expressed in terms of R as follows. The force, $2RP_{min}$, acts at the centroid, and

$$d_1 = R - \frac{Y}{3} \tag{27}$$

Stability requires that

$$\begin{aligned} \frac{\tau_{max}}{P_{min}} &\leqq \frac{3d_1}{2R} \\ &\leqq \frac{3R - Y}{2R} \end{aligned} \tag{28}$$

where the limits of Y are zero and 2R.

The parameter X_T (Figure 4.4-14) represents the maximum compressive pressure, and $(2R - Y)$ the cleavage or separation along the vertical diameter. Thus, to completely suppress cleavage, $(2R - Y)$ must equal zero, and $Y = 2R$. By substituting in the equation above, the limiting value of P_{min} is obtained:

$$\begin{aligned} P_{min} &= 2\,\tau_{max} \\ &= 2R\rho n \end{aligned} \tag{29}$$

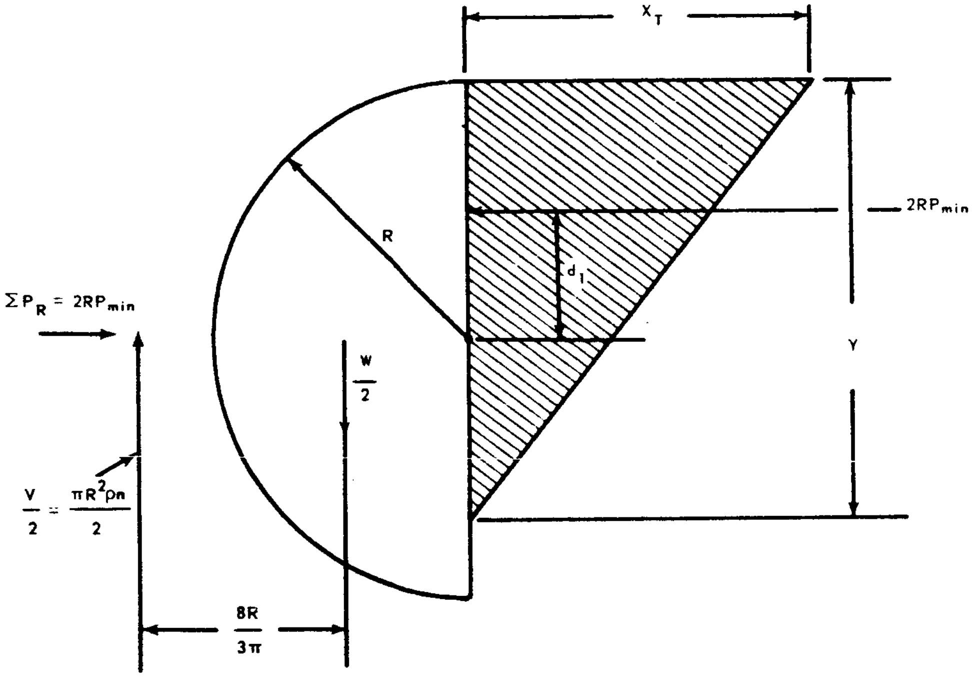

Fig. 4.4-14 – Model of tube bundle with triangular pressure distribution

These equations show that the radial pressure must equal or exceed twice the maximum shear stress to completely suppress cleavage. However, carrying the investigation further, the integrity of the bundle can be maintained with limited separation of the tubes along the critical diameter. Permitting a separation that extends to the core axis ($Y = R$), the minimum radial pressure necessary is reduced to half the former value, and

$$P_{min} \geqq \tau_m \tag{30}$$

The separation of the lower tubes under this condition is limited to the compressive strain along the top half of the critical diameter. Thus, the compressive strain and, hence, the tube separation is insignificant. The compressive pressure, X_T, for this limited separation case is the same as that for complete tensile suppression.

Regardless of the viewpoint used, the minimum radial pressure required to prevent slippage in a tube bundle supported in shear is a function of the maximum shear stress, τ_m, at the periphery. An adjustment factor, C_1, is used such that

$$\begin{aligned} P_{min} &= C_1\,\tau_{max} \\ &= C_1\,R\rho n \end{aligned} \tag{31}$$

For hexagonal tubes with a coefficient of friction equal to zero, C_1 must be greater than 1.73. For a coefficient of friction equal to 0.2, C_1 reduces to 1.3. To fully suppress any cleavage, i.e., separation, along the vertical diameter, C_1 must be 2. With small separations permitted extending to the core axis, C_1 is reduced to 1. It must be realized that C_1 must always remain greater than unity. If it were not, Mohr's circle theory shows that there would be tensile forces across some interfaces in the region where the maximum shear stress occurs. Since tensile forces cannot be transmitted, separation occurs.

For the 141D design, P_{min} was set equal to τ_{max}, and separation was permitted to the core axis when the maximum acceleration forces occurred. Pending a more refined analysis, however, it appears that a value of C_1 greater than 1.3 should be maintained to prevent gross distortion.

4.4.3.2 Internal Pressure Distribution

It is assumed that the pressure on an average hexagonal tube within the bundle is the same as the externally applied pressure, and that a triangular pressure distribution occurs along the vertical diameter to resist the distorting couple due to acceleration forces. The pressure distribution can be found by superposition. Figure 4.4-15 shows the geometric model used in analysis. The general equation is

$$X_T = X_R \pm (2)\left(\frac{h}{R}\right)\tau_m \tag{32}$$

where h is measured from the core axis. Substituting for X_R, the following dimensionless pressure evaluation is developed:

$$\frac{X_T}{R\rho n} = C_1 + \frac{\Delta S_R}{R\rho n} \pm \frac{P_{auto}}{R\rho n} \pm (2)\left(\frac{h}{R}\right) \tag{33}$$

The first three terms are factors related to X_R, and their summation equals or exceeds the last term to suppress cleavage. This pressure evaluation can be used to determine the proper value for C_1.

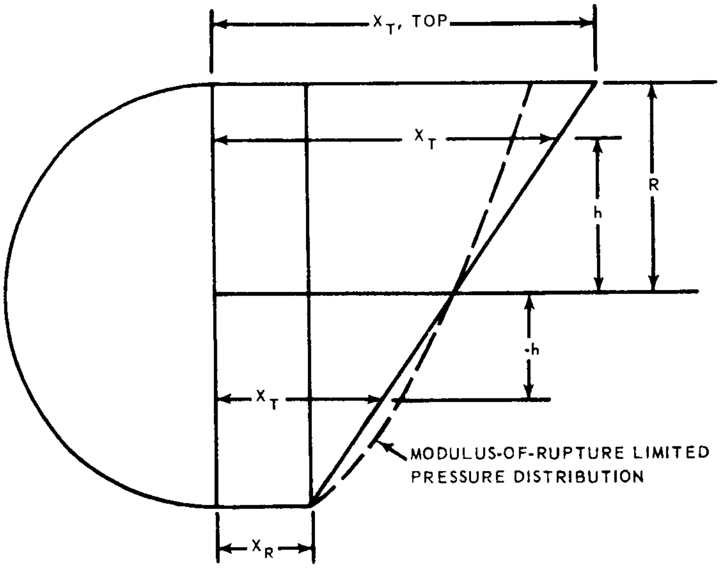

Fig. 4.4-15 – Model used for determining tube bundle internal pressures due to shear radial support

When limited separations are permitted in the tube bundle, the maximum short time design pressures on individual tubes can be obtained from the relationship

$$\frac{X_T}{X_R} = \frac{4}{3 - \frac{2n}{C_1 n_o}} \tag{34}$$

Limited separations can be expected if either

$$\frac{X_R}{R\rho n} \leq 2 \text{ or } \frac{C_1 n_o}{n} \leq 2 \text{ occur} \tag{35}$$

For the maximum design short time pressure, where $C_1 = 1$, Equation (34) reduces to

$$\frac{X_T}{R\rho n} = 4 \tag{36}$$

Equations (32) and (34) are combined and plotted versus the dimensionless value of radial pressure, $X_R/R\rho n$, in Figure 4.4-16. The dotted lines indicate where, and to what extent separations may be expected. In the 141D design $X_R/R\rho n$ varied between 1 and 1.62 as Δ went from zero to maximum. The resulting maximum tangential pressures, X_T, due to the maximum acceleration forces are shown in Figure 4.4-16 as points A, B, and C. Separation existed even with the maximum radial pressure because of the low design preload wherein $C_1 = 1$, and the case of no-separation was assured only below half the design acceleration force, i.e., $n/n_o = 2/4$.

The assumption of a triangular pressure distribution is probably conservative. The modulus-of-rupture type of distribution is more realistic, and is shown as the dotted curve on Figure 4.4-15. The actual short time pressure, X_T, therefore, is probably lower than that given by Equations (32) and (34).

4.4.4 INTEGRATED PRINCIPLES OF RADIAL SUPPORT

Using the integrated principle of radial support, the tube bundle is externally supported by both hydrostatic and shear systems as shown by the geometric model in Figure 4.4-17. Significant reductions occur in both the minimum pressure required to assure tube bundle integrity and the maximum loading pressure, X_T, on the tubes. The effectiveness around the circumference of each system is graphically shown in Figure 4.4-18.

4.4.4.1 External Support

The system spring rate is developed similar to the method used for hydrostatic support, with the additional resistance of the vertical component for tangential or shear forces as shown in Figure 4.4-19. The former assumptions apply, but, in addition, the deflection must be the same to maintain the assembly as a unit.

$$\begin{aligned}
nW &= \sum_0^{2\pi} \text{vertical components of radial and tangential forces} \\
&= \sum_0^{2\pi} \left[P_R \cos\theta + P_T \sin\theta\right] \\
&= \sum_0^{2\pi} \left[S_R\,(Rd\theta L)\,\delta(\cos^2\theta) + S_T\,(Rd\theta L)\,\delta \sin^2\theta\right] \\
\frac{nW}{L} &= RS_R\delta \int_0^{2\pi} \cos^2\theta\, d\theta + RS_T\delta \int_0^{2\pi} \sin^2\theta\ \theta \\
&= RS_R\delta \left[\frac{\theta}{2} + \frac{\sin^2\theta}{4}\right]_0^{2\pi} + RS_T\delta \left[\frac{\theta}{2} - \frac{\sin^2\theta}{4}\right]_0^{2\pi} \\
\frac{nW}{L} &= \pi R\delta(S_R + S_T).
\end{aligned} \tag{37}$$

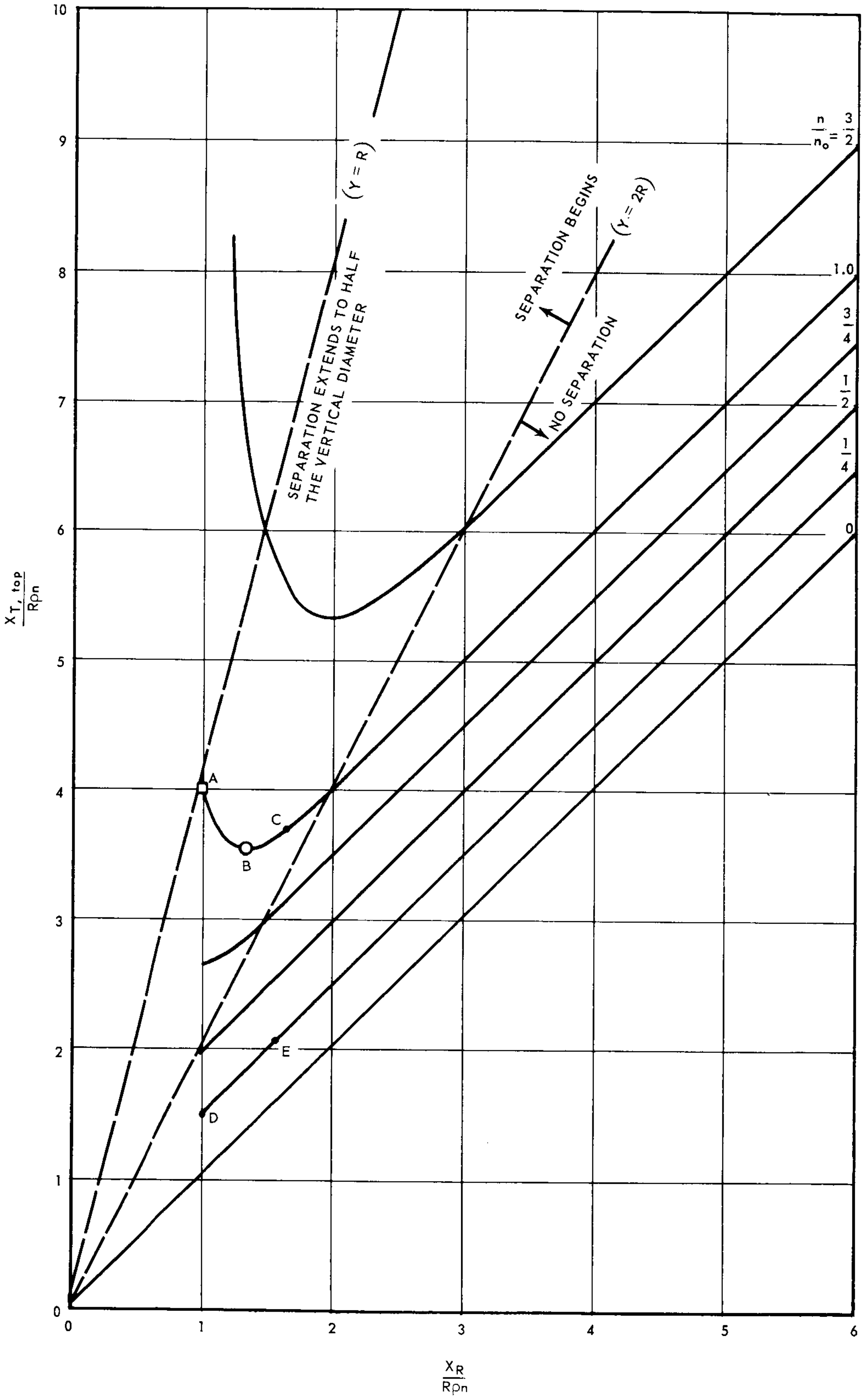

Fig. 4.4-16–Dimensionless plot of tangential pressure as a function of radial pressure

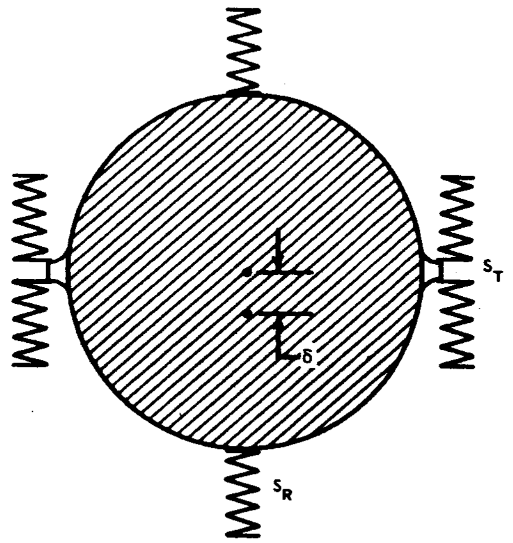

Fig. 4.4-17 – Geometric model of the integrated radial support system

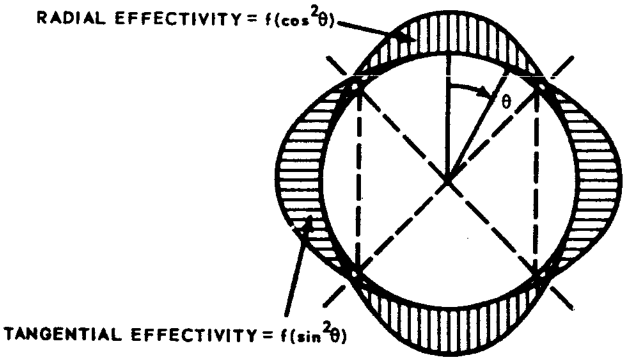
RADIAL EFFECTIVITY = f(cos²θ)
θ
TANGENTIAL EFFECTIVITY = f(sin²θ)

Fig. 4.4-18 – External forces with an integrated radial support system

Letting f equal the fraction of the total support furnished by the hydrostatic system in resisting acceleration forces, Equation (37) can be written as

$$\delta S_R = \frac{fnw}{\pi RL} = f(R\rho n) \tag{38}$$

and

$$\delta S_T = (1-f)(R\rho n) \tag{39}$$

Ample external loading to support the tube bundle is assured by satisfying the two equations above.

The minimum pressure on the tube bundle to prevent distortions during accelerations must satisfy both external systems, and occurs when f = 0.5. This is derived as follows:

$$P_{min} \geq f(R\rho n) \tag{40}$$

$$P_{min} \geq (1-f)(R\rho n) \tag{41}$$

Within the bundle, sufficient pressures must be established to limit separations caused by short-time shear forces, and the methods and implications of the pure shear system previously discussed apply. For simplicity, the integrated support system is designed so that

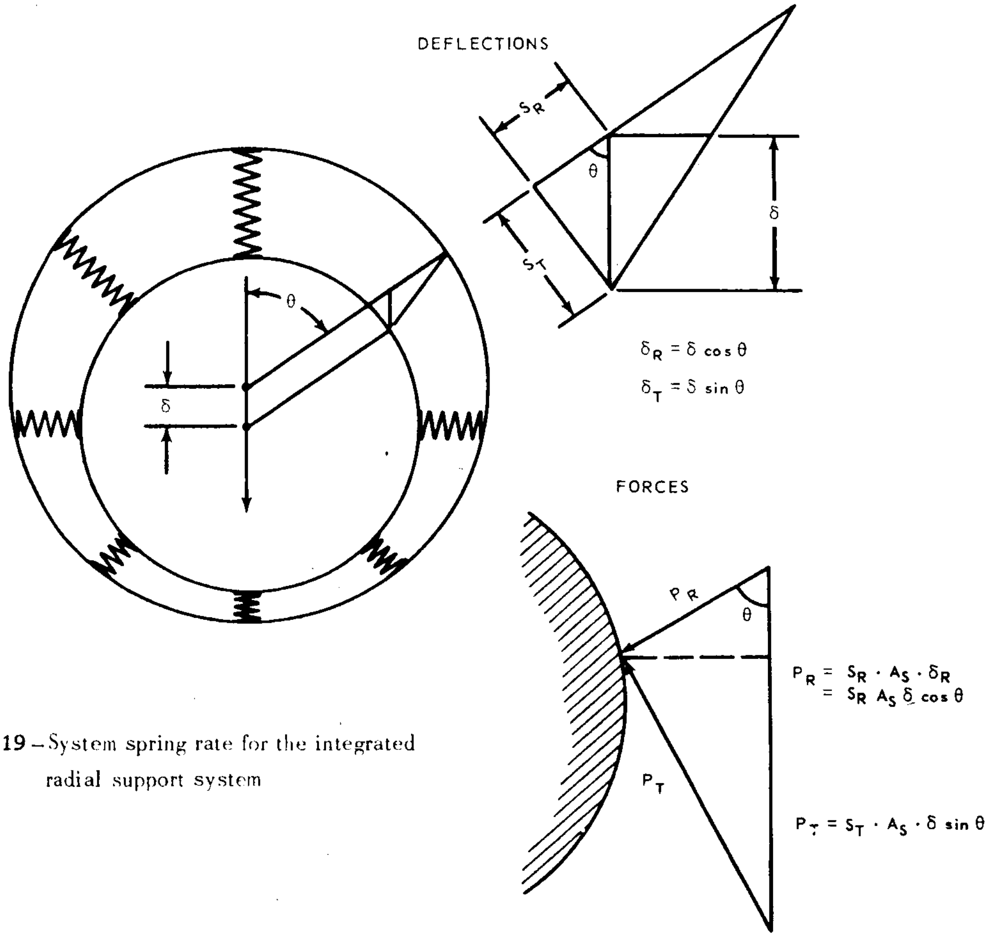
DEFLECTIONS
S_R
S_T
θ
δ
$\delta_R = \delta \cos\theta$
$\delta_T = \delta \sin\theta$
FORCES
P_R
P_T
$P_R = S_R \cdot A_S \cdot \delta_R$
$= S_R A_S \delta \cos\theta$
$P_T = S_T \cdot A_S \cdot \delta \sin\theta$

Fig. 4.4-19 – System spring rate for the integrated radial support system

no separation is permitted along the vertical diameter. Accordingly, both of the following conditions must be met:

$$P_{min} \geq (2-3f)(R\rho n) \tag{42}$$

$$P_{min} \geq (3f-2)(R\rho n) \tag{43}$$

The dimensionless minimum radial pressure, C_1, is shown for values of f ranging from full hydrostatic support (f=1) to full shear support (f=0) in Figure 4.4-20. When half of the inertia load support comes from the hydrostatic system and all separation is suppressed, C_1 is equal to one half, see point b in Figure 4.4-20.

4.4.4 2 Integrated Pressure Distribution

Using the hydrostatic principles of radial support, the internal pressures due to acceleration forces are highest on the lower tubes as shown in Figure 4.4-6 For shear support, the internal pressures are maximum on the upper tubes as shown in Figure 4.4-14. For the integrated system, a reduction in both minimum pressure, P_{min}, and the maximum pressure, X_T, occurs.

Using Equations (7) and (32), the tangential pressures on the tubes are given by

$$X_T = X_R \pm \left(\frac{h}{R}\right)(2-3f)(R\rho n) \tag{44}$$

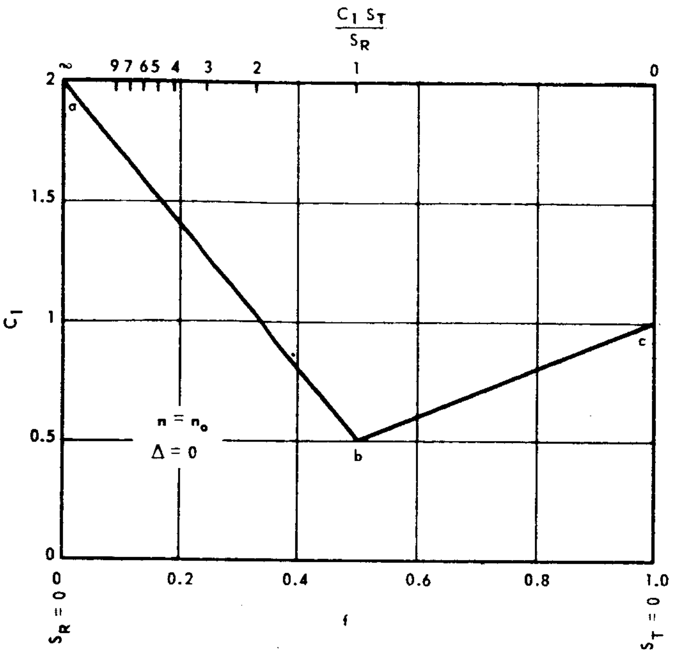

Fig. 4. 4-20 – Plot of C_I as a function of f for use with the integrated radial support system

Expressed in dimensionless form with the actual inertia load assumed equal to the maximum design value ($n=n_0$) and considering the maximum pressure (h=R) at either the top or bottom of the vertical diameter, the tangential pressure becomes

$$\frac{X_T}{R\rho n} = C_1 + \frac{\Delta f}{\delta_a} \pm \frac{P_{auto}}{R\rho n} \pm (2-3f) \qquad (45)$$

The dimensionless maximum radial pressure, $X_R/R\rho n$, is plotted for the integrated system in Figure 4. 4-21. Zero autoclaving and no separation are assumed. The maximum values for expansion, Δ , result in the highest radial pressure. Experience has shown that the value of the term, $\Delta f/\delta_a$ in Equation (45) can be held at 0. 5 when Δ is maximum. Thus, line dh is raised above P_{min} where shear predominates. The radial pressure for higher values of f is dependent on Δ/δ_a, and an estimate of the maximum radial pressure, X_R, as a function of f can be obtained. In the 141D, Δ/δ_a was approximately 4. Thus, points d, f, k, p describe the long-time pressures that the designer encounters depending on the type of suspension chosen.

Pressure increases within the bundle during accelerations are described by the last term of the Equation (45) for both bottom and top locations along the vertical diameter. A dimensionless plot of these short-time pressure increases for the integrated system are shown in Figure 4. 4-22. Point b is of special significance since it shows the calculated value at which tangential pressures are the same during acceleration loading. Figure 4. 4-23 shows the maximum tangential pressure that occurs when combining accelerational loading with the minimum radial pressure to assure bundle integrity.

Pressure superposition diagrams are shown in Figure 4. 4-24 and graphically portray Equation (45) with the previously identified assumption. For the case of f equal to 2/3 and the preload consistent with Figure 4. 4-20, the cancellation of acceleration-induced pressure forces within the bundle is readily visualized. The bottom diagram shows an arbitrary radial pressure, X_R, that is greater than P_{min}, and assumes equal hydrostatic and shear support. This value of X_R, 2. 5, results with a Δ/δ_a ratio of 4, as shown in Figure 4. 4-21.

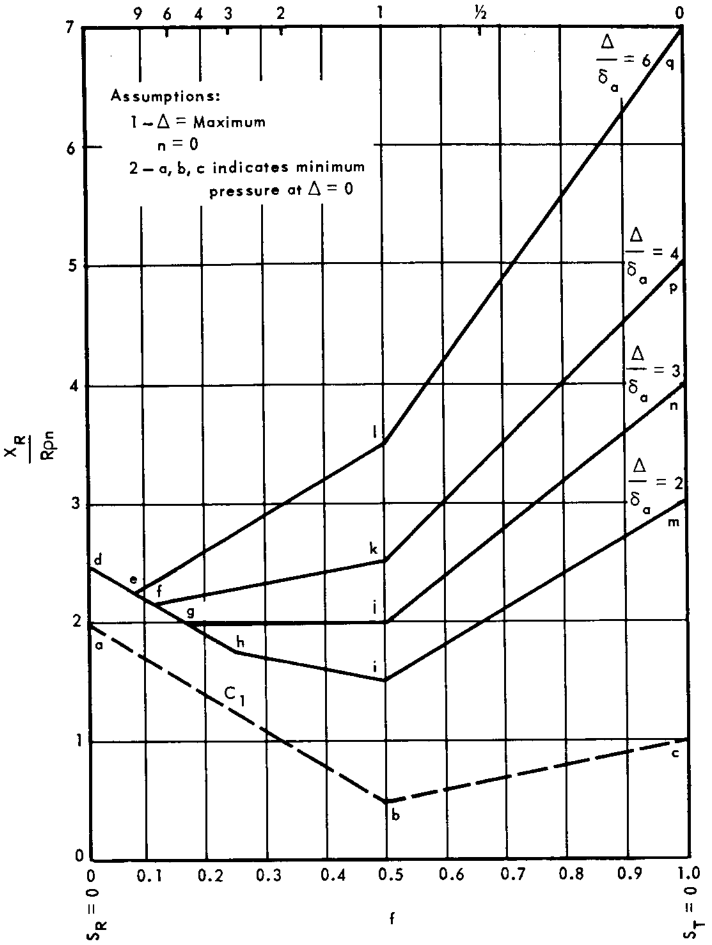

Fig. 4.4-21 – Dimensionless maximum radial pressure in the integrated radial support system

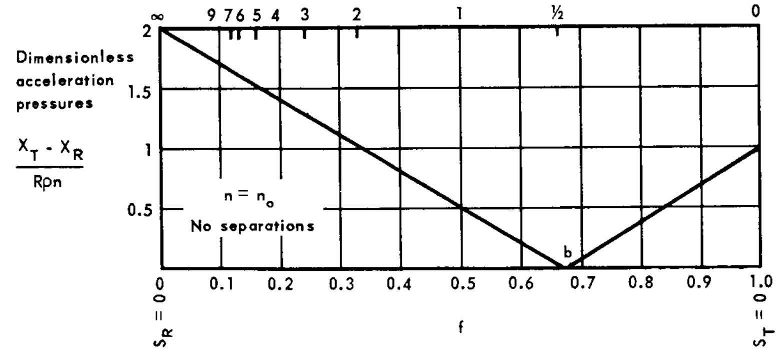

Fig. 4.4-22 – Plot of short-term pressure increases in the integrated radial support system

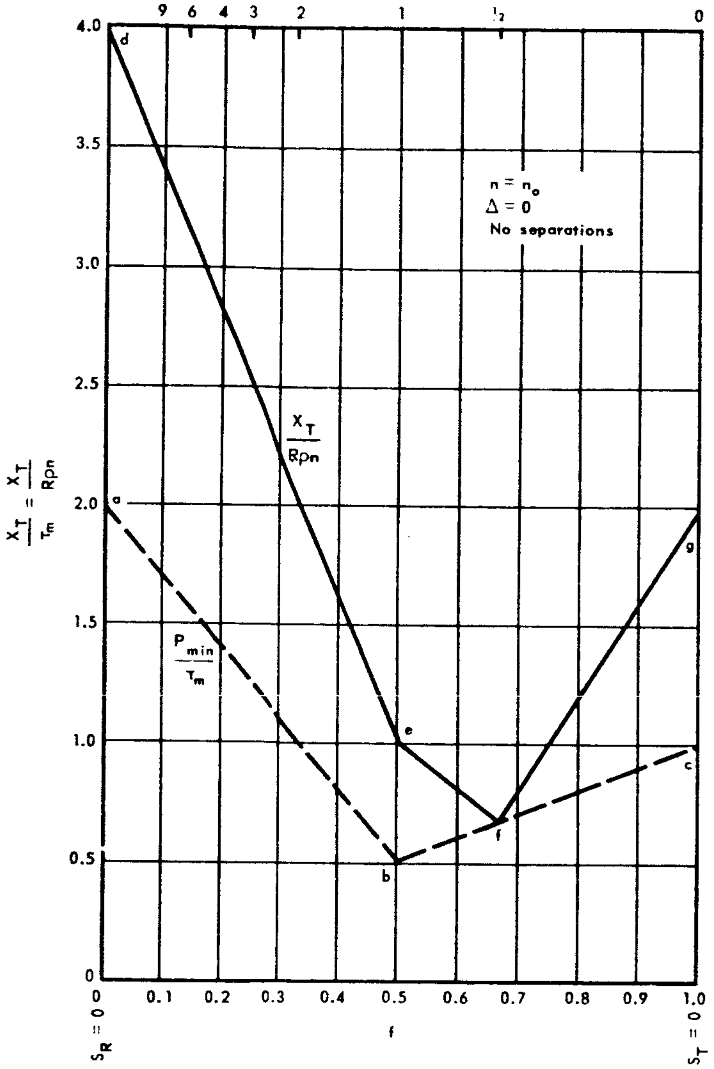

Fig. 4.4-23 – Plot of minimum tangential pressure for combined accelerational loading and minimum radial pressure

The value of the resulting dimensionless maximum pressure, X_T, is 3 and the value of the minimum pressure occurring at the bottom of the bundle is 2.

The maximum accelerational loading is added to the maximum radial pressure curves to obtain the highest dimensionless tangential pressure, X_T, and is shown in Figure 4. 4-25

In summary, if no separations are permitted and Δ/δ_a = 4, an f of 0.5 represents the least value. The minimum pressure is 0.5 Rρn, Figure 4. 4-20, and the highest short-time pressure, X_T, within the bundle is 3Rρn. When f = 0, X_T increases to 4.5 Rρn; in a pure static system the value would be 6 Rρn, or one-third greater. With sophisticated design and suppression of shear stresses, the maximum dimensionless pressures within the tube bundle can be kept between 2 and 3. Values of Δ/δ_a between 3 and 4 have been used in GE-ANPD past designs.

4. 4. 5 COMPARISON OF THE RADIAL SUPPORT SYSTEMS

The integrated support system provides significant reductions in mechanical stresses in the fuel tubes. A greater margin of safety exists if an accidental acceleration larger than the design value is experienced. For example, to meet the design criteria listed in

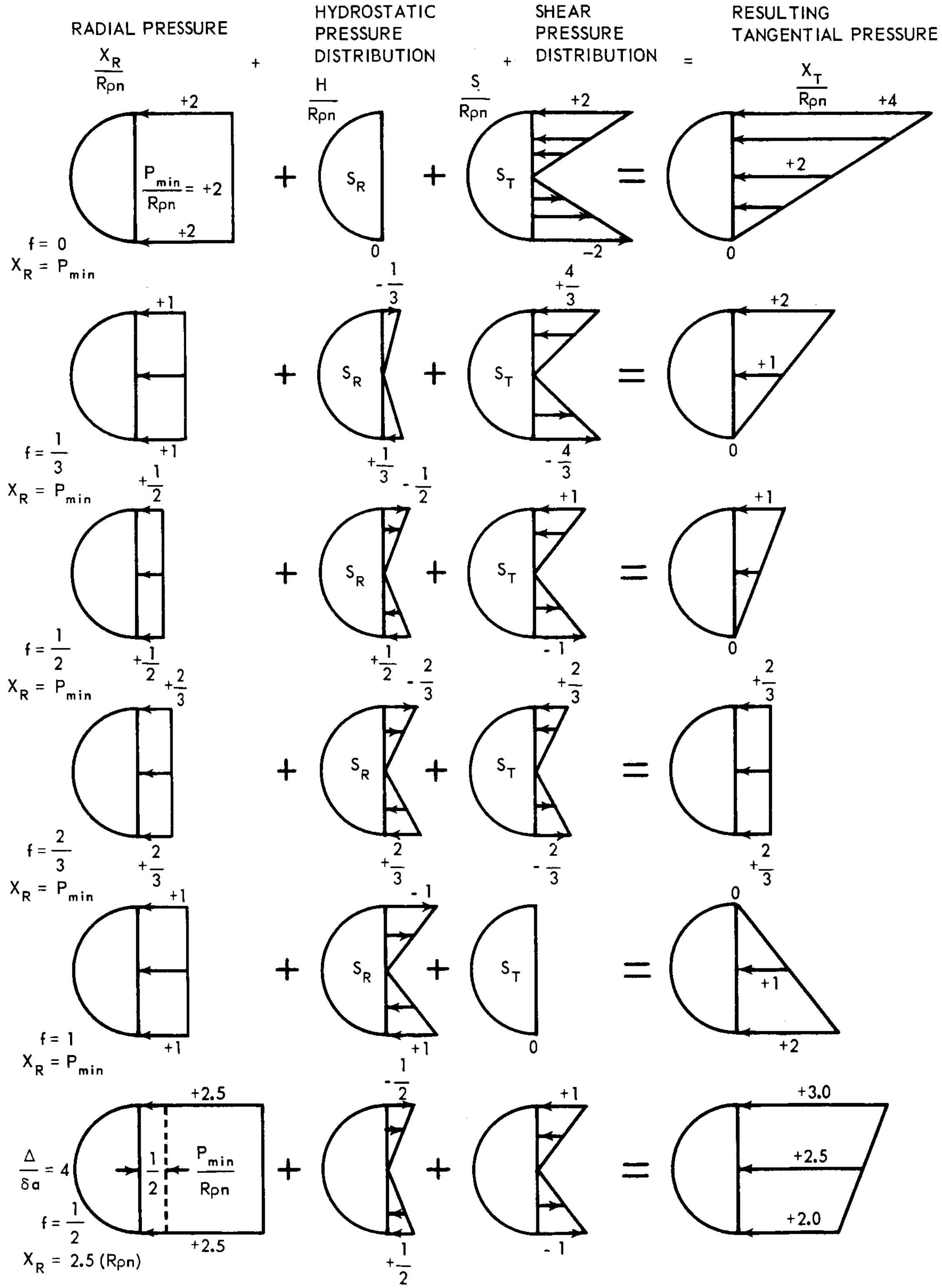
RADIAL PRESSURE
$\frac{X_R}{R\rho n}$
+
HYDROSTATIC PRESSURE DISTRIBUTION
$\frac{H}{R\rho n}$
+
SHEAR PRESSURE DISTRIBUTION
$\frac{S}{R\rho n}$
=
RESULTING TANGENTIAL PRESSURE
$\frac{X_T}{R\rho n}$
+2
$\frac{P_{min}}{R\rho n} = +2$
+2
f = 0
$X_R = P_{min}$
S_R
0
+2
S_T
−2
+4
+2
0
+1
$-\frac{1}{3}$
$+\frac{4}{3}$
+2
S_R
S_T
+1
$f = \frac{1}{3}$
$X_R = P_{min}$
+1
$+\frac{1}{3}$
$-\frac{4}{3}$
0
$+\frac{1}{2}$
$-\frac{1}{2}$
+1
+1
S_R
S_T
$f = \frac{1}{2}$
$X_R = P_{min}$
$+\frac{1}{2}$
$+\frac{1}{2}$
- 1
0
$+\frac{2}{3}$
$-\frac{2}{3}$
$+\frac{2}{3}$
$+\frac{2}{3}$
S_R
S_T
$f = \frac{2}{3}$
$X_R = P_{min}$
$+\frac{2}{3}$
$+\frac{2}{3}$
$-\frac{2}{3}$
$+\frac{2}{3}$
+1
- 1
0
S_R
S_T
+1
f = 1
$X_R = P_{min}$
+1
+1
0
+2
+2.5
$-\frac{1}{2}$
+1
+3.0
$\frac{\Delta}{\delta a} = 4$
$\frac{1}{2}$
$\frac{P_{min}}{R\rho n}$
+2.5
+2.0
$f = \frac{1}{2}$
$X_R = 2.5\,(R\rho n)$
+2.5
$+\frac{1}{2}$
- 1

Fig. 4.4-24– Superposition diagrams of the integrated radial support system

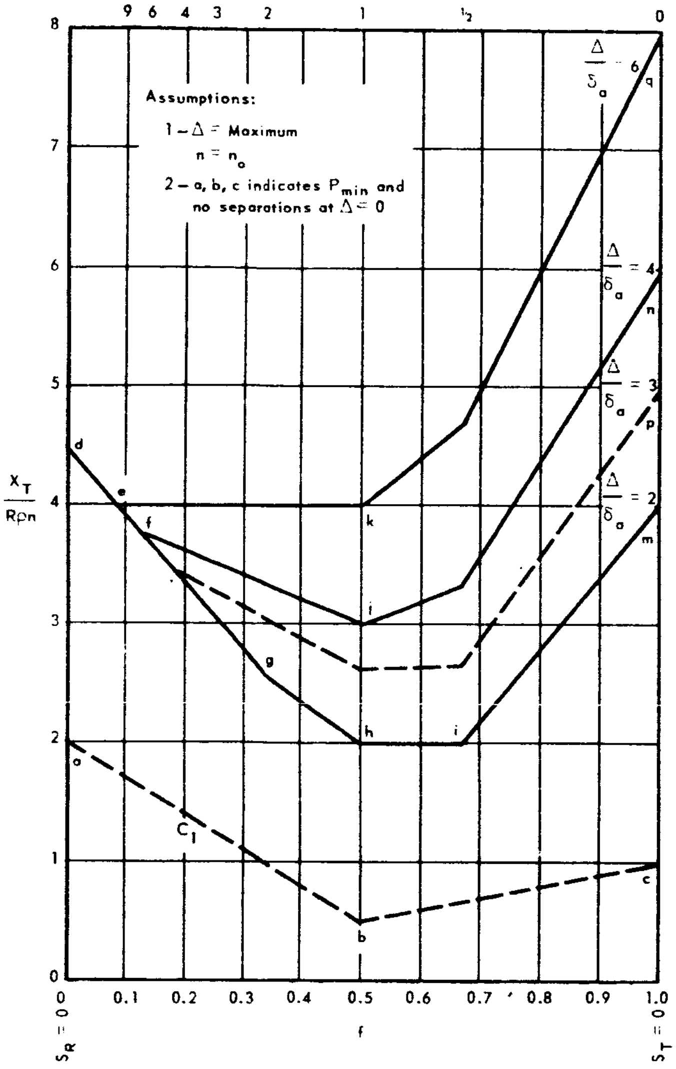

Fig. 4.4-25 – Plot of maximum tangential pressure for combined accelerational loading and maximum radial pressure

section 2.1, the core endures an ultimate load of 1.5 times the limit load without failure. For past GE-ANPD designs, this has represented accelerational loads of 6 G's.

Each of the three systems has its particular merits when considering acceleration forces. Since shear stresses are nonexistent in the pure hydrostatic system, this system is inherently quite dependable. The system offers design simplicity, both analytically and structurally. Its disadvantage is the high radial pressure, although this may be eased by careful design. Spring tolerance adjustors and large allowable deflections, δ_a, are almost mandatory.

The pure shear support introduces short-term high tangential pressures. Because of the brittle nature of the ceramic tubes, short duration of these pressures affords no relief. Nonetheless, the maximum pressures are usually lower than with hydrostatic support. Suppression of all separation is desirable, but the chief concern is the shear-carrying ability within the bundle. Unfortunately, the maximum shear stresses tending to cause slippage occur in the outer reflector where the tubes are often undersized to correct for thermal expansion. Thus, internal displacements may result.

When support is effected by the integrated shear and hydrostatic system, bundle loading and stability pressures are considerably reduced. The lower shear-carrying requirement in the outer reflector helps reduce likelihood of slippage. However, to achieve an integrated system, it is necessary to buy the complications of both systems. Large variations in the load sharing ability, as measured by f, should be expected between analytical predictions and test data. The recalcitrants probably are uncertain side frictional support of the hydrostatic contribution and slippage in areas of large shear stresses. The analytical principles indicate that a balanced support, f equal to 0.5, is a reasonable design value.

4.4.6 TUBE BUNDLE VIBRATION

The following discussion is divided into external effects and internal effects. The external effects are those resulting when the tube bundle vibrates as a rigid bundle and may adversely effect the integrity of the supporting systems. The internal effects are those occurring between tubes within the tube bundle, and may adversely effect the integrity of the bundle itself.

4.4.6.1 External Effects

Two modes of vibration of a unit bundle within the shell have been studied. In one mode, the bundle and shell axes remain parallel but translate, while in the other mode the axes have a relative pitching rotation. The two modes are shown schematically in Figure 4.4-26. For the first mode, the deflection under static load is computed from Equation (3), or (37), and substituted in the familiar formula

$$f_n = \frac{1}{2\pi}\sqrt{\frac{g}{\delta_{st}}} \tag{46}$$

$$= \frac{3.127}{\sqrt{\delta_{st}}} \text{ cps} \tag{47}$$

where

g = gravitation constant, 386 inch/sec^2
f_n = natural frequency in cycles per second, cps
δ_{st} = static deflection, inch

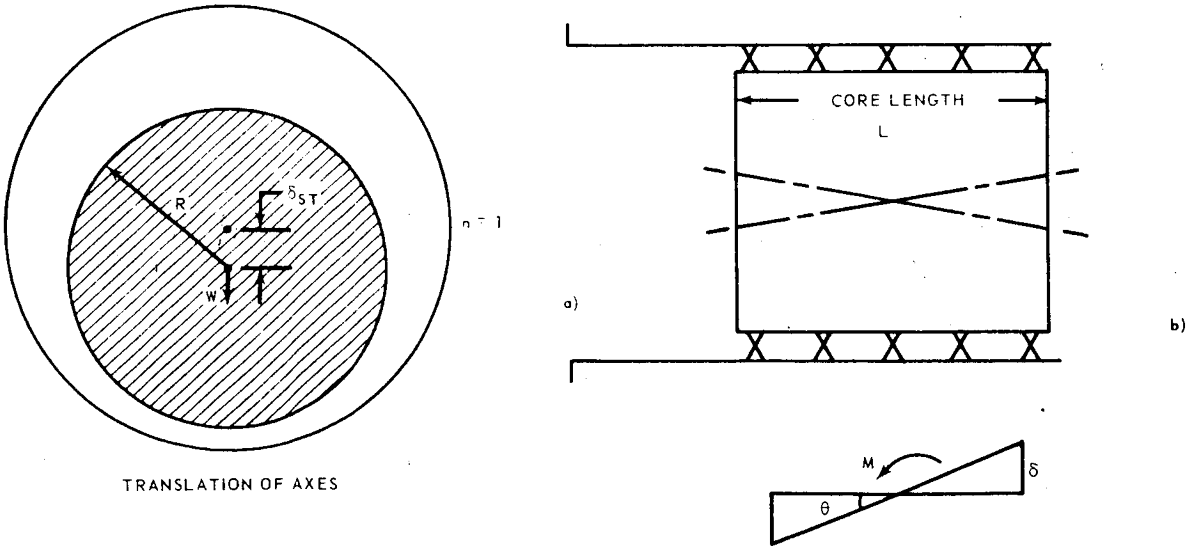

TRANSLATION OF AXES

PITCHING OF AXES

Fig. 4.4-26 – Modes of external vibration

All GE-ANP ceramic reactors have been designed for ±0.12 inch allowable deflection during an inertial load factor of four. Therefore, the natural frequency in translation is readily estimated as 9 cps. A log-log plot of Equation 47 is quite useful.

When a portion of the radial support system vibrates as a part of the tube bundle, that portion of the support system weight should be included with the tube bundle weight. In the three-tier mockup subsequently described, this factor represented 1/3 of the total spring weight and increased the effective weight of the vibrating tube bundle by 3 percent.

Considering the hydrostatic mode of radial support, as the bundle deflects vertically under acceleration loads the horizontal force introduces large side frictional loads which restrain bundle movement. This damping force is large and is dependent on (1) the radial pressure times the frictional coefficient at the springs, and (2) the lateral stiffness of the springs. An inherent problem of the pure hydrostatic support system is that, as the vibrations are dampened out, the tube bundle may come to rest in an eccentric position. When the damping is large, design allowance may be necessary in alignment of the control rods, axial structure, and spring cooling channels. Damping is discussed further in the next section, three-tier mockup tests.

For a missile or airplane, the gust load factors are of short duration. They do not constitute impact-type loads because of the aeroelastic effects of the airframe and the fact that the gust velocity builds up gradually from zero as the airframe penetrates the gust. An estimate of gusting derived from civil transport data was used. Figure 4.4-27 shows the decrease in amplitude of the vibration in a tube bundle supported as shown in Figure 4.4-3 with a coefficient of friction equal to 0.1. Figures 4.4-28 and 4.4-29 show a comparison between the vibratory effects of gust loading and short-term loading, respectively, and with frictional coefficients of zero and 0.1.

In the second mode of external vibration the rotation of the bundle axis is assumed to produce a load on the suspension system proportional to the distance from the center. This load is converted to deflection by dividing by the integrated spring rate. From the deflection (δ), the angle of rotation, (θ), in terms of an imposed moment is computed. The angle is set equal to one radian and the moment and torque are computed.

The natural frequency in pitching is given by the formula

$$f_n = \frac{1}{2\pi}\sqrt{\frac{K}{I_M}}, \qquad (48)$$

where the mass moment of inertia is

$$I_M = \frac{W}{4g}\left[R^2 + \frac{L^2}{3}\right] \qquad (49)$$

and the torque required to produce an angle of twist of one radian is equal to

$$K = \frac{M}{\theta} \qquad (50)$$

From Figure 4.4-26, the angle, θ, is equal to

$$\theta = \frac{2\delta}{L}. \qquad (51)$$

Since

$$\delta = \frac{Mc}{IS_j}, \qquad (52)$$

and

$$\frac{I}{c} = \frac{RL^2}{6R} = \frac{L^2}{6}, \qquad (53)$$

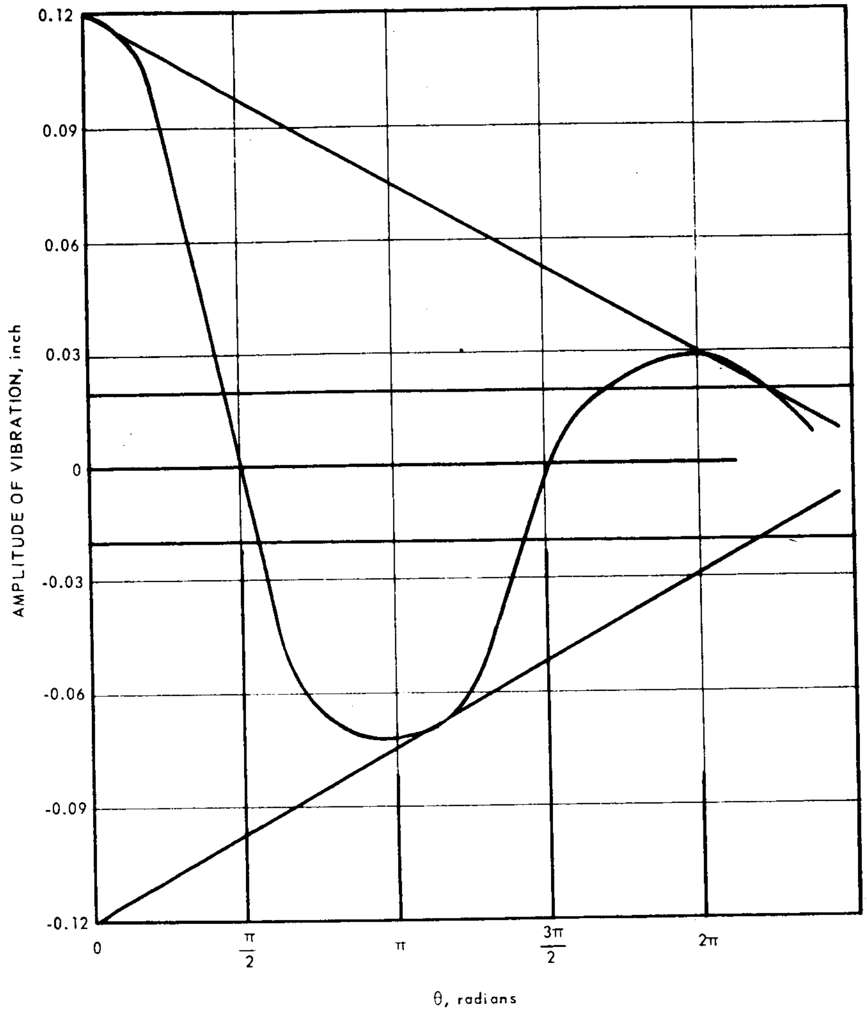

Fig. 4.4-27 – Frictional dampening with hydrostatic radial support and coefficient of friction of 0.1

the integrated spring rate, S_j, is

$$S_j = \left(\frac{W}{L}\right) - \frac{1}{\delta_{st}} . \tag{54}$$

Through substitution, Equation (50) is reduced to torque, as follows:

$$K = \frac{L^2 W}{12 \delta_{st}} . \tag{55}$$

Equation (55) is combined with Equations (48) and (49) to give an approximation to the natural frequency in pitching in cycles per second

$$f_n = 3.127 \sqrt{\frac{L^2}{\delta_{st}[3R^2 + L^2]}} \tag{56}$$

Thus, the typical tube bundle reactor limited to a 0.12-inch deflection vertically at an inertia load of four had a pitching natural frequency of approximately

$$f_n \approx 10 \text{ cps}$$

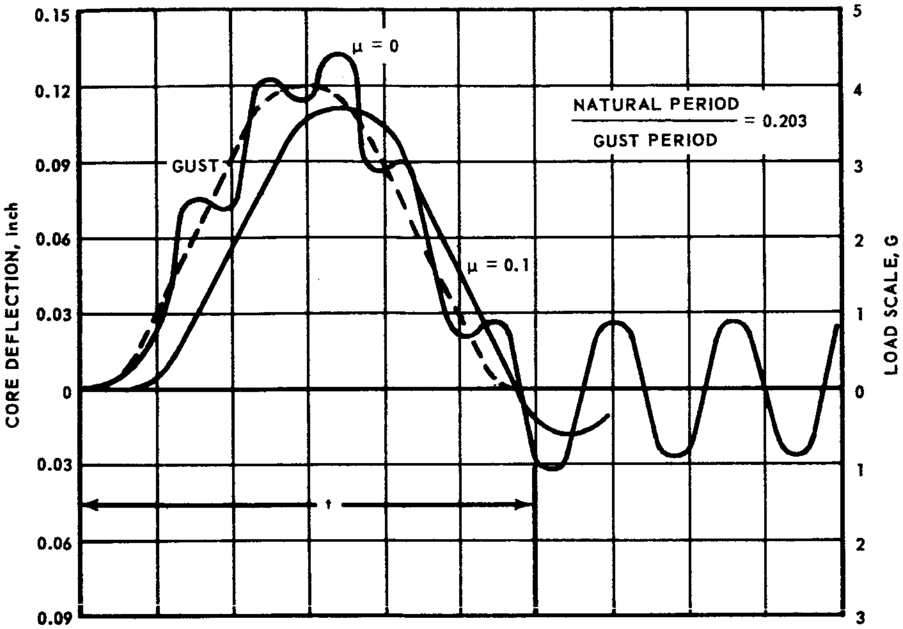

Fig. 4.4-28 - Frictional dampening of vibration induced by gust loading

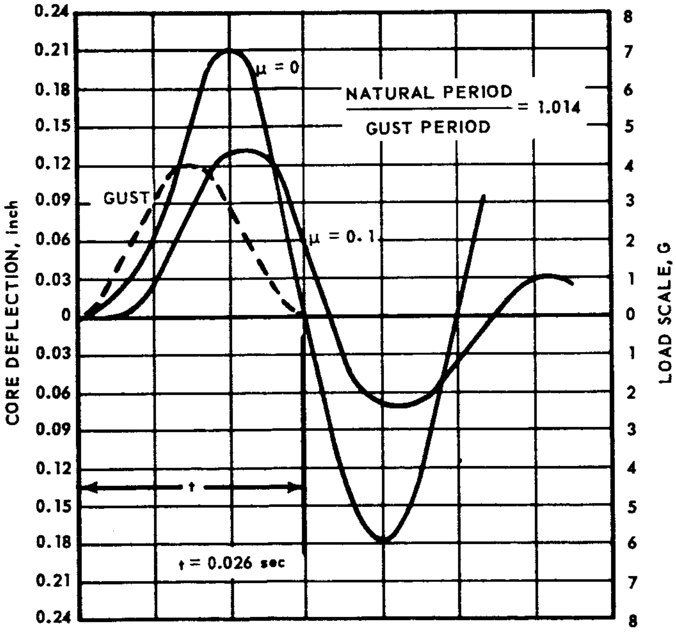

Fig. 4.4-29 - Frictional dampening of vibration induced by short-term loading

4.4.6.2 Internal Effects

These effects do not lend themselves to an analytical treatment. However, the two phases of development testing indicate the relatively low importance of these effects. One phase of the testing was to study the bridging of a load around a cavity in the bundle. The second phase was to define locations and magnitude of separations. The mockup used was similar to the full scale three-tier version subsequently described, but had a 30-inch diameter, was 10 inches long, and consisted of two tiers of tubes.

Bridging around cavities - The number of tubes that could be removed from the mockup before collapse occurred during vibration was determined. A vibration of 0.002-inch amplitude and 83 cps was imposed upon the mockup and a group of tubes was removed from the lower quadrant of the mockup. Rows of tubes were then removed to produce progressively larger cavities. The vibration environment was held constant for a ten-minute dwell period after each removal. The final removal of tubes led to a hexagonal cavity approximately 13 inches across flats. The mockup remained stable under vibrational loads with this large cavity for a test period of 15 minutes, and showed the inherent stability of the tube bundle. The tubes adjacent to the cavities did not crack; this observation implied that a large pressure magnification at the cavities probably did not develop.

Separation - The locations and magnitudes of separations within the bundle were investigated with respect to the input disturbing force. The average radial spring pressure was 10.5 psi. Although the tubes measured were definitely moving 180 degrees out of phase with one another, the magnitude of displacement was so small that only a tendency toward separation can be said to exist.

4.4.7 THREE-TIER MOCKUP TESTING

Development testing with the three-tier full scale tube bundle mockup showed that the tangential component of the internal pressure was only partially effective. Equation (37) was modified to allow for a tangential spring rate defectiveness, C_2, as follows:

$$\frac{nW}{L} = \pi R\delta \left(S_R + C_2 S_T\right) \qquad (57)$$

The C_2 factor has been verified during development testing and the data presented below have a high level of confidence.

4.4.7.1 Test Program

Before assessing C_2, a brief description of the mockup is appropriate. The tube bundle had a diameter of 56 inches and was 14.5 inches long.

The radial support system consisted of staggered elliptical leaf springs each covering a 10-degree arc and a 2-inch core length. Pressure pads covering a 5-degree arc and continuous over the length of the tube bundle distributed the spring load to the reflector tubes. The spring reactions were transmitted through adjustors to a semi-rigid shell. The shell was 59 inches in diameter, 21 inches long, and 0.37 inch thick. The core mockup was 50 inches in diameter, and built up of hexagonal tubes whose across-flats dimension statistically averaged to 0.372 inches. The 3-inch thick outer reflector hexagon bars statistically averaged 0.365 inches across flats, therefore producing slight radial cracks, or voids, uniformly around the tube bundle. The reflector bars were undersized primarily to allow for expansion differences that can occur following reactor shutdown when the core is quickly cooled relative to the outer reflector. The shear ties between the outer reflector and the structural shell were shown previously in Figure 4.4-8.

The tube bundle was built up from three full length tubes. Triangular groups of 24 tubes furnished a natural stagger or overlap throughout the tube bundle. The groups alternated with 3 full length tubes (4.83 inches) and 2 full length tubes with 1/2 length tubes at the ends. Larger ceramic hexagon tubes (radial arches), each displacing 19 smaller tubes, provided access through the tube bundle for axial-support tie bars when desired. During a portion of the mockup tests, a thin-wall stainless steel liner with an equivalent outer diameter of 11 inches was placed at the center of the core.

The tangential spring rate effectiveness factor, C_2, was evaluated for the mockup by comparing the calculated spring rate obtained from Equation (37) with the experimentally measured value by the following rationalization. Values of both S_R and S_T used in the equation were measured for typical springs outside the mockup. The results, plotted in Figure 4.4-32, illustrated the softening of the tangential spring rate as the spring gap, h, or the radial pressure decreased. Assuming that the springs act at their full theoretical value in both the radial and tangential direction, it follows from Equation (57) that the ± 4n displacement is given by

$$\delta = \frac{2nW}{L\pi R}(S_R + C_2 S_T) \qquad (58)$$

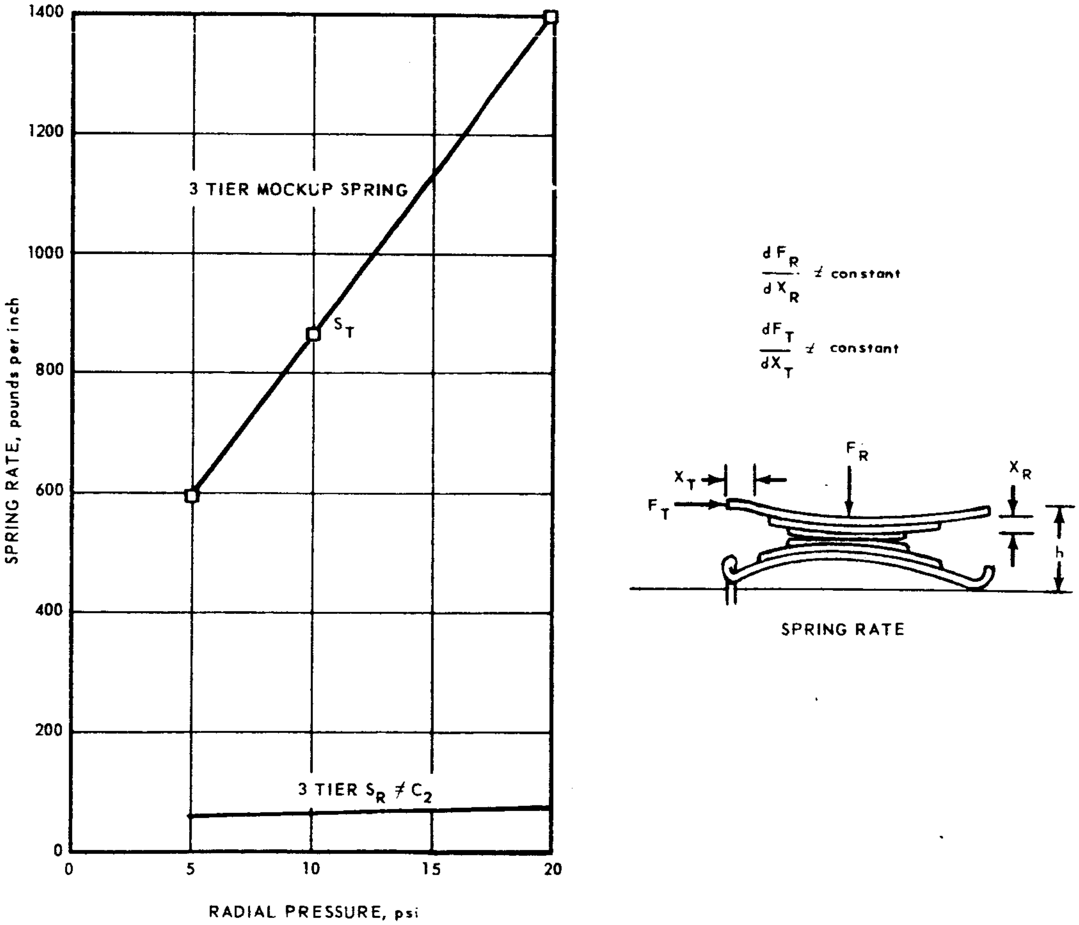

Fig. 4.4-32 – Variation of radial and tangential spring rates

By applying S_R and S_T values from Figure4. 4-32,the theoretical variation of displacement versus radial pressure is determined. The results of this calculation are shown in Figure4.4-33labeled as $C_2 = 1$.

The test procedure was to shock the mockup while it was in a given configuration in successive 1 G increments from 1 to 5 G's. The specimen was then rotated 180° upon the sled, reversing the direction of the applied acceleration. The reversal forced the tube bundle into its extreme static location within the shell. The test data are graphically presented in references 13 and 14 and clearly show the effect of variation of parameters. The nature of the shock phenomenon, however, needs further explanation.

The acceleration caused by the pure square wave is shown in Figure4. 4-34,curve A. Due to harmonics and other distortions, the pure wave is shown by curve B; this curve reproduces a true typical acceleration record as copied from an oscillograph recording. Figure4. 4-34,curve C illustrates a typical displacement transducer trace and shows the static component of displacement as well as the dynamic peak.

Data from a typical transducer are shown in Figure4. 4-35,curve A. The dimension S denotes the static component of displacement from the pre-test zero reference for the particular transducer; R denotes the residual displacement in the unaccelerated state. Reversal of the specimen on the sled reverses the direction of the trace displacement, as shown here after test number 28, when rotation occurred. Curve B, Figure4. 4-35,shows the technique used to present most of the data recorded in one series of 90 tests. The saw tooth chart represents the average displacement of the core from the zero reference and the dots around each tooth represent the scatter of individual displacement values. The data reduction technique is shown in Figure4. 4-36.The total displacements A and B were the values used to plot the data shown in Figure4. 4-33.

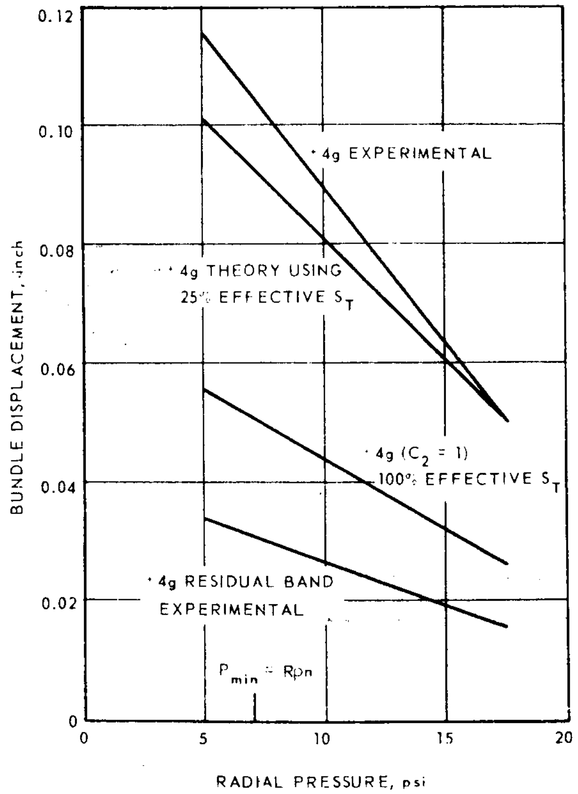

Fig. 4. 4-33 – Tangential spring rate effectiveness in the three-tier mockup

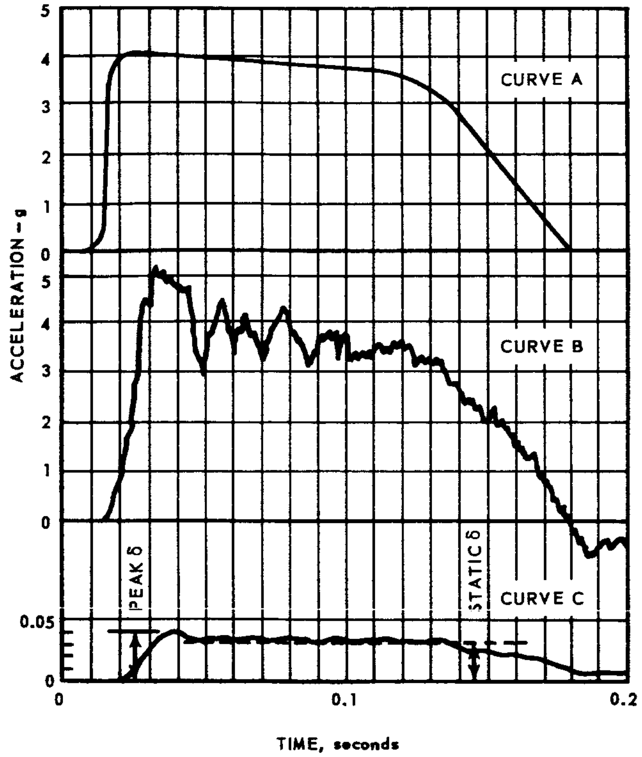

Fig. 4.4-34 – Shock phenomenon used in three-tier mockup data analysis

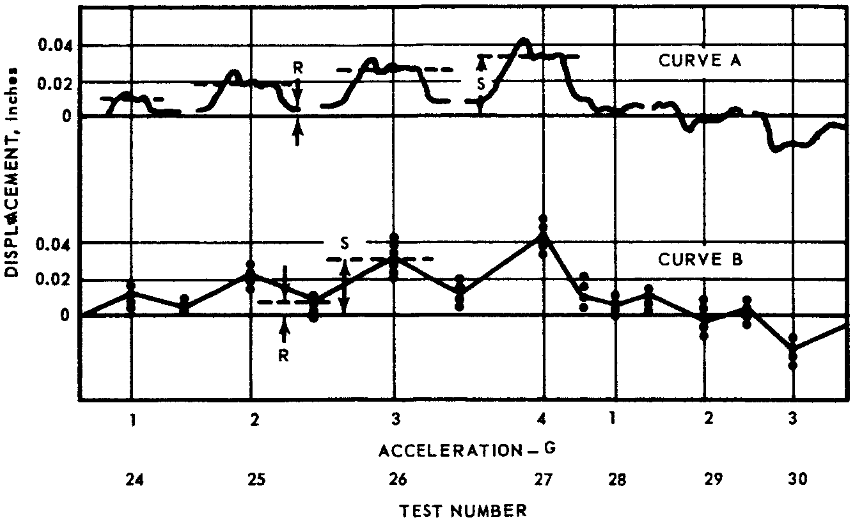

Fig. 4.4-35 – Typical transducer traces for three-tier mockup testing

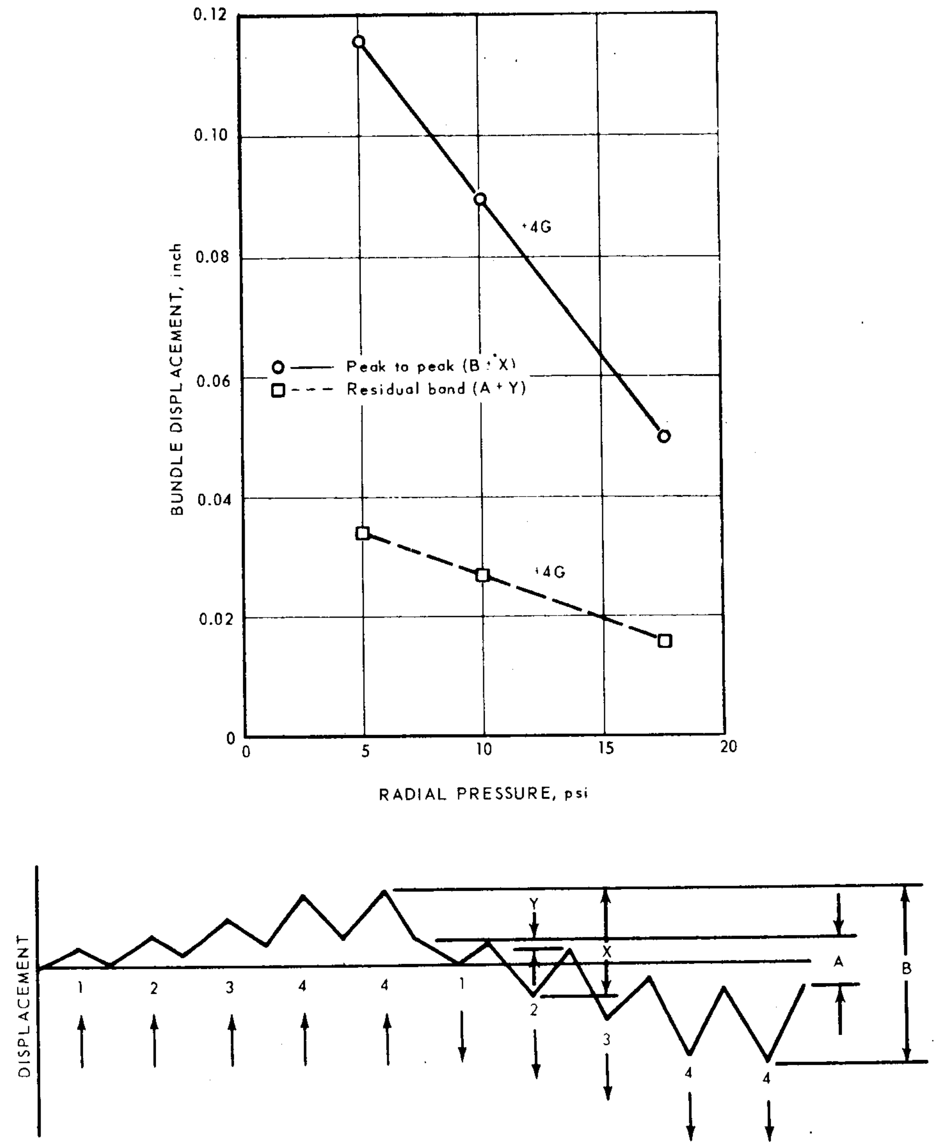

Fig. 4.4-36 – Data reduction technique used with three-tier mockup data

4.4.7.2 Effective Tangential Spring Rate

Test data of the type indicated in Figures 4.4-34 through 4.4-36 showed that the maximum effectiveness of the tangential spring action was not realized in the three-tier mockup. By comparing the calculated and true value of the effective tangential spring rate, a tangential effectiveness of 25 percent was assumed for design purposes. The theoretical and experimental data are shown in Table 4.4-1.

A few additional notes concerning the mockup experience are as follows. First, the assumption in the derivation of Equation (37) that the displacement of the tube bundle varies linearly with the acceleration was verified, i.e., nW/δ was constant. Therefore, linear extrapolation on the basis of tube bundle weight is valid. Secondly, although several reassemblies of the mockup were made, only one set of springs and one set of ceramic tubes were utilized during the tests. Consequently, the tests explored only one ratio of tangential to radial spring rates, C_2S_T/S_R, as a function of preload condition. It has been assumed that changing to a spring of lesser radial spring rate (larger ratio of C_2S_T/S_R) has only a

TABLE 4. 4-1

TANGENTIAL SPRING RATE
EFFECTIVENESS FROM THREE-TIER
MOCKUP DATA

		Theoretical ($C_2=1$)		Experimental		
X_R	n	$\frac{S_T}{S_R}$	f	$\frac{S_T}{S_R}$	f	C_2
5	2	10	0.1	2.5	0.4	26%
5	4	10	0.1	1.6	0.6	17%
10	2	12	0.08	3.4	0.3	30%
10	4	12	0.08	2.5	0.4	22%
17.5	2	15	0.07	5	0.2	34%
17.5	4	15	0.07	3.7	0.27	25%

Note: $P_{min} = \frac{n_o W}{RL} = \frac{4(2300)}{(28)(14.5)} = 7.2$ psi

linear effect on displacement. Thirdly, the tests established that the use of a mechanical shear tie arrangement contributes to the retention and centering of the tube bundle. The total residual displacement, or hanging up, of the core within the shell after acceleration loads remained at a minimum, and the deflections experienced were 1/3 of the value that would occur for a pure hydrostatic system wherein $C_2 S_T = 0$. Fourth, it should be emphasized that the experimental data shown are based on steady inertial loads, depicted by S on Figure 4. 4-35. The overshoot effects inherent in extremely short rise time (impact) loadings were not evaluated.

In practice, the dynamic deflection peak probably would not occur as it did with the input square-wave acceleration produced by tne particular Hyge shock test rig. As would be expected, the maximum dynamic deflection overshoot measured in the mockup tests occurred when the + 5-G acceleration followed the -5-G (180° reversal). The critical factor to be determined when estimating the dynamic peak, if it exists, is the short interval of time during which the acceleration load is applied. For the 141D design, an increase in the static displacement of 50 percent as peaking allowance was made, although this amount is probably unduly conservative.

4. 4. 7. 3 Internal Spring Rate

The previous rationalization of test data established that the tangential spring rate observed during mockup testing was only partially effective, and that a value for C_2 of 0.25 was reasonable. The experimental work further established that there is a zone of relative displacement within the core itself as seen from the data shown in Figure 4. 4-37. As indicated therein, the displacements within the tube bundle vary with the distance outward from the axis. It appears as if an additional spring system is contained within this region of the core assembly and effectively acts in series with the tangential spring rate, with the summation of the tangential and the additional spring systems acting in parallel between the shocking device (Hyge sled) and the tube bundle.

Denoting the additional spring system by S_X, the integrated spring rate is expressed as follows:

$$\frac{nW}{\delta} = \pi RL \left(\frac{S_T S_X}{S_T + S_X} + S_R \right) \qquad (59)$$

It follows that

$$\frac{S_T S_X}{S_T + S_X} = C_2 S_T \qquad (60)$$

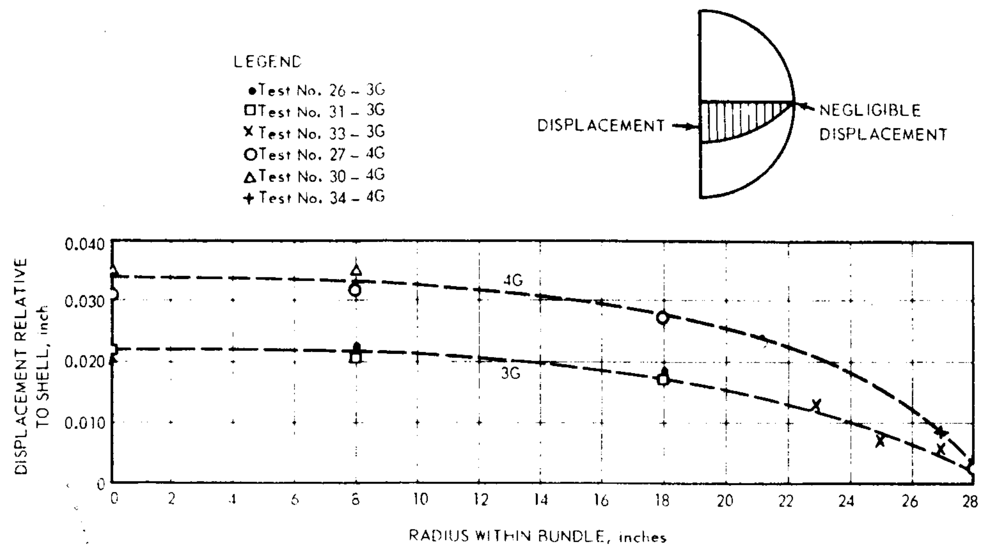

Fig. 4. 4-37 – Displacements within tube bundle during three-tier mockup testing

and, for $C_2 = 0.25$,

$$S_X = \frac{S_T}{3} \tag{61}$$

The experiments showed that the displacement is elastic, i.e., the original situation is restored and a permanent set is not observed. Furthermore, the data showed that S_X remained constant for a given radial pressure.

The internal displacement of Figure 4. 4-37 apparently are related to the undersized reflector bars. The reflector bars were 0.365 inch across flats while the tubes which represented the core were 0.372 inch across flats. The discrepancy in size creates gaps in the reflector region which, in turn, permits some movement of the rods and tubes with respect to one another. Numerous photographs were taken, but failed to produce any detailed knowledge of the nature of the deflections because of the very small motion between adjacent tubes.

The following expression correlates the tangential spring effectiveness with the fraction of transverse support furnished by the hydrostatic and shear systems:

$$\frac{C_2 S_T}{S_R} = \frac{1 - f}{f} \tag{62}$$

This expression was used in deriving the design plots of section 4. 4. 4.

4. 4. 7. 4 Vibration Dampening

The fundamental frequency of the system for axial translation is expressed by Equation (46). However, δ static is determined by Equation (57) using the proper value for C_2. Natural frequency correlations made with three-tier mockup data using both vibration test data and shock data gave values generally 5 percent on the low side. The slight reduction of the natural frequency is to be expected with a dampened system.

Oscillations noted in the oscillograph recordings were used in evaluating the shock data for vibration dampening since the square-wave acceleration applied to the system would normally cause it to vibrate at its natural frequency. The duration of the steady acceleration was approximately 0.12 second, and any harmonic motion induced by the square wave having a period less than 1/2 or 1/3 of the 0.12 second impulse was discernible on these records.

The amplitude of oscillations is a function of the dampening in the system and the amount of energy input. The dampening in turn, is directly related to the friction and the radial pressure. Figure 4.4-38 shows a sketch illustrating the nature of the recorded data.

To evaluate the dampening characteristics, the line A - A was drawn through the average displacement level indicating the static displacement during the square wave acceleration input and the actual amplitudes of the excursions or swings were plotted on semilog graph paper. The charts of various transducer outputs showing bundle vibration following 5-G accelerations imposed on a 5 psi radially spring-loaded system showed a linear decrease in amplitude of vibration with time. The linear decrease of amplitude implied that a viscous-type dampening was occurring in the system. At first, this seems contradictory to the fact that no viscous devices were present. However, friction at the large number of individual surfaces effectively may be additive to produce viscous-type dampening with a constant linear decrease in the amplitude of the vibration. It is logical to expect that not all friction surfaces act simultaneously at the instant displacement begins, but that more surfaces become effective as the displacement increases. The total energy being dissipated in friction would then increase exponentially as a function of core displacement, and the overall effect would simulate viscous-type dampening.

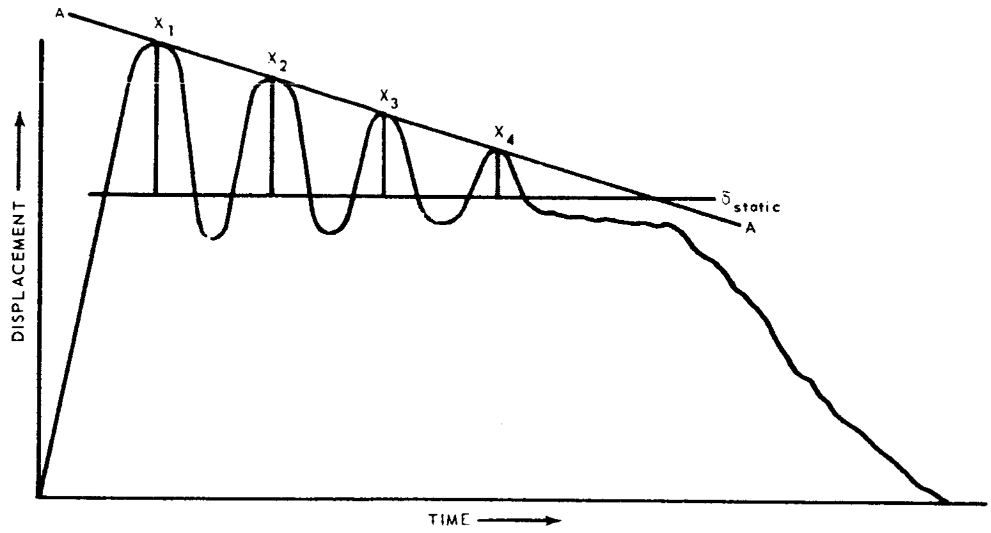

Fig. 4.4-38 – Dampening characteristics in the three-tier mockup

The dampening ratio, as evaluated from shock tests, was approximately 0.3 at 10-psi radial pressure and increased to 0.4 at 17.5 psi.

4.4.8 PRESSURE MAGNIFICATION IN THE TUBE BUNDLE

The large number of elements that make up the tube bundle are not identical in size but vary within the manufacturing tolerance. This tolerance permits some elements to accept more load than others in the form of local pressure concentrations. Both experimental and analytical means have been used in attempts to assess the magnitude of these pressure concentrations.

One analytical approach assumes that undersized tubes may be assembled adjacent to each other to produce cavities within the tube bundle. Pressure concentrations are expected to occur around the cavity due to the bridging of the load. By applying the analogy of a disc with a hole in it and under external pressure, the stress at the edge of the hole can be determined as a function of the hole size relative to the size of the disc, as shown in Figure 4. 4-39. Thus, a pressure concentration factor, C_3, may be determined. For a homogeneous bundle without a cavity, $P_o = \sigma_\theta = \sigma_R$. When a cavity is introduced with a radius up to 1/2 that of the bundle radius, the tangential pressure is approximately 3 times the radial pressure and the inward radial pressure is zero, i.e.,

$$\sigma_\theta = C3P_o, \text{ and} \ldots \; C_3 = 2\left(\frac{R_B^2}{R_B^2 - R_C^2}\right) \tag{63}$$

also

$$\sigma_R = 0, \text{ and} \ldots \; C_3 \approx 3 \text{ when} \frac{R_C}{R_B} \gtrsim 0.5 \tag{64}$$

Another analytical approach shows that, neglecting friction, a single undersize tube will produce a local pressure adjacent to it of twice the average pressure. From the same considerations, an adjacent pair of undersized tubes will introduce a pressure concentration factor, C_3, three times the average pressure, P_o. Figure 4.4-40 illustrates this concept through the use of force polygons. The largest value of C_3 found during the 141D design was 3.0.

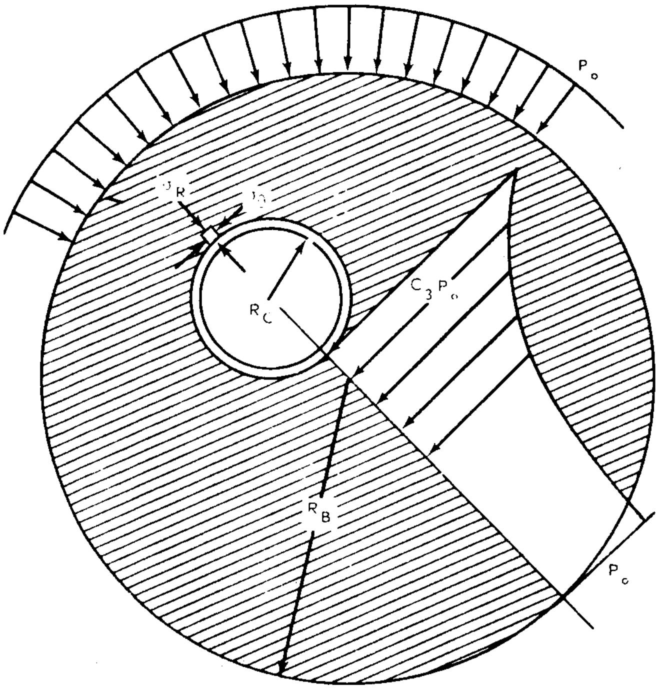

Fig. 4. 4-39 – Load bridging around a hole in the tube bundle

Several experimental attempts to determine the pressure concentration factor were largely unsuccessful. Strain gages attached to various small and large tube bundle mockups failed to measure dimensional changes as the radial pressure, shock, and vibratory forces were varied. Another test measured the load required to initially slide groups of tubes in a pressurized bundle. The variability of the frictional coefficient and the unknown pressure distribution, i.e., whether two, three, four, five, or six sides were actually loaded, caused doubt whether the maximum or an average-maximum value was measured. A third test introduced successively larger cavities into a pressurized tube bundle, and could be considered a count-the-cracked-tubes approach. The stability of the tube bundle in redistributing loads and

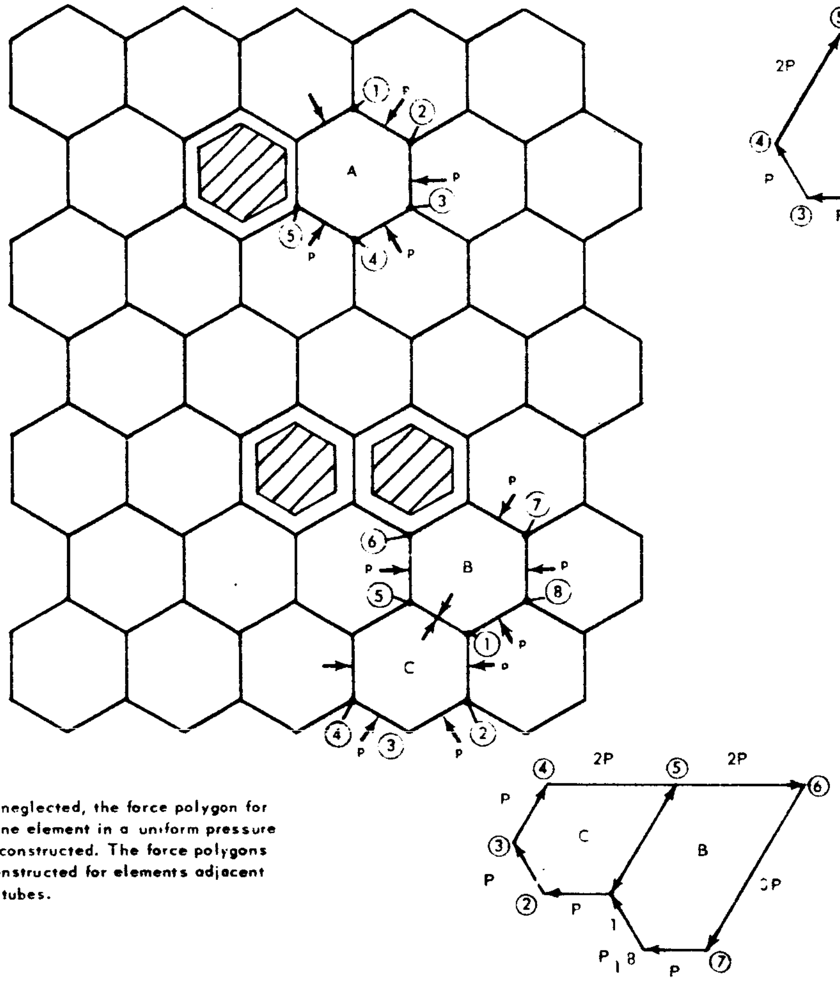

If friction is neglected, the force polygon for stability of one element in a uniform pressure field can be constructed. The force polygons shown are constructed for elements adjacent to undersize tubes.

Fig. 4.4-40 – Force polygons for elements adjacent to undersize tubes

bridging around the cavities was impressively demonstrated but tubes did not fail. Qualitatively, however, the tests gave confidence that excessively large concentration factors do not exist.

A pressure concentration factor, C_3, of three has been chosen on the basis of analytical and experimental data and is currently being used.

4.4.9 EFFECTS OF CORE LINER FIT ON TUBE BUNDLE PRESSURE DISTRIBUTION

When a large axial cavity is provided through the tube bundle, a thin walled tube or liner may be used to form the cavity and assure the integrity of the tube bundle. Ideally, the liner structure acts only as a substitute for the ceramic parts removed and does not alter the magnitude or direction of pressures and load paths. However, with manufacturing tolerances and differential thermal expansions, it is impossible to guarantee a perfect fit, and the effects of oversize and undersize fits must be evaluated.

Figure 4.4-41 is a plot of conditions within the tube bundle that are dependent upon fitup. All factors are normalized for simplification. The ordinate is the ratio of tangential pressure, S_T, to radial spring pressure, P_0. The abscissa is the ratio of the cavity radius, r, divided by the bundle radius, R. Curve A represents the case in which the liner is completely undersized such that it is actually free to ride within its hole while imparting zero

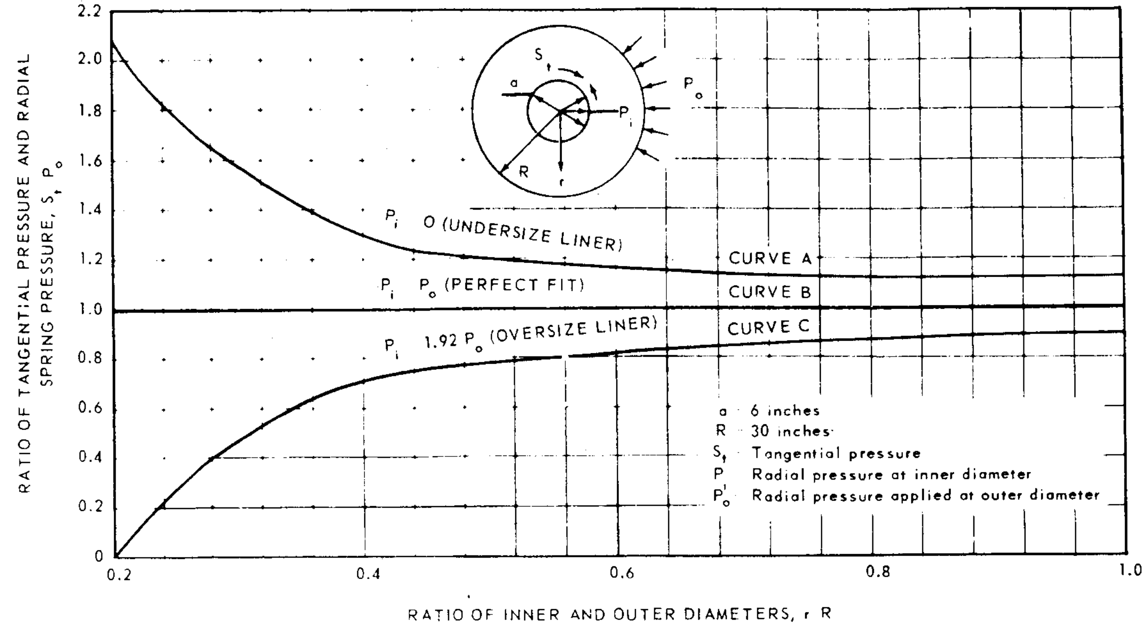

Fig. 4.4-41 – Tangential pressures in core due to core-liner fit and radial-spring loading

pressure against the core and merely serving to retain loose tubes. Resulting tangential pressures within the bundle reach a maximum of 2.08 times the external pressure at the inside by applying the stress concentration analogy. Curve B represents the ideal case of hydrostatic equilibrium where all pressures are equivalent to the external pressure. Curve C represents an oversize liner in which the tangential pressures at the liner interface approach zero but the radial pressure approaches 1.92 times the spring pressure. It should be noted here that any further increase in liner pressure is impossible because the bundle, being unable to support tensile pressures, will begin to separate, thus moving the apparent inner radius farther and farther out until eventually the internal pressure will equal the external pressure.

4.4.10 DIMENSIONAL STACKUP OF THE TUBE BUNDLE

4.4.10.1 Statistical Theory

The dimensional stackup of the tube bundle is predicted by semi-empirical methods based on statistical treatment of tube dimensional tolerances. Past analysis has shown that the dimensions of the tightest assembly of hexagonal tubes are characterized by the across flats dimension of the tubes and an interstitial gap between the tubes. The following statistical analysis is based on the geometry and nomenclature defined in Figure 4.4-42.

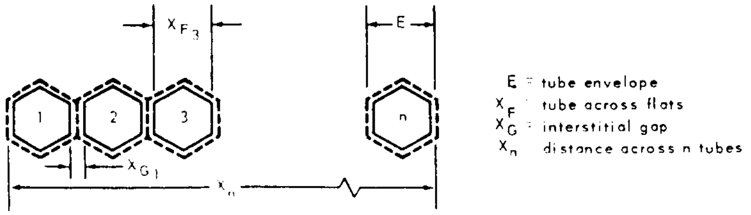

Fig. 4.4-42 - Geometry and nomenclature used in tube bundle dimensional stackup

Figure 4.4-42 shows that the following relationship applies:

$$X_n = \sum_{i=1}^{n} X_{Fi} + \sum_{i=1}^{n-1} X_{Gi} \tag{65}$$

From the definitions of averages:

$$\sum_{i=1}^{n} X_{Fi} = n\bar{X}_F, \sum_{i=1}^{n-1} X_{Gi} = (n-1)\bar{X}_G \tag{66}$$

Therefore, the average measurement across n tube is:

$$\bar{X}_n = n\bar{X}_F + (n-1)\bar{X}_G \tag{67}$$

From statistics, given the standard deviations of the gap and across flats:

$$S_n^2 = nS_F^2 + (n-1)\,S_G^2 \tag{68}$$

It is evident from the above equations, that the measurements across tubes in a tight assembly may be predicted, given the statistical distributions of the tube across flats' measurements and the interstitial gap.

The distribution of the across flats' measurements is readily obtained from sample inspections of the production tubes. If the production has not begun, then the distribution may be assumed as normally distributed with an estimated percentage between the upper and lower tolerance limits. As an example, assume that the tubes in a given tube bundle have their tolerance limits across flats specified as 0.3180 ±0.0020 inches. Assuming that the mean dimension of all tubes is 0.3180 inch, and that 95 percent of all tubes fall within the limits of ±0.0020 inch, the standard deviations, σ_F, equals 0.0020/1.96, or 0.00102 inch.

The interstitial gap cannot be measured directly. Semi-empirical analyses using various assemblies of various size tubes has shown that the gap is primarily dependent upon the variation (or standard deviation) of the flats dimensions and the radial pressure imposed upon the tube bundle. The relation developed from the test analysis which described approximately 96 percent of the gap variation is

$$\mu_G = -0.001365 + 6.1052\ \sigma_F - 1789.73\ \sigma_F{}^2 - 0.025283\ \sigma_F P \tag{69}$$

where μ and σ describe the population distribution rather than the sample distribution described by $\bar{X}$ and S, and P is the average radial pressure on the tube bundle. From the same analysis, $\sigma_G = 0.00328$. Using $\sigma_F = S_F = 0.00102$ and P = 30 psi, $\mu_G = 0.0022$.

The tube bundle stackup can now be predicted, using the above equations and the following values for the various parameters:

$\bar{X}_F = 0.3180$
$S_F = 0.00102$
$\bar{X}_G = 0.0022$
$S_G = 0.00328$

The tube bundle is assumed to be built up into a radius equal to 85 tubes placed flat-to-flat. The predicted individual dimensions of the outer radius for the average assembly are equal to

$\bar{X}_{or} = 85\ (0.3180) + 84\ (0.0022)$
$\bar{X}_{or} = 27.215$
$S_{or}^2 = 85\ (0.00102^2) + 84\ (0.00328^2) = 992.1396 \times 10^{-6}$
$S_{or} = 0.0315$

where the subscript or applies to the outer radius.

For an average assembly, 95 percent of the values are expected to lie within the region $\bar{X} \pm 1.965$, or 27.215 ± 0.062; and 99.7 percent are expected to lie within the region $\bar{X} \pm 35$, or 27.215 ± 0.095 (the linear dimensions are inches).

4.4.10.2 Experimental Test Program

Careful dimensional measurements were made of all tubes in several sets of tubes. (These samples represented a wide variety of sizes and dimensional tolerance conditions.) The dimensions measured are shown in Figure 4.4-43. Three across-flats measurements (at the middle and at each end) were taken on each set of flats. The average of these measurements was taken as an individual piece of the data in calculations for the statistical parameters $\bar{X}_F$ and S_F. The camber was measured as "plus" or "minus" depending upon the concavity or convexity of the particular flat. All six surfaces were measured and entered into the calculations. For tubes having opposite sides parallel, the mean camber is equal to zero except for any inspection bias. Three corner angles were measured on each tube by an optical comparator for calculation of its variance (the mean angle must equal 120 degrees except for inspection bias). The sets of tubes were then assembled in various fixtures to determine the stackup characteristics for each set of tube attributes.

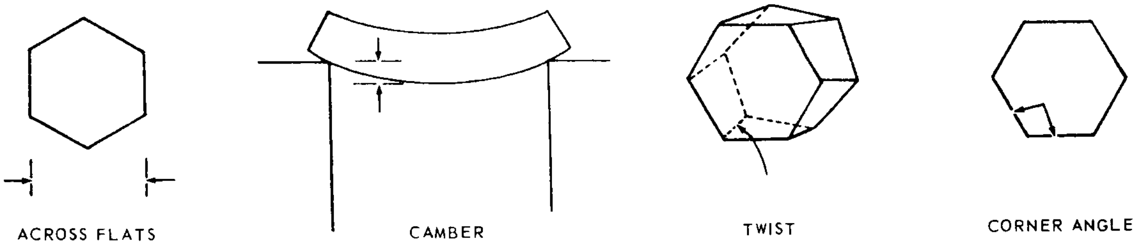

Fig. 4.4-43 – Tube measurements for core definition studies

An analysis of the test data was performed using statistical methods to determine the correlation between the tube attributes and the overall dimensional characteristics of the assembly. Specifically, the analysis determined the statistical distribution parameters for the interstitial gap as a function of the distribution parameters of the attributes.

The first step in the analysis was to assume an equation and independent variables for the correlation for the mean interstitial gap. The assumed equation was a second order equation with unknown coefficients. Coefficients then were calculated by methods of least squares using the experimentally determined values of the interstitial gap and the measured values of the tube attributes. The variance of the mean interstitial gap was calculated from the magnitude of the residual between the mean gap as given by the equation and the experimental data.

The precision of the equation, and therefore the authenticity of the assumed independent factors and form of the equation in predicting the experimental data, was determined by the percentage of the calculated variance of the gap dependent on the variation of the input data. The equation and independent variables were iterated until agreement reached an acceptable value.

The following equation was assumed for correlation of the experimental data:

$$\mu_G = a_0 + a_1 \sigma_F + a_2 \sigma_F^2 + a_3 \sigma_F P \qquad (70)$$

where:

a_0, a_1, a_2, a_3 = unknown constants
P = average radial pressure, psi

After several iterations, the analysis produced the following values for the coefficients:

$a_0 = 0.0013649671$
$a_1 = 6.1052021$
$a_2 = 1789.7309$
$a_3 = 0.025283227$

Analysis of the variance indicated that 96.7 percent of the variability of the residuals from the semi-empirical equation for the mean interstitial gap was attributed to the variation of the input experimental data. This indicated that approximately 3.3 percent of the variability could be attributed to causes not accounted for in the equation, including camber, twist, corner angles, and possibly unknown factors.

4.4.11 DISPLACEMENTS OF THE TUBE BUNDLE

Displacement of all major components of the tube bundle must be carefully analyzed to establish the extreme movements of the components during all operating conditions. The displacements are classified in three categories; manufacturing, thermal, and mechanical. Data from these analyses are used to design gas seals, control rod coolant channels, clearance requirements, and possible interferences. Also, the data is used in determining loads on various components due to (1) the barrel-shaping resulting from the longitudinal temperature gradient and (2) non-uniform expansions of the support systems. The displacements relative to the shield and pressure vessel are normally included in this analysis.

Manufacturing displacements - These displacements are due primarily to the tube bundle stackup, or core definition. The category also includes the usual scrutiny of assembly tolerances of mating parts since these tolerances must be added to the other categories to establish proper limits.

Thermal displacements - This category includes displacements caused by thermal expansions. Many tedious calculations are often required to fully identify the relative effects of contributors in this category. Steady state component temperature distributions are usually available. Transient conditions, however, require careful analysis. The progressive differences of thermal expansion of the various components must be compared during both startup and shutdown. Metallic parts have higher densities and expansion coefficients; their different coolant requirements can cause design difficulties since their thermal motions lag those of the tube bundle with which they are in intimate contact. Clearances must also be established within the radial and longitudinal support structures for an inadvertent startup runaway condition wherein the fuel elements may exceed their design temperatures and expansions at a time the restraining structures remain cold.

Mechanical displacements - The third category, mechanical displacements, is due to deflection of the various parts under load. These loads may result from aerodynamic drag on the parts, dynamic loads, frictional resistance to movement between bundle components, etc. The first two sources of these deflections represent normal structural design problems. Friction, however, must be regarded as "always hurting." A good practice is to provide a design which can withstand a frictional coefficient ranging between zero and twice the predicted value.

4.4.12 LONGITUDINAL PRESSURE BETWEEN TUBES

Longitudinal restraint of the tube bundle is provided by the axial support structure located both forward and aft of the tube bundle. The tube bundle is trapped but not preloaded by these components. Adequate clearance space must be provided to permit the tube bundle and the metallic structure to expand independently as individual temperatures and material properties dictate. Since the aerodynamic load is usually the principal load, the tube bundle normally bears against the aft structure with a gap at the forward end. The mechanical stresses in the fuel elements resulting from loads introduced by the axial support system have been found to be low in magnitude.

Although axial loading of the tubes is not as critical to their performance as radial loading, it has been investigated rather intensively for other considerations. At first glance the picture appears simple but, on closer examination, axial loading is nearly as complex as radial loading. Complexities are introduced primarily by the radial pressure and the resultant friction between elements that resists and distributes axial loads. This friction enables the bundle to perform as a load-carrying member and also introduces loads in addition to the aerodynamic forces caused by the relative thermal displacements of the external supporting sturcture. Axial loads are introduced into the core bundle by the effect of the pressure drop through the core, by friction through the radial pressure pads when relative displacements between the shell and bundle occurs, by friction from the liner (if it exists) when relative motion between liner and bundle occurs, and by bearing from the retainer plates. Internal loading also produces body forces within the bundle.

The design philosophy is that frictional forces and body forces can be exerted in either direction, but that loads from pressure drop are always directed aft and reactions from the aft retainer structure are always directed forward. It is possible to visualize very high pressure loadings locally at the aft restraint if friction within the bundle is considered to react against the load due to pressure drop, plus an inertial load, plus the two frictional loads from the perimeter due to local reactions between the aft retainer and the aft face of the tube bundle. However, the load on any individual tube is friction-limited and larger loads only spread the area of the reaction so that this limit is not exceeded. The maximum element loading is given by the product of the circumference, the total length of the tube through the core, the radial pressure, X_R, and the coefficient of friction.

The aerodynamic drag on a single tube normally is not significant.' Because the load is friction-limited and because creep tends to distribute the load more uniformly, it is considered a short-time loading.

4.5 MECHANICAL DESIGN DETAILS OF COMPONENTS IN THE TUBE BUNDLE

4.5.1 INTRODUCTION

The descriptive material in this section covers the detailed design analysis of the more important components of the tube bundle. The fuel element is explored in depth. Mechanical, thermal, residual, and combined stresses within the tube are discussed, together with its ability to accommodate thermal stresses. Other components discussed are the outer reflector tubes and transition pieces, as well as the components that form axial cavities through the bundle, i.e., the radial arch and core liner.

Data from in-pile and laboratory testing under simulated operating conditions are presented, and the data are correlated by suitable stress analysis methods. The agreement of the test data with basic materials properties is demonstrated and the analytical stress evaluation procedures are described.

It is important that the reader realizes that some failures are to be expected, and that a limited number of cracked ceramic tubes is not detrimental providing a configuration such as the tube bundle is employed wherein the pieces are contained and the mechanical loads are redistributed. The text also shows various methods of analysis which help define the stress and strength distribution curves such as shown previously in Figure 4.3.1-1.

4.5.2 MECHANICAL STRESSES IN FUEL ELEMENTS

4.5.2.1 Loads

The fuel element is a short hexagonal tube subject to external loading. These external loads, in turn, cause deflections and their resultant principal stresses. Because of the three-dimensional redundancy within the tube bundle, the loads on a tube can only be approximated, and judgment of the part of the designer is a key consideration in obtaining a reliable design.

Two major mechanical loadings are imposed on the fuel elements due to the radial pressure produced by the springs of the radial support system and the redistribution of this pressure between the many pieces in the tube bundle. These two loadings are identified as beam loadings and ring loading, caused as follows:

1. Beam loading resulting from the pressure restraining or forcing deflection of the fuel elements.
2. Ring loading resulting from the pressure concentrations tending to crush the fuel elements

For the case of beam loading, the fuel element acts as a simple beam with a concentrated load, resulting from the pressure, applied at the center to restrain or force the deflections; the deflections arise from such varied causes as manufacturing tolerance for camber and external surface dimensions, thermal camber, and core barrelling. This loading condition produces bending stresses in the axial direction. For the case of ring loading, bending stresses are induced in a tangential direction, or normal to the tube axis. Ring loading produces the highest stresses when the pressure acts on opposite faces of the hexagonal tube.

Loads imposed on the fuel elements are further classified as available loads, P_a, and conforming loads, P_{cnf}.

Available Load, P_a - This load is the maximum concentrated load caused by maldistribution of internal loading pressure within the tube bundle. It is approximately equal to

$$P_a = X C_3 A$$

where: X = pressure loading, C_3 = pressure magnification factor, and A = projected area of this tube; since

$$A = 1.155 \; W \; s$$

where: W = across flats dimensions of the tube s = length of tube (maximum possible span)

the available loads are equal to

$$P_{a,T} = X_T\, C_3\, (1.155\ Ws)$$

and

$$P_{a,R} = X_R\, C_3\, (1.155\ Ws)$$

X_T is the short time maximum pressure loading in the bundle, X_R is the long time loading, and C_3 is the pressure magnification factor. The pressure is assumed to act on the projected area of the tube, i.e., the across-corners dimension times the length. Although an axial load magnification factor may exist due to the overlapping or stacking of elements, it is considered to be unity.

Conforming Load, P_{cnf} - This parameter is the concentrated load necessary to completely force or restrain the tube deflection, δ. It is the load required to nest or straighten a tube. It is computed from the familiar beam formula

$$P_{cnf} = \frac{48\ E\delta I}{s^3}$$

4.5.2.2 Tube Deflection

Manufacturing tolerance, thermal camber, and core barrelling influence the deflections. Manufacturing tolerances result in tubes with slightly different cross sectional dimensions. The outside surface of the tubes, if ground, generally will have little, if any, camber. It is assumed that tube deflections due to tolerance, δ_{tol}, can occur both radially and tangentially in the tube bundle.

Thermal camber is the bowing of an element due to a linear temperature gradient across the diameter of the fuel tube. The radius of curvature of a uniform bar to rectangular section that has one face at a uniform temperature T, the opposite face at a uniform temperature T + ΔT, and a linear temperature gradient between these faces is as follows:

$$R = \frac{d}{\Delta T\, \alpha_i}$$

where d is the distance between the hot and cold faces and α is the linear coefficient of thermal expansion. The thermal deflection, $\delta_{\Delta T}$, is calculated by the following equation, using the nomenclature shown in Figure 4.5.2-1.

$$R^2 = (R - \delta_{\Delta T})^2 + \left(\frac{s}{2}\right)^2 = R^2 - 2\,R\,\delta_{\Delta T} + \delta_{\Delta T}^2 + \frac{s^2}{4}$$

When $\delta_{\Delta T}$ is small, $\delta_{\Delta T}^2$ may be neglected, and

$$2\,R\,\delta_{\Delta T} = \frac{s^2}{4}$$

$$\delta_{\Delta T} = \frac{s^2}{8\,R} = \frac{\Delta T\,\alpha\, s^2}{8\,W}$$

The thermal bowing, $\delta_{\Delta T}$, is restrained by the available load, therefore, an axial stress results. Causes of thermal bowing are discussed later, but thermal camber is significantly important in the radially outer regions of the tube bundle.

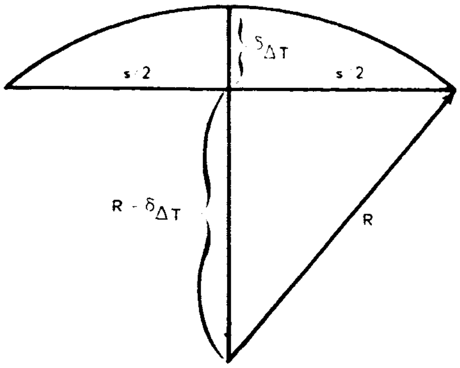

Fig. 4. 5. 2-1 – Model used for calculating thermal deflection

The nonlinear longitudinal temperature distribution through the tube bundle causes the outer surface of the bundle to assume a curved shape similar to a barrel. This action is called core barrelling, δ_{brl}, and is assumed to occur in the radial direction only.

All possible tube deflections are directional. Thus, the design tube deflection acting tangentially in the bundle is

$$\delta_T = \delta_{\Delta T} + \delta_{tol}$$

and the design tube deflection occurring radially in the bundle is

$$\delta_R = \delta_{\Delta T} + \delta_{tol} + \delta_{brl}$$

4.5.2.3 Axial Stresses

If the available load is greater than the conforming load, the axial stress is dependent on the total deflection of the tubes acting as a simple beam. For $P_a \geqq P_{cnf}$,

$$\sigma_z = \frac{P_{cnf}\, s\, c}{4\, I} = \frac{12\, E\, \delta_R\, c}{s^2}$$

where

c = distance from neutral axis
I = moment of inertia

When D is the bore diameter, the maximum stress (in the inner fibers) at the center of the span is

$$\sigma_{z,A} = \frac{6 E D\, \delta_R}{s^2}$$

The maximum stress occurs furthest from the neutral axis on the tube flat, and is equal to

$$\sigma_{z,D} = \frac{6 E W\, \delta_R}{s^2}$$

When the available load is less than the conforming load, the tube will not experience the total deflection and the stress is simply a function of the load available, $P_{a,T}$. For $P_a \leq P_{cnf}$,

$$\sigma_{z,A} = \frac{(P_{a,T})\, s\, c}{4\, I} = \frac{(P_{a,T})\, s\, W}{8\, I}$$

When the length (span) of the fuel elements is kept short enough to assure that the available load is less than the conforming load, larger tolerances, thermal camber, and other deflections are permissible. Costly finish grinding of the tube exterior may be eliminated.

4.5.2.4 Ring Stresses

The maximum pressure concentrations acting on opposite faces of the hexagonal tube must be evaluated to compute the highest ring bending stresses. When the available load exceeds the conforming load, the difference appears as a uniformly distributed load on the tube. The conforming load is assumed to act over a 1-inch length of the tube, and is added to the distributed load to produce the maximum pressure concentration acting on opposite faces of the tube. Other investigations studying the effects of shear distribution of the load within the tube and the reduction of stress under concentrated loading when the tube is loaded as a beam tended to confirm the assumption of the 1-inch load length for the 140E fuel element. When $P_a > P_{cnf}$, the tangential tensile stress is equal to

$$\sigma_\theta = \left[\frac{P_a - P_{cnf}}{S\ s} + \frac{P_{cnf}}{s}\right]\frac{\sigma}{P}$$

where

S = one-half of the across-corners dimension
σ/P = ratio of unit stress to unit loading pressure

When $P_a < P_{cnf}$,

$$\sigma_\theta = \left(\frac{P_a}{s}\right)\left(\frac{\sigma}{P}\right)$$

The tangential stress varies circumferentially around the element and is a function of the wall thickness and the loading condition. Figures 4.5.2-1a and 4.5.2-2 show the results of a photoelastic analysis of the boundary stress distribution in hollow hexagons for the extreme cases of 2 and 6 sided loading. As the number of sides that are loaded increases, the maximum tensile stress decreases until only compression exists in the element with the 6 sides fully loaded. Fig. 4.5.2-3 shows the effect of wall thickness on the maximum stress based on the principle of consistent deformations.

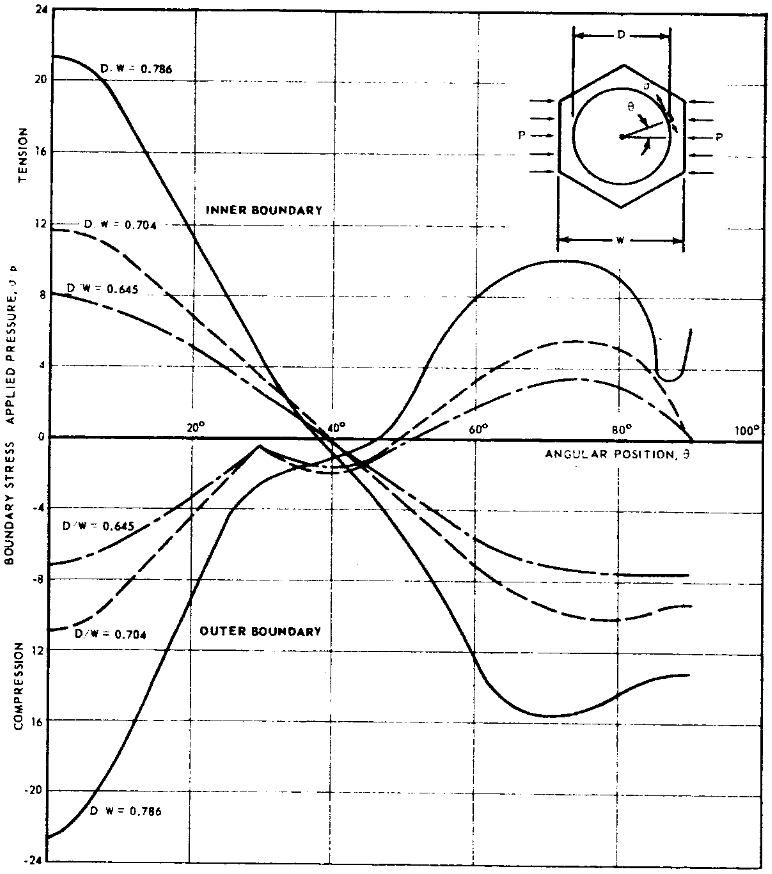

Fig. 4. 5. 2-1a – Boundary stress distribution on hollow hexagons with a uniform pressure load applied to two opposite faces

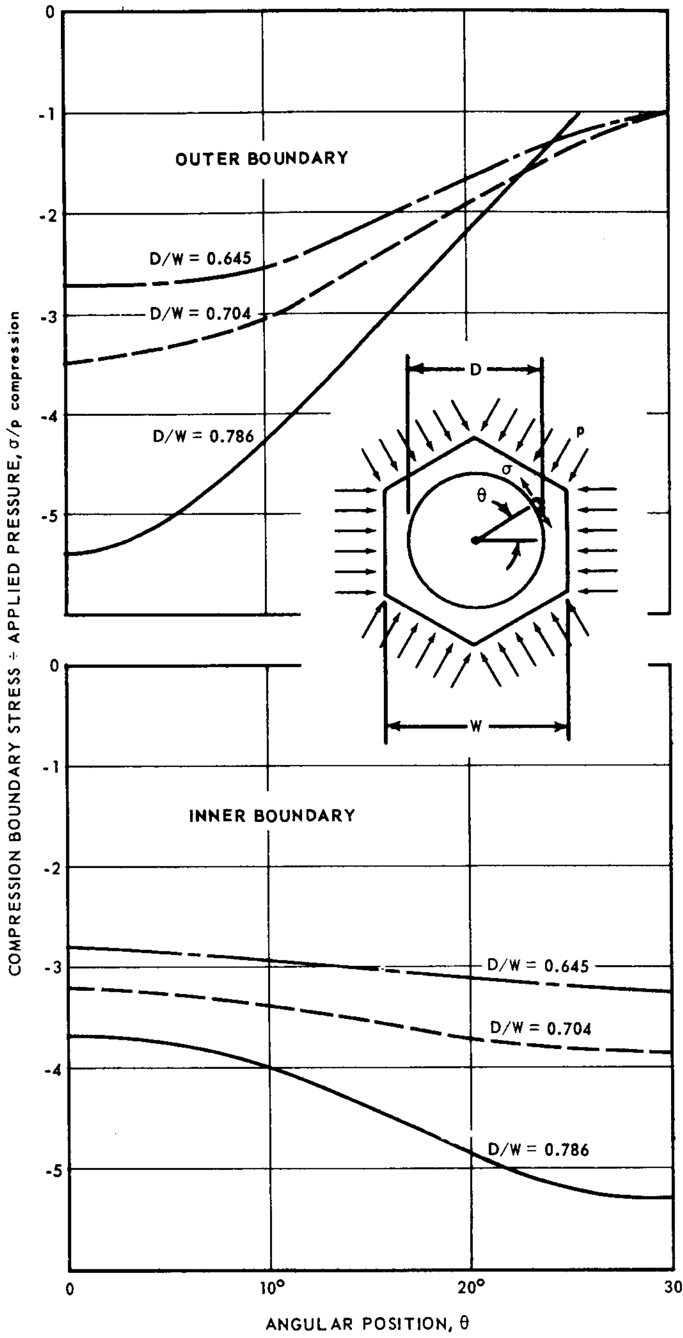

Fig. 4.5.2-2-Boundary stress distribution on hollow hexagons with a uniform pressure load applied to six outside faces

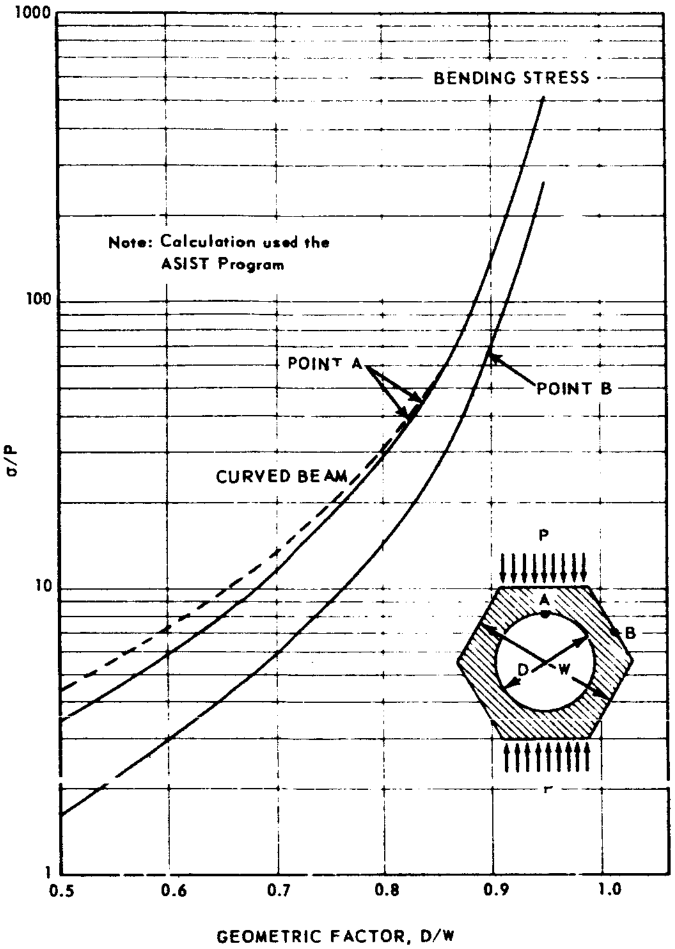

Fig. 4. 5. 2-3 – Ring bending stress of hollow hexagons with a uniform pressure load applied to two opposite faces

4.5.3 Thermal Stresses in Fuel Element

4.5.3.1 Thermally Induced Stresses Encountered in Reactor Operation

Fission heat is generated in the fuel elements essentially uniformly throughout any one fuel element, but the generation rate varies as a function of radial and axial position in the core. This section deals with the analytical and experimental thermal stress resistance of a single fuel element. (See Figure 4.5.3-1) In Section 4.5.4 the combined mechanical and thermal stresses will be shown as a function of location in the reactor. For simplicity, the argument will be developed for a circular tube of infinite length, having a concentric circular bore, unclad, with internal heat generation and all heat removed from the bore of the tube. The effect of different methods of heat input, cladding, end effects, and the hexagonal outer shape will be discussed after the basic argument has been developed for the more simple geometry. The details of the stress analysis have been deferred to the Appendix.

Two assumptions necessary for the stress analysis are: (1) that the principle of superposition applies, i.e. that the stress solution can be developed for the circular geometry and that the effect of the hexagonal shape, finite length, and the addition of cladding can be superposed upon the circular tube solution, and (2) that the materials behave as a linear Maxwell model, i.e. that creep deformation is a linear function of stress. Vandervoort and Barmore[1] have shown that BeO creep deformation rates are a linear function of stress in the temperature range 1370-1540°C. Chang[2] has shown similar behavior to 1700°C and Fryxell[3] has observed the same behavior for BeO at 1200°C.

The generation of heat within the fuel tube and the removal of the heat from the bore of the tube causes a radial temperature gradient across the tube wall, which induces initially the thermal stresses shown in Figure 4.5.3-2 if it is assumed that the material is stress free at the temperature corresponding to the mean temperature ($\overline{T}$) of the tube. The axial (Z) and circumferential (θ) stresses at the inner walls are tensile and at the outer wall compressive due to the restraint imposed by the tube geometry and the difference in thermal expansion between the outer fibers at a temperature greater than the mean temperature and the inner fibers at a temperature lower than the mean temperature. However, different stress patterns result from (1) continued operation at steady state temperature and power extraction, (2) a change in the mean temperature level such as cooling to room temperature or temperature cycling, and (3) a change in the temperature gradient (power level) such as power cycling at a particular temperature level.

When the radial temperature gradient is rapidly established at a high temperature level followed immediately by shutdown, the thermal stresses may be determined directly from elastic theory, with consideration of the

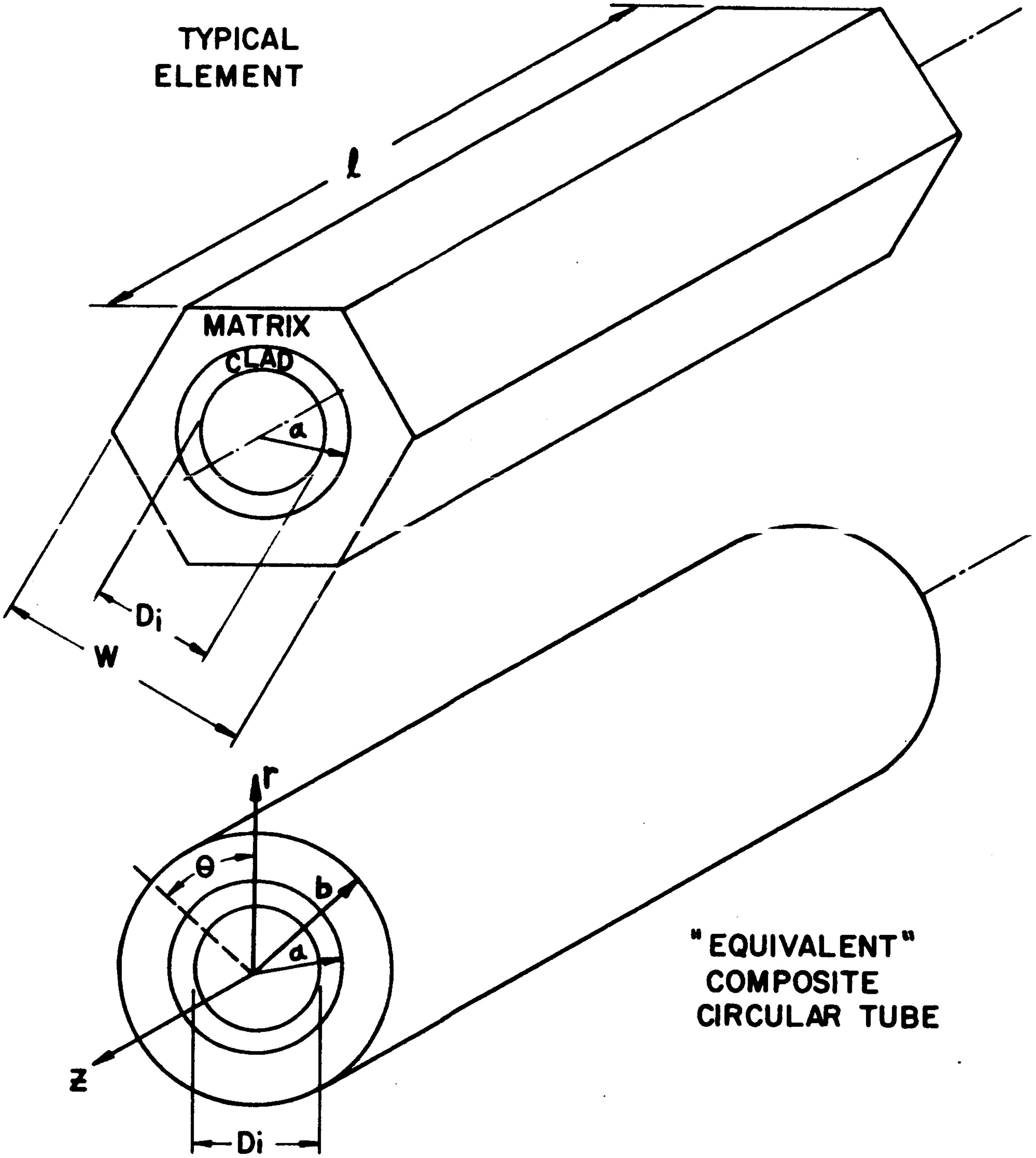
TYPICAL ELEMENT
ℓ
MATRIX
CLAD
a
Di
W
r
θ
b
a
z
Di
"EQUIVALENT" COMPOSITE CIRCULAR TUBE

Fig. 4.5.3-1 Typical fuel element geometry and equivalent circular tube

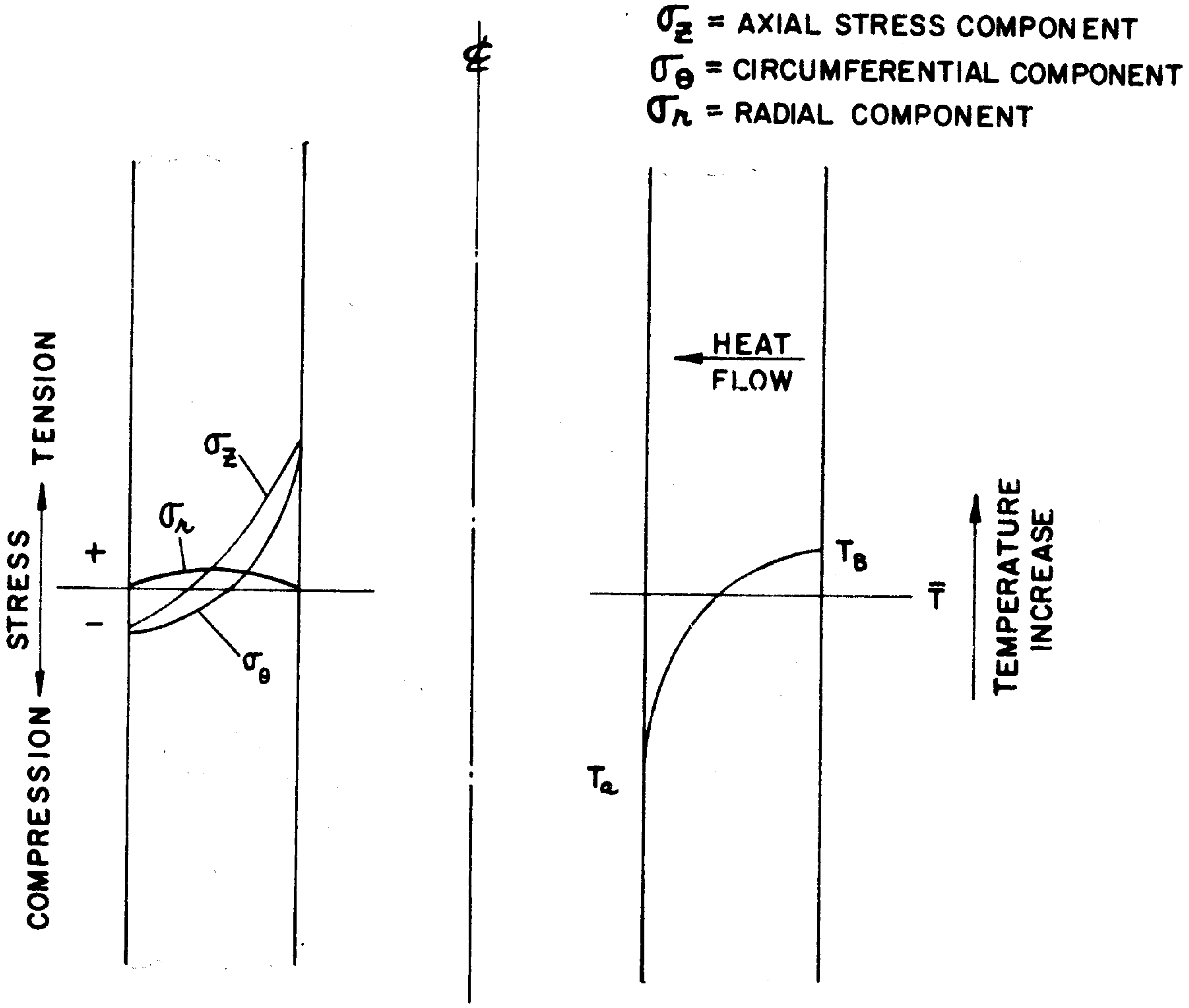
σ_z = AXIAL STRESS COMPONENT
σ_θ = CIRCUMFERENTIAL COMPONENT
σ_r = RADIAL COMPONENT
℄
COMPRESSION ← STRESS → TENSION
+
−
σ_z
σ_r
σ_θ
HEAT FLOW
T_B
T_a
$\bar{T}$
TEMPERATURE INCREASE

Fig. 4.5.3-2 Radial temperature profile and initial thermal stress distribution for a round tube with internal heat generation and power extraction at the bore

transient conditions during heating and cooling. The maximum steady state stresses occur when the desired power level is established at the operating temperature and the component will fail if the maximum tensile stress locally (inner fibers) exceeds the ultimate tensile strength of the material at that temperature. The stress components shown in Figure 4.5.3-2 appear when the radial temperature gradient shown is imposed by extracting power from the tube bore. These stresses are elastic and will disappear if the temperature gradient is immediately removed.

However, if the tube is held at the operating temperature and power level, the initial elastic stresses will relax by creep deformation. The local strains required to reduce the stress are very small and do not produce a significant change in the shape of the body. However, the coolest fibers (inner surface) are stretched and the hottest fibers (outer surface) are shortened. Consequently, when the temperature gradient is removed after creep deformation the shortened fibers are in tension and the lengthened fibers are in compression, the opposite stress of the initial conditions. Immediate cooling to room temperature, before reverse creep deformation occurs, results in a residual stress in the tube at the lower temperature. The residual thermally induced stresses at room temperature are usually greater than those initially present at the elevated temperature because of the higher elastic moduli at lower temperatures. When the strength of the material locally is exceeded by the increasing residual stress during cooling, local failures such as small cracks can result which relieve the stress. Naturally, the larger the radial gradient, the larger the stress and the more severe the damage to the tube will be if the material strength is exceeded. Figure 4.5.3-3 depicts schematically a typical power-temperature - time cycle and the corresponding behavior of the maximum stresses that would occur at the inner and outer fibers of the tube. The situation is shown where the maximum elastic tensile stress on the inner fiber does not exceed the material strength at the operating temperature, but the residual tensile stress on the outer fiber does exceed the material strength at room temperature thus resulting in damage to the tube by some degree of cracking.

The stress pattern during thermal cycling after creep deformation at a particular power extraction level is shown schematically in Figure 4.5.3-4. After the initial relaxation, repeated thermal cycling (at a rate fast enough to insure no subsequent creep deformation during heating and cooling) applies the maximum tensile stress at the outer fiber at room temperature and removes the stress when reheated to the original high temperature-power extraction condition.

On the other hand, if the power level is changed from a high level to a lower level and back while maintaining temperature, stresses of reverse sign appear with each cycle if enough time is permitted between cycles for the stresses to relax by creep deformation. Since this reversal occurs at a constant temperature, the stress levels will be no higher than the initial elastic

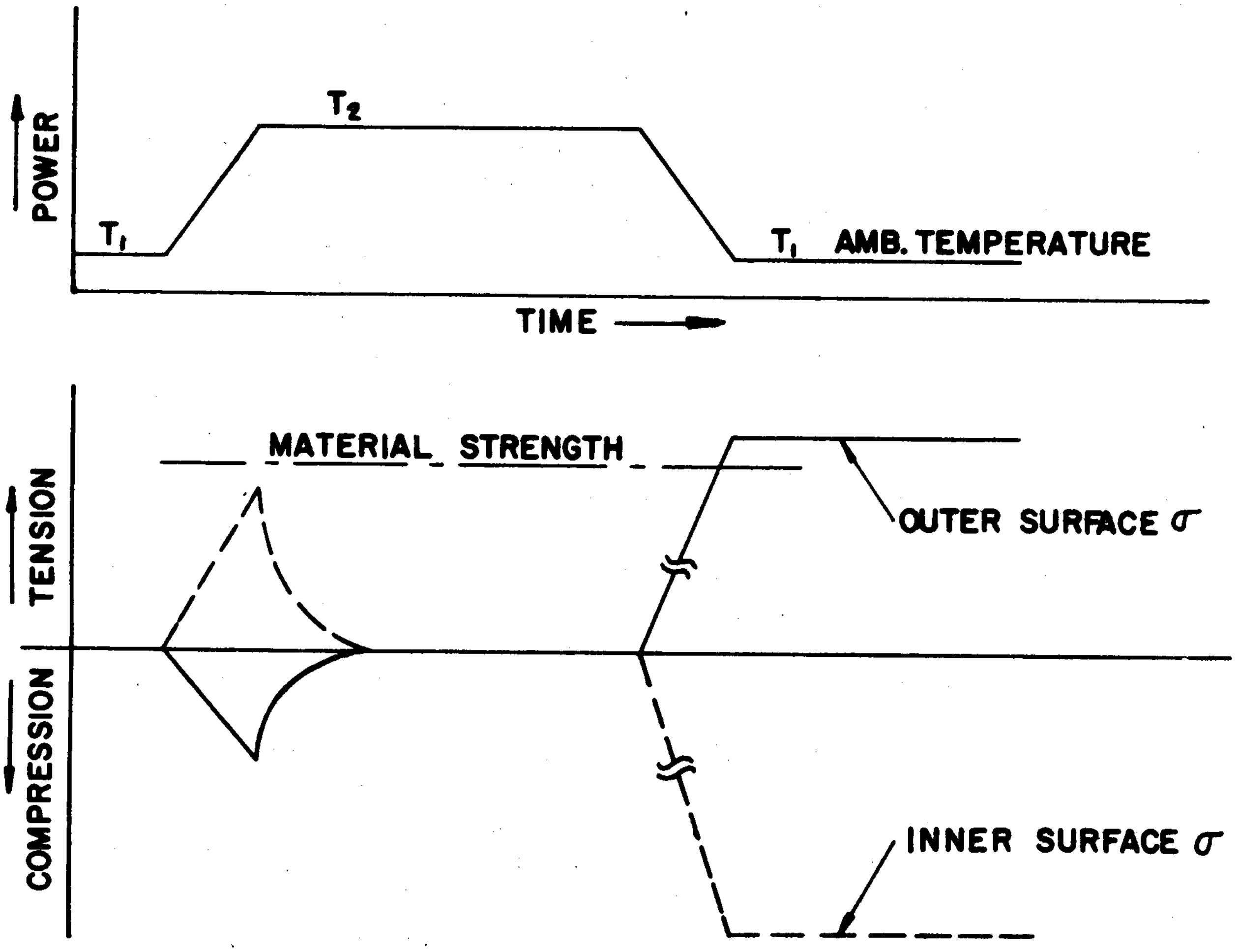
POWER
T_2
T_1
T_1 AMB. TEMPERATURE
TIME
TENSION
COMPRESSION
MATERIAL STRENGTH
OUTER SURFACE σ
INNER SURFACE σ

Fig. 4.5.3-3 Typical power-temperature-time cycle showing inner and outer fiber circumferential stress patterns as a function of time where the residual outer fiber stress exceeds the material strength on cooling

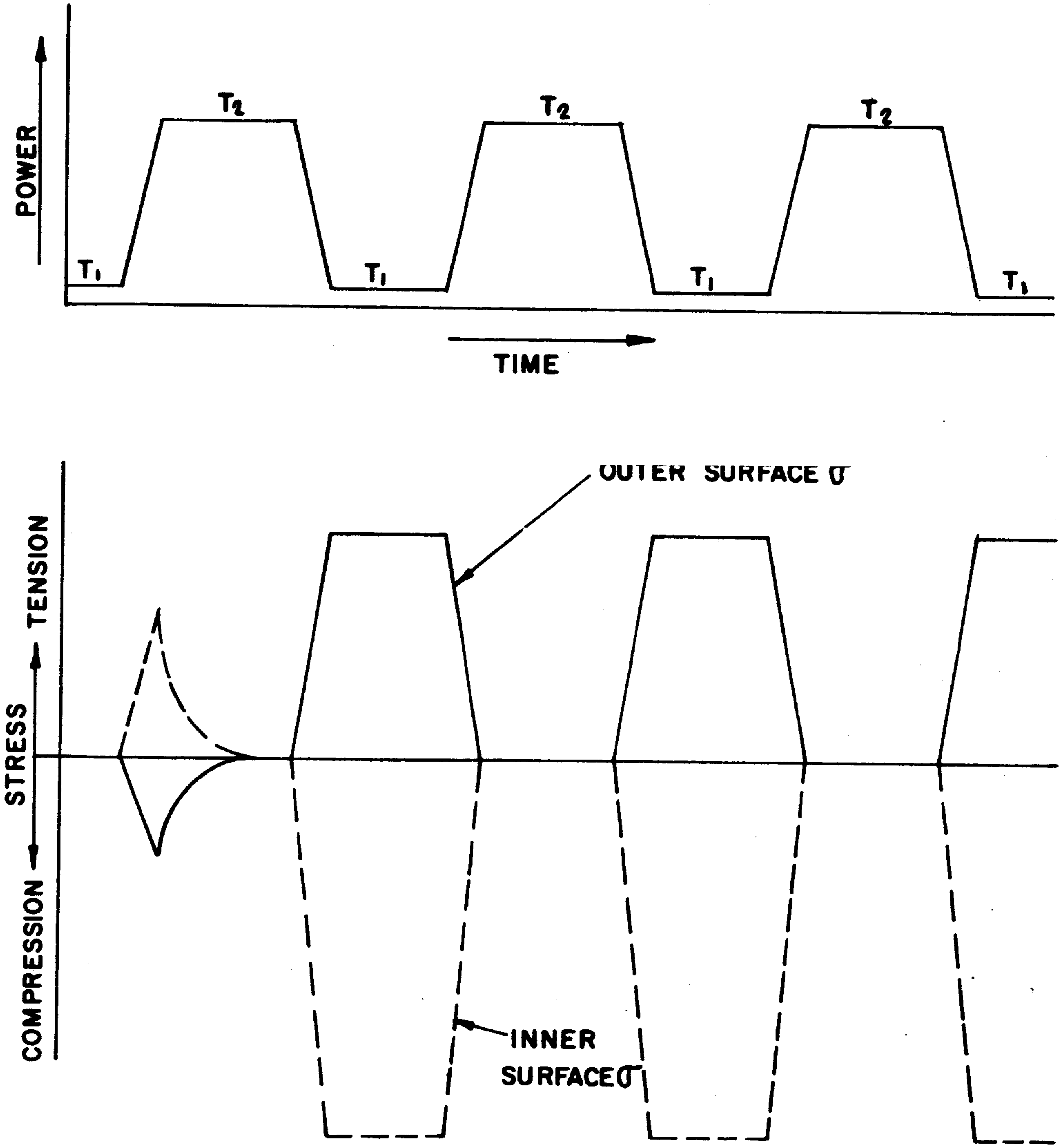
POWER
T_1
T_2
TIME
STRESS
TENSION
COMPRESSION
OUTER SURFACE σ
INNER SURFACE σ

Fig. 4.5.3-4 Schematic representation of inner and outer surface circumferential stresses during temperature cycling from a high-temperature (T_2) to ambient temperature (T_1)

stress at the operating conditions until the final return to ambient conditions. This cycle is depicted schematically as Figure 4.5.3-5.

In actual operation variations in operating temperature and reduction in power could occur simultaneously which would result in some combination of the above two cycles. It can be seen that a knowledge of the rate of creep deformation is vital in determining the stresses at a given time in the fuel tube.

The initial elastic stress either axial (Z) or circumferential (θ) at the surfaces of a simple homogeneous circular tube of infinite length can be calculated from the normal elastic equation:

$$\sigma_i = \sigma_z = \sigma_\theta = \frac{E\,\alpha}{1-\nu} \, (\bar{T}-T_s)$$

where

σ_i = initial elastic stress

σ_z = longitudinal stress at the surface

σ_θ = circumferential stress at the surface

E = Young's modulus at $\bar{T}$

α = coefficient of thermal expansion at $\bar{T}$

ν = Poisson's ratio

$\bar{T}$ = mean temperature of the body

T_s = temperature at surface in question

However, because these operating stresses can relax with time at temperature by creep deformation, it is necessary to add a term which will acount for the stress as a function of time. Since BeO behaves as a linear Maxwell material, neglecting first stage creep, the stress at any point simply decays exponentially with time. The stress at any point as a function of time is therefore

$$\sigma_t = \sigma_i \, e^{-\beta t}$$

σ_t = stress remaining at time, t

$\sigma_i = \sigma_z = \sigma_\theta$ = initial operating stress

β = rate constant (function of temperature)

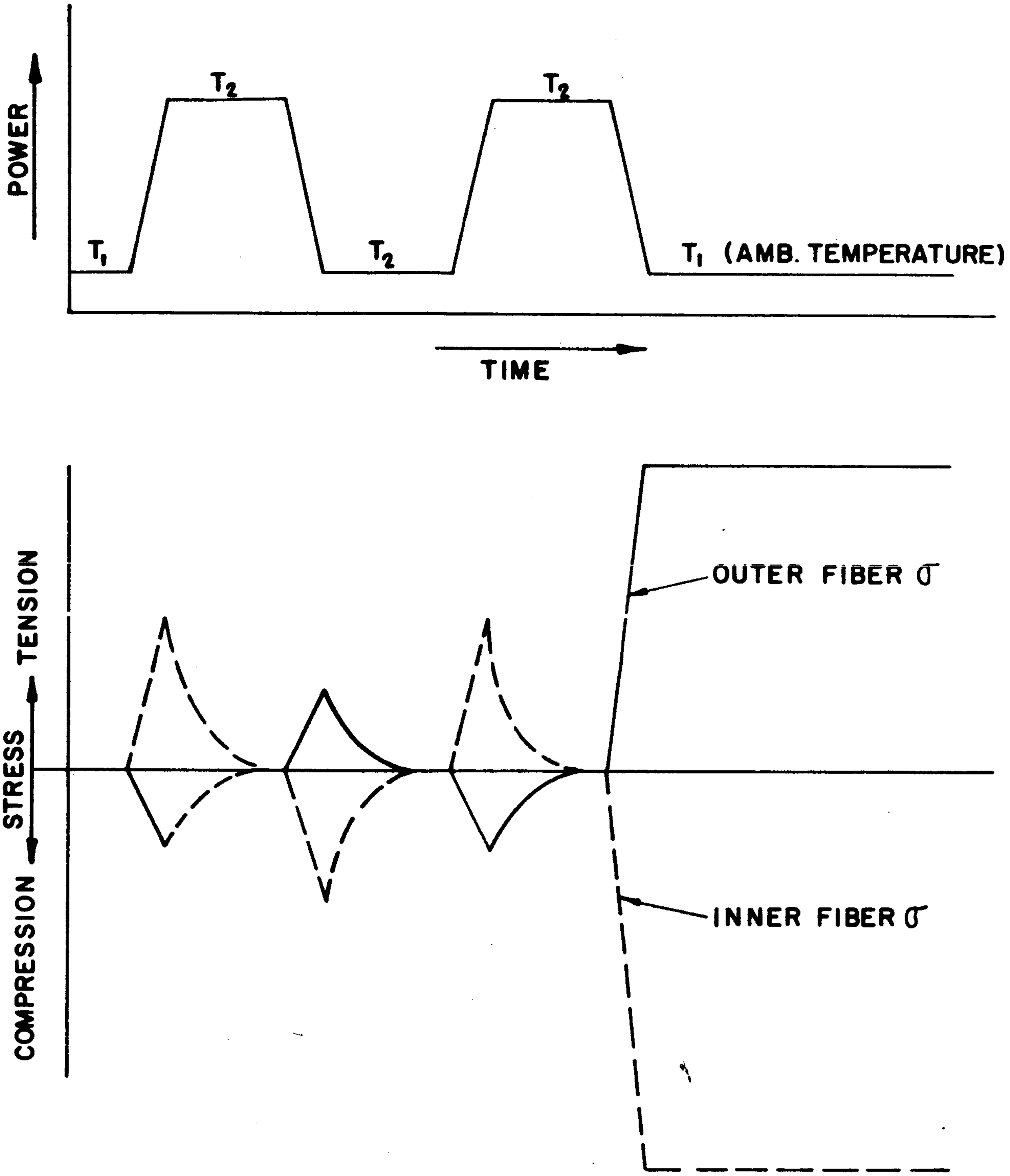
POWER
T₁
T₂
T₂
T₂
T₂
T₁ (AMB. TEMPERATURE)
TIME
TENSION
STRESS
COMPRESSION
OUTER FIBER σ
INNER FIBER σ

Fig. 4.5.3-5 Schematic representation of inner and outer surface circumferential stresses during power cycling at a constant high-temperature level

Upon cooling to room temperature the residual stress in the tube is a function of the amount of relaxation $(1-e^{-\beta t})$ that occurred at the initial operating temperature and is dependent upon the elastic modulus of the material at room temperature rather than at the initial operating temperature. This can be related by:

$$\sigma_{res} = - \sigma_i (1-e^{-\beta t}) \left(\frac{E_{RT}}{E_{OT}}\right)$$

where

$\sigma_{res} = \sigma_{z\ res}$ or $\sigma_{\theta\ res}$ = residual stress at room temperature

$\sigma_i = \sigma_z$ or σ_θ = initial operating stress

E_{RT} = Young's modulus at room temperature

E_{OT} = Young's modulus at operating temperature

Relaxation experiments performed by Battelle Memorial Institute[4] in four point bending indicate that at 2500°F stresses relax to about 70 percent of the initial value in 10 minutes and to about 45 percent in 1 hour. Extrapolation indicates that in 20 hours at 2500°F essentially all of the initial stress has relaxed. The relaxation rate constant, β, is not well defined; however, sufficient data have been obtained from compressive creep and bend relaxation tests to evaluate with good engineering accuracy the time when complete relaxation occurs. Riley[5] has obtained an approximate value for β of 0.20 at 2500°F from compressive creep data, neglecting first stage creep. This value of β indicates complete stress relaxation in 20 hours, which is in good agreement with the extrapolated bend relaxation results obtained by Battelle. Since only limited data were available for relaxation rates, Riley proposed using Larson-Miller parameters and the 2500°F data to obtain times at other temperatures for an equivalent amount of relaxation to occur.

For a tube that is hexagonal on the outer surface with a concentric circular bore, the initial operating stress components are modified by the application of a correction factor multiplier (H) to the solution of the equivalent circular tube. A finite difference program for the case of internal power generation was used to compare the effect of the hexagonal outer shape to the simple circular geometry as a function of the ratio between the circular bore dimension (D_i) and the "across flats" dimension (W) of the outer hexagon surface. The finite difference program indicated that the maximum circumferential elastic stresses for a tube having a hexagonal outer surface occur opposite the center of the flats on the inner surface, and at the center of the flats on the outer surface. The maximum axial stresses occur at the hexagonal corners on the outer surface and opposite the center of the flats on the inner surface. The radial stresses are small compared to axial and tangential stresses and are not considered in the present discussion.

The maximum residual tensile stress occurs at the center of the hexagonal flat on the outer surface as a result of the stress reversal on cooling after creep deformation has occurred. It was observed that the vast majority of tubes that failed during cooling did so by developing a longitudinal crack down the center of a flat. The cracks were initiated at the outer surface and propagated radially inward. This mechanism of failure is that predicted from the above analysis if the tangential residual stress exceeds the material strength.

When desirable to evaluate the stresses near the ends of the tube, a treatment similar to the hexagonal correction is used, i.e. a correction factor is used as a multiplier to the solution obtained for the equivalent circular tube of infinite length. The detailed analysis of the end correction is given by Timoshenko and Goodier[6] and further discussed in the Appendix.

A cladding material has not yet been found which has thermal expansion characteristics identical with that of the matrix material although very close matches have been possible. Differential expansion between the cladding and matrix materials induces stresses even in an isothermal assembly. When a cladding is bonded to the matrix each superposes a stress upon the other, the magnitude of which is a function of the properties of the different materials and the relative thicknesses of each. The thermally induced stresses in a clad tube can be expressed as the sum of two terms: (1) the stress due to the component's own temperature gradient, and (2) the stress due to the interaction forces at the clad-matrix interface required to maintain continuity. Since the equations which account for the effect of cladding are cumbersome, they are given with the complete stress analysis in the Appendix.

4.5.3.2 Experimental Procedures

The philosophy in the test program was to perform sufficient non-nuclear bench tests to: (1) screen different fuel element designs for thermal stress resistance, (2) confirm the analytical stress analysis, (3) correlate thermal stress resistance to mechanical strength properties, and (4) conduct environmental proof tests to establish the effects of such variables as thermal cycling, power cycling, and moisture content of the coolant air on the fuel element. This philosophy relies on being able to simulate reactor thermal stress conditions in the non-nuclear bench tests. The method chosen to induce thermal stresses was to heat the tube outer surface by radiant heating while extracting power by passing cooling air through the bore of the tube.

It is physically impossible to match the complete radial temperature profile obtained by nuclear fission (internal power generation) by radiant heating of the tube outer surface (external heat input). However, by proper choice of power levels, a given temperature difference can be established between the mean tube temperature and the inner surface temperature so that a radiant heat test can induce a stress on the inner surface equivalent to that obtained by nuclear heating. When the inner surface stresses are matched, using radiant heating, the outer surface stresses are higher by a factor of about 1.8. In a like manner, if the outer surface and the mean tube temperature are matched, the stresses produced on the inner surface of the tube are less by radiant heating than by nuclear heating. This difference in temperature profiles and, consequently, stress profiles, does not nullify the use of radiant heating as a test method; however, tests must be designed to investigate a particular phase of the cycle and not the complete cycle at one time. For example, if it were desired to simulate by radiant heating a particular residual room temperature tensile stress produced in a reactor, the outer surface to mean body temperature difference by the two methods of heating would be matched on the tube for a period of time sufficient for complete relaxation of stresses to occur at the temperature in question. Then upon cooling to room temperature an equivalent maximum outer surface stress would be generated even though gradient across the entire wall would be different. In a like manner, if the inner surface maximum elastic tensile stress was the target stress to simulate, the temperature difference between the inner surface and the mean body temperature would be matched. Figure 4.5.3-6 shows schematically the difference in temperature profiles produced by the two methods of heating when power levels are adjusted to produce an equivalent inner fiber elastic stress at the same inner fiber temperature.

Therefore, by matching the proper temperature differences, it was possible to simulate a required stress at a given location on the tube by radiant heating in bench tests. Tests ranging in time from 1/2 to 1000 hours, with and without thermal or power cycling, were performed over an operating temperature range from 1000 to 1500°C, and at heat fluxes at the inner bore as high as 24 cal/sec-cm^2 (0.6 Btu/sec-in^2).

To determine thermal stress resistance of tubes the usual procedure was to establish the heat flux required to cause a given percentage of tubes to crack due to the residual stress on cooling to room temperature. The tube was maintained at the operating conditions for a period of time sufficient for the initial elastic stress to completely relax by creep deformation before rapidly cooling to room temperature. Using this procedure, the thermal stress resistance was evaluated at or near room temperature and, consequently, was compared to room temperature modulus of rupture strength (4 point bending, 3 inch span, 0.06 inch/min head travel rate, third point loading).

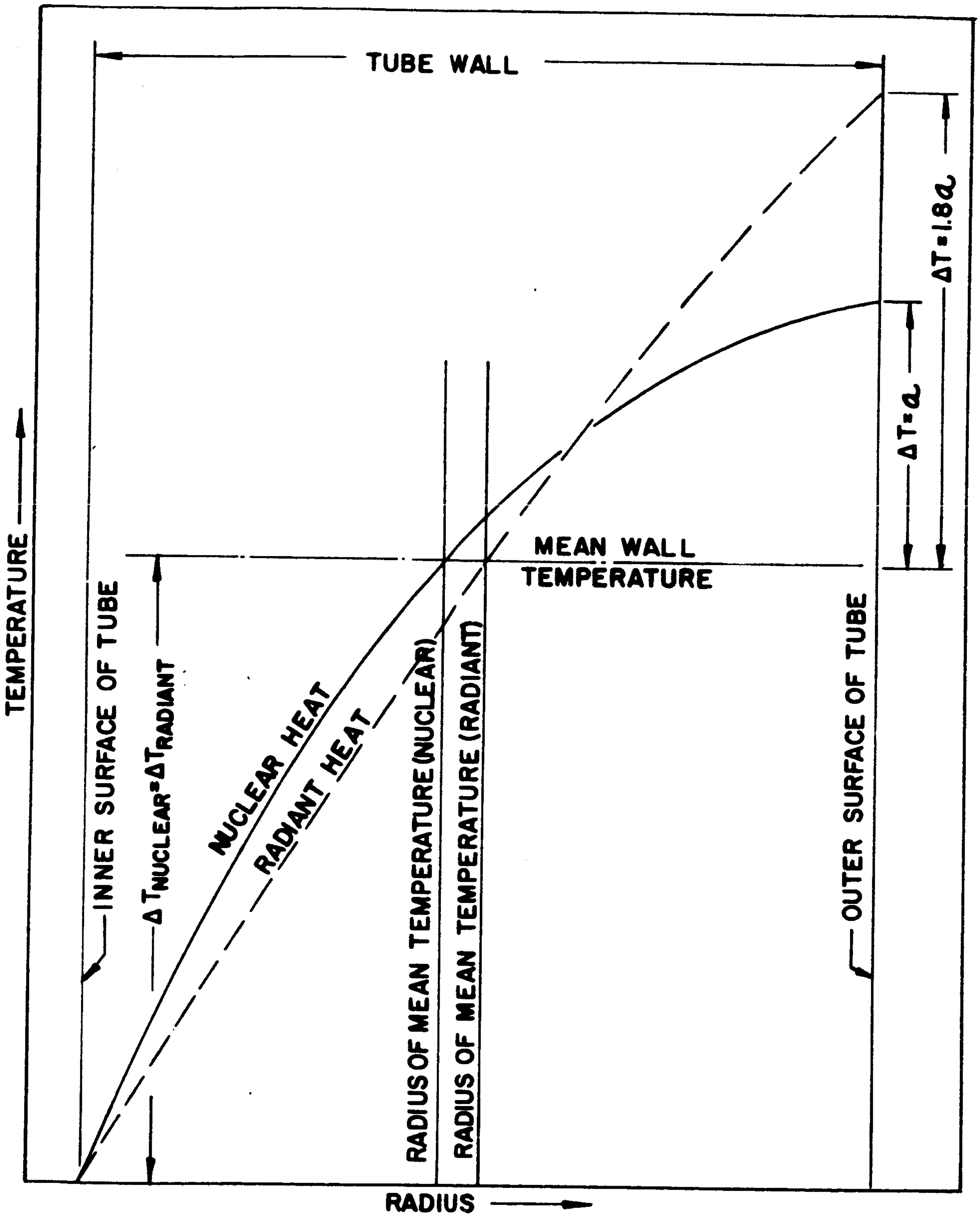

Fig. 4.3.5-6 Comparison of radial temperature profiles by radiant (external power input) and nuclear (internal power generation) heating, typical

An advantage in evaluating stress resistance based upon the residual stress is that by imposing a thermally induced residual stress on a tube to some level below the ultimate strength of the material, it is possible to check the residual stress calculations by applying strain gauges and by using stress relief methods which was done on a limited number of specimens.

Bench Test Equipment - Bench tests were performed on single tubes in specially designed furnaces[7], one type of which is shown as Figure 4.5.3-7. This furnace uses a tungsten helix coil as a radiant heating element. In addition, furnaces were designed in which the heat was supplied from a series of parallel tungsten rods, resistively heated, surrounding the fuel tube in a "birdcage" fashion, while still another type of furnace employed an inductively heated tungsten muffle as the heat source. In all cases the tungsten was in a relatively static inert atmosphere of dry nitrogen or argon. This inert gas was also in contact with the outside of the fuel tube while air flowed through the tube bore as the coolant. Later furnace designs used a BeO muffle between the tungsten heat source and the tube so that the fuel tube could be in an air atmosphere on both sides.

Inspection Criteria - Since the strain in the tubes could not be measured while on test, it was necessary to use other methods to evaluate thermal stress resistance of the tubes. A useful method was a visual and zyglo* (fluorescent dye penetrant) inspection of the tube after test for cracks and observation of the crack pattern. For consistency, in comparing test results, a crack severity rating was established by which tubes could be compared. Six categories were used to rate the tubes based upon the types of cracking. These categories were:

Type I	Tube free from stress damage as determined by visual and zyglo inspection.
Type II	Minor imperfections that do not fully penetrate the tube wall, i.e. minor surface crazing.
Type III	Single transverse crack that fully penetrates tube wall but does not separate tube.
Type IV	One or two longitudinal cracks (generally on opposite flats of a hexagonal tube).
Type V	More than two cracks that fully penetrate the tube wall but do not separate tube.
Type VI	Multiple cracks and crazing accompanied by splintering or separation of the tube.

---

* Tradename of Magnaflux Corporation, Chicago, Illinois

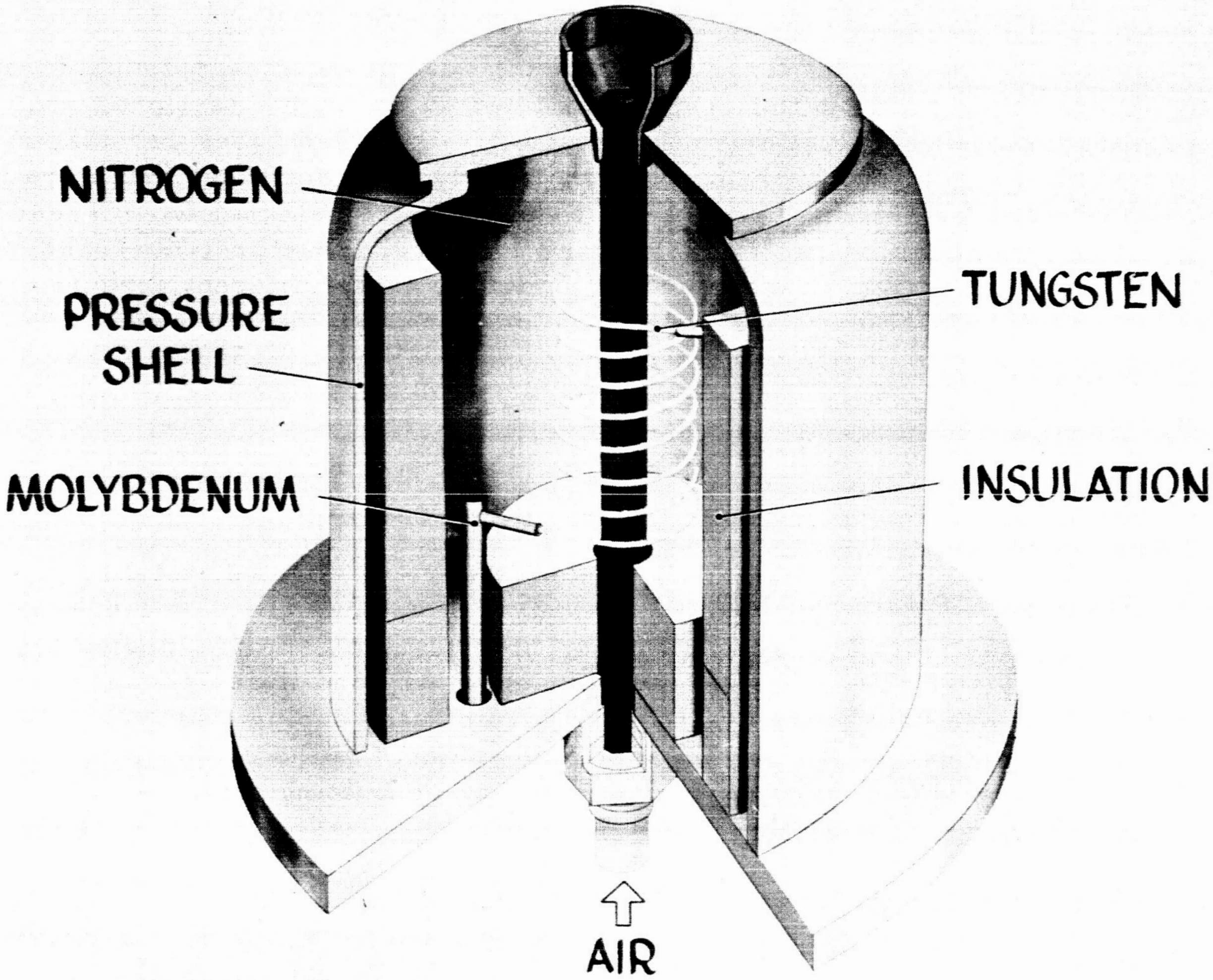
NITROGEN
PRESSURE SHELL
MOLYBDENUM
TUNGSTEN
INSULATION
AIR

Fig. 4.5.3-7 Schematic drawing of resistively heated tungsten helix furnace used for non-nuclear bench tests of fuel tubes

Only tubes with a crack rating of VI were catastrophically damaged. Tubes with ratings I and II were uncracked; and, of course, their performance was unimpaired. Tubes having crack ratings of III, IV, or V were exposed to a stress in excess of material strength capabilities but were not damaged beyond a point which would interfere with transmitting of structural loads, conducting heat, or restricting the airflow passage.

In-Pile Tests - The final phase of the test program was to perform in-pile tests to confirm the results obtained in the bench test program. The irradiation cartridges were composed of six fueled tubes per stage surrounded by unfueled tubes and rods of BeO which acted as insulators and were used to support thermocouples for the test specimens. These cartridges were tested in the Oak Ridge Research Reactor (ORR) and the Materials Testing Reactor (MTR). Some twenty different irradiation cartridges of either a single stage or four stage design were tested and evaluated as to thermal stress resistance. Figure 4.5.3-8 shows an exploded view of a typical single stage irradiation tube bundle with other ceramic components used in the cartridge.

4.5.3.3 Experimental Results

Some 1200 single tube dynamic bench tests were performed, totaling over 125,000 hours of test time, in the evaluation of various ceramic fuel tube designs. These tests included: (1) long time tests at specific design points to evaluate tube integrity under steady state conditions, (2) short time tests to evaluate effects of thermal strain rates during start-up transients, (3) tests under severe moisture contents in the coolant, (4) tests designed to evaluate different cladding or coating materials, (5) tests designed specifically to establish a particular residual thermal stress in the tube when brought to room temperature, and (6) tests to determine thermal stress resistance of a tube design.

For examples of experimental results obtained in the program, (1) two different test series are shown in which the resistance to thermally induced residual outer fiber tangential stresses is compared to pretest room temperature modulus of rupture strength of the material, (2) the effect of the residual stresses on the post-test room temperature modulus of rupture strength is shown, (3) an example is presented in which the thermally induced residual stress calculated to be in a tube outer fiber is measured using strain gauges, and (4) results of the in-pile irradiation test program are compared to pretest room temperature modulus of rupture strength.

Factorial Experiment: Residual Stress vs. Operating Temperature, Heat-Flux, and Time - The first example is of a series of tests performed on a particular element which employed a fueled BeO matrix having a cladding material on the inside surface. A statistical factorial experiment was performed in which the variables were inner bore temperature,

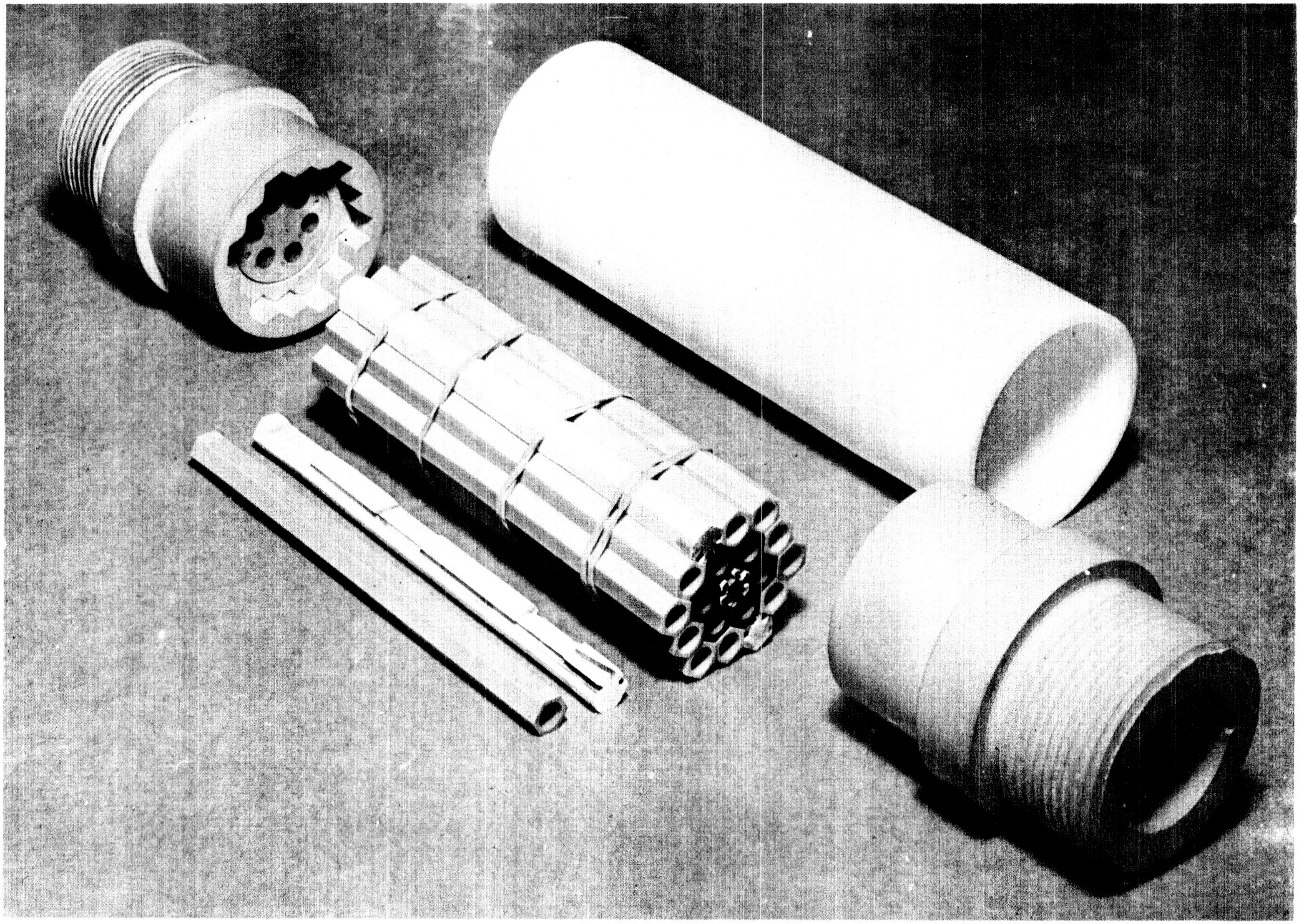

Fig. 4.5.3-8 View of typical single stage fuel tube irradiation test cartridge and other ceramic components showing six fueled tubes surrounded by unfueled tubes

time, and inner bore heat flux, making a total of 27 different combinations. Each of the 27 test conditions was [illegible] 5 times. Care was taken not to heat and extract power in a manner which would permit the initial operating stress to exceed the material strength. Therefore, if a tube was to fail, it would do so as a result of the residual outer fiber stress exceeding the material strength. Table I lists the results of the experiment in order of increasing residual outer fiber circumferential stress and the percent of the tubes that cracked for the 27 combinations of inner bore temperature, heat flux, and time at operating conditions. The results of the test are shown in Figure 4.5.3-9 grouped in intervals of 4,000 psi and compared to the room temperature modulus of rupture (4 points, 3 inch span) for the tubes. It can be seen that the thermal stress resistance curve is above the modulus of rupture distribution curve.

Residual Stress Resistance of Coated Tubes - Similar results were obtained in another test series comprising 81 tubes having thin vapor deposited coatings on the inner surface of fueled BeO tubes. In this series, all tubes were tested at an inner bore temperature of 2500°F for times ranging from 20 to 1000 hours, sufficient for complete stress relaxation. The percent of tubes crack free at five different stress levels (residual outer surface tangential stress) and the distribution curve for the room temperature modulus of rupture strength are shown as a function of stress in Figure 4.5.3-10. These particular tubes were of lower strength than those in the first case but, again, the same pattern appears; that is, the thermal stress resistance curve is above the room temperature modulus of rupture distribution curve.

Effect of Residual Stress on Post Test Modulus of Rupture Strength - The modulus of rupture strength of a tube measured at room temperature after a thermally induced residual stress has been imposed is reduced because of the residual tensile stress in the outer fibers of the tube. Modulus of rupture strength of tubes that had operated at power extraction and temperature conditions designed to produce a tangential residual outer surface tensile stress equal to approximately 50, 70, and 90 percent of the pretest annealed strength was reduced by 22, 30, and 46 percent respectively. The strength of control tubes of each group after annealing of the residual stresses had essentially recovered. From this series it would appear that the reduction in the bending strength is equal to about half of the maximum residual tangential tensile stress which occurs at the center of a flat on the outer surface. From the finite difference solution for hexagonal tubes, the predicted ratio of axial to circumferential stress at the center of the flat would be about 0.6 for tubes having the D_i/W ratio used. Therefore, the reduction in the post test modulus of rupture strength appears to be reduced by an amount approximately equal to the value of the longitudinal stress component at the center of the flat. The maximum longitudinal stress appears from the finite difference solution at the hexagonal corners but is only about 10 percent higher than at the center of the flats.

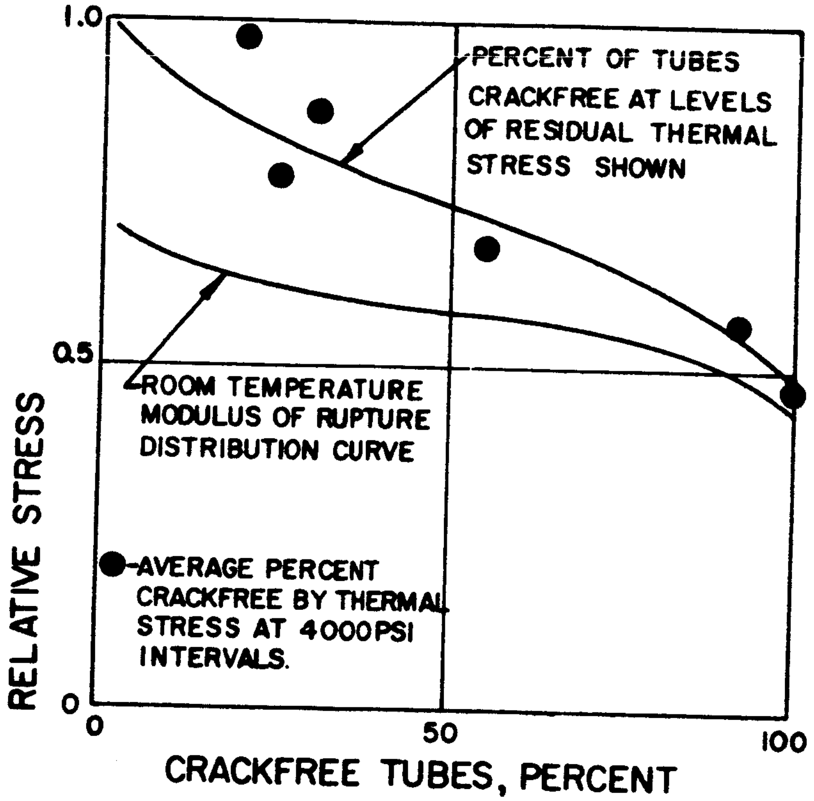

Fig. 4.5.3-9 Room temperature residual thermal stress resistance distribution curve of fueled-BeO tubes compared to distribution curve for room temperature modulus of rupture, factorial experiment

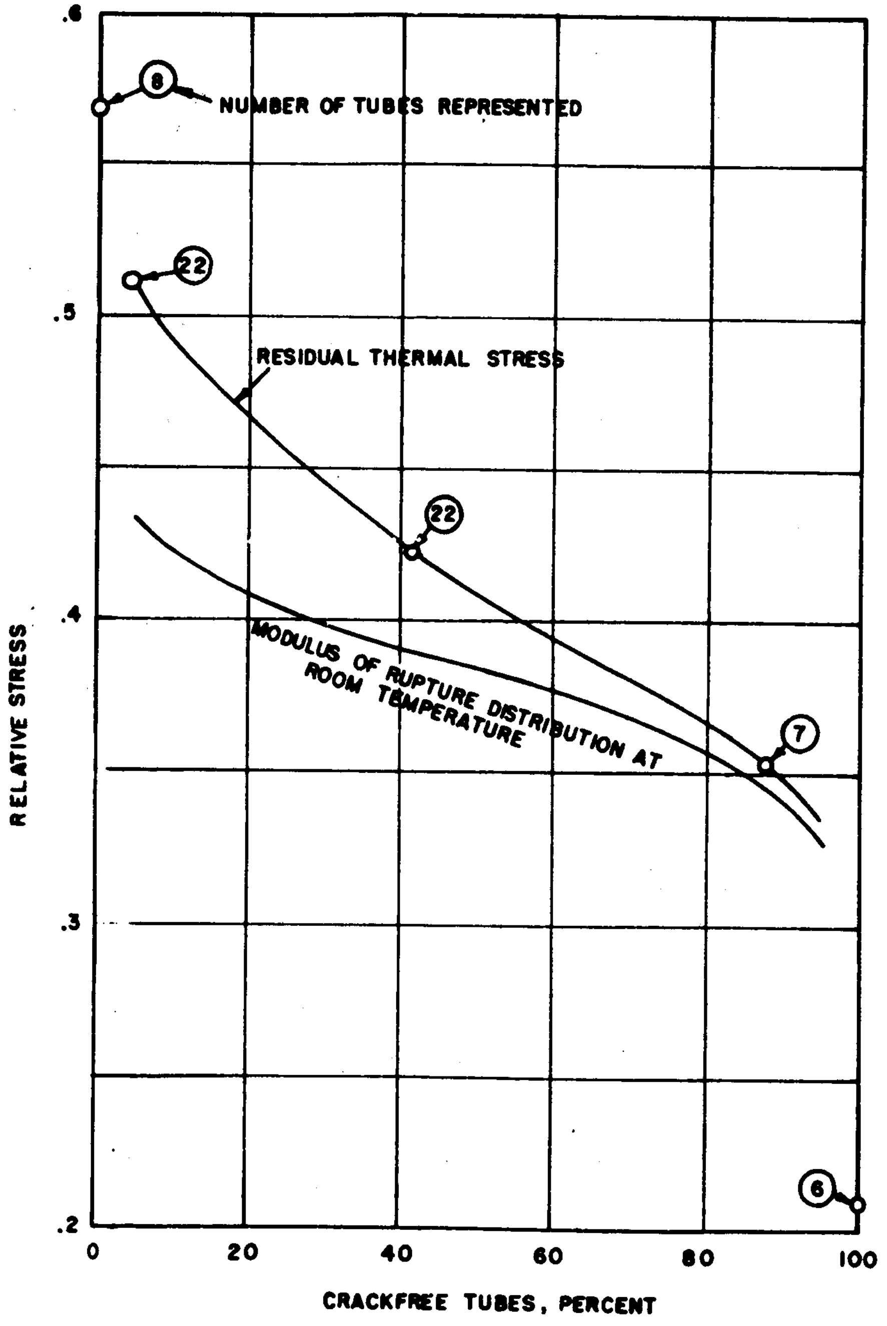

Fig. 4.5.3-10 Room temperature residual thermal stress resistance distribution curve of thin coated fueled-BeO tubes compared to room temperature modulus of rupture distribution curve

Confirmation of Calculated Residual Stress by Strain Gauge Measurements

The accuracy of the circumferential outer surface residual stress calculation was checked by use of strain gauges. The gauges were attached to the center of a hexagonal flat at 0.5 inch increments down the length of a tube. The residual strain on the outer surface was measured by grinding away the inside wall in small increments and measuring the strain release resulting from the removal of the complimentary stress on the inner bore. Reproducible data were obtainable for the circumferential strain, but the longitudinal component was not successfully measured. The effect of the longitudinal component of strain is to add a factor which would vary from zero to a maximum which would be the product of the circumferential strain multiplied by Poisson's Ratio. Figure 4.5.3-11 is a plot of the circumferential residual tensile stress at the center of a hexagonal flat as calculated from strain gauge measurements. The two curves show the limits of the tangential stress profile along the length of the tube if (1) no axial component of strain were present, and (2) if the strain in both the tangential and axial directions were equal. The actual case would be expected to fall within these boundaries. The maximum tangential stress which was calculated for this particular tube falls about half-way between the boundaries. From this measurement it appears that the longitudinal stress is about 50 percent of the tangential stress at this location, about the same as predicted by the finite difference analysis, and that the stress calculations describe the actual stress conditions to a good degree of accuracy.

Figure 4.5.3-11 also shows the typical variation in the circumferential residual stress component resulting from the radial temperature gradient along the length of the tube in the bench tests as a result of the rather short heated zone in the furnaces and the use of ambient cooling air. Even as severe as this longitudinal temperature profile is, the stresses resulting directly from the longitudinal temperature gradient are small compared to those resulting from the radial temperature gradient.[9]

Results of In-Pile Nuclear Tests - Results at least equal to those obtained by the radiant heating tests were observed in tests conducted to evaluate the stress resistance of fueled tubes under nuclear conditions. Figure 4.5.3-12 shows the test results compared to a room temperature modulus of rupture distribution curve for the tubes. As can be seen, several of the tests had no cracked tubes at relative residual stress levels about twice the value of the minimum modulus of rupture strength. It is possible that this is the result of some annealing of the residual stresses due to the shutdown procedure in the in-pile tests.

These results indicate that the radiant heating tests were more severe than the nuclear heating tests and therefore the results of radiant heating tests can be assumed to be conservative in estimating thermal stress resistance of the tubes relative to the nuclear tests.

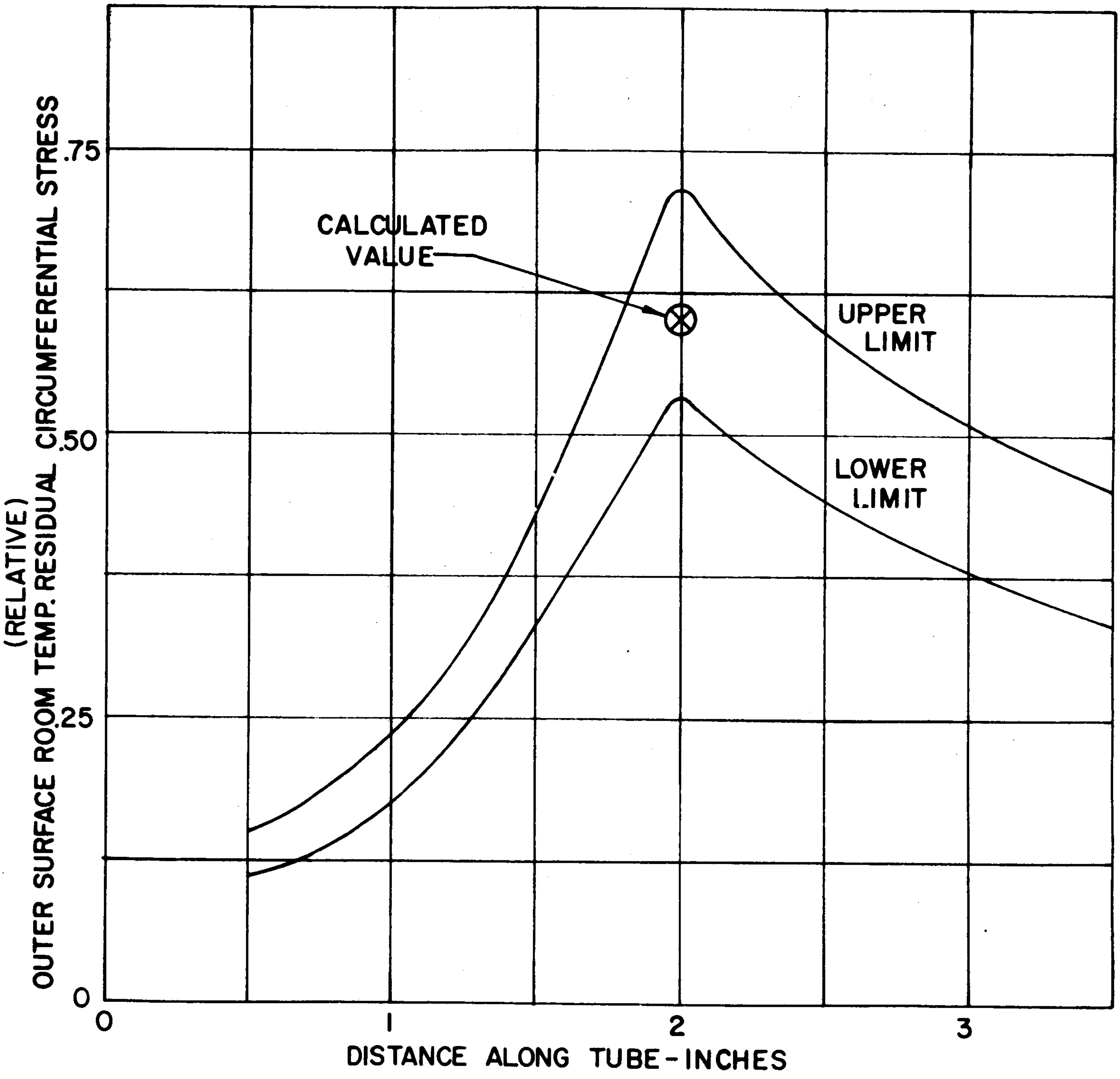

Fig. 4.5.3-11 Outer surface room temperature residual circumferential stress profile from strain gauge-stress relieve methods compared to maximum calculated outer surface residual circumferential stress. Longitudinal stress profile results from a longitudinal temperature gradient in the non-nuclear test

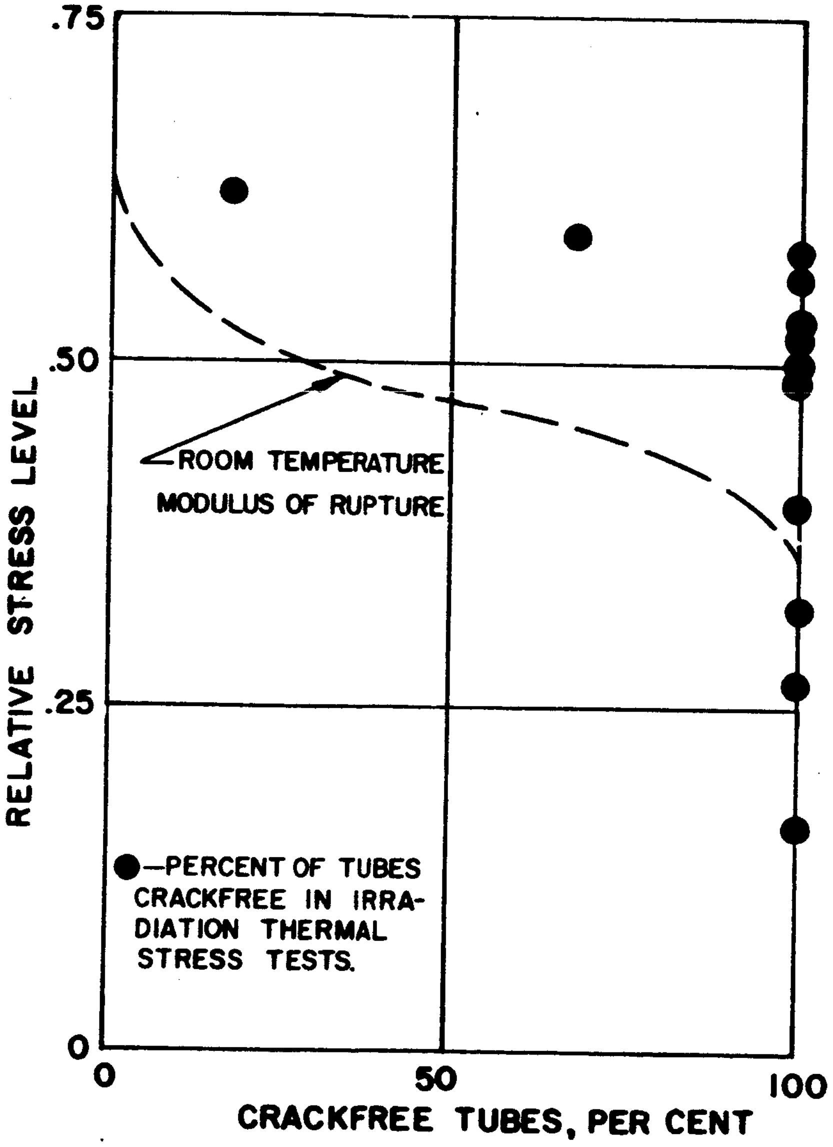

Fig. 4.5.3-12 Comparison of irradiation room temperature residual thermal stress test results to room temperature modulus of rupture strength. Each point represents the results of a single irradiation test of six fueled BeO tubes

4.5.3.4 Discussion of Results

It was possible in this program to (1) define the problem, (2) relate thermal stress resistance to mechanical strength measurements, (3) perform tests by imposing stresses by radiant heating and correlate these results with stresses imposed by nuclear heating, and (4) impose a calculated thermally induced room temperature residual stress and actually measure the amount of the stress with strain gauges and stress relief methods.

Of the many different test series performed, in no case was the resistance to thermally induced residual stresses less than the strength of the material as determined by four point modulus of rupture tests at room temperature. Figure 4.5.3-13 shows the thermally induced residual stress at which 50 percent of the tubes tested cracked (light bars) compared to the average value of the room temperature modulus of rupture strength (dark bars) for the same series. The tubes of the first series shown had small transverse cracks at the corners of the hexagonal outer surface which reduced the modulus of rupture strength but did not affect the resistance to a tangential stress component maximum at the center of the flats.

One probable reason for the resistance to thermally induced stresses being greater than resistance to stresses imposed by four point bending is that when thermally induced stresses are imposed upon the tube, small stress relief cracks can form which relieve the stress without necessarily going to complete rupture of the tube. On the other hand, in the bending test when the initial fiber failure occurs, continued application of the load results in immediate propagation to failure. In the post-test analysis of a thermal stress test, if the small stress relief cracks cannot be observed by the inspection method used, the tube would be considered as not cracked which would indicate a better resistance to thermally induced stresses than actually exist.

The pattern of the cracks observed offered a good indication of the stress responsible for cracking. For example, the most common crack pattern observed for a tube that had been exposed to too severe a thermal stress was the longitudinal cracks, (generally two, on opposite flats of the hexagonal outer surface, at the thinnest section) extending from the hottest portion of the tube out toward the ends. This crack pattern was typical of those resulting from the transerve stress component on the outer surface exceeding the material strength on cooling to room temperature. Some tests were performed at stress levels such that the outer fiber circumferential stress was exceeded resulting in longitudinal cracks, but with not enough energy release to cause the crack to propagate completely through the wall to the inner surface. Such tests verified that the maximum tensile stress causing the crack was in fact the outer surface circumferential component. If on heating, the inner surface stresses exceeded the material strength and a crack propagated through the tube wall, enough coolant air from the bore would

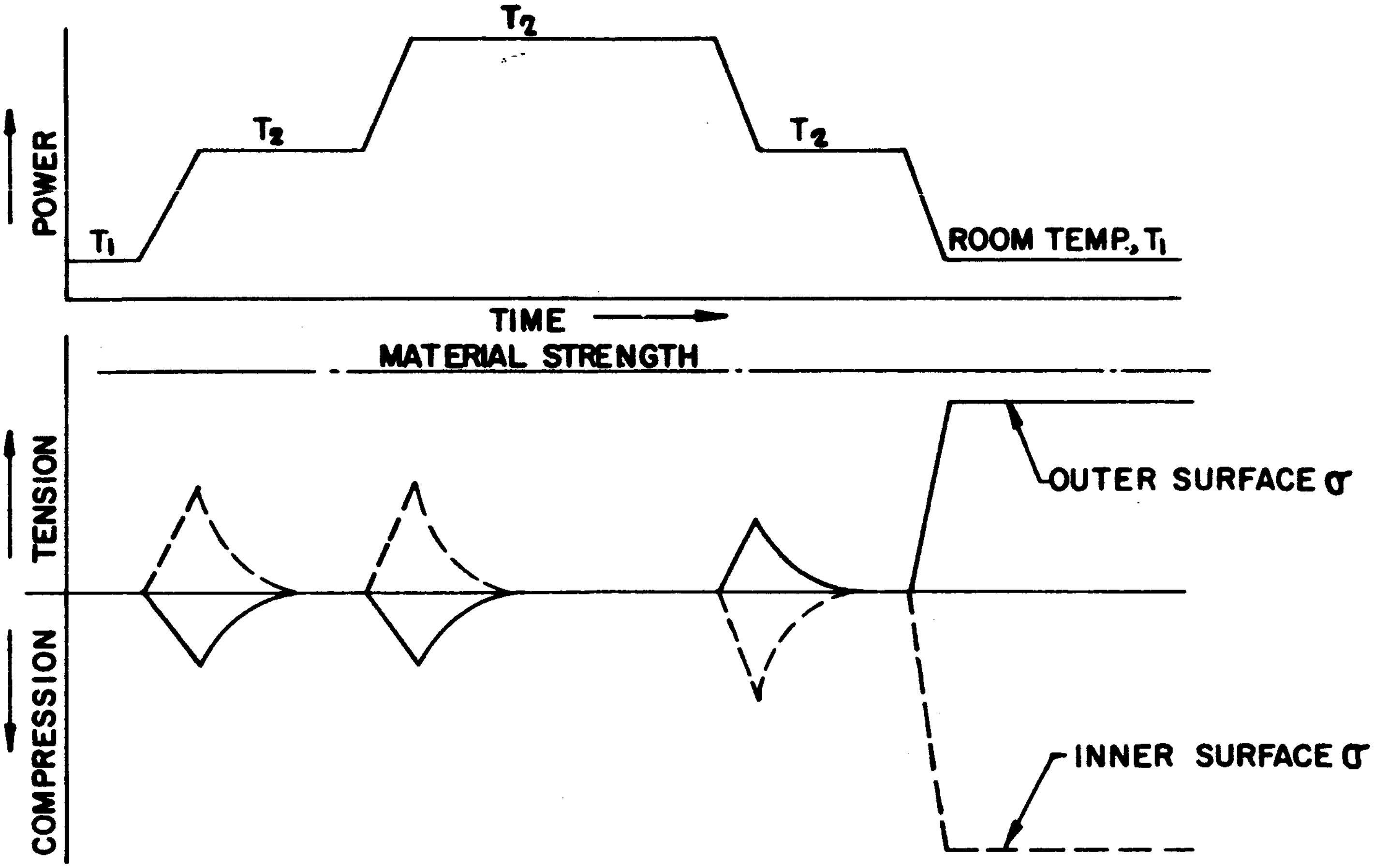
T₂
T₂
T₂
T₁
POWER
ROOM TEMP., T₁
TIME
MATERIAL STRENGTH
TENSION
COMPRESSION
OUTER SURFACE σ
INNER SURFACE σ

Fig. 4.5.3-13 Comparison of room temperature residual stress resistance and room temperature modulus of rupture strength compared at the stress level where 50 percent of the tubes cracked for six different series of BeO tubes

permeate into the inert atmosphere of the furnace chamber enclosing the tungsten heating elements that almost immediate failure of the tungsten heating coil would result, signalling that a crack had occurred in the tube.

Occasionally tests were performed in which too severe a longitudinal temperature gradient was imposed on a tube. Although normally the stresses resulting from the longitudinal temperature gradient were small compared to those resulting from the radial temperature gradient, on occasion a poorly assembled test setup would produce a sudden sharp increase in the longitudinal temperature profile. This usually resulted in a transverse crack in the tubes when the axial component resulting from the longitudinal temperature profile was superposed upon the axial stress component resulting from the radial temperature profile. However, in normal reactor operation stresses resulting from the longitudinal temperature profile are of even less consequence than in a radiant heating test.

When one considers the various ramifications associated with the relaxation of the operating stresses, it can be seen that this phenomenon can be used to advantage in permitting operation at power levels in excess of those that would be possible if the stresses did not relax with time. In order to show this experimentally, tests were performed according to a cycle shown schematically as Figure 4.5.3-14. Here the operating temperature was established but the maximum power extraction level was reached by steps allowing sufficient time at the lower level for the elastic stresses to relax before the material strength was exceeded. After relaxation had occurred, the power level was raised to a value twice that which had previously been shown to be sufficient to rupture a similar tube in unscheduled heating and cooling cycles. Before cooling to room temperature from the high level of power extraction, the power level was reduced in steps while maintaining the temperature so that relaxation of stresses could result before a residual stress developed of a magnitude sufficient to crack the tube. The results were as expected, the tubes were brought through the cycle without evidence of cracking. The practical application of this principle of operation in an actual,reactor is somewhat questionable since scheduled shutdowns cannot always be assured.

4.5.3.5 Summary and Conclusions

Radiant heating of the outer surface (external heat input) of a tube with power extraction at the bore can be used successfully to simulate certain thermal stresses resulting from nuclear power extraction (internal heat generation) with all heat removed at the bore if a particular stress at one location of interest is considered in one test. Thermally induced residual stresses produced by both methods of heating can be correlated to the pretest modulus of rupture strength.

The maximum elastic tensile stress occurring on the circular bore of a tube having a hexagonal outer surface is the circumferential component of

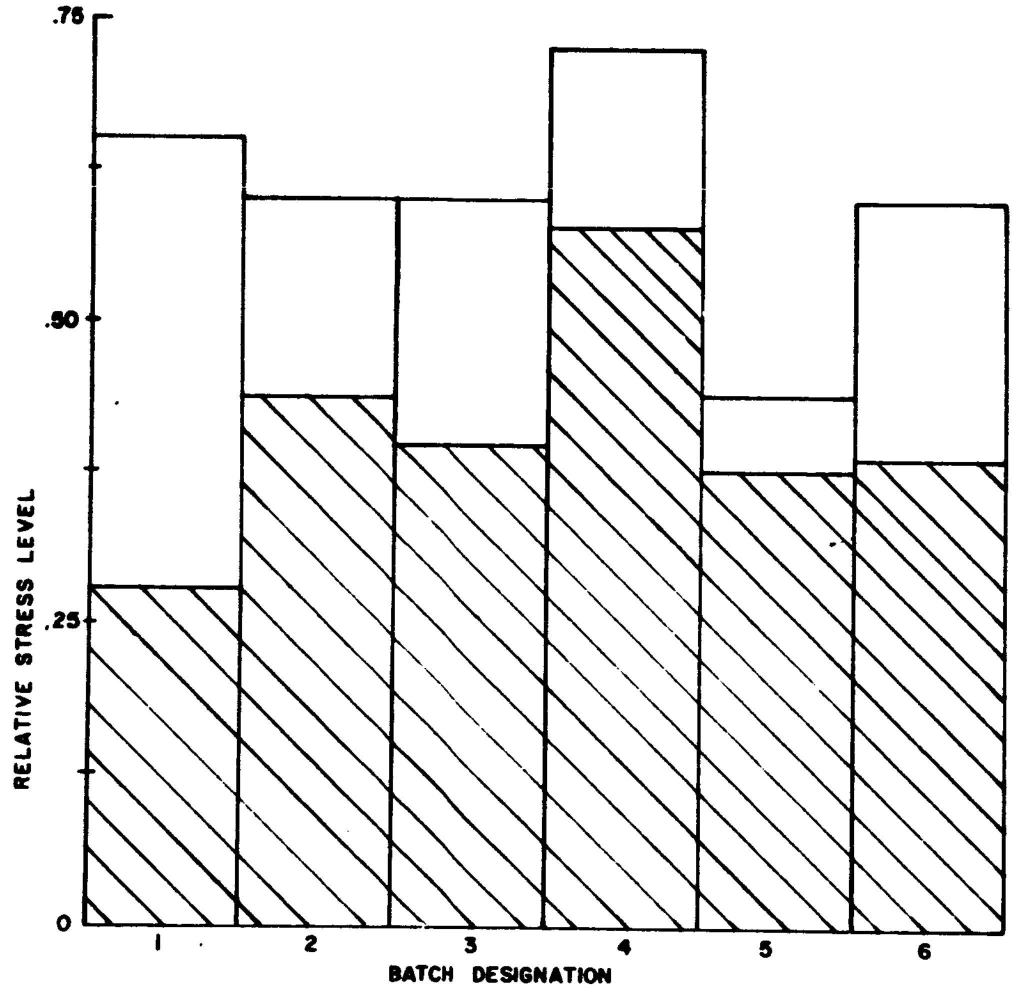

NOTE: TOPS OF BARS INDICATE OUTER-FIBER RESIDUAL THERMAL STRESS AT WHICH 50 PERCENT OF TUBES CRACKED. DARKENED PARTS OF BARS INDICATE AVERAGE MODULUS-OF-RUPTURE AT ROOM TEMPERATURE.

Fig. 4.5.3-14 Typical power-temperature-time cycle showing intermediate stress relaxation power levels in excess of those which would crack tube during unscheduled heating and cooling

the stress resulting from a radial temperature gradient across the tube wall and occurs at the thinnest wall section during heating to elevated temperatures. With time at temperature, this elastic stress can relax completely by creep deformation. The maximum elastic tensile stress occurring on the outer surface of the tube is at the thinnest section and is the circumferential component of the stress resulting from the removal of a radial temperature gradient after creep deformation occurs. Immediate cooling to ambient temperature from the operating temperature after creep deformation causes a high residual stress on the outer fibers which is the tensile stress of greatest magnitude encountered in the normal cycle of heating, long time steady state operation, and cooling to ambient temperatures.

Calculated values of room temperature residual outer fiber stresses can be confirmed using strain gauges and stress relief methods.

A residual tensile stress on the outer surface of a tube will reduce the room temperature modulus of rupture strength by an amount approximately equal to the axial residual stress component.

By scheduling heating, cooling, and power extraction rates so that stress relaxation can occur to and from the maximum power extraction level, the maximum allowable level can be significantly increased over that which would be possible with unscheduled heating and cooling. Practical application of this principle, however, may be difficult to achieve.

4.5.3.6 Acknowledgement

Section 4.5.3 was contributed by B. A. Chandler.[24] Additional acknowledgement is given to J. M. Botje, R. W. Brisken, A. J. Butterfield, B. A. Chandler, J. B. Conway, R. G. Cook, L. A. Feathers, J. H. Holowach, P. E. Lowe, J. E. McConnellee, D. R. Riley, A. L. Ross, D. G. Salyards, A. D. Smith and others of the former Aircraft Nuclear Propulsion Department of the General Electric Company for their efforts in thermal stress analysis and the testing program.

TABLE 4.5.3-1

FACTORIAL EXPERIMENT RESULTS IN TERMS OF INCREASING OUTER-FIBER RELATIVE RESIDUAL STRESS

Relative Outer-Fiber Residual Stress	Bore Temp. °C	Relative Heat Flux at Bore	Time at Temp-Power hours	Percent of Tubes Crack-Free
.02	1260	.65	0.5	100
.04	1260	.85	0.5	100
.05	1260	1.0	0.5	100
.34	1370	.65	0.5	100
.40	1260	.65	10.0	100
.44	1450	.65	0.5	100
.44	1370	.85	0.5	100
.55	1260	.85	10.0	100
.56	1370	1.0	0.5	60
.58	1450	.85	0.5	100
.60	1260	.65	50.0	100
.62	1370	.65	10.0	100
.64	1370	.65	50.0	80
.66	1450	.65	10.0	80
.66	1450	.65	50.0	0
.72	1260	1.0	10.0	60
.75	1450	1.0	0.5	20
.76	1260	.85	50.0	60
.78	1370	.85	10.0	20
.80	1370	.85	50.0	0
.83	1450	.85	10.0	60
.83	1450	.85	50.0	0
.92	1260	1.0	50.0	60
.95	1370	1.0	10,0	0
.97	1370	1.0	50.0	40
1.0	1450	1.0	10.0	0
1.0	1450	1.0	50.0	0

4. 5. 4 ALLOWABLE STRESSES AND COMBINED TOTAL STRESSES

The total stresses at any point in the fuel element are obtained by combining the individual stress contributors algebraically and using the principal of superposition. The time of occurrence, location, and direction must be considered in the combination. Stress combinations are primarily directed toward determining the maximum tensile stresses since these stresses are of greater importance than compressive stresses.

Total combined stresses are found for (1) initial elastic tensile stresses occuring during operation and (2) the residual tensile stresses at room temperature following shutdown from nuclear operation. The combination of residual temperature stresses assumes that complete relaxation has occurred and, consequently, gives the maximum value. Figure 4. 5. 4-1 shows the location of developed stresses and the nomenclature used for stress combinations. The following four combinations have been found to be of primary concern:

σ_θ, A - The operating elastic tangential tensile stress at point A located away from the tube end, m

σz, A - The operating elastic axial tensile stress at point A located at the center of the tube, s/2

σ_θ, B - The residual tangential tensile stress at point B located at the ends of the tube, e

σ_z, D - The residual axial tensile stress at point D located at the center of the tube, s/2

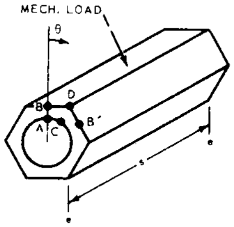

Note: No Cladding
+ indicates tension
- indicates compression

LOCATION OF MAXIMUM STRESS	INITIAL OPERATING STRESS (Elastic Stress at Temperature)			RESIDUAL STRESS (Room Temperature)
	TANGENTIAL, σ_θ			σ_θ, Res
	Maximum[1] Thermal	Maximum Mechanical	Maximum Combined	Maximum Combined
A	+ m[2]	+ $\theta = 0°$ m	+ m	- m
B	- e[3]	- $\theta = 0°$ (< B´) e	- e	+ e
C	+ (< A) m	+ $\theta = 30°$ (< A) m		
D	0			

[1] Use tangential thermal stress factor, H_θ.
[2] m – indicates maximum stresses occur away from ends.
[3] e – indicates end correction factor, e_b, must be applied. Maximum tangential stresses occur at tube ends.

	AXIAL STRESS, σ_Z			σ_Z, Res
	Maximum[1] Thermal	Maximum Mechanical	Maximum[2] Combined	Maximum Combined[2]
A	+	+ $\theta = 180°$	+	-
B	- (< D)	- $\theta = 0°$ (< D)		
C	+ (< A)	+ $\theta = 150°$ (< A)		
D	-	- $\theta = 30°$	-	+

[1] Use axial thermal stress factor, H_Z.
[2] Maximum combined axial stresses occur at center.

Fig. 4. 5. 4-1 – Maximum combined thermal stresses

The data of Fig.4. 5. 4-1 apply to an unclad tube. However, the data for clad tubes are similar, but differ in magnitude.

The stresses for the four combinations identified above are shown in Figures 4. 5. 4-2, 4.5.4-3 and 4.5.4-4 as a function of the fractional length through the core. Curves of this type graphically present a quick summary of the stress conditions, and especially if the allowable stress is included in the curves.

The design criteria for the 141D fuel elements required that the ultimate stress (1.5 times the limit stress) be compared to the minimum modulus of rupture (average modulus of rupture minus three standard deviations). The limit stress would necessarily occur at one of the above four points.

The validity of these stress calculations has been demonstrated by extensive development testing, the results of which are discussed in APEX-914, "Ceramic Reactor Materials."

4. 5. 5 OTHER COMPONENTS IN A TUBE BUNDLE

4. 5. 5. 1 OUTER REFLECTOR

Reflector tubes and rods are designed by the same general methods as the fuel elements. Due to the lower heat generation in these unfueled ceramic pieces, the thermal stresses are low. Mechanical loadings are approximately the same as those in the fuel tubes. However, because of the large radial temperature gradient that normally exists across the outer reflector, the thermal camber is much greater than in the fuel elements. Since the resulting axial stress may become a primary concern, a good design fix is to increase the stiffness (moment of inertia) of the unfueled ceramics. This is accomplished by shortening the elements or by increasing the across-flats dimension. The latter method would be economically desirable since the number of parts is greatly reduced.

The lower temperature level of the reflector parts usually precludes relaxation of the internal stresses, and may eliminate the need for cladding beryllia pieces. Also, a slight undersizing of the outer reflector pieces is incorporated in the design to permit differential thermal expansions.

4. 5. 5-2 TRANSITION PIECES

Transition pieces are used at each end of the core to serve as a manifold for coolant entering and leaving the fuel element passages. The pieces also act as end reflectors. At the inlet end, coolant enters one large hole and is distributed to seven, nineteen, or more tube passages. At the discharge end, the coolant is recombined before passing through the axial structure. The design permits the use of fewer, large-diameter holes in the metallic end retainers, and penalties caused by flow passage misalignment are decreased.

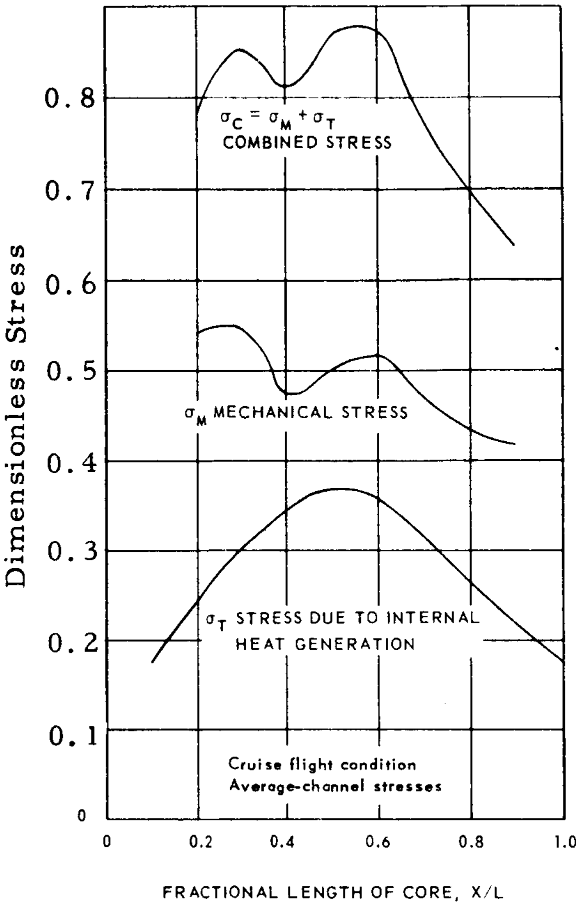

Fig. 4. 5. 4-2 – Operating elastic axial tensile stress, $\sigma_{Z,A}$, **in typical fuel elements**

Fig. 4. 5. 4-3 – Operating elastic tangential tensile stress, $\sigma_{\theta,A}$, in typical fuel elements

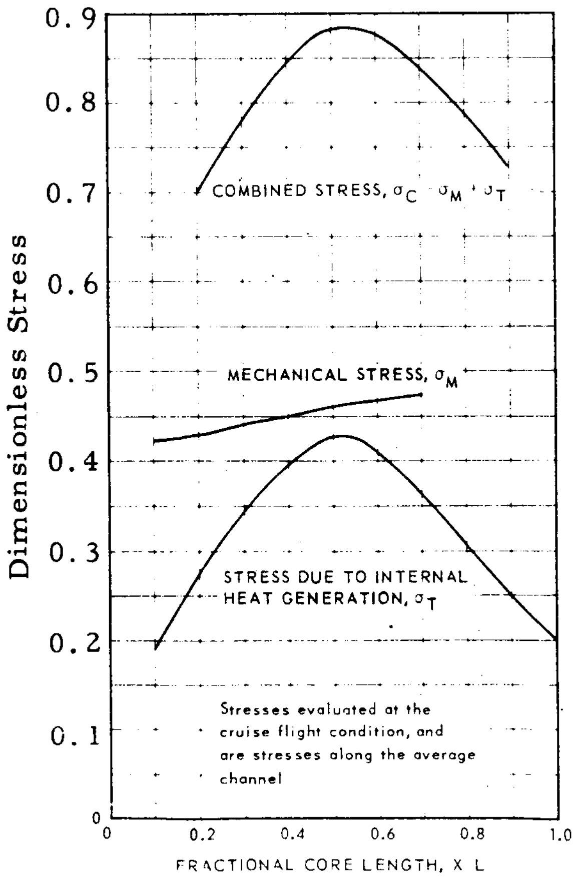

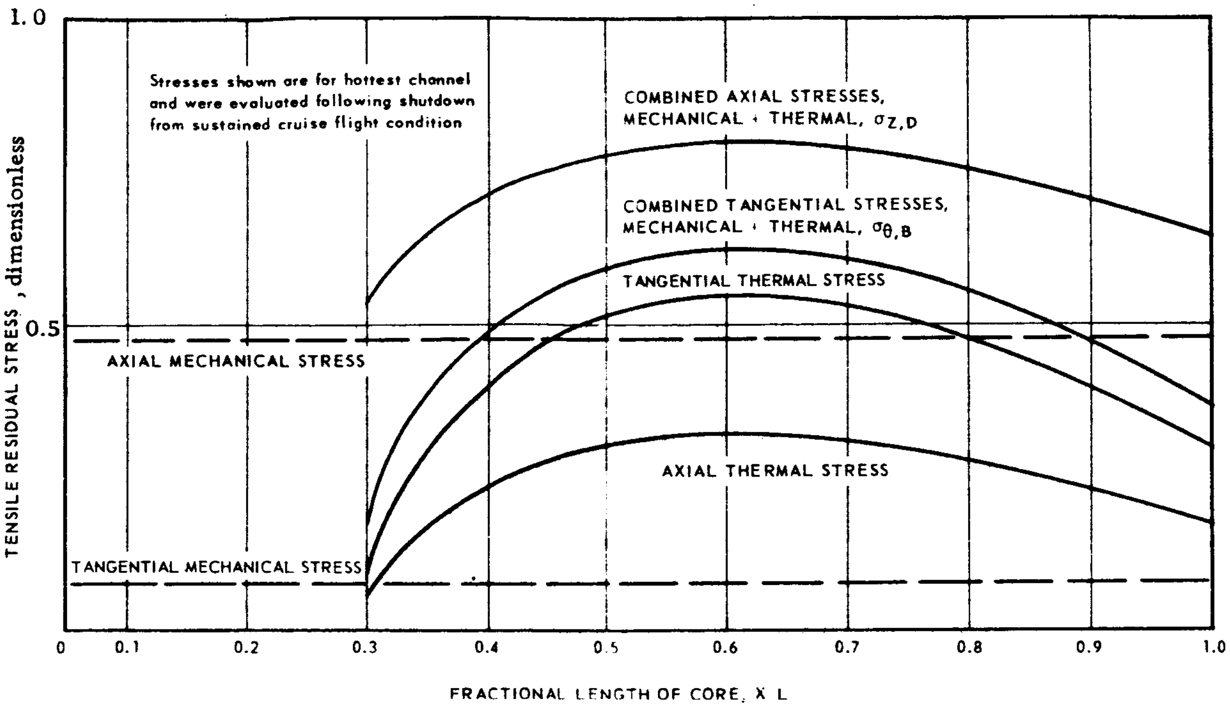

Fig. 4. 5. 4-4 – Residual stress in typical fuel elements at room temperature

Fig. 4.5.5-1 is a photograph of a typical cluster of seven aft end transition pieces. They are arranged in three axial lengths to stagger the tubes throughout the tube bundle in groups of seven or nineteen. This prevents misalignment of the tubes and maintains a shear plane across the diameter of the core.

Relative to the fuel element conditions, the rate of secondary heat generation is low whereas the heat transfer area and heat transfer coefficients are comparable. Therefore, operating temperatures are but slightly above that of the coolant, and the temperature gradient in the web is low. However, variations in coolant discharge temperatures from adjacent fuel channels, especially at the outer radius of the core, introduce an additional temperature gradient in the web between the holes.

Analysis of the stress within the walls of two adjacent channels at different temperatures is approximated by assuming the ligament between the holes as a fixed plate of minimum ligament thickness. The gradient is assumed linear and the resulting stress is approximated by the familiar equation

$$\sigma = \frac{E\alpha\Delta T}{2\,(1-\nu)}$$

Mechanical loading on the transition piece results from the radial spring pressure. Two loading conditions are considered; (1) ring loading due to the radial pressure in the bundle, and (2) axial shear loading which develops when a group of tubes transmits a friction load normal to the front face of the transition piece. The ring loading is assumed to act on opposite sides of the transition piece at the critical section, and the shear load acts on the critical web shear area. The stresses in the transition piece are calculated by using simplified models of the actual component since exact solutions are not available because of the complexity of the part.

4.5.5-3 Radial Arch Pieces

Radial arch pieces in the 141D reactor were aligned longitudinally to provide an axial cavity approximately 1.5 inches in diameter through the tube bundle for the control rod and its support tube. Figure 4.5.5-2 shows a group of typical radial arch pieces. The inside diameter of the radial arch is determined by the thermal insulation around the support tube, the radial differential motions of the related reactor components, and the necessary clearances, especially relative to the control rod chain drive. The outside configuration is determined by the number of hexagonal tubes replaced and coolant void requirements.

Several design choices are available. The cavity may be formed by simply removing a sufficient number of small tubes to assure clearance with tube interlocking being relied on to maintain the cavity. However, failure of a tube lining the cavity might permit pieces of the tube to become wedged against the support tube.

Another choice, a metallic arch, appears promising. It can be used to line the inside of the cavity and provide containment of a possibly fractured ceramic tube. Mechanical loads can be redistributed through a small deflection in a thin wall arch ($D/W \approx 0.95$ and a wall thickness ≈ 30 mils have been studied). Thermal stresses in the metallic member are of little concern, but the major drawback to the metallic arch is the currently existing temperature limit of metallic materials, e.g., 2000°F for nickel based alloys. Insulation could be removed from the metallic support tube housing the control rod, and placed around the arch. One or two layers of unfueled cooling tubes surrounding the arch would supply sufficient reduction in temperature. For neutron economy, the arch diameter and the wall thickness would be minimized, and, for maximum neutron economy, the support tube could be eliminated and the control rod guided by the metallic arch. When the support tube serves both as an axial support member and as a metallic arch, it is subjected to a bending load as well as axial tension. The bending load results from the radial spring pressure forcing

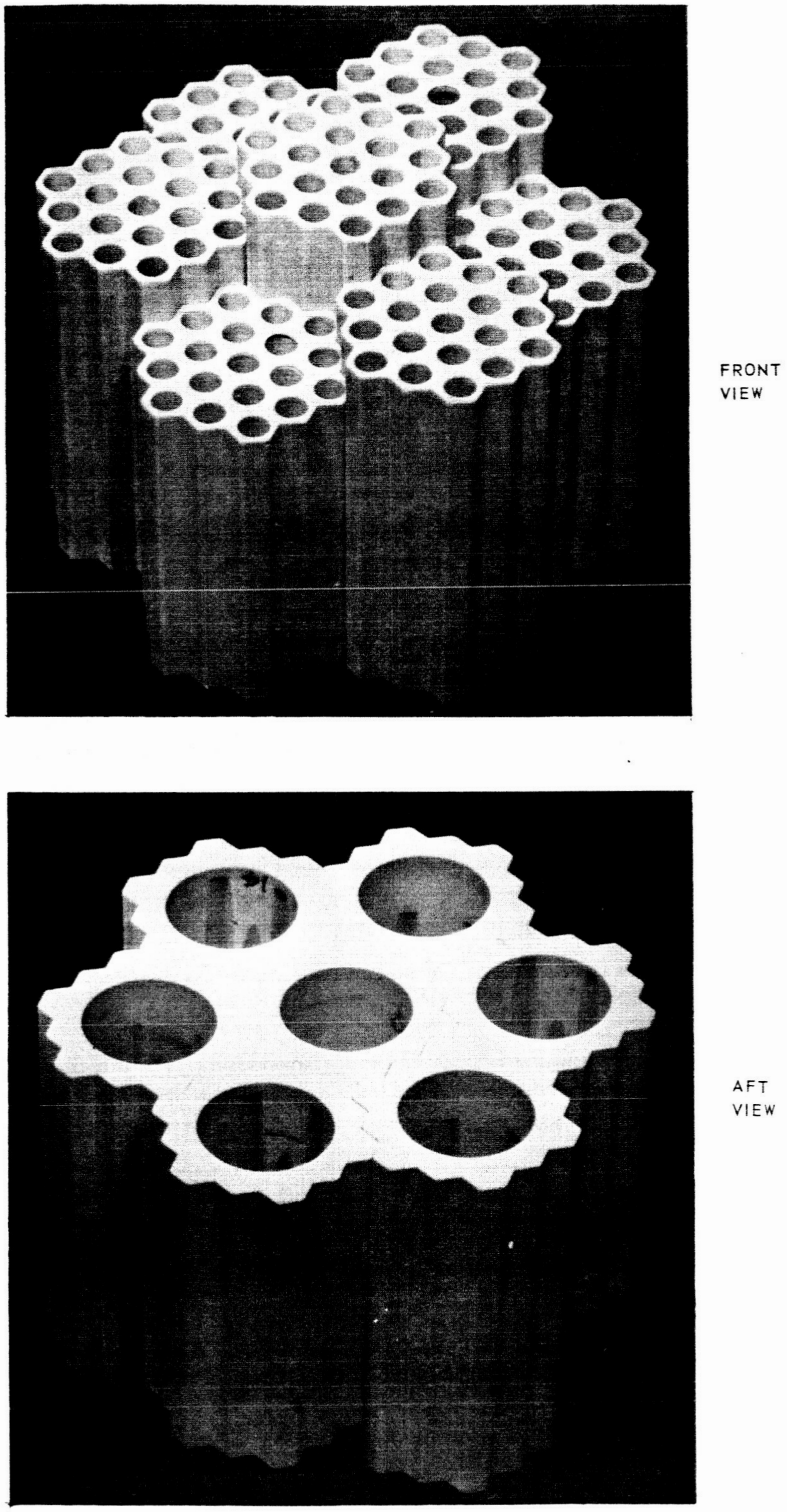

FRONT VIEW

AFT VIEW

Fig. 4.5.5-1 – Aft end transition pieces (C-23486)

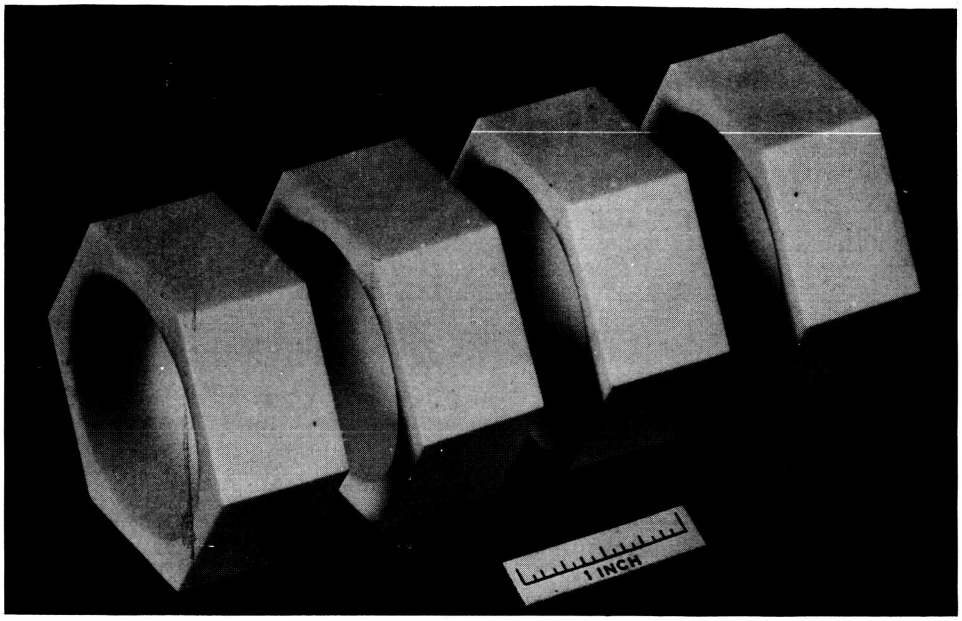

Fig. 4.5.5-2 - Radial arch pieces (C-23775)

the metallic tube to conform to the general barrel shape of the tube bundle resulting from the longitudinal temperature profile. This load, of course, increases with increasing core radius and/or increased barrelling and the adjacent fuel elements or reflector tubes may experience large crushing loads. Further, the bending stresses in the support tube must be combined with the axial stresses; this is often an untenable situation at high operating temperatures.

Choosing a ceramic arch leads to a higher temperature capability. It can be made either as a single hexagonal tube or segmented in the manner of a Roman arch, thus forming a tube. The segmented arch has approximately one-fourth the axial thermal stress as that in the equivalent hexagonal tube. However, the reduction in thermal stress is not totally realized. The segment must be unrestrained to relieve the stress. But if enough load is available to eliminate thermal camber, the stresses are the same as for the restrained full length tube. The design should be optimized dimensionally such that insufficient load is available to remove the thermal camber. The segmented arch eliminates one of the major design uncertainties of the single tube arch; namely, thermal stresses due to circumferential temperature variations. The wall thickness is chosen to obtain the minimum combined thermal and mechanical stresses. External cooling may be preferred to internal cooling since the latter often adds to the arch heat arising in surrounding tubes.

Mechanical stresses result from the pressure load imposed by the radial springs. The highest stress level is encountered when two opposite sides of the arch are loaded. The resulting load is calculated by assuming that the maximum pressure in the tube bundle tangential direction acts on the projected area of the arch and causes a distributed pressure.

Thermal stresses result from the temperature gradients needed to conduct secondary heat to the convective boundary. Two temperature gradients must be considered: (1) the radial temperature gradient through the thickness of the arch and (2) the circumferential temperature gradient around the perimeter of the arch due to non-uniform heat removal and the exponential decrease in the heating rate across the arch. These stresses are computed for an infinite cylinder with the same inner diameter and cross-sectional area as the arch. Corrections are then applied to account for the hexagonal outer surface and finite length.

For the infinite circular cylinder case, cooled on the outside surface, insulated on the inside surface, with internal heat generation, the maximum tensile stress occurs at the outside surface of the cylinder. This thermal stress is equal in both the axial and tangential directions, and is calculated by the following equation:

$$\sigma_{\theta,z} = 43,200 \frac{E\alpha}{k\,(1-\nu)} q''' \left[\frac{(1.05W)^2}{32}\right] \left[1 - 3\frac{D^2}{(1.05W)^2} - 4\,\frac{\frac{D^2}{(1.05W)^2} \ln\left(\frac{1.05W}{D}\right)}{1 - \left(\frac{1.05W}{D}\right)^2}\right] He, \text{ psi}$$

where

D = Inside diameter of cylinder, inches
W = Distance across flats of hexagon, inches
E = Modulus of elasticity, psi
k = Thermal conductivity, Btu/hour - feet - $^{\circ}F$
q''' = Heat generation rate, Btu/second - inches^3
α = Instantaneous coefficient of thermal expansion, inch/inch - $^{\circ}F$
H = Correction factor for the hexagonal shape
e = Correction factor for the finite length

The circumferential thermal gradient results primarily from uneven cooling of the external surface of the arch. The temperature gradients are approximated by:

$$(T - T_{avg}) = T_o \sin N\theta$$

where

$(T - T_{avg})$ = Amplitude of sine wave at any point, $^{\circ}F$
T_o = Maximum amplitude of sine wave, $^{\circ}F$
θ = Angular coordinate degrees
N = Number of temperature waves in 360 degree circumference

Radial arch stresses due to the circumferential temperature gradients are calculated by the following equation:

$$\sigma = \left(\frac{E}{1-\nu}\right) T_o \sin N\theta$$

where σ = Stress, psi
λ = Stress factor
E = Modulus of elasticity, psi
α = Coefficient of thermal expansion
ν = Poisson's ratio
$T_o \sin N\theta$ = Magnitude of temperature fluctuation

The stress factor, λ, is a function of the ratio of the length to the inside diameter of the radial arch. This ratio must be optimized so as to minimize the stress. The effect of varying the L/D ratio on the stresses arising from the circumferential temperature gradient is evaluated using the analytical method given in reference 60. The results of an analysis of the case where $N = 12$ are shown in Figure 4. 5. 5. 3

4. 5. 5-4 CORE LINER

The design of the core liner is primarily concerned with buckling, the lowest possible mode of failure being that having three full sine waves since any lesser mode is fully restrained by the core geometry. External pressure is taken as the maximum spring force, increased by an oversized-liner load multiplier of 2, to which is added any pressure differential due to coolant flow.

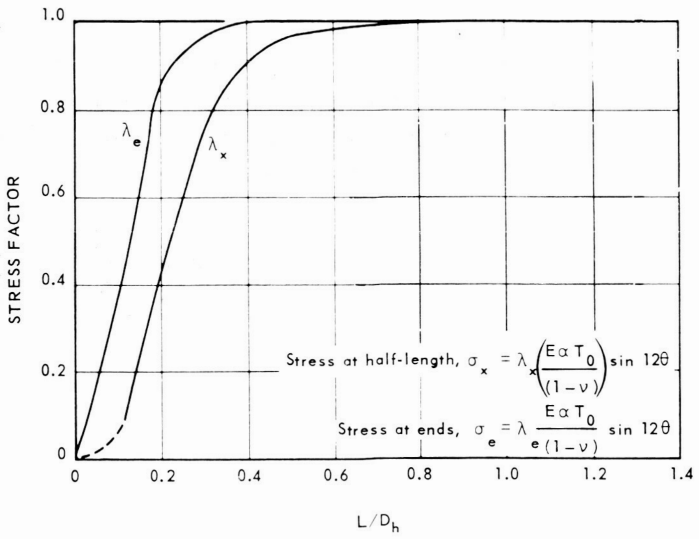

Fig. 4. 5. 5-3 – Thermal stress factors for radial arch thermal analysis

Biaxial deflection of the ring depends on (1) original out-of-roundness of the liner, and (2) out-of-roundness of the cavity in the tube bundle. The latter is a function of the probability of fuel tubes with outer dimensional tolerances being at certain locations. By use of core definition analysis, adjusted for tube size and envelope tolerance, the maximum required deflection is calculated as previously discussed.

The outer surface of the liner is duodecagonal in shape, and leads to large variations in wall cross section. As there is no readily available technique for the analysis of such a shape, calculations are based upon a circular ring of equivalent area, and adjusted by empirical factors. For example, a liner of two-tier length was subjected to uniform external pressure until failure occurred by buckling. The test fixture was designed to restrict the liner to failure by buckling inward only, and the liner was unrestrained longitudinally. Buckling occurred as shown in Fig.4. 5. 5-4. The failure resulted from an effective pressure of 285 psig, as compared to a calculated pressure to cause failure of 180 psig.

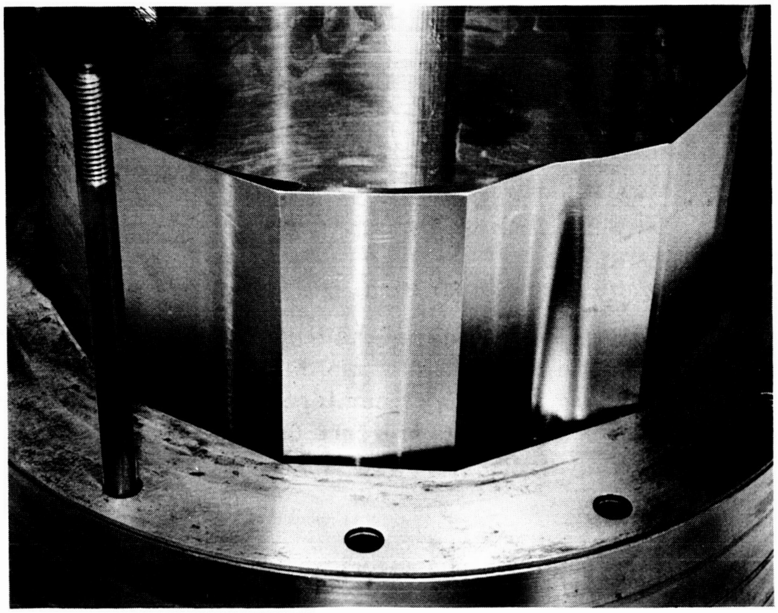

Fig. 4. 5. 5-4 – Buckling failure in two-tier deep core liner test (U-38843D)

4. 6 DESIGN DETAILS OF COMPONENTS IN THE RADIAL SUPPORT SYSTEM

The design principles of the exostructure supporting the core in a tube-bundle reactor are discussed in section 4. 4. The material in this section includes a discussion of some major design parameters, spring materials and design properties, and other aspects of component design. The 141D reactor is used as an example, although the design details are generally applicable to other tube bundle configurations.

Radial support through straps, belts, pneumatic actuators, encapsuled steam pillows and other "clever" devices is excluded, and the discussion is confined to the more versatile and predictable spring systems for enveloping the bundle.

4. 6. 1 DESIGN PARAMETERS

The unit stresses in all components of the tube bundle are directly affected by the radial support system. Many variables are introduced that cause numerous iterations throughout the design cycle. It is important, therefore, that the significant design parameters are identified and their interrelationship established early in the design. The significant parameters include the type of support to be utilized, tube bundle deflections, materials temperature limitations, the desired radial gap, and the autoclaving effect. Weight and radial space limits lead to the choice of a multileaf spring with its high configuration efficiency. An important factor, however, is the relative ease of providing positive shear ties between the shell and pressure pads. The spring assembly provides a rigid support tangentially while maintaining radial flexibility for deflections and expansions of the tube bundle. The problem of sliding friction inherent with key supports is largely eliminated.

4. 6. 1. 1 Type of Support

An initial choice of a simple hydrostatic suspension, a pure shear suspension, or the more complex integrated suspension is required. Specifically, the long time radial pressure, X_R, and the short time tangential pressure, X_T, must be minimized; a minimum unitizing pressure, P_{min}, must be assured, and the deflections of the tube bundle must be limited. The first two pressures are a function of the radial spring rate, S_R, and are readily determined as previously described. The minimum pressure is normally the radial preload when the differential expansion, Δ, is zero; this minimum pressure (radial preload) assures that the tube bundle may then be considered as a rigid body in subsequent design analysis.

The shear suspension system was chosen for the 141D reactor since the choice was necessary before the advantages of the integrated support were fully realized. The larger radial pressure resulting from the large differential expansions, and low allowable deflection led to abandoning the simpler hydrostatic support.

Since the radial support structure represented about a fourth of the reactor weight (including the pressure pads), several alternate systems were investigated. On the surface, a more promising approach was the corrugated shell. Both the springs and the cylindrical shell were replaced by a pliable shell hugging the core bundle. Detailed analysis, however, showed that the corrugated shell was less efficient, and weighed approximately 50 percent more when designed for the same elastic properties.

4. 6. 1. 2 Tube Bundle Deflections

To determine the required allowable deflection, the following displacements of the tube bundle relative to the structural shell must be combined: bundle internal displacements, tolerance allowances, peak deflection due to dynamic loading, and the design motion due to acceleration forces. Displacements within the bundle due to the possible use of undersized reflector tubes are rather intangible. Since the other internal displacement appear only as a function of the shear portion of the support forces, initial limits can be assigned from existing test data of the three-tier mockup. The eccentricity tolerance resulting during assembly of a five-foot diameter tube bundle and structural shell is largely determined by the fixtures used, and economics plays a large part in setting the design allowable total deflection. A maximum of 30 mils eccentricity was allowed in the 141D design. If acceleration forces are applied during extremely short periods of time, impact loading may result and dynamic deflection peaking may become a design requirement. Although impact loading was not considered a design requirement, clearances were provided for 1-1/2 times the normal deflection at maximum acceleration.

If the hydrostatic suspension predominates, the bundle deflection due to acceleration is readily determined along with maximum tube pressures as previously shown. For pure shear support, the deflection is essentially independent of radial deflections and a rather rigid system can be designed with very small deflections. Caution, however, should be exercised to prevent shock loads being transferred to the tube bundle.

4. 6. 1. 3 Temperature Limitations in Spring Materials

Spring temperatures must be kept below 1100° to 1300°F depending on the time-stress relationships of the currently available material and severe heat removal problems may exist. Low coolant temperatures, though desirable, may not be available, as shown by the inlet-air total temperature and speed relationship shown in Fig 4. 6-1. For the nuclear ramjet missile, a radial support system other than springs is indicated for Mach numbers higher than approximately 3. 5 at sea level. Often a variation of the coolant inlet temperature exists. In the 141D design, spring off-design temperatures exceeded the long-time design temperature by 200°F while stresses remained approximately the same. Heating rate predictions in the spring may vary widely during design. For example, the design allowed for a range from minimum to maximum, or 0. 57 to 1. 75 times nominal heating rate. Further, the calculated temperature distribution within the springs may vary by as much as 200°F. Design conservatism may be reduced after operating experience is gained, and the amount of coolant flow may be adjusted to their required values if provisions are properly made in the initial design.

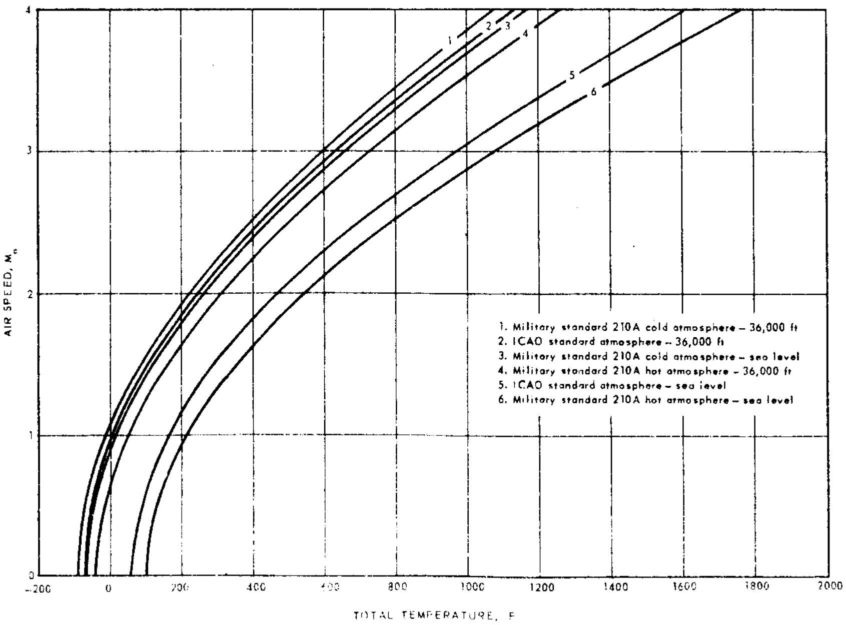

Fig. 4. 6-1 – Total inlet air temperature versus air speed

4. 6. 1. 4 Temperature Considerations in the Structural Shell

Since allowable stresses of the metallic structural shell decrease with increasing temperature, it seems desirable to keep the shell cool. A cold shell - hot core, though, results in a large differential thermal expansion, Δ, and it may be necessary to spell out a minimum, as well as a maximum design temperature for the shell. Higher temperatures may also have a beneficial effect in some materials by annealing out possible radiation damage, e. g., loss of ductility. It should be remembered that the maximum differential expansion, Δ, may actually occur during transient conditions such as startup, and all design points must be evaluated.

4. 6. 1. 5 Radial Gap

Another important parameter when choosing a radial support system is the radial gap occupied by the system. In a nuclear ramjet missile study, the drag was decreased approximately 8 percent for a decrease of 1 inch on the radius. The reactor-shield assembly weight varied approximately 3 percent per inch on the radius. In a nuclear rocket application, however, the radial support system weight rather than radial thickness would probably predominate - the hydrogen tanks and vehicle overall diameter are already large.

4. 6. 1. 6 Autoclaving Pressure

In order to establish the desired amount of coolant flow through the radial-spring cooling channels, it has been necessary to provide additional resistance to restrict the flow. When the resistances are placed at the exit end of the channels, an increasingly positive external-pressure differential is developed along the length of the tube bundle. This pressure difference exerts an autoclaving effect on the tube bundle similar to the effect of the radial spring pressure. During some operating conditions, the autoclaving pressure may become greater than the spring pressure. (A basic assumption in this discussion is that the pressure external to any individual tubular element within the bundle is equal to the pressure within the bore of the tube.) The use of a single gross resistance at the inlet end of the core leads to an obvious parallel, but reverse condition.

To reduce and control the autoclaving pressure, the radial spring coolant may be orificed after passing over each row, or stage, of springs. Thin, channel-shaped baffles may be used to enclose the spring and provide a means of orificing. When proper orificing is provided, the pressure profile through the spring region nearly matches the pressure profile through the reactor core and autoclaving effect on the fuel elements is minimized or eliminated.

4. 6. 2 SPRING DESIGN

4. 6. 2. 1 Materials Considerations

A spring is a mechanical device for storing energy. To achieve minimum weight, the material not only should be effectively utilized but also capable of carrying a sustained high stress. Using currently available materials, however, a temperature environment above approximately 900°F causes lowering of certain material properties such as yield point and modulus of elasticity. Furthermore, the maximum operating temperatures are limited to prevent metallurgical changes such as exceeding the aging temperature in a precipitation hardening material. At times stability may be improved by initial overaging, higher than normal aging temperature, although other desirable properties such as yield strength may decrease.

The most significant limiting phenomenon in high temperature spring design is relaxation, i. e., reduction of load with time under conditions of constant deflection. Relaxation normally is considered as a combination of plastic and anelastic strain. The former is a permanent change in shape resulting from deformation above the elastic limit, and it is not recoverable upon load removal. The anelastic strain is defined as a change in shape resulting from time-dependent deformation, and may be recoverable with time if the load is removed while at temperature. Since tube bundle design cannot permit spring unloading cycles, any load recovery due to the recovery of anelastic strain is ignored as a design consideration.

One of the best currently available spring materials for high-temperature stability is Rene' 41. Extensive relaxation tests have been run in the range of 900° to 1200°F and 70,000 psi to 100,000 psi stress. Results of 100- and 1000-hour tests are shown in Figure 4.6-2. The percent relaxation indicated is the loss in load-carrying ability of the material. As shown by the data in this figure, relaxation can be reduced by heating the spring, prior to use in the assembly, at a load and temperature slightly exceeding the operating conditions. This heat treatment greatly reduces the initial high relaxation rate normally apparent in the first few hours of service. At GE-ANPD, it is accomplished by preloading to 10 percent above operating stress at a temperature 10 percent above operating.

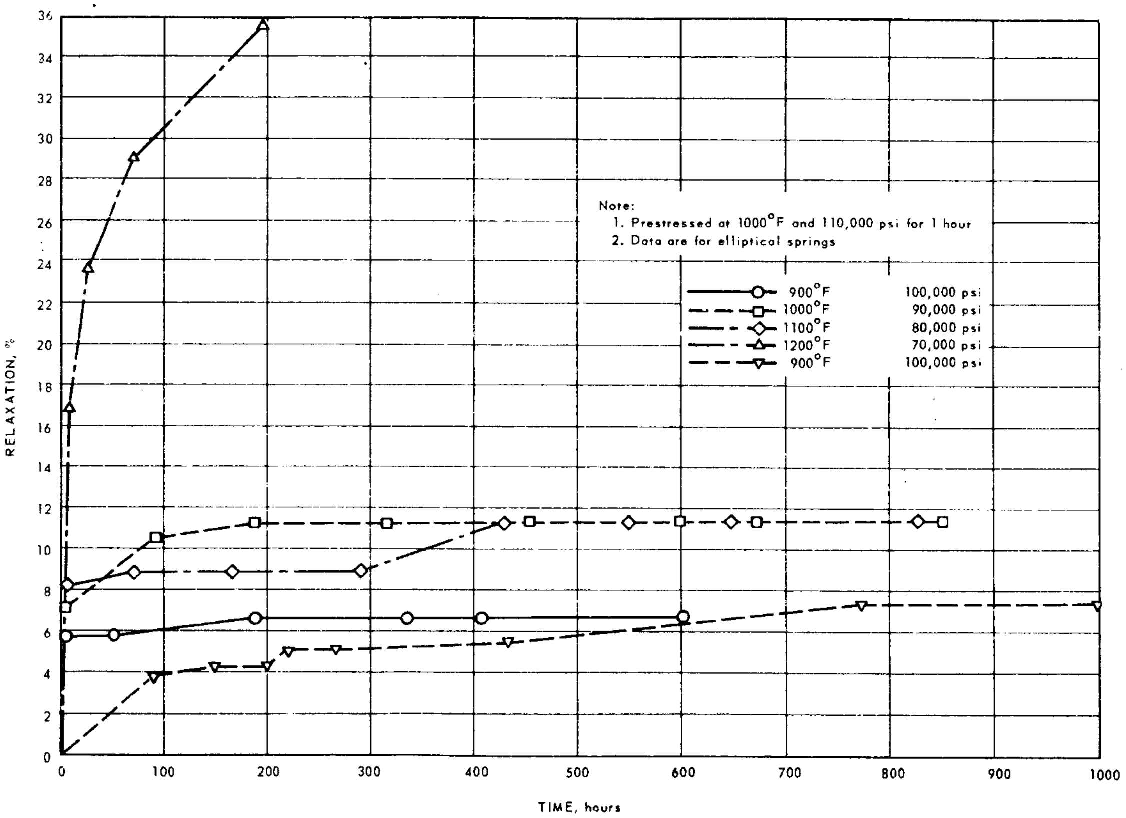

Note:
1. Prestressed at 1000°F and 110,000 psi for 1 hour
2. Data are for elliptical springs

Fig. 4.6-2 – Spring relaxation as a function of time and temperature for Rene' 41 material

The spring design is further complicated by radiation damage. Little is known on the subject, especially concerning precipitation-hardenable materials. Ductility and rupture strength may be greatly decreased and the yield point increased. Presumably, relaxation rates would be less under the same time-temperature-stress conditions for irradiated springs compared to unirradiated. Reference 64 describes in-pile tests conducted in early 1962 on Rene' 41 samples. For a fast flux of 10^{19} nvt and 1200°F, the 100-hour material rupture strength apparently was reduced 20 percent. Unirradiated control specimens exhibited approximately 107,000 psi rupture strength and irradiated specimens exhibited approximately 87,000 psi. Ductility was reduced to between 1 and 2 percent after irradiation, compared to between 6 and 12 percent before irradiation.

From the previous discussion, it is apparent that spring failure may occur, not as decreased load on the tube bundle which might be tolerated, but as broken springs, a much more hazardous type of failure.

4.6.2.2 Effective Utilization of Material in Springs

In many cases it is desirable to estimate quickly the amount of material that must be put into a spring for given requirements of spring rate and maximum spring force. The parameters involved are the maximum allowable stress, cross section, and configuration of the spring. This section ties the parameters together properly so as to permit quick estimates of material required for springs of various shapes, even before specific designs and design calculations are made.(15)

The following nomenclature is used in the subsequent formulae:

P	Applied load carried by the tension or compression spring
P_{max}	Maximum load to be carried by tension or compression spring
d	Maximum deflection to be obtained from tension or compression spring
C_1	Spring rate of tension or compression spring
C_2	Spring rate of torsion spring
M	Applied torque carried by the torsion spring
M_{max}	Maximum torque to be carried by torsion spring
ϕ	Twist obtained from torsion spring
σ	Normal stress
σ_c	Extreme fiber stress of cross section
σ_g	Greatest normal stress anywhere in spring
σ_{max}	Maximum allowable normal stress
τ	Shear stress
τ_c	Maximum shear stress of cross-section
τ_g	Greatest shear stress anywhere in spring
τ_{max}	Maximum allowable shear stress
A	Cross sectional area of spring
r	Radius of gyration of spring cross section
L	Length of spring (in case of a helix, to be measured along the helix, i.e., active length of wire)
V	Volume of material in active portion of spring
V_{min}	Minimum volumes required
E	Young' s modulus
G	Shear modulus
ν	Poisson' s Ratio
ψ_1	Cross-sectional efficiency of spring
ψ_2	Configuration efficiency of spring
ψ	Overall material utilization factor of spring
K	Wahl' s correction factor for stress concentration in helical springs.

The stored external energy in extension and compression springs is given by the following equation:

$$P_{max}\frac{d}{2} = \frac{P^2}{2C_1} \qquad (1)$$

For torsion springs, the equation is as follows:

$$M_{max}\frac{\phi}{2} = \frac{M_{max}^2}{2C_2} \qquad (2)$$

The stored internal strain energy of a spring is equal to

$$\int_0^V \frac{\sigma^2 dV}{2E} = \frac{\psi V \sigma^2_{max}}{2E} \tag{3}$$

for springs where the cross section is loaded in tension, compression, or bending; and

$$\int_0^V \frac{\tau^2 dV}{2G} = \frac{\psi V \tau^2_{max}}{2G} \tag{4}$$

for springs where the cross section is loaded in torsion.

The stored external energy must equal the stored internal strain energy; hence one of the following equations applies:

$$\left.\begin{aligned} \frac{P^2_{max}}{C_1} &= \frac{\psi V \sigma^2_{max}}{E} \\ \frac{P^2_{max}}{C_1} &= \frac{\psi V \tau^2_{max}}{G} \\ \frac{M^2_{max}}{C_2} &= \frac{\psi V \sigma^2_{max}}{E} \\ \frac{M^2_{max}}{C_2} &= \frac{\psi V \tau^2_{max}}{G} \; . \end{aligned}\right\} \tag{5}$$

The overall material efficiency of a spring is defined as follows:

$$\psi = \psi_1 \psi_2 \; . \tag{6}$$

In establishing ψ_1 and ψ_2, it is assumed that in at least at one point of the spring the maximum allowable stress is reached and that this stress is nowhere exceeded.

The cross-sectional efficiency of springs loaded in tension, compression, or bending is equal to

$$\psi_1 = \frac{1}{A\sigma_c^2} \int_0^A \sigma^2 dA \; , \tag{7a}$$

and, for torsion,

$$\psi_1 = \frac{1}{A\tau_c^2} \int_0^A \tau^2 dA \; . \tag{7b}$$

It should be noted that $\psi_1 = 1$ if the stress is constant over the entire cross section. Table 4.6-1 shows ψ_1 for various cross sections. When cross sections are loaded in torsion, ψ_1 is shown for the case where τ_{max} is prescribed, and for three specific ratios of τ_{max}/σ_{max} where σ_{max} is prescribed.

TABLE 4.6-1

CROSS-SECTIONAL EFFICIENCY OF SPRINGS, Ψ_1

Cross Section And Comments	Loaded In Tension Or Compression	Loaded In Bending[a]	Loaded In Torsion			
			τ_{max} Is Prescribed	σ_{max} Is Prescribed, $\nu = 0.28$, and $\tau_{max}/\sigma_{max} =$		
				0.625	0.577	0.500
General Case	1	$(r/c)^2$				
▯ Rectangle	1	0.333				
□ Square	1	0.333	0.307	0.307	0.262	0.197
○ Thin-wall circle	1	0.500	1.000	1.000	0.852	0.640
▨ Full circle	1	0.250	0.500	0.500	0.426	0.320

[a] r = radius of gyration; c = distance from neutral axis to extreme fiber.

The configuration efficiency of a spring is defined as

$$\psi_2 = \frac{1}{L\sigma^2_{max}} \int_0^L \sigma_c^2 \, dL \text{ or } \frac{1}{L\tau^2_{max}} \int_0^L \tau_c^2 \, dL. \qquad (8)$$

It should be noted that $\psi_2 = 1$ if $\sigma_c = \sigma_{max}$ or $\tau_c = \tau_{max}$ all along the spring. Table 4.6-2 shows ψ_2 for several spring configurations.

With ψ established, the volume of material required for the spring can be calculated from the applicable Equation (5), as shown in the following equations:

$$\left.\begin{aligned} V &= \frac{P^2_{max}}{\sigma^2_{max}} \frac{E}{C_1\psi} \\ V &= \frac{P^2_{max}}{\tau^2_{max}} \frac{G}{C_1\psi} \\ V &= \frac{M^2_{max}}{\sigma^2_{max}} \frac{E}{C_2\psi} \\ V &= \frac{M^2_{max}}{\tau^2_{max}} \frac{G}{C_2\psi} . \end{aligned}\right\} \qquad (9)$$

As an example, assume that a cantilever beam is to be used as a spring to satisfy the following conditions:

P_{max} = 1000 pounds
C_1 = 2000 pounds per inch
σ_{max} = 50,000 psi
E = 25 x 10^6 psi.

The first line of Equation (9) applies. The cross-sectional efficiency, ψ_1, for a beam with rectangular cross section is 0.333, Table4.6-1; for uniform cross section, the config-

TABLE 4.6-2

CONFIGURATION EFFICIENCY OF SPRINGS, ψ_2

	Configurations and Comments	ψ_2
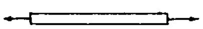	Prism in tension or compression	1
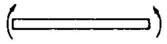	Prism in pure bending[a]	1
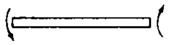	Prism in torsion	1
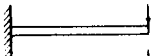	Prism as cantilever[a]	0.333[d]
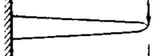	Uniform stress cantilever[a]	1
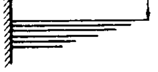	Multi-leaf spring[a]	≤ 1
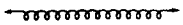	Helix as tension or compression spring[a, b]	$1/K^2$
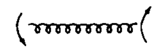	Helix as torsion spring	1
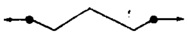	Various corrugated narrow strips[a, c]	0.333
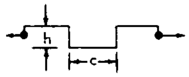	Formulas at right take only bending stresses into account.	$\frac{h+3c}{3(h+c)}$
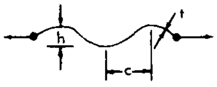 	Approximate correction factor for direct stress is $[3h/(3h+t)]^2$	$\sim\frac{h+1.5c}{3(h+c)}$

---

[a] In the case of wide sections in relation to thickness, use $E/(1-\nu^2)$ instead of E in Equations 3, 5, and 9.

[b] K is Wahl's Correction Factor for helical springs, or applicable portion thereof.

[c] Do not apply in the case of curvature out of plane, e.g., bellows.

[d] The value of $\psi_2 = 0.333$ for a prism as cantilever applies also to prisms in other types of bending, providing the extreme fiber stress varies uniformly along the length, from zero to maximum or from maximum negative to a numerically equal maximum positive stress.

uration efficiency ψ_2 is also 0.333, Table4.6-2. Hence, the overall material efficiency ψ is $(0.333)\cdot(0.333) = 0.111 = 1/9$, and

$$V = \frac{(1,000)^2}{(50,000)^2}\,\frac{25,000,000}{2,000\cdot 0.111} = 45 \text{ inches}^3 .$$

The ideal case of $\psi = 1$, i.e., where all material is stressed to σ_{max} under the load P, is found in a rod or tube in tension or compression. Unfortunately, other design considerations usually preclude this type of spring because of the great length required to obtain a reasonable spring rate. In the case of a compression spring, stability (buckling) must also be considered. In the case of a tension spring, some gain is possible through telescoping tubes; with fairly close fits, the stability of compression tubes should not be a problem. A thin-wall tube in torsion also gives favorable material utilization, but again space and buckling considerations impose serious limitations.

A helix used as a tension or compression spring has a material utilization factor of ψ = 0.5 for a solid round cross section, Wahl factor neglected, and $\tau_{max}/\sigma_{max} = 0.625$. If a helix were made from a thin-wall tube, the material utilization factor would approach unity. A helix used as torsion spring has a material utilization factor equal to one-half that of a similar helix used as a tension or compression spring.

The overall material efficiencies of given springs are calculated by means of the following equations:

$$\left.\begin{aligned}
\psi &= \frac{P_{max}^2}{\sigma_{max}^2}\,\frac{E}{C_1 V} \\
\psi &= \frac{P_{max}^2}{\tau_{max}^2}\,\frac{G}{C_1 V} \\
\psi &= \frac{M_{max}^2}{\sigma_{max}^2}\,\frac{E}{C_2 V} \\
\psi &= \frac{M_{max}^2}{\tau_{max}^2}\,\frac{G}{C_2 V}\ .
\end{aligned}\right\}\quad \psi = \frac{V_{min}}{V} \qquad (10)$$

For any linear spring, the efficiency of material utilization can be obtained for a given load P or M (not necessarily the maximum) if the greatest stress σ_g or τ_g in the spring and the spring deflection are known. The spring volume then can be established. For this case, P or M are substituted for P_{max} and M_{max}, respectively; and σ_{max} or τ_{max} are replaced by σ_g and τ_g, respectively. C_1 and C_2 are calculated from Equations (1) and (2), respectively. In this case,

$$\left.\begin{aligned}
\psi &= \frac{P^2}{\sigma_g^2}\,\frac{E}{C_1 V} \\
\psi &= \frac{P^2}{\tau_g^2}\,\frac{G}{C_1 V} \\
\psi &= \frac{M^2}{\sigma_g^2}\,\frac{E}{C_2 V} \\
\psi &= \frac{M^2}{\tau_g^2}\,\frac{E}{C_2 V}\ .
\end{aligned}\right\} \qquad (11)$$

As an example, assume that a circular ring of mean radius R, wall thickness t, and width w, is loaded by two diametrically opposite loads P. The spring volume is $2\pi Rtw$, its greatest bending moment 0.3183 PR, and its deflection $0.149\ PR^3/IE$. The spring rate is as follows:

$$C_1 = \frac{IE}{0.149R^3} = \frac{wt^3E}{1.788R^3}\ .$$

The greatest stress is as follows:

$$\sigma_g = \frac{6 \times 0.3183PR}{wt^2} \doteq \frac{1.9098PR}{wt^2}\ .$$

The first line of Equation (11) applies, and the overall efficiency of material utilization is as follows:

$$\psi = \frac{p^2 \ w^2 t^4}{1.9098^2 p^2 R^2} \times \frac{1.788 \ R^3 E}{wt^3 E \ 2\pi rtw} = 0.0780 \ .$$

The poor efficiency of material utilization in a ring used as a spring results from the moderate cross-sectional efficiency and the combined low configuration efficiency, i.e., zero bending moment.

4.6.2.3 Design Details of Leaf Springs

The initial step in determining the design details of a leaf-spring system to be used in the radial support structure is shown in Figure 4.6-3a. A linear spring rate is assumed. After fixing the values of the radial spring rate, (S_R), the minimum radial pressure (P_{min}), the design differential expansion (Δ), and the allowable deflection (δ_a), the abscissa of Figure 4.6-3a are established. The ordinates are established by the method of construction shown. The radial pressure distribution around the tube bundle is shown schematically to the right in Figure 4.6-3a; values are fixed by the design data as previously shown in Figure 4.4-3. Having chosen the material and its allowable stresses, the stress-deflection curve is drawn as shown in Figure 4.6-3b.

The allowable material stresses used to derive Figure 4.6-3b are probably selected as follows:

Stress Allowable	Load Application	Critical
σ_a (psi)	long time $(n = 1)$	10% relaxation stress
σ_b	short time $(n = n_o)$	0.2% yield minus 2 standard deviations
σ_c	short time $(n = n_o)$	Stress for rupture at temperature in 1000 hours
σ_d	short time $(n = n_o)$	Stress for rupture in 1000 hours at temperature and integrated lifetime fast neutron flux

These points are plotted on the appropriate deflection line (i.e., $n = 1$ or $n = n_o$). For the linear spring rate, a line connecting the origin to the lowest allowable stress value describes the desired spring characteristics. Preliminary data of this type are useful to the designer in the early design iteration stages, especially if hydrostatic suspension is being used.

The second step is to complete the configuration and material choice as previously discussed. Additional considerations, of course, may be encountered peculiar to a particular reactor and its application.

After completion of the above two preliminary steps in the detailed design, it is necessary to compute the values of the three directional loads applied to the spring and their resultant stresses. Figure 4.6-4 shows the direction of these loads (radial, tangential, and axial), and defines the nomenclature used for the analysis. The inner and outer sets of leaves are assumed to be symmetrical and to exhibit comparable loading characteristics. For cases of nonsymmetry, the design merely requires that the proper parameters be inserted in the general formulae.

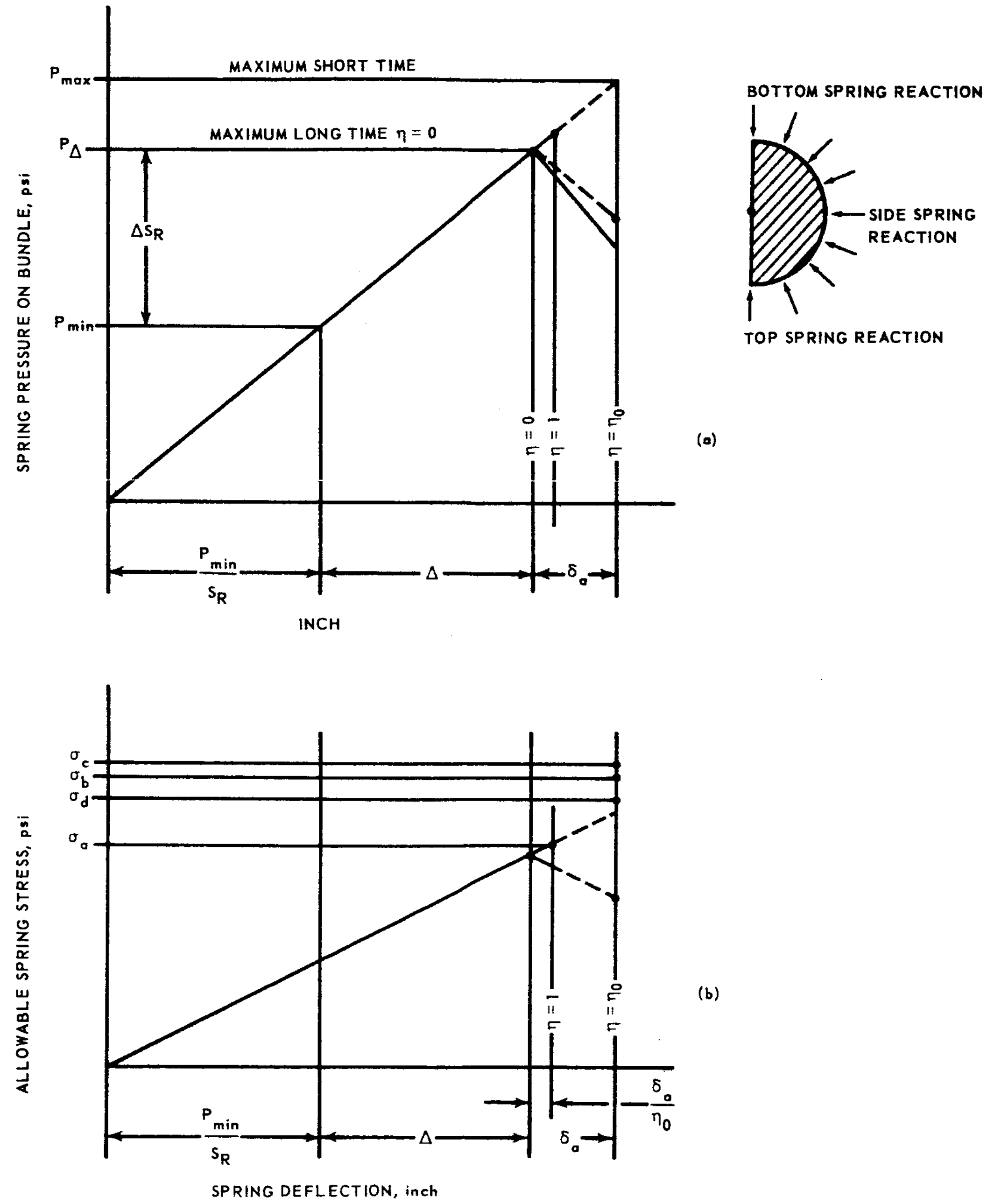

MAXIMUM SHORT TIME
MAXIMUM LONG TIME $\eta = 0$
P_{max}
P_Δ
ΔS_R
P_{min}
SPRING PRESSURE ON BUNDLE, psi
$\eta = 0$
$\eta = 1$
$\eta = \eta_0$
$\frac{P_{min}}{S_R}$
Δ
δ_a
INCH
(a)
BOTTOM SPRING REACTION
SIDE SPRING REACTION
TOP SPRING REACTION
σ_c
σ_b
σ_d
σ_a
ALLOWABLE SPRING STRESS, psi
$\eta = 1$
$\eta = \eta_0$
(b)
$\frac{\delta_a}{\eta_0}$
$\frac{P_{min}}{S_R}$
Δ
δ_a
SPRING DEFLECTION, inch

Fig. 4.6-3 - Desired spring characteristics at operating temperature

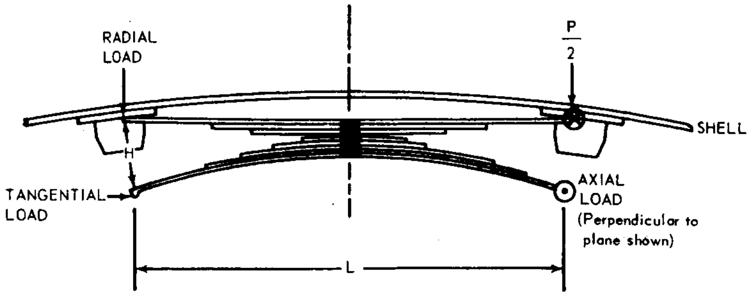

NOMENCLATURE

P - Radial spring load
E - Modulus of elasticity at design temperature
δ_{TC} - Total radial spring deflection
σ_R - Bending stress due to radial deflection
N - Number of leaves
h - Leaf thickness
b - Spring width
L - Effective length
o = Subscript, outer spring set
i - Subscript, inner spring set
H - Spring gap

Fig. 4.6-4 – Leaf spring loads and nomenclature

Radial Loads

Since the two sets of springs are assumed to be symmetrical,

$$\delta_{Tl} = \delta_o + \delta_i$$

$$= \frac{3PL^3}{8Eb\, N_o\, h_o^3} + \frac{3PL^3}{8Eb\, N_i\, h_i^3}$$

Stresses in the leaves of the springs are as follows. For the outer spring,

$$\sigma_{R_o} = \frac{4E\, \delta_o\, h_o}{L_o^2}$$

and, in the inner spring,

$$\sigma_{R_i} = \frac{4E\, \delta_i\, h_i}{L_i^2}$$

Tangential Loads

Tangential loads are encountered as the springs tend to resist bundle movement during accelerational loads. In a hydrostatic system, this is a function of the friction at the ends of the spring as well as its lateral stiffness, as previously shown in Figure4.4-2. In a shear system, the load is guaranteed by shear ties or keys, and the load can be calculated, knowing the shear flow to the periphery. These loads are found by means of virtual-work solutions of the redundant reactions between the springs and their loading points. A typical set of formulae is shown in reference[3] . It should be noted that the spring stresses are reduced proportionally with reductions in the distorting couple caused by the product of the tangential load and the spring gap. Accordingly, optimizing the spring design is favored by minimizing the radial gap.

Axial Loads

The tube bundle shifts in an axial direction relative to the shell to accommodate axial thermal expansions in the tube bundle and/or the supporting structures. These movements are resisted by an axial friction load on the springs, the magnitude of which is determined by the radial pressure and the frictional coefficient. The resultant twisting of the springs may be significant and should be evaluated. For a leaf spring, the friction force on the leaf produces a tipping moment. The latter is carried by a combination of differential bending and torsion in the leaves, and a 10-percent increase in the radial bending stress may be typical. Since the moment arm is again the radial gap, the latter should be kept small. A wider spring (measured axially) also reduces the stresses due to axial forces. A reduction in the frictional coefficient is another obvious solution, but difficult to achieve.

4.6.3 Structural Shell

The outer shell acts to confine the radial support system and the tube bundle. Although the shell can serve as the primary pressure shell, the GE-ANP ceramic systems provided separate shells, thus facilitating remote separation of the reactor from the turbomachinery. The reactor structural shell was cantilevered from the forward or cool end. The mechanical stresses in a shell this size never seem to present major problems since the moment of inertia is sufficiently large to carry the reactor loads with ample margins of safety. Normal shell design can be applied.

Compressive buckling, bending buckling, shear buckling, and external pressure buckling should be investigated during the stability study. Since most of the information relative to cylindrical buckling is empirical and based on test results, and also since information is not available on the buckling of perforated cylinders, a program of model testing to verify the use of Horvay's analysis applied to cylinders is desirable.

The overall weight of the shell may be reduced by using internal stiffening rings. The primary requirement which indicated the use of the stiffening rings in the 140E design was the external pressure load. At certain operating conditions the pressure outside the shell was approximately 40 psi greater than the pressure inside the shell near the aft end. The minimum thickness of a plain cylinder which would remain stable against the external pressure was 0.245 inch. The ribbed shell was 0.125 inch thick and had buckling stability during pressure differentials up to 90 psi.

4.6.4 PRESSURE PADS

Pressure pads are used to distribute the concentrated loads from the radial springs uniformly around the ceramic bundle. Primary loads in the pads are the compression load of the springs and a bending caused by the axial temperature profile in the tube bundle. The loads are not large and the pad is not considered a critical component unless further severe requirements are imposed.

4.6.5 SPRING RETRACTORS AND ADJUSTORS

A means of spring retraction is useful to permit clearance between the radial spring system and the tube bundle during initial assembly; the retractors may again be employed at final remote teardown to release the spring loads in desired increments. They can be designed to provide a window in the shell through which net growth or reduction in the tube bundle diameter may be measured remotely in a hot shop without reactor disassembly. A screwlike device with a built-in locknut is perhaps the most reliable device.

The adjustors are used to compensate for tolerances and variations in the tube bundle and structural shell dimensions, thereby reducing the value of the design Δ. Adjustors are almost mandatory with a hydrostatic suspension since the relatively large radial spring rate is necessarily accompanied by a very short spring travel from minimum pressure to free height. In a pure shear suspension system the adjustors can often be eliminated because of the low radial spring rate.

4.7 DESIGN DETAILS OF COMPONENTS IN THE AXIAL SUPPORT SYSTEM

4.7.1 SIGNIFICANT DESIGN PARAMETERS

Frictional drag of the coolant on the walls of the channels within the many tubes constituting the tube bundle appears as an axial force transmitted to the axial support system. Additional aerodynamic loads due to the differential static pressures acting on the front and rear of the tube bundle also appear as an axial force on the axial support system. Inertial loading is treated as an axial pressure equal to the product of the mass and its acceleration, and uniformly distributed over the tube bundle cross-sectional area.

Differential thermal expansion causes differences in total axial expansion at different radii. As the individual pieces move axially with respect to each other, friction is created and causes redistribution of axial forces. This is especially apparent at the interface between the core and the outer reflector where the reflector temperature changes lag those in the fuel tubes during transients. Peripheral friction opposes relative axial motion between the tube bundle and the radial support springs, especially during transient conditions, and the reaction of this frictional force appears in the axial support system. It is evident, from this standpoint, that frictional forces should be minimized and that a low radial compressive spring force should be used.

Thermal stresses due to the radial temperature profile of the coolant discharge are of extreme importance, and should be carefully analyzed early in the design. The high temperatures associated with a ceramic reactor normally preclude the use of the familiar tube sheet for axial support. High oxidation rates and low tensile properties of the available materials, together with high thermal stresses, are not compatible with high loadings on the plate.

Three types of axial supporting structures are discussed below, as follows:

1. Modified tube-sheet designs wherein the tube sheet is divided into sectors and is internally cooled
2. Small retainer plates individually supported by axial tension rods
3. Dome, or Roman arch, structures in compression

4.7.2 MODIFIED TUBE SHEET

4.7.2.1 Description

This type was used as the aft-retainer assembly in one reactor. It provided longitudinal support of the tube bundle against aerodynamic drag forces, friction, and aft acceleration loads. The assembly consisted of 12 independent 30-degree sectors that were simply supported at the inside radius by the shaft tunnel, and near the perimeter by the rear shield outer section. Individual sectors rather than a continuous plate were chosen for (1) compatibility with available brazing furnaces, and (2) reducing thermal stresses in the structure.

The assembly was a sandwich-type tube sheet having two parallel plates separated by tubes that served the dual purpose of providing shear ties for the plates and passages through the tube inside diameters for tube-bundle discharge coolant. An artist's view of a sector complete with components is shown in Figure 4.7 . Figures 4.7-2 the aft-retainer assembly layout.

Sectors of the assembly were supported and oriented as indicated below:

Location	Relative Motion	Method
Center	Rotation	Keying sector to center hub, and keying center hub to liner
	Radial	Pin-type connection between hub and sector, and hub slides inside liner
	Inertial	Supported by liner
Perimeter	Rotation and displacement due to inertia	Supported in shear by springs and structural shell
	Radial	Radial springs allow differential thermal expansion

The mean temperature of the aft-retainer sectors was controlled by coolant flowing radially inward between the side plates and over the structural tubes. Each of the 12 sectors was a sealed, self-contained unit obtaining its coolant from annular external duct and discharging the coolant at the center hub. Thin 0.010-inch foil, welded along radial edges of each sector, provided a seal for the coolant. Two retractable bellows assemblies per sector formed cooling passages from the external duct to the perimeter of the retainer

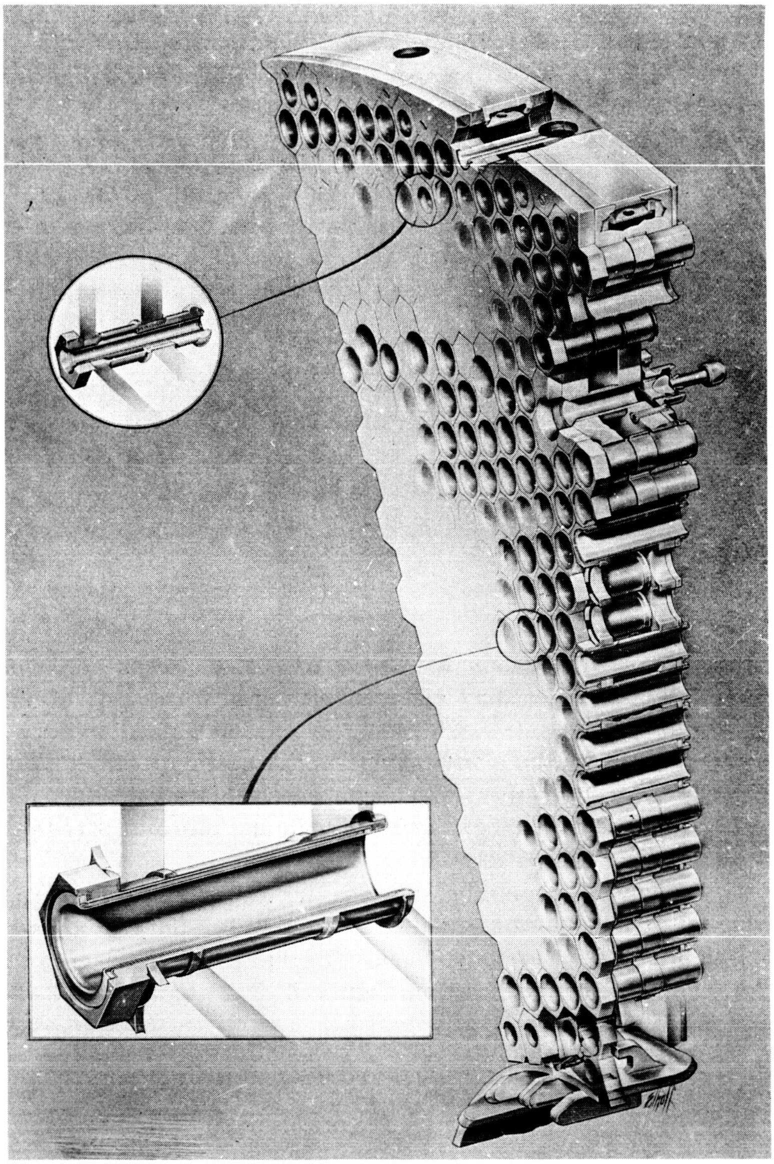

Fig. 4.7-1 – Sector of aft-retainer assembly (Neg. DI-533)

sectors and permitted differential motion between the structural shell and the retainer. A remotely adjustable orifice in each bellows assembly was located just outside the structural shell and regulated the amount of coolant flowing into the sectors.

The outer reactions of the aft-retainer sectors were transmitted to the rear shield outer section through free-swiveling linkages of ball-and-socket design. These linkages permitted radial and tangential differential motion between the rear shield and retainer sectors to allow for differential thermal expansion as well as reactor deflection from inertial loads. Four linkages per sector were located on a chord perpendicular to the center radius to match closely the expected sector deflection, although the worst-case loading assumed that two of these linkages carried the entire sector load. Discharge coolant from the control rod guide tubes maintained the linkage below 1200°F, the design temperature.

All components of the aft-retainer assembly were remotely removable for maintenance following nuclear operation. Handling lugs and data instrumentation lead disconnects were provided.

4.7.2.2 Methods of Analysis

Each sector is treated analytically as a radial beam simply supported with its outer end overhanging its support. The location of the inner support at the tunnel is dictated primarily by the tunnel and liner diameters. The outer support is located to obtain approximately equal stresses due to positive and negative beam moments.

For purposes of gross analysis all stresses are assumed constant about any circumferential section and vary only with radius and loading. The structure is assumed to approach a sandwich concept having continuous shear ties. Secondary bending of the plate induced by the shear ties is negligible because the large tubes are located on close centers. Calculations assume that the plate supports all bending stresses.

To obtain maximum calculated stresses in the perforated plate, a stress concentration factor of seven is used to allow for loss of material as well as the stress concentration at the holes. This factor is conservative when compared with perforated-plate stress enlargement factors presented in reference 1. An experimental stress analysis study, performed by GE-ANPD, also shows that the assumed factor of seven is conservative. Fig.4. 7-4 shows the stress enlargement factor plotted against the ligament efficiency as derived from the experimental program.

The total loading is a function of (1) relative deflections of the supports for the aft-retainer sectors caused by thermal expansion, (2) pressure drop through the tube bundle, (3) inertial loads on the tube bundle, and (4) friction within the tube bundle during deformation. The internal friction varies with the radial pressure on the tube bundle and the coefficient of friction. Analyses of a number of cases are necessary to determine maximum loads and most severe load distributions on the retainer sectors, on the inner support (tunnel), and on the outer support (rear shield). Load cases are selected that were physically possible, and other cases are analyzed for design changes that might relieve loading conditions. The most severe load conditions are established, and the various components are analyzed for these conditions.

An overall "worst-case" condition then is developed for the mechanical design of the sectors. The reasonings and assumptions used to derive the worst case are shown in Figure 4. 7-5 and explained as follows.

Experimental evidence from hot-airflow tests in the three-tier mockup indicated that the tube bundle moves in concentric rings when it deforms under load. For a given radial spring pressure (P_O), coefficient of friction (μ), and length of core (L), the frictional load as any radius may be as follows (Figure4. 7-5a):

$$F = 2\pi r L \mu P_O \qquad (1)$$

For convenience, the pressure drop through the core and the aft inertial load are treated as an equivalent pressure acting on the aft surface of the core. (An aft inertia load of 1 G is equivalent to 3.54 psi pressure on the aft-retainer assembly.) The shear at any radius was equal to the air load on the area inside of that radius, as given by

$$V = \pi P_O (r^2 - r_1^2) \qquad (2)$$

The maximum shear occurs at the outer radius of the tube bundle so that, as the air load increases, the entire tube bundle moves against the retainer sectors, as shown in Figure 4. 7-5b. The inner support is assumed to have deflected aftward away from the retainer. If the air load on the tube bundle (now rigidly supported at the outer support) is further increased, successive slip rings are developed in the bundle as radii are reached wherein shear and friction forces are equal, Figure4. 7-5c. The retainer then acts as a cantilever fixed at the outer support and loaded as shown in Figure4. 7-5d. The friction at the outside radius of the tube bundle and the air load on the bundle outside of the outer support

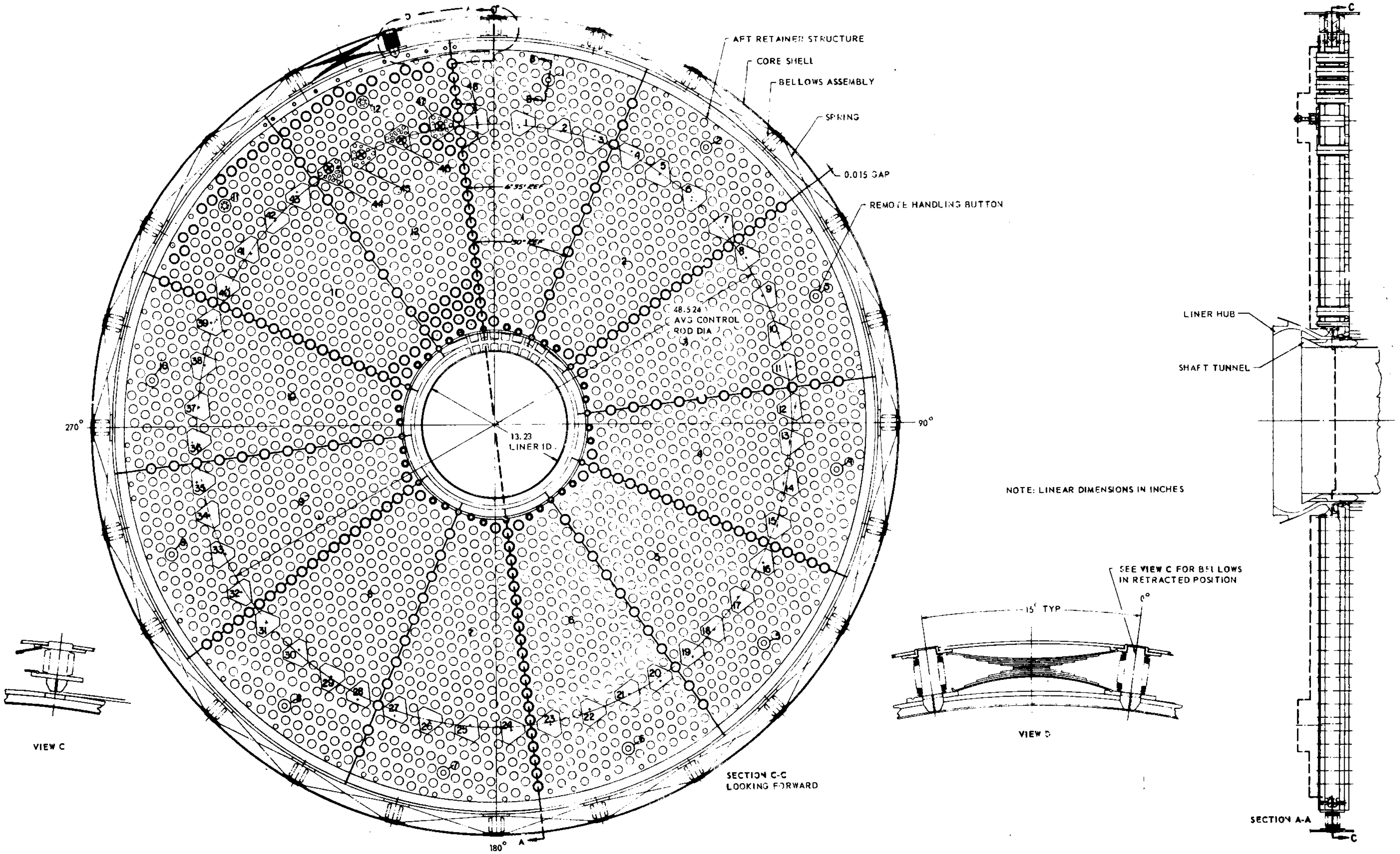
AFT RETAINER STRUCTURE
CORE SHELL
BELLOWS ASSEMBLY
SPRING
0.015 GAP
REMOTE HANDLING BUTTON
48.524
AVG CONTROL
ROD DIA
13.23
LINER ID
270°
90°
180°
A
SECTION C-C
LOOKING FORWARD
VIEW C
15° TYP
0°
SEE VIEW C FOR BELLOWS
IN RETRACTED POSITION
VIEW D
NOTE: LINEAR DIMENSIONS IN INCHES
LINER HUB
SHAFT TUNNEL
SECTION A-A
C

Fig. 4.7-2-Layout of an aft-retainer assembly

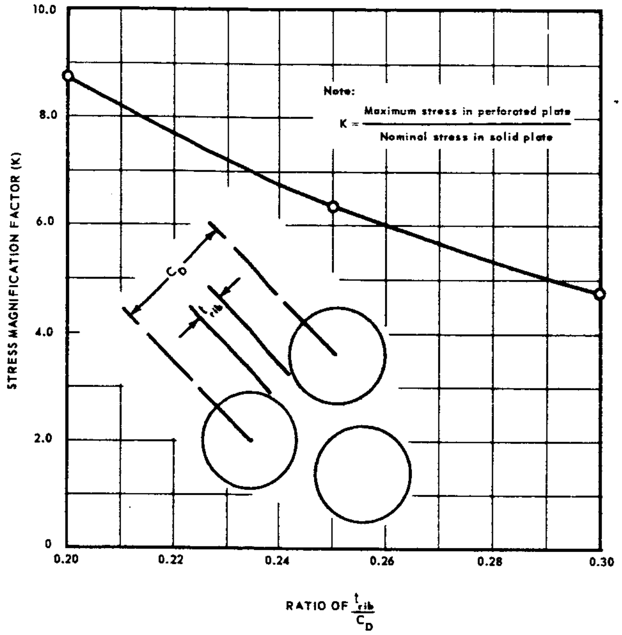

Fig. 4.7-4 – Stress enlargement factor for maximum stress in a perforated plate

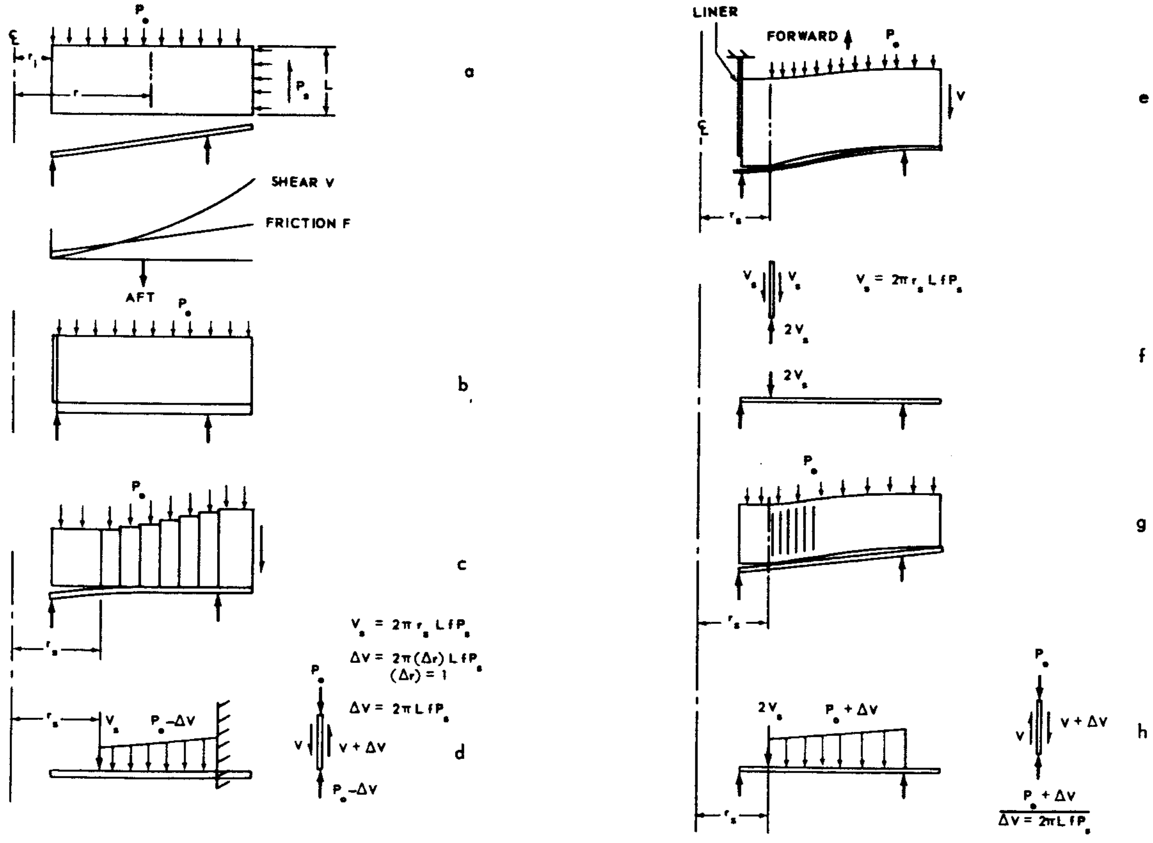
P_e
℄
r_i
r
P_s
L
a
SHEAR V
FRICTION F
AFT
b
c
r_s
V_s
$P_e - \Delta V$
$V_s = 2\pi r_s L f P_s$
$\Delta V = 2\pi(\Delta r) L f P_s$
$(\Delta r) = 1$
$\Delta V = 2\pi L f P_s$
V
V + ΔV
$P_e - \Delta V$
d
LINER
FORWARD
V
e
V_s
$2V_s$
$V_s = 2\pi r_s L f P_s$
f
g
$2V_s$
$P_e + \Delta V$
V + ΔV
$\frac{P_e + \Delta V}{\Delta V = 2\pi L f P_s}$
h

Fig. 4.7-5 – Aft-retainer-plate loading analysis

serve to keep the retainer sectors in equilibrium. This loading condition is then investigated for several air loads (long and short time), and for the effects of varying the radial pressure.

After the condition shown in Fig.4.7-5d is reached, the inner support is assumed to move forward again (due to changes in temperature) and forces the retainer against the deflected shape of the core, Fig.4.7-5e. The liner is assumed to be forward against its stop so that friction to resist motion of the core is developed on both the inside and outside radii. Initially, the sectors touch the tube bundle and develop a concentrated load equal to twice the frictional load on a single row of tubes, Fig.4.7-5f. As the inner support continues to force the sectors forward, successive slip rings develop in the tube bundle as shown in Fig.4.7-5g. The outer support deflects sufficiently to keep the sectors from picking up a balancing moment from the core and becoming a simple support. The limiting load case is shown in Fig. 4.7-5h wherein the sector is loaded by a concentrated load of 2 V_S plus a distributed load applied between the area of 2 V_S and the outer support. Again, this condition is examined for (1) varying positions of the concentrated loads, (2) several air loads, and (3) the effect of varying radial pressure.

The structural integrity of the retainer sector is dependent on the stress-rupture strength of the structural material; accordingly, the total life is calculated for a composite mission. Considering the design, a maximum hot spot temperature was assumed to exist over the entire life of the component, and occurred at a hot channel whose radial position was unknown and whose width could extend over an entire circumference. Since a maximum possible loading condition on the retainer also occurred as a ring load, the locations of maximum stresses and temperatures could have been coincident. The maximum loads were combined with the appropriate maximum temperatures and time deviations to produce the equivalent life for a particular portion of the operating profile. A summation of these equivalent life spans then was compared with material properties for compatibility.

Several operating conditions were lumped together for ease in design. These conditions represented a worst-case operating condition as shown below.

Condition	Retainer Loading, psi	Time At Load, hr	Equivalent Life Versus Condition 1	Allowable Stress, psi	Percent Of Equivalent Life
1	12	905	905.0	9,000	12.8
2	35	0.1	31.8	26,300	0.5
3	27	75	5,900.0	20,200	83.4
4	19	20	237.0	14,250	3.3
Totals		1,000.1	7,073.8		100.0

When calculating tube stresses, the small change in shear across the diameter of the tube ends is neglected. The shear stress in the brazed joints is considered to be distributed the same as that due to tube bending. In addition, a factor of two is applied to the braze stress to cover the uncertainty of braze penetration at the worst location.

4.7.2.3 Thermal Insulation

Thermal insulation is used to isolate the retainer sectors from their surrounding sources of heat. The insulation consists of (1) a zirconia spacer on the forward face, (2) an insulating tube within the structural tubes, and (3) a Thermoflex blanket on the aft surface. The hexagonal-shaped zirconia spacer also transmits compressive forces from the tube bundle transition pieces to the aft-retainer assembly. A shoulder on the zirconia spacer rests in a countersunk hole on the face of the retainer sectors, and resists frictional loads arising from differential thermal expansions of the tube bundle and the retainer sectors.

The insulating tube is a self-contained unit made from a tube of high density insulation (24 lbs/ft^3 Johns Manville Company Thermoflex) sandwiched between two metallic foils. The inner foil is a 0.008-inch seamless tube while the cover sheet is a 0.002-inch foil wrapped around the outer surface of the insulation. Aft drag loads on the tubes are transmitted by a forward ring welded to the sheathing foils. The resultant load on the tubes is less than 1 pound per tube. Several 0.03-inch diameter holes are provided in the inner and outer sheaths to prevent external collapsing air-pressure loads as might occur during a sudden depressurization caused by an engine stall or scram.

Those tubes carrying core discharge-air are made of palladium - 10 percent rhodium with an outer foil of palladium. Tubes used in the outer reflector region are exposed to relatively lower temperatures (<2000°F) and are made from Inco 702.

Insulation on the aft face of the retainer is fabricated from a 0.10-inch thick blanket of high density Thermoflex and a 0.025-inch cover sheet made of Inco 702. Each sector has five sections of insulation with overlapping edges on its back surface, and held in position by cylindrical clips welded to the protruding structural tubes. Vent holes are provided in the cover sheet to allow for sudden depressurization. Inco 702 is used as the cover material since the design temperature was below 2000°F and tests have indicated that a 0.02-inch thick foil of Inco 702 operates at least 1000 hours without detrimental oxidation if kept below 2000°F.

Design details of the insulation are contained in reference 68.

4.7.3 SMALL RETAINER PLATES INDIVIDUALLY SUPPORTED BY AXIAL TENSION RODS

4.7.3-1 Description

A support structure of small retainer plates axially restrained by tension tubes that pierce the tube bundle has been successfully demonstrated. The principal components of the system are the retainer plates, the support tubes, the support tube aft flanges, and the support tube forward extensions. The arrangement of the parts is shown in Figure 4.7-7. The tube bundle region shown in Figure 4.7-7 shows a typical cartridge formed by cementing together the individual tubes associated with each retainer plate for ease of handling during assembly. Prior to final reactor assembly, the cement is burned out and the radial support system maintains the tube bundle integrity.

The primary objective of this method of axial support is to resist axial deformations of the tube bundle by providing a uniform reaction at the aft face of the tube bundle through all operating conditions. At initial reactor startup, the axial pressure forces are resisted by frictional forces from the radial support system, and no aft movement occurs. The tube bundle axial thermal growth, relative to the structural shell, centers around its midpoint. The support tubes are normally unloaded as they approach their design temperatures due to their higher coefficient of thermal expansion relative to the ceramic tube bundle. The total pressure force is proportional to the radius squared and frictional resistance to tube bundle movement is a function of the first power of the radius (as previously shown). Thus, the tube bundle must slip aftward at its outer radius until the retainer plates and support tubes take up the load. If no friction existed in the tube bundle, each support tube would support the uniform pressure load ahead of its retainer plate. High frictional forces between tubes, resulting from the radial pressure, however, cause bundles of many tubes to act as a unit. Since each support tube assumes a slightly different length, a redundant axial structure exists wherein the stresses in each tube are dependent on its deflection.

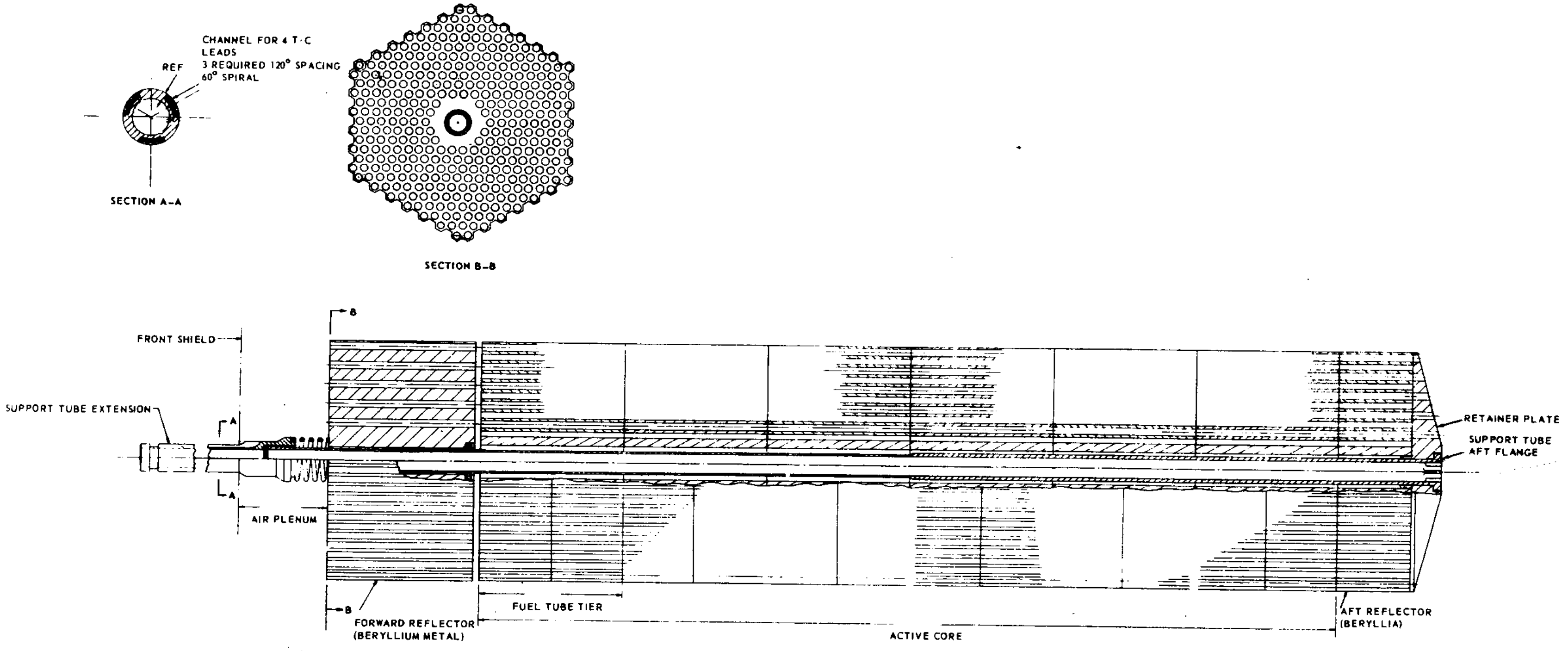

CHANNEL FOR 4 T-C LEADS
3 REQUIRED 120° SPACING
60° SPIRAL
REF
SECTION A–A
SECTION B–B
B
FRONT SHIELD
SUPPORT TUBE EXTENSION
A
A
AIR PLENUM
B
FORWARD REFLECTOR (BERYLLIUM METAL)
FUEL TUBE TIER
ACTIVE CORE
AFT REFLECTOR (BERYLLIA)
RETAINER PLATE
SUPPORT TUBE AFT FLANGE

Fig. 4.7-7 – Axial support system using small retainer plates and axial tension rods (Dwg. 139R851)

Further changes in the incremental lengths of the support tubes may be caused by manufacturing tolerances and temperature profiles through the tube bundle.

During engineering tests, typical maximum mismatched strains for Inconel X support tubes were approximately 0.12 percent. An initially short tube will stretch to the maximum mismatched strain before the bulk of the tension tubes begin sharing the load. If the tube bundle remains undistorted, the short tube will continue to deflect until its total strain includes the deflection aftward of the tube bundle due to the spring rate of the integrated support system. The additional strain on the short tube can be estimated from the allowable stress in the average guide tube divided by the modulus of tensile elasticity of the metal at operating temperature. Any plastic strain occurring in the average loaded support tube would permit further bundle movement and consequently add to the total strain in the short tube. Thus, the tensile unit stress in the shortest, and probably coolest, support tube can be found by multiplying the total strain by the modulus of elasticity. The short support tube, having a deflection limit, experiences a decrease in load and stress as the plastic strain increases and cycling of the pressure load will not change this condition. The assumption is made, of course, that the frictional force does not approach zero due to vibrational excitation - numerous vibration tests at GE-ANPD have validated this assumption.

However, the load resulting from the mismatched strain in the short tube will usually be capable of distorting the aft face of the tube bundle with a hexagonal column of tubes the size of the hexagonal plate being displaced forward the distance of the initial mismatch. Consequently, the load in the short tube is reduced to equal the frictional force preventing the hexagonal column from further movement. This frictional force equals the column surface area times the pressure loading on this surface times the actual coefficient of friction.

A load-relief device may conveniently be placed in series with the support tube to prevent axial distortion of the tube bundle to assure almost equal loads on all retainer plates to equalize the loads and unit stresses among the support tubes, and to reduce the maximum stress. The force device used at GE-ANPD has been a preloaded spring which begins deflecting when the support tube force exceeds the preload value. Its spring constant, compared to the support tube, is low and the deflection causes a slight but controllable increase in load. The preload is normally set by dividing the total aft force by the number of supporting tubes. As a minimum, the total preload on the tube bundle must exceed the side restraint imposed by the peripheral friction to assure a return of the bundle to its original position during reactor shutdown.

4.7.3.2 Methods of Analysis

Mechanical bending stresses in the retainer plates are approximated by applying a uniform lead on its face that is resisted at the center of the plate by the support tube flange. Using the nomenclature shown in Fig.4.7-9,

$$\sigma_{mech} = \theta \frac{PR^2}{t^2} \frac{1}{\eta}$$

where

P = unit pressure

t = thickness of plate adjacent to center hole

η = ligament factor, $\frac{S - D}{S}$

θ = stress constant shown in Figure 4.7-10

A more rigorous solution may be used to calculate the theoretical mechanical stresses by dividing the plate into several concentric rings, calculating the rotation of each ring due to moments, loading, and applied loads, and then equating the rotations at each boundary. Having done this, there are n simultaneous equations in n unknowns to be solved, wherein

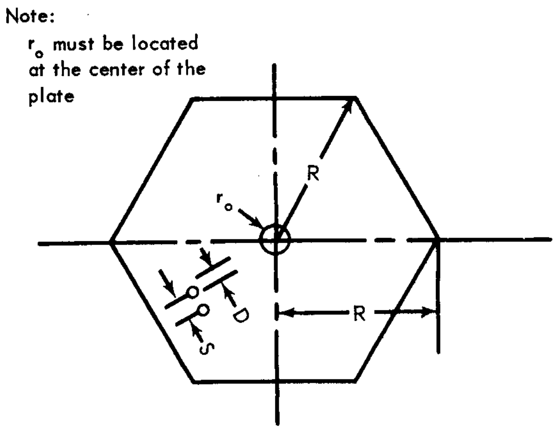
Note:
r_o must be located at the center of the plate
R
r_o
D
S
R

Fig. 4.7-9 – Nomenclature for small retainer plate stress analysis

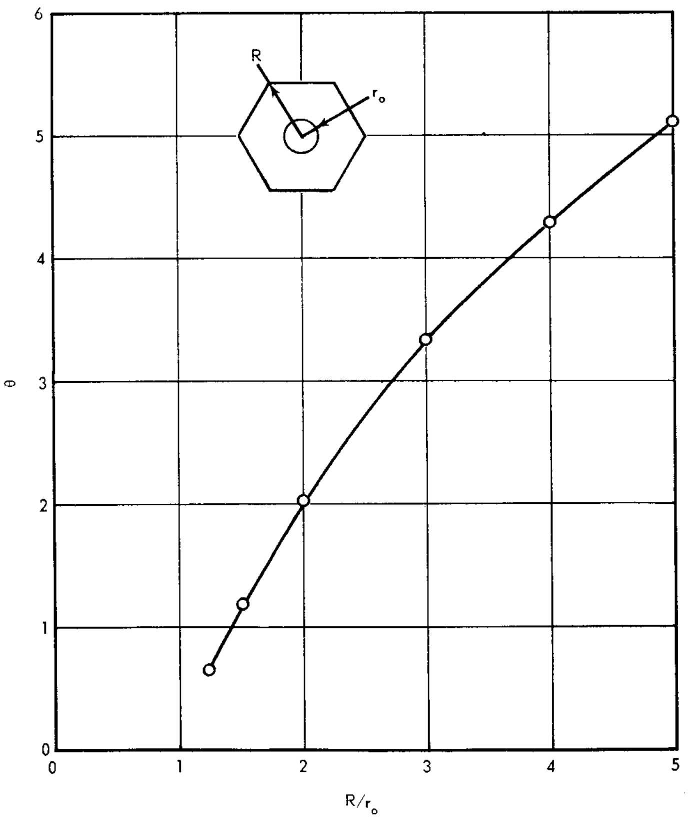

Fig. 4.7-10 – Stress constant used for calculating bending stresses in a small retainer plate

Fine Temperature Gradients

This temperature gradient is manifested by a depression in temperature at the center of the plate due to the cooler support tube flange. Theoretical thermal stresses are calculated using Computer Program 311, "Thermal Stresses in a Hollow or Solid Disc." The solution requires that two computer runs be made, one for the inner solid portion of the plate and the other for the outer perforated area, as required to satisfy the input data requirements of the program for material properties. These two solutions are then superimposed, with certain refinements, to obtain a complete solution.

4.7.3.3 Results of Full Scale Mockup Tests

Both axial static pressure tests and gas dynamics tests were conducted on a three-tier mockup in which the tube bundle was 56 inches in diameter and 14.5 inches long; Figure 4.7-8 shows the retainer plate pattern used in the mockup. The static tests simulated air drag loads on the tube bundle by application of hydrostatic pressure on a neoprene diaphram on the forward face of the tube bundle with the load being absorbed by retainer plates supported from the rear by support columns.

Some conclusions reached as a result of these tests are as follows:

1. The preload in the longitudinal force device should be large enough to prevent gross movement under maximum loads.
2. Retainer plate loads should be absorbed by support tubes placed at the center of pressure of the plate. Eccentric loadings will produce a moment which may cause axial displacement of tubes.
3. The tube bundle slips aft as a unit and returns to its initial position. The average coefficient of friction is 0.3 at the time of slip at the periphery of the tube bundle.
4. The core acts as a unit and continues to function even with the loss of several retainer plates. During the course of testing, up to 19 of the core plates were backed off without disturbing the bundle integrity. Friction distributed the aft load to the remainder of the plates and the aft face remained plane. It should be noted, however, that a few loose reflector tubes might be lost with the loss of a retainer plate, but that the loss of tubes is limited and not progressive. This self-healing feature of a tube bundle is a worthwhile design tool.
5. Temperature cycling does not cause radial displacement of the bundle centerline with respect to the shell and the tube bundle does not settle in the shell.
6. The rear face of the tube bundle remains plane with the exception of the reflector area where slip occurs. Sliding is normally expected between the two outermost rows of tubes where the ratio of axial force to peripheral friction force is highest. During these tests, however, the slip pattern was jagged and extended up to 2 inches toward center. One explanation is the non-uniformity in size between the reflector bars and the fuel tubes. The average across flats dimension of the bars was only 0.365 inch compared to 0.372 inch for the tubes. Radial arches in this vicinity also may have contributed to the discontinuity. A second possible explanation was the eccentric loading required on many of the reflector retainer plates. The eccentric loading consequently permitted the outer plates to tilt and introduced high radial loads as mentioned in item 2, above.

4.7.4 DOME, OR ROMAN ARCH, STRUCTURES IN COMPRESSION

To reach its full potential, a ceramic reactor operating in an oxidizing atmosphere must eventually receive axial support from ceramic or refractory materials. Since these materials are inherently sensitive to tensile stresses, an arch structure composed of small ceramic blocks loaded in compression appears inevitable. Several geometric and material variations have been proposed at GE-ANPD, and one promising type, the ceramic dome assembly of interlocked tubular shapes, is briefly discussed.

the unknown quantities are the unknown moments. After solving for the moments, the stresses are obtained by use of appropriate formulae.

Two types of thermal stresses should be evaluated, those due to the gross radial temperature profile of the coolant leaving the tube bundle, and those due to the fine temperature profiles in the plates caused by the cooling effect of the support tube flanges.

Gross Temperature Gradients

The region of the aft retainer plates most strongly influenced by these gradients lies at the interface between the core and the outer reflector since the outer reflector is normally strongly overcooled temperaturewise relative to the fuel elements.

Three design guides for reducing these stresses are worth mentioning. First, it may be desirable to use separate retainer plates for the outer reflector, and, by the proper arrangement of support tubes, the retainer plates can be unitized at the knee of the temperature curve, approximately one inch outside of the interface. Secondly, the radial temperature profile of the coolant leaving the reflector region may be linearized. Thirdly, outer reflector coolant temperatures may be increased if several components of the radial support system are thermally isolated from other sources conducting heat into the region.

The following equation is used for estimating the thermal stresses in a regular polygonal plate due to a one-dimensional parabolic gradient:

$$\sigma_{th} = \gamma E \alpha \Delta T$$

Values of the stress factor γ are shown in Fig.4. 7-11 for regular polygons of N sides. These data are derived from the clamped-plate analogy method described in reference 2. The curves shown were derived from two points (values for γ for triangles and squares) and the fact that the slope of the curve must be zero for a circle. The indicated value for the hexagonal geometry is 0.26; a photoelastic study yielded experimental data that agreed within 5 percent of this value.

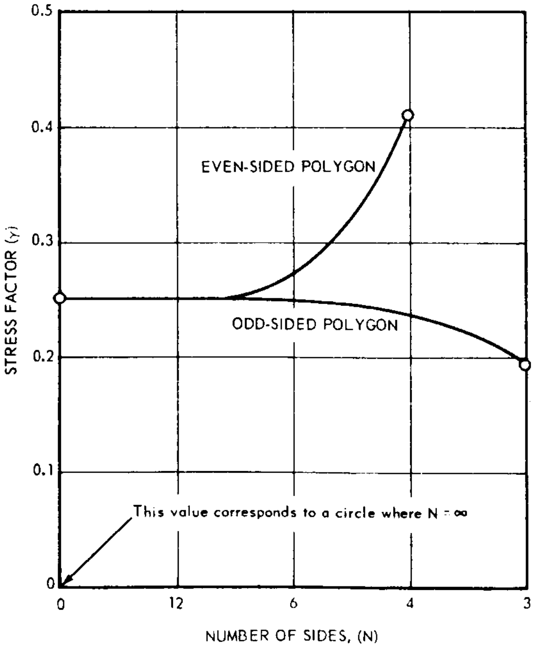

Fig. 4.7-11 – Thermal stress factor for approximating thermal stress in polygons with a one-dimensional parabolic thermal gradient

The dome is built up of a bundle of hexagonal tubes whose across flats dimension is larger than that of the fuel tubes. Coolant discharged from several channels is combined in a transition piece and flows aft through a matching channel in the dome pieces. Axial pressure, inertial, and friction forces are transmitted to the face of the dome tube bundle, and appear either as a uniform pressure, or as distinct rings whose maximum load is friction-limited through slippage. At the perimeter of the assembly, the drag loading and thrust is transmitted to a reinforced ring on a structural shell through linkage bars which permit differential radial expansion between tube bundle and shell. Under zero drag load conditions, the integrity of the structure is maintained by radial springs similar to those surrounding the tube bundle. Misalignment of channels is virtually eliminated by overlapping the tubes throughout the aft structure.

Shear is transmitted tube-to-tube within the dome by interlocking rabbet joints or similar devices. Friction between the tubes not only augments the load-carrying ability but also assists in maintaining dome integrity in the event of a local failure. In addition to giving fewer parts, using larger tubes in the dome results in thicker walls and a greater freedom in the design of the interlocks. Although thermal stresses in the wall increase with increasing wall thickness, the comparatively low rate of secondary heating in this region permits considerable latitude in the design.

Several critical areas must receive careful design treatment:

1. The differential expansion between the ceramic assembly and the shell, together with the height of the dome, are closely related to the longitudinal displacement required of the bundle relative to its containing shell. Rotation of the linkages requires the reactor to move forward against the frictional resistance of the radial spring system. Startup and shutdown conditions must be carefully evaluated.
2. The radial pressure exerted by the thrust of the arch is inversely proportional to the dome height. Therefore, to maintain stresses in the dome-tubes at a suitable level, the dome height must be minimized.
3. Axial stresses due to mechanical loading in the dome-tubes are probably minor for most designs. Tangential stresses resulting from compressive ring loading may require careful evaluation.

The significant advantages of this type of longitudinal support are as follows:

1. The high temperature capability of ceramics permits full utilization of fuel element capabilities by not limiting coolant discharge temperatures.
2. Building blocks for the dome can be made of neutron reflecting material. However, caution must be exercised to prevent an aft-peaking longitudinal power profile.
3. The relatively low density of ceramic materials reduces internal heat generation; material temperatures will not greatly exceed coolant discharge temperatures.
4. Since high prestress loading is not required, stresses in components are directly proportional to drag loading and maximum material efficiency is obtained.
5. The oxidation resistance of the ceramic materials is good, thus eliminating the necessity to develop coatings.

All fabrication techniques required to produce the ceramic pieces required in current versions of the dome are known, and further development is not required.

4.8 General Comments on Techniques of Reactor Handling

The following general comments are applicable to the tube bundle reactor concept, but, with proper interpretation, they may also be applied to other ceramic reactor concepts.

A system of reducing the many thousands of small pieces to a relatively few, easily handleable subassemblies is almost mandatory. Of particular merit is the cartridge assembly method wherein an adhesive is used to bind a number of the small ceramic elements into a manageable group with the adhesive being removed after the tube bundle is assembled. At GE-ANPD, the bundle is divided into a pattern of cartridges of quasi-hexagons, each perhaps six inches across flats and running the full ceramic tube bundle length, including any transition pieces. Fixtures are used to initially orient the ceramic elements and a color coding system similar to that used for electrical resistors is used to identify individual pieces. Glue, applied as a 0.1-inch wide band at tube ends, holds the subassembly together during inspection, handling, shipping, and assembly procedures. The cement represents a minute portion of the tube bundle volume ($< 0.05\%$); and the effect on the subcritical multiplication constant is negligible. Tolerance stackup because of the cement is negligible, but fixtures must be used to assure proper mating of adjacent cartridges. A cement with a low volatizing temperature and leaving a minimum of residue is used; isobutylmethacrylate represents an acceptable cement. Following cement burnout, the subassembled cartridges lose their identity and the tube bundle is fully unitized.

Cartridges of single element length are shown in Figure 4.8-1 prior to cement removal. Figure 4.8-2 shows the same mockup after heating to approximately 600°F. Note that the subassemblies are no longer apparent due to disappearance of the adhesive. A three tier tube bundle assembly prior to glue burnout is shown in Figure 4.8-3. Other photographs of this reactor mockup were shown previously.

The initial reactor loading is accomplished from the center radially outward using standard critical experimental procedures. Each cartridge contains boron steel wires to poison out the reactivity as it is loaded into the assembly. The system contains a sufficient number of poison wires so that control rods are not required even when the reactor is fully assembled.

A disadvantage of the tube bundle reactor is the inability to remotely replace the fuel elements. In fact, maintenance is limited to the axial retainers and control rods since the reactor is accessible only from the ends. Inspection ports may conveniently be provided for possible visual inspection of a portion of the face of the ceramic bundle. Ports may also be provided in the structural shell for measuring bundle dimensional changes following operation.

Criticality hazards affecting disassembly procedures are (1) the possibility of inadvertently achieving criticality in the reactor assembly at the beginning of disassembly by accidental premature removal of the transport rods and (2) the possibility of storing either virgin or spent fuel element and moderator pieces in an arrangement that could achieve dry criticality. Experiments to determine the density of beds of randomly packed fuel elements indicate that the inherent void fractions are high enough to preclude dry criticality. However, it is possible to obtain a dense, systematic packing that has a higher multiplication constant than that of the reactor itself. This condition occurs with an assembly in which a large fraction of the solid outer reflector pieces are distributed uniformly within the region of the core. This array has (1) a higher moderator fraction than the unperturbed reactor core and (2) a greater multiplication constant because of the larger core and thinner reflector.

Studies of handling and storage procedures involving fuel elements include criticality considerations of a flood or other incidents by which the fuel elements may become submerged in water. Following reactor disassembly, all ceramic reactor parts normally are stored under water. The fuel elements should be stored in pool containers designed in a manner that limits the number of fuel tubes that can be loaded into any single container. All containers then could be stacked in columns located on racks located in the pool. Precautions of this type are required to prevent a supercritical geometry inadvertently being achieved during storage of spent fuel.

Considerations must be given to decay heating and the radiation environment during the [illegible] disassembly and storage procedures for handling a nuclearly hot reactor; significant criticality hazards may also be caused by improper handling techniques. This subject is discussed in APEX-908, "XNJ140E Nuclear Turbojet."

REFERENCES

1. R. R. Vandervoort and W. L. Barmore, 64th Annual Meeting, American Ceramic Society, New York, April, 1962. (To be published)

2. R. Chang, J. Nucl. Matls. 1, (1959) 174.

3. R. E. Fryxell and B. A. Chandler, Pacific Northwest Regional Meeting, American Ceramic Society, October, 1962. (To be published)

4. F. D. Kingsbury, General Electric, Nuclear Materials and Propulsion Operation, private communication.

5. D. R. Riley, GE-ANPD, Report DC 60-6-40, June, 1960.

6. Timoshenko and Goodier, Theory of Elasticity, 2nd Ed. McGraw-Hill, New York, 1951.

7. J. B. Conway and D. G. Salyards, GE-NMPO, APEX-660, August, 1961.

8. A. S. Thompson, J. Aero. Sciences, 19, (1952), 476.

9. E. Melan and H. Parkus, "Warmespennungen", Springer-Verlag, Vienna, 1953.

10. R. F. Redmond, et al., Battelle Memorial Institute Report (Unclassified) BMI-1422, February, 1960.

11. R. G. Cook, "Gas-Cooled High-Temperature Nuclear Reactor Design Technology", GE-NMPO, APEX-800B, June 30, 1962.

12. Ross, A. L., "Thermal Stress Analysis of Finite Sections", GE-ANPD, APEX-480, January 20, 1959.

13. Ansted, K. B., Cole, J. M., Loehrke, R. I., Ratterman, E., Smith, W. A., and Woike, O. G., "140E Radial Support Structure", GE-NMPO, APEX-733, July 20, 1961.

14. Ratterman, E., "The Dynamics of the D140 Reactor Core Mockup; A Correlation of Experiment and Theory", GE-NMPO, APEX-636, June 13, 1961.

15. Meier, J. H., "Investigation of a Corrugated Shell as an Elastic Support of a Bundle of Rods", GEL, APEX-615, April, 1961.

16. Merrill, G., and Besserer, C. W., Principles of Guided Missile Design, D. Van Nostrand, 1956.

17. Thompson, A. S., and Rodgers, O. E., Thermal Power from Nuclear Reactors, J. Wiley & Sons, Inc., New York.

18. Larson, F. R., and Miller, J., "A Time-Temperature Relationship for Rupture and Creep Stresses," ASME Transactions, Vol. 74, 1952, pp. 765-775.

19. Robinson, E. L., "Effect of Temperature Variation on the Long-Time Rupture Strength of Steels," ASME Transactions, Vol. 74, 1952, pp. 777-781.

20. Boley, B. A., and Weiner, J. H., Theory of Thermal Stress, John Wiley & Sons, New York, 1960.

21. Sokolnikoff, I. S., Mathematical Theory of Elasticity, 2nd Ed., McGraw-Hill, New York, 1956.

22. Garber, A. M., "Aerospace Engineering", Vol. 22, No. 1, 1963, pp. 126-137.

23. Nadai, A., Theory of Flow and Fracture of Solids, McGraw-Hill, New York, 1950.

24. Chandler, B. A., and McConnellee, J. E., "Thermal Stress Evaluation of Ceramic Fuel Elements", To be published.

APPENDIX A

FUEL ELEMENT THERMAL STRESS ANALYSIS

General

This analysis includes only those thermal stresses directly associated with the extraction of power from an individual element in the reactor and the corresponding bench test simulation of this problem. Fuel elements in a reactor will also be subject to thermal stresses from other sources, but these will all be directly related to the detailed design of the particular reactor.

These "other" sources of fuel element thermal stresses are: (1) external constraint of the free thermal deflections of the individual elements and (2) non-uniform temperature distributions associated with asymmetries of the reactor core in the vicinity of an individual fuel element. Thermal stresses of this type are parasitic in the sense that they are not directly associated with the extraction of power from the reactor. Clever design is necessary to minimize and if possible eliminate these parasitic thermal stresses.

The thermal stresses associated with the extraction of power cannot be eliminated, but they can be minimized by use of an optimum geometry for the fuel element. The results of this analysis are presented in a form which should aid the reactor designer in this optimization process.

Elastic Analysis

The basic approach used in this analysis is to calculate the thermal stresses which would exist in an "equivalent" circular tube and then apply "appropriate" correction factors to account for the fact that the actual element has a hexagonal outer surface. The equivalence is based upon having the same cross-section area in both cases and hence the same total power generation for a given volumetric heating rate.

The "appropriate" correction factors are obtained from a finite difference computer solution of the plane strain thermal stress problem for a tube with the same actual configuration as the fuel tube but without a clad at the inner surface.

The equivalent circular tube solution was used because: (1) the finite difference solution is not readily adaptable to the case with a thin clad at the bore and (2) the cost of running the finite difference solution is several orders of magnitude greater than the cost of using the equivalent circular tube approach.

Thermal Stress Analysis of the Equivalent Circular Tube

The solution to the problem of calculating the thermal stresses in a hollow circular tube due to an axisymmetric temperature distribution is readily available in the literature.(6) The solution for the axisymmetric thermal stress problem in a composite circular tube is obtained by using the available solutions for a single hollow tube together with the necessary compatibility and equilibrium conditions at the interface between the clad and the matrix. Using this approach, the resulting thermal stress components can be expressed as the sum of two terms as follows:

$$\sigma = \begin{bmatrix}\text{The stress due to the component's} \\ \text{(clad or matrix) own temperature} \\ \text{gradient.}\end{bmatrix} + \begin{bmatrix}\text{The stress due to the inter-} \\ \text{action forces required to} \\ \text{maintain continuity at the} \\ \text{clad-matrix interface.}\end{bmatrix}$$

$$= \sigma\ (\text{thermal}) + \sigma\ (\text{interaction}) = \sigma_T + \sigma_I \qquad \text{(A-1)}$$

In order to utilize a linearized thermal expansion approach as discussed in appendix B, it is necessary to separate the interaction stresses into two parts.

$$\sigma_I = \begin{bmatrix}\text{Interaction stress due to} \\ \text{the difference in mean tem-} \\ \text{peratures of the clad and} \\ \text{the matrix.}\end{bmatrix} + \begin{bmatrix}\text{Interaction stresses due to} \\ \text{an isothermal temperature} \\ \text{change of the element from} \\ T = T_{REF} \text{ to } T = \overline{T}\end{bmatrix}$$

$$= \sigma_{I1} + \sigma_{I2} \qquad \text{(A-2)}$$

The σ_T stresses for the general case of a long tube of outer radius, B , inner radius, A, and radius to any generic point, r, are given by Timoshenko(6) as:

$$\sigma_{T\theta} = \left(\frac{E}{1-\nu}\right)\left(\frac{1}{r^2}\right)\left[\left(\frac{r^2 + A^2}{r^2 + B^2}\right)\int_A^B \epsilon_T r\, dr + \int_A^B \epsilon_T r\, dr - \epsilon_T r^2\right]$$

$$\sigma_{Tr} = \left(\frac{E}{1-\nu}\right)\left(\frac{1}{r^2}\right)\left[\left(\frac{r^2 - A^2}{B^2 - A^2}\right)\int_A^B \epsilon_T r\, dr - \int_A^r \epsilon_T r\, dr\right] \qquad \text{(A-3)}$$

$$\sigma_{TZ} = \left(\frac{E}{1-\nu}\right)\left[\left(\frac{2}{B^2 - A^2}\right)\int_A^B \epsilon_T r\, dr - \epsilon_T\right]$$

The interaction stresses, σ_I, are obtained from Lame's classical solution for a thick walled tube subject to radial pressure loads at the inner or outer surface as the case may be. (The fuel element in question is actually a thin walled tube. Lamé's solution is used to keep the analysis general.)

For the case of a general tube, subject to both internal pressure, P_i, and external pressure, P_O, the equations are:

$$\sigma_\theta = \frac{P_i A^2 - P_O B^2}{B^2 - A^2} - \frac{A^2 B^2}{r^2} \left(\frac{P_O - P_i}{B^2 - A^2} \right)$$

$$\sigma_r = \frac{P_i A^2 - P_O B^2}{B^2 - A^2} + \frac{A^2 B^2}{r^2} \left(\frac{P_O - P_i}{B^2 - A^2} \right) \qquad \text{(A-4)}$$

σ_z = a constant to be determined by the compatibility conditions at the interface

The boundary conditions are:

$$\begin{array}{llll} \text{at} & r = b & \sigma_r = 0 & \\ \text{at} & r = a & \sigma_{rc} = \sigma_{rm} = P & \\ & & \epsilon_{\theta c} = \epsilon_{\theta m} & \text{(A-5)} \\ & & \epsilon_{zc} = \epsilon_{zm} & \\ \text{at} & r = D_i/2 & \sigma_r = 0 & \end{array}$$

In addition the axial equilibrium condition is:

$$\int_A \sigma_z \, dA = 0 \qquad \text{(A-6)}$$

Combining (A-1) thru (A-6), the interface pressure, P, is obtained as:

$$P = \frac{(a_{22} + a_{12})\,(\bar{\epsilon}_{Tc} - \bar{\epsilon}_{Tm})}{a_{11}\,a_{22} - a_{12}\,a_{21}} \qquad \text{(A-7)}$$

where,

$$a_{11} = \frac{K_c}{E_c} + \frac{K_m}{E_m}$$

$$a_{12} = \frac{\nu_c}{E_c} + \frac{\nu_m A_R}{E_m}$$

$$a_{21} = \frac{2\,a^2\,a_{12}}{a^2 - (D_i/2)^2}$$

$$a_{22} = \frac{1}{E_c} + \frac{A_R}{E_m}$$

$$K_c = \frac{a^2 + (D_i/2)^2}{a^2 - (D_i/2)^2} - \nu_c$$

$$K_m = \frac{b^2 + a^2}{b^2 - a^2} + \nu_m$$

$$A_R = \frac{a^2 - (D_i/2)^2}{b^2 - a^2}$$

$\bar{\epsilon}_T$ = Mean thermal expansion of the component

Substituting this into equations (A-4) and (A-6) yields

$$\sigma_{IZ_c} = \left(\frac{a_{11} + a_{21}}{a_{22} + a_{12}}\right) P \qquad \text{(A-8)}$$

$$\sigma_{IZ_m} = A_R\ \sigma_{IZ_c}$$

Substituting back into equation (A-4) and (A-5) and thence into equation (A-1), yields the complete axisymmetric thermal stress solution for the long composite tube. The resulting principal stresses at the interface and at the surfaces are presented in Table 3*.

The temperature solutions required to complete this analysis are readily available in the literature(8) and hence only a summary of the required solutions is presented in Table 2*. To simplify the application of these solutions, the geometry factors G_1 through G_5 are plotted in Figures 15 through 18.

Appendix D presents a sample problem which illustrates the application of this method of analysis.

Hexagonal Tube Correction Factors

A finite difference solution(10) was used to obtain correction factors to be applied to the equivalent circular tube solution. Denoting these correction factors by H, the stress components in the actual hexagonal tube in terms of the corresponding stress components in the equivalent circular tube may be written as:

$$\sigma = H(\sigma_T + \sigma_{I_1}) + \sigma_{I_2} \qquad \text{(A-9)}$$

The correction factors do not apply to the σ_{I_2} stresses since these are not associated with the temperature gradient through the tube wall. Strictly speaking

---

*In Tables 2 and 3, the notation $G_n(\rho_m)$ is the functional notation meaning G_n is a function of the independent variable ρ_m etc.)

TABLE 2

COMPOSITE TUBE TEMPERATURES

Temperature Difference	Internal Heat Generation	External Heat Flux
$\bar{T}_m - T_b$	$-\dfrac{q'''_m b^2}{k_m} G_2(\rho_1)$	$\dfrac{a q''_a}{k_m} G_3(\rho_2)$
$\bar{T}_m - T_a$	$\dfrac{q'''_m b^2}{k_m} G_1(\rho_1)$	$\dfrac{a q''_a}{k_m} G_3(\rho_1)$
$\bar{T}_c - T_a$	$\dfrac{q'''_m a^2}{2 k_c} \left[(\rho_2^2 - 1) G_3(\rho_4) - 2 R_q G_2(\rho_3)\right]$	$\dfrac{a q''_a}{k_c} G_3(\rho_4)$
$\bar{T}_c - T_o$	$\dfrac{q'''_m a^2}{2 k_c} \left[(\rho_2^2 - 1) G_3(\rho_3) + 2 R_q G_1(\rho_3)\right]$	$\dfrac{a q''_a}{k_c} G_3(\rho_3)$

$$\bar{T} = T_b + (\bar{T}_m - T_b) - \left(\frac{R_A}{1 + R_A}\right)(\bar{T}_m - \bar{T}_c)$$

$$R_A = \text{Area Ratio} = \frac{1 - \rho_3^2}{1 - \rho_1^2}$$

$$R_q = \text{Heat Generation Ratio} = \frac{q'''_c}{q'''_m}$$

$$\rho_1 = \frac{a}{b} ; \ \rho_2 = \frac{b}{a}$$

$$\rho_3 = \frac{D_i}{2a} ; \ \rho_4 = \frac{2a}{D_i}$$

$$G_1(X) = \frac{1}{8}\left[X^2 - 3 - \frac{4 \ln X}{1 - X^2}\right]$$

$$G_2(X) = \frac{1}{8}\left[X^2 + 1 + \frac{4 X^2 \ln X}{1 - X^2}\right]$$

$$G_3(X) = -\left[\frac{1}{2} + \frac{\ln X}{1 - X^2}\right]$$

$X = \rho_1, \rho_2, \rho_3$, or ρ_4 as required

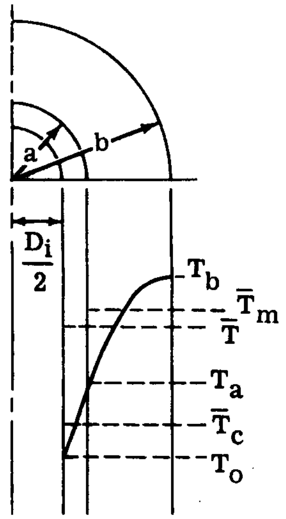

TABLE 3

COMPOSITE TUBE THERMAL STRESSES

Location	Stress ↓	Matrix			Clad		
	Component →	σ_T	σ_{I1}	σ_{I2}	σ_T	σ_{I1}	σ_{I2}
Outer Surface	σ_θ	$\frac{E_m \alpha_m^*}{1 - \nu_m} (\overline{T}_m - T_b)$	$G_4 [L(\rho_1) - 1] P_1$	$G_4 [L(\rho_1) - 1] P_2$	$\frac{E_c \alpha_c^*}{1 - \nu_c} (\overline{T}_c - T_a)$	$- G_4 L(\rho_3) P_1$	$- G_4 L(\rho_3) P_2$
	σ_r	0	0	0	0	$- G_4 P_1$	$- G_4 P_2$
	σ_z	$\frac{E_m \alpha_m^*}{1 - \nu_m} (\overline{T}_m - T_b)$	$G_5 P_1$	$G_5 P_2$	$\frac{E_c \alpha_c^*}{1 - \nu_c} (\overline{T}_c - T_a)$	$- \frac{G_5 P_1}{R_A}$	$- \frac{G_5 P_2}{R_A}$
Inner Surface	σ_θ	$\frac{E_m \alpha_m^*}{1 - \nu_m} (\overline{T}_m - T_a)$	$G_4 L(\rho_1) P_2$	$G_4 L(\rho_1) P_2$	$\frac{E_c \alpha_c^*}{1 - \nu_c} (\overline{T}_c - T_o)$	$- G_4 [L(\rho_3) + 1] P_1$	$- G_4 [L(\rho_3) + 1] P_2$
	σ_r	0	$- G_4 P_1$	$- G_4 P_2$	0	0	0
	σ_z	$\frac{E_m \alpha_m^*}{1 - \nu_m} (\overline{T}_m - T_a)$	$G_5 P_1$	$G_5 P_2$	$\frac{E_c \alpha_c^*}{1 - \nu_c} (\overline{T}_c - T_o)$	$- \frac{G_5 P_1}{R_A}$	$- \frac{G_5 P_2}{R_A}$

$P_1 = E_m[\alpha_m^*(\overline{T}_m - \overline{T}) + \alpha_c^*(\overline{T} - \overline{T}_c)]$

$P_2 = E_m \overline{T}(\alpha_m^{**} - \alpha_c^{**})$

$\rho_1 = \frac{a}{b}$; $\rho_3 = \frac{D_i}{2a}$

$L(X) = \frac{1 + X^2}{1 - X^2}$ (See Figure 19)

R_A = Area ratio $= \frac{1 - \rho_3^2}{1 - \rho_1^2}$

G_4, G_5 - Geometry factors - see figures 17 and 18

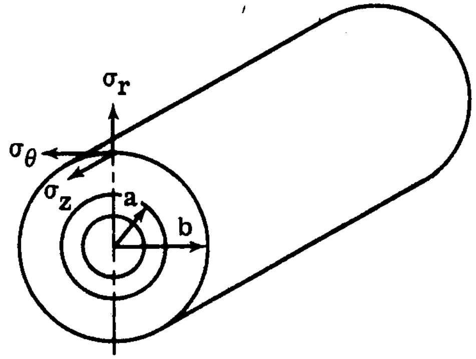

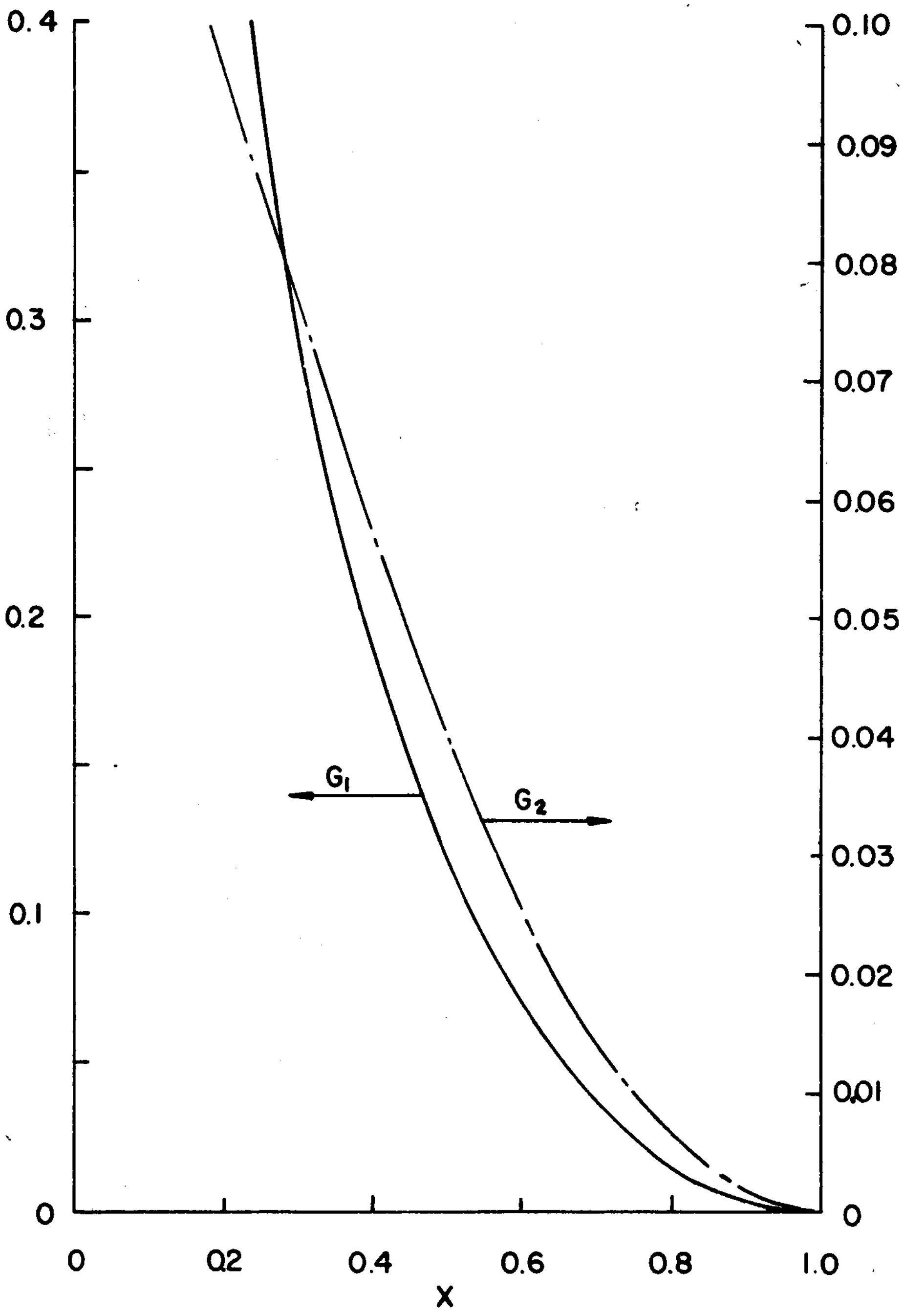

Fig. 15 Internal Heat Generation Case: Heat transfer geometry factors, G_1 and G_2, as a function of the dummy independent variable, X. To obtain more accurate values of G_1 and G_2, use the original equations:

$$G_1(X) = 0.125\,[X^2 - 3 - (4\,\ell n\,X)/(1 - X^2)]$$

$$G_2(X) = 0.125\,[X^2 + 1 + (4\,X^2\,\ell n X)/(1 - X^2)]$$

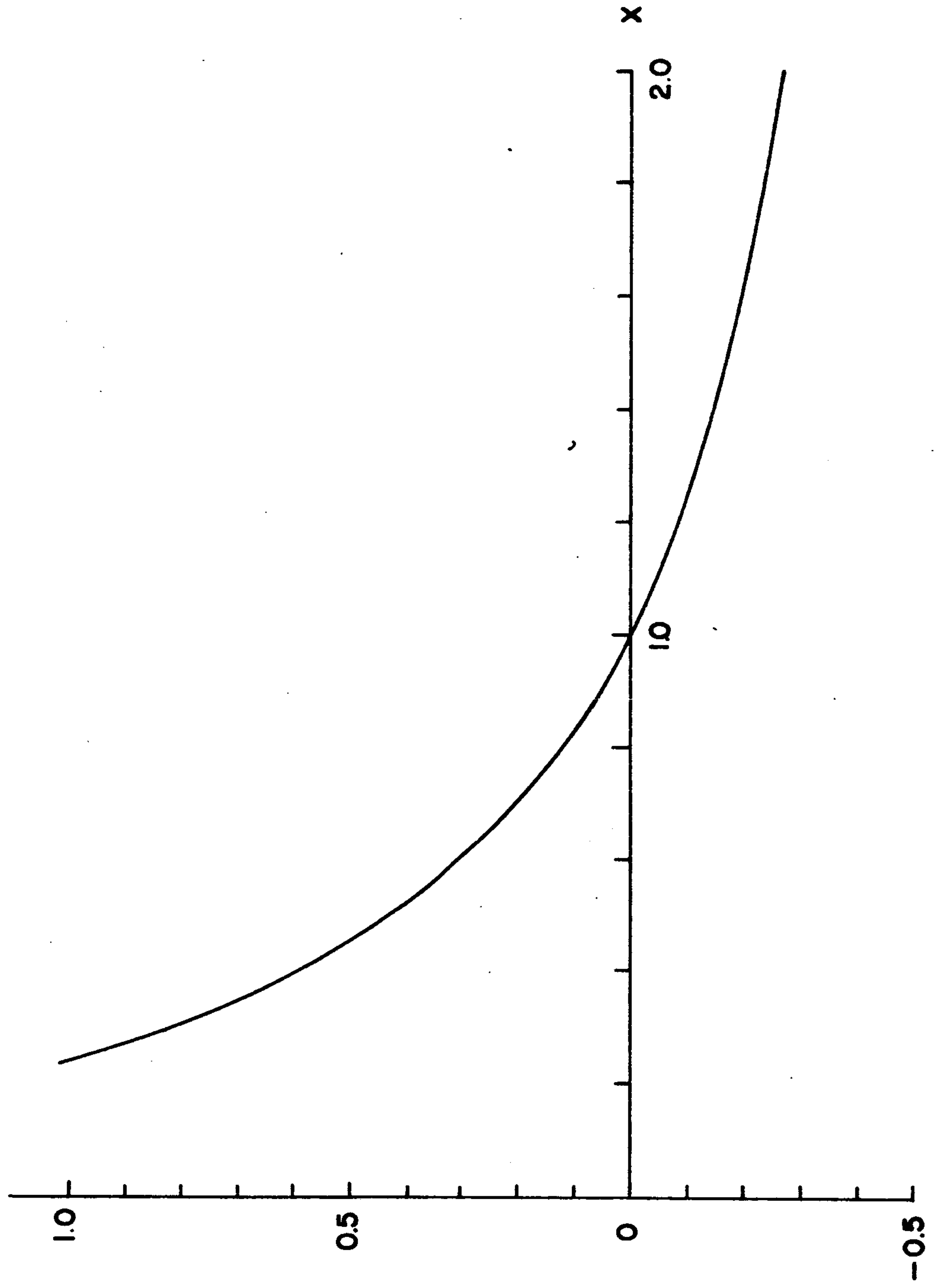

Fig. 16 External Heat Flux Case: Heat transfer geometry factor G_3 as a function of the dummy independent variable, X. To obtain more accurate values of G_3, use the original equation:

$$G_3(X) = -[0.5 + (\ell n X)/(1 - X^2)]$$

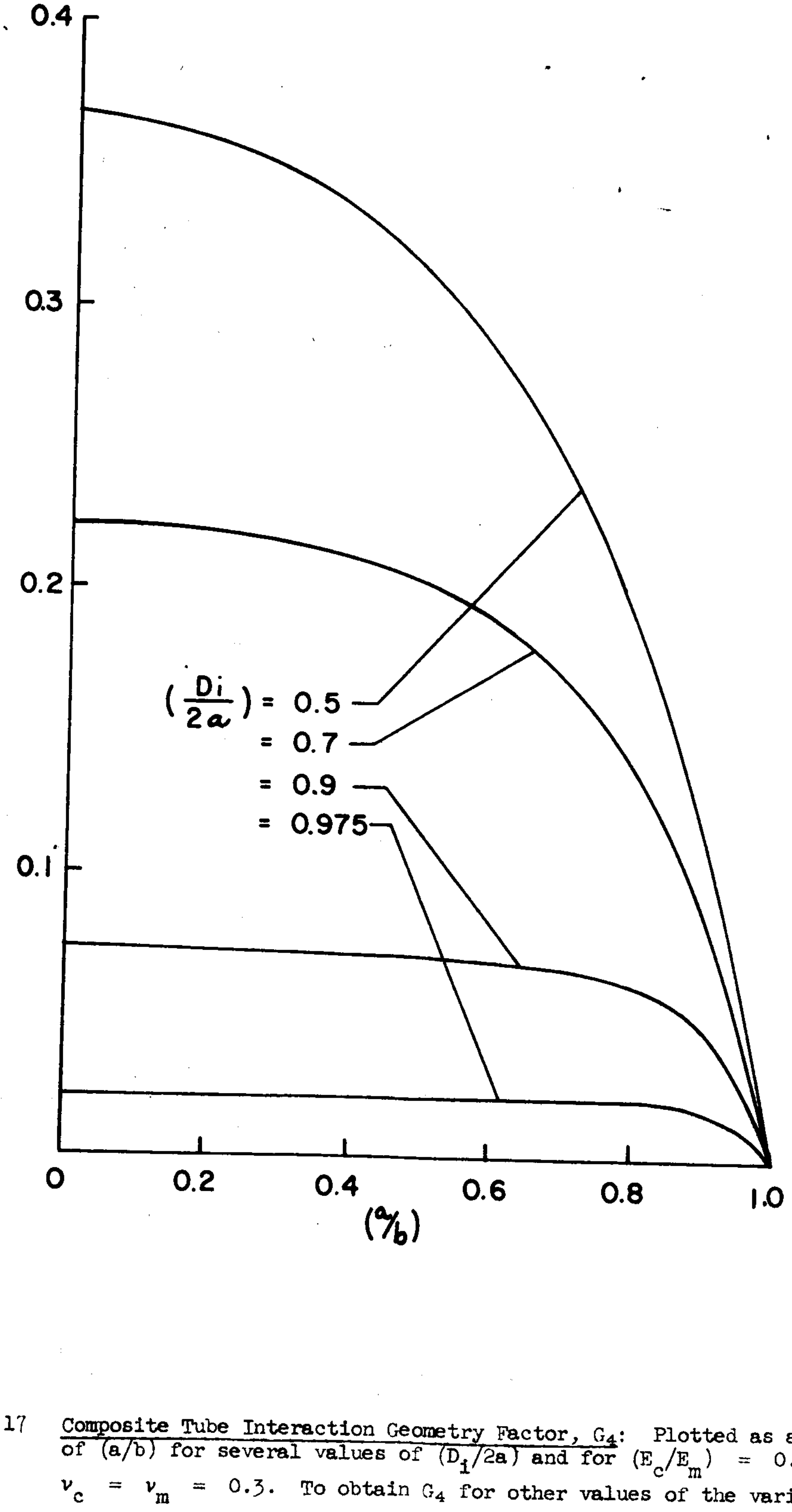

Fig. 17 Composite Tube Interaction Geometry Factor, G_4: Plotted as a function of (a/b) for several values of $(D_i/2a)$ and for $(E_c/E_m) = 0.5$ and $\nu_c = \nu_m = 0.3$. To obtain G_4 for other values of the variables, the original equation is: $G_4 = (a_{22} + a_{12})/[E_m(a_{11}a_{22} - a_{12}a_{21})]$ where the symbols are as defined in equations A-7.

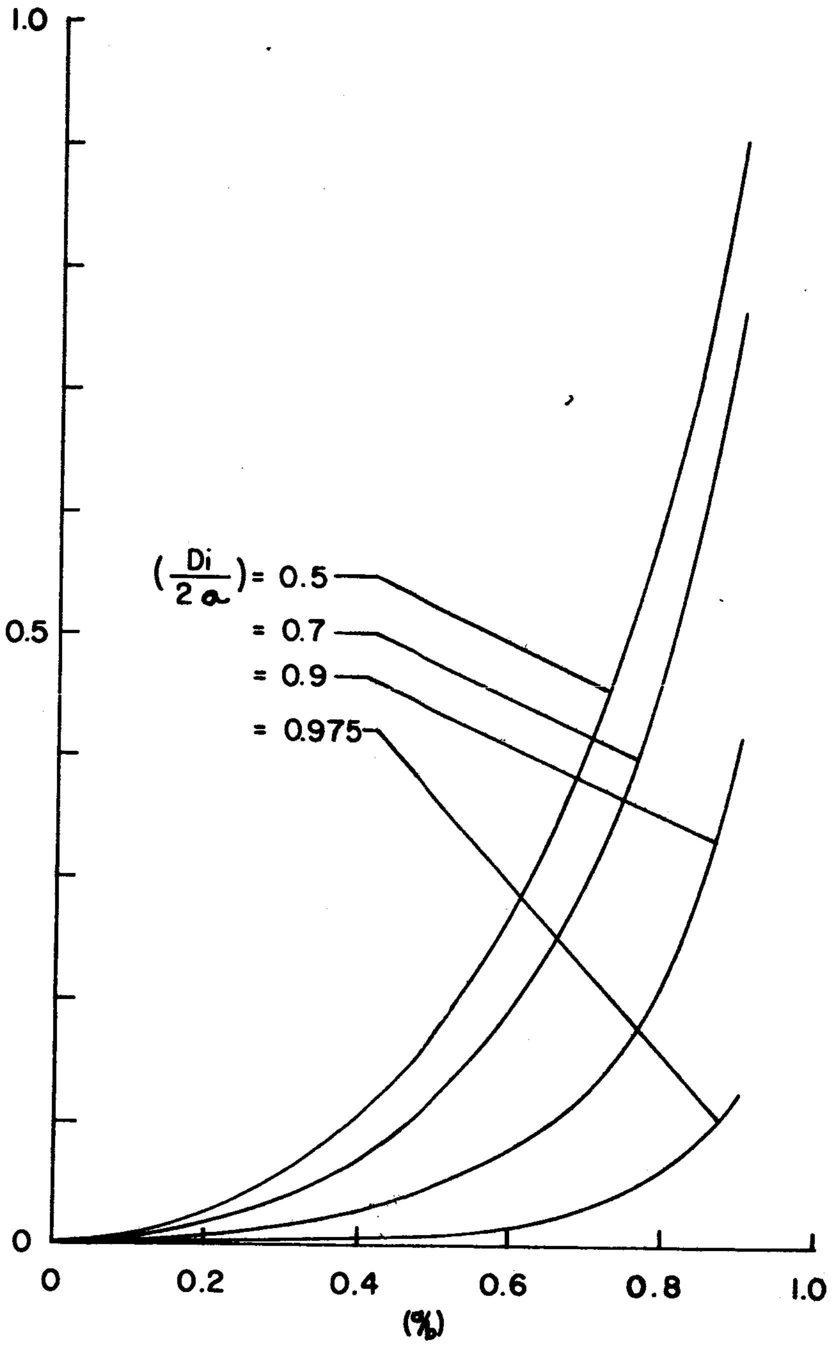

Fig. 18 Composite Tube Interaction Geometry Factor, G_5: Plotted as a function of (a/b) for several values of $(D_i/2a)$ and for $(E_c/E_m) = 0.5$ and $\nu_c = \nu_m = 0.3$. To obtain G_5 for other values of the variables, the original equation is: $G_5 = (a_{11} + a_{21})\, R_A/[E_m(a_{11}a_{22} - a_{12}a_{21})]$, where the symbols are as defined in equations A-7.

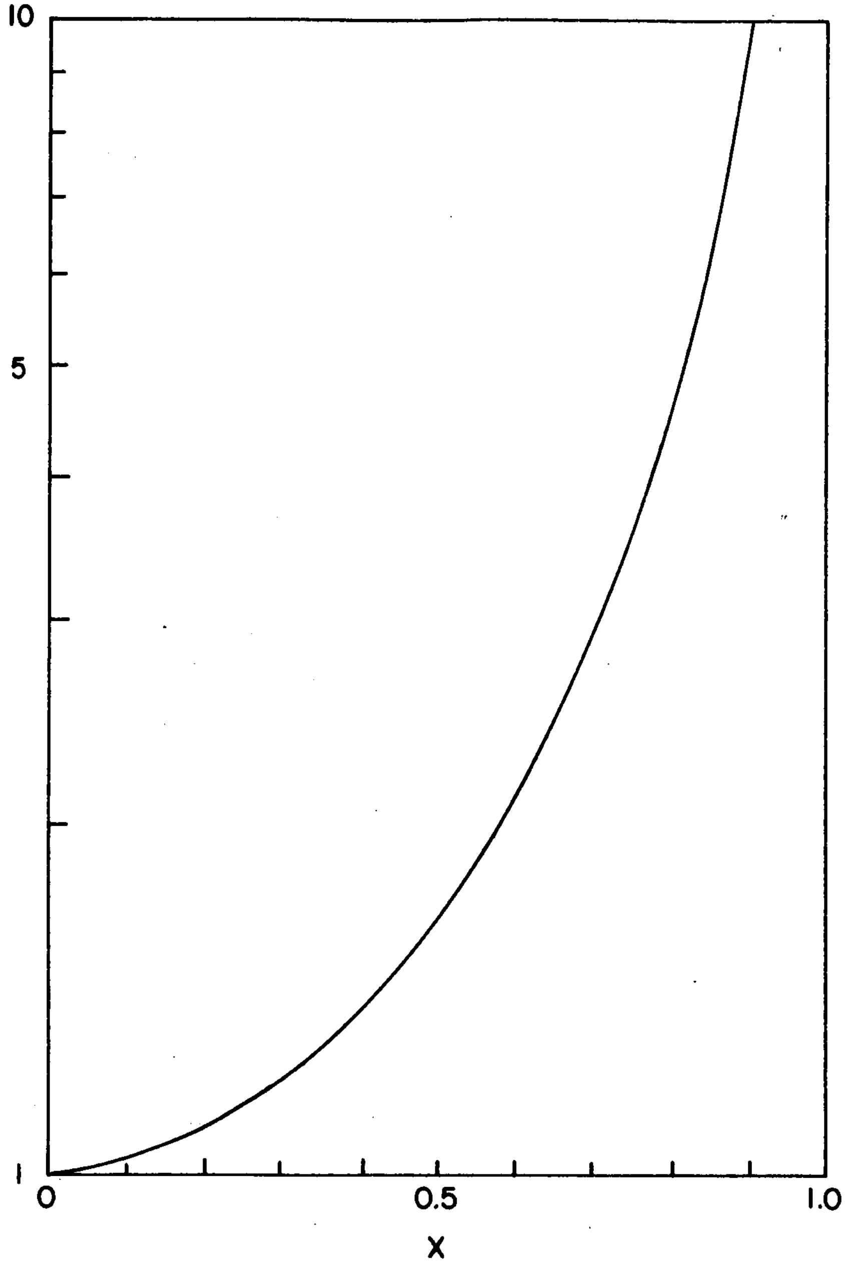

Fig. 19 **Lamé Coefficient, L:** Plotted as a function of the dummy independent variable, X. To obtain more accurate values of L, use the original equation: $L(X) = (1 + X^2)/(1 - X^2)$.

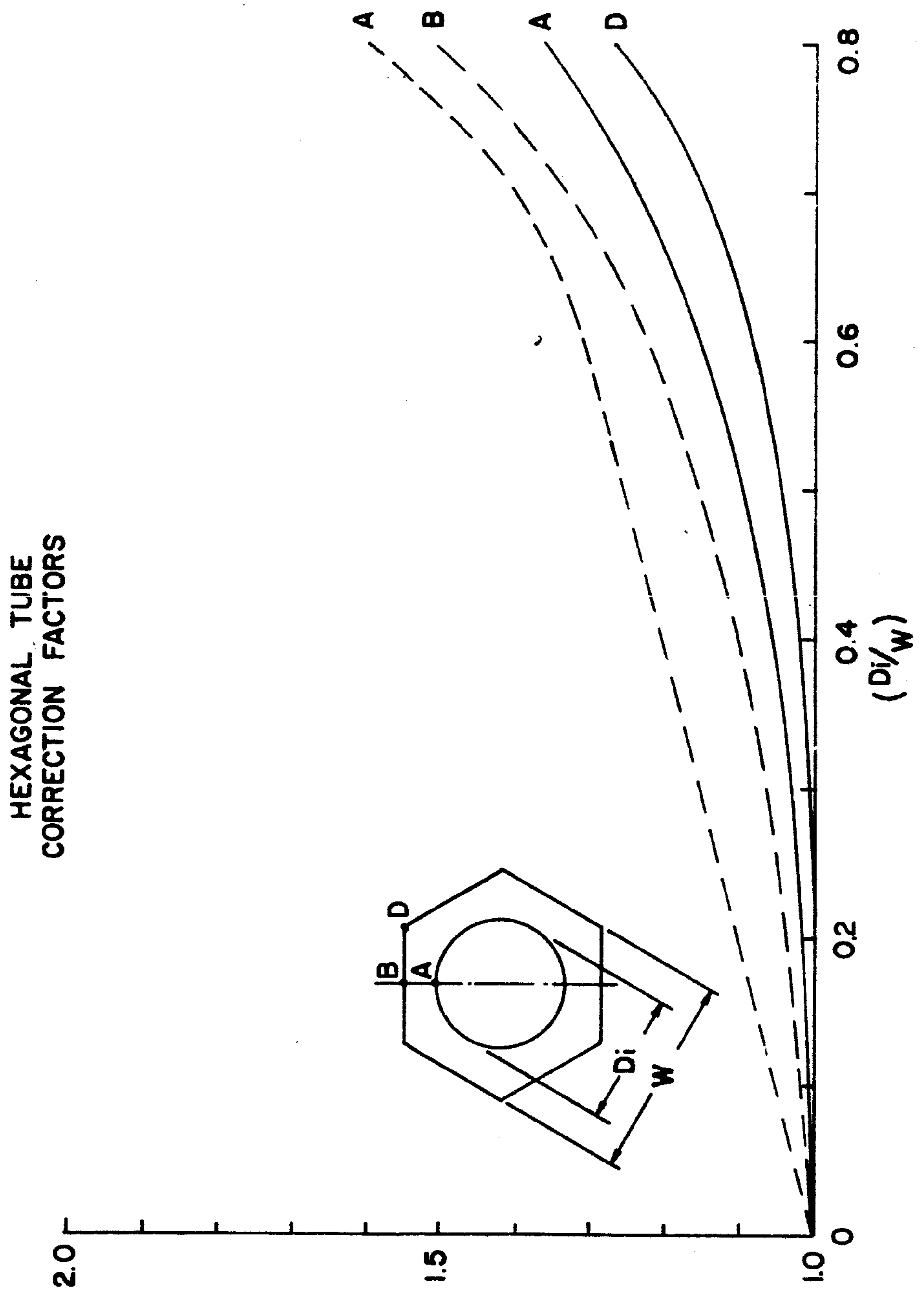

Fig. 20 Hexagonal Tube Correction Factors at the Critical Points: Plotted as a function of (D_i/W) for the case of uniform internal heat generation. The dashed lines are the correction factors for the circumferential stress (σ_θ) at the points A and B. The solid lines are the correction factors for the axial stress (σ_z) at the points A and D.

there should be another correction factor associated with the σ_{I2} stresses. For the fuel element in question, the clad was so thin that it was obvious that this effect could be neglected. In a system with a clad cross-sectional area which is not small in comparison to the matrix cross-sectional area, this effect would have to be investigated further.

The value of H is a function of the location and direction of the stress component in question. The hexagonal tube correction factors for the critical points are plotted as a function of the (D_i/W) ratio in Figure 20 for the internal power generation case. In this analysis, it was assumed that the factors were also sufficiently accurate for use in the external heat flux case. Again the use of this assumption was made possible only by the fact that the tube was basically a "thin walled" tube. For a thick walled tube, the correction factors would be significantly different.

End Correction Factors

The solution discussed so far is valid only for sections "sufficiently far" removed from the ends of the tube. (By St. Venants Principle, "sufficiently far" in this case would be about three tube wall thicknesses.) At the tube ends the axial stresses must vanish. This produces a local redistribution of stress near the tube ends which is called the end effect. In general, the end effect is difficult to evaluate. In this case, however, since the tube is thin walled, it was assumed that the approach used by Timoshenko(6) is sufficiently accurate to evaluate the end effects. The actual calculations were performed by treating the end effect in the same manner as was done for the hexagonal tube effect, i.e.

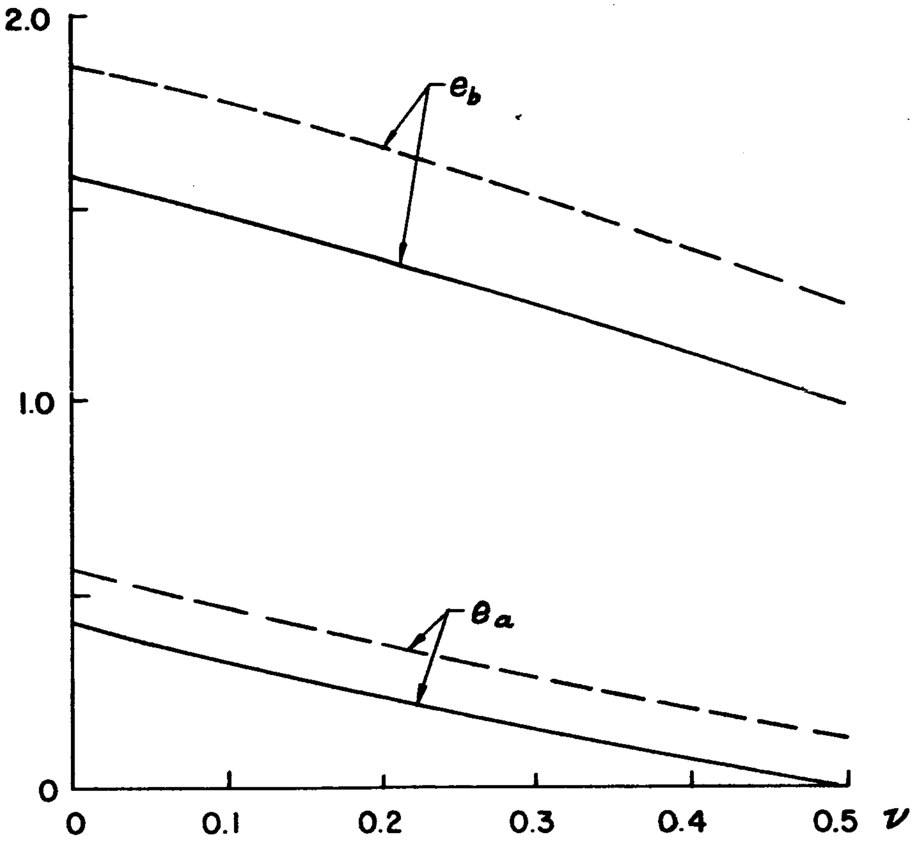

Fig. 21 Approximate End Correction Factors: Plotted as a function of Poisson's Ratio, ν, for both the internal heat generation (dashed lines) and external heat flux (solid lines) cases. The factor e_a applies to the circumferential (σ_θ) stress at the bore of the tube while the factor e_b applies to σ_θ at the outer surface of the tube.

by applying a multiplying correction factor to the basic long tube solution. Denoting these end correction factors by e, the final form of the elastic stress solutions is:

$$\sigma = e\,H\,(\sigma_T + \sigma_{I_1}) + \sigma_{I_2} \qquad \text{(A-10)}$$

Figure 21 shows plots of these end correction factors as a function of Poisson's ratio for both the internal heat generation and external heat flux cases.

Residual Stresses

Residual stresses will be present in a fuel element upon return to room temperature after prolonged operation at high temperature. These residual stresses arise due to the inelastic deformations which occur in the element during operation. The residual stresses are normally difficult to evaluate due to the complex nature of multi-axial creep deformations. In the special case of a Maxwell solid, the principle of superposition applies, hence the residual stresses can be evaluated in an elementary manner.

As an illustration, consider the case of a single, unclad, circular tube subject to a constant internal heat generation rate during operation and cooled at the bore.

Figure 22 illustrates the manner in which the initial elastic stresses are relaxed by the trade-off between the elastic and creep components of the total strain. The situation illustrated is specifically for the axial components of stress and strain. The total axial strain, ϵ_z, at any point will be the sum of

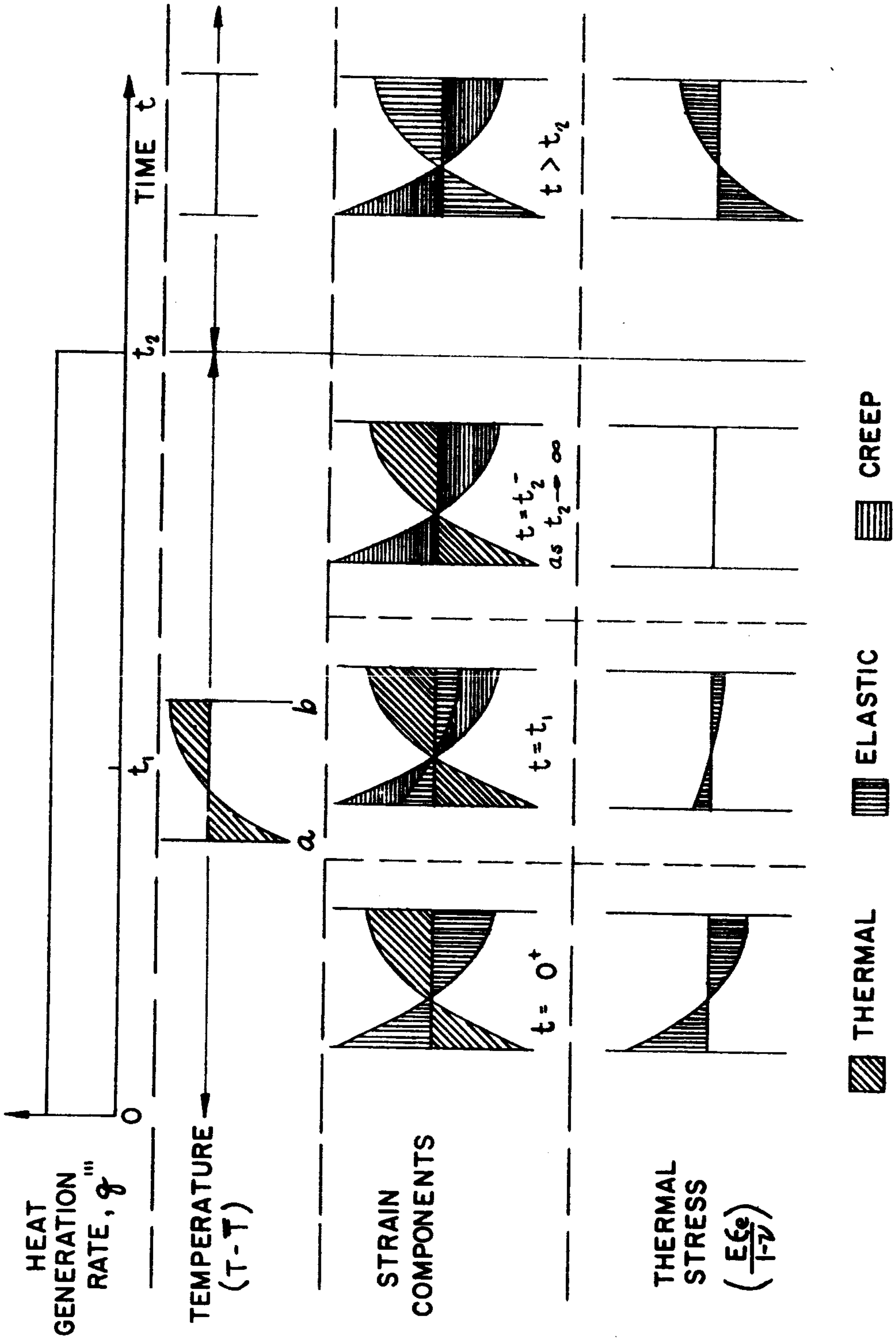
HEAT GENERATION RATE, q'''
TEMPERATURE $(T-\bar{T})$
STRAIN COMPONENTS
THERMAL STRESS $\left(\frac{E\epsilon_e}{1-\nu}\right)$
0
t_1
t_2
TIME t
a
b
$t = 0^+$
$t = t_1$
$t = t_2^-$
as $t_2 \to \infty$
$t > t_2$
THERMAL
ELASTIC
CREEP

Fig. 22 Development of residual thermal stresses.

the elastic, ϵ_e; creep, ϵ_c; and thermal, ϵ_T, strains.

$$\epsilon_z = \epsilon_e + \epsilon_c + \epsilon_T \qquad \text{(A-11)}$$

A long tube will be in a condition of plane strain except locally at the ends. This means that the total strain, ϵ_z, must be a constant which in this case is simply the mean thermal strain. The thermal strain can be expressed as:

$$\epsilon_T = \bar{\epsilon}_T + \epsilon_T^1 \qquad \text{(A-12)}$$

where $\bar{\epsilon}_T$ is the mean thermal strain

ϵ_T^1 is the variation from the mean

Substituting this back into equations (A-11) yields

$$\epsilon_z - \bar{\epsilon}_T = \epsilon_e + \epsilon_c + \epsilon_T^1 = 0 \qquad \text{(A-13)}$$

therefore,

$$\epsilon_e + \epsilon_c = -\epsilon_T^1 \qquad \text{(A-14)}$$

For $0 < t < t_2$ the temperature distribution (and hence ϵ_T^1) remains constant therefore, (Ref. Figure 22)

$$\epsilon_e + \epsilon_c = \text{Constant} \qquad \text{(A-15)}$$

Therefore as relaxation due to creep occurs, there is a simple trade-off between the elastic and creep components. If operation is continued until the elastic stresses are completely relaxed, the situation depicted by the third column of figures in Figure 22 will exist. Theoretically this time is infinite for a Maxwell solid, but for all practical purposes this time is finite and may be of the order of minutes. When the internal heat generation is removed at $t = t_2$:

$$\epsilon_z = \epsilon_e + \epsilon_c + \epsilon_T \qquad \text{(A-16)}$$

$$= \epsilon_e + \epsilon_c^*$$

where, ϵ_c^* = is the creep strain existing immediate prior to $t = t_2$

ϵ_z = 0 (since the mean thermal strain is now zero)

therefore,

$$\epsilon_e = - \epsilon_c^* = - \epsilon_{eo} \qquad \text{(A-17)}$$

where,

ϵ_{eo} is the initial elastic strain at $t = 0$

Therefore for the case of complete relaxation, the residual elastic strains are the negative of the initial elastic operating strains.

The residual elastic stresses will generally be much higher than the initial elastic operating stresses due to the fact that the room temperature modulus of elasticity is much greater than the modulus of elasticity at the operating temperature.

The strain components in the other directions will basically behave in the same manner. Also the strain components arising from the interaction between the matrix and the clad can be treated in a similar manner.

APPENDIX B

TEMPERATURE DEPENDENCE OF MATERIAL PROPERTIES

The small temperature range associated with most engineering applications permits the analyst to neglect the local variation of material properties with temperature. Reactor fuel elements have such high maximum operating temperatures and such a wide operating temperature range that all assumptions of this nature must be carefully evaluated for the particular application. For the BeO fuel elements in this case, it turns out that for steady state operating conditions the usual assumptions (with one exception) are still valid since the local temperature variation is small relative to the mean tube temperature.

The single exception is the coefficient of thermal expansion of the materials. Even in this case, the local variation with temperature could be ignored if only one material were involved. However, in this case, since the clad and base materials are dissimilar a more sophisticated approach is required.

There will be some temperature at which the element is initially isothermally stress free. This temperature will be referred to as the reference temperature, T_{REF}. Note that this temperature is a function of the manufacturing cycle and can be altered by simply annealing the element at a temperature above the equicohesive point of either of the component materials.

The thermal expansion of materials is generally a non-linear function of temperature. To avoid the associated analytical complications in thermal stress calculations, the expansion properties are generally approximated by a linear relationship of the form:

$$\epsilon_T = \alpha \Delta T \qquad \text{(B-1)}$$

where, ϵ_T = thermal expansion per unit length

α = a linear coefficient of thermal expansion

ΔT = a temperature increment

There are many possible ways of defining α. The most commonly used definitions are:

(1) The instantaneous coefficient of thermal expansion, α_i is defined as the slope of the thermal expansion curve at the temperature in question.

(2) The mean coefficient of thermal expansion, α^{**}, between T_1 and T_2 is defined as the slope of the secant to the thermal expansion between temperatures T_1 and T_2.

The instantaneous coefficient of thermal expansion is used in thermal stress calculations with reasonable accuracy where the temperature range is small. If the temperature range is large the actual thermal strain, ϵ_T, must be used in the calculations. When two or more materials are combined into a composite body as in the case of a clad tube, the use of a single value of the expansion coefficient is no longer possible even though the temperature range is small. Figure 23 graphically illustrates this point. From Figure 23, one sees that the difference

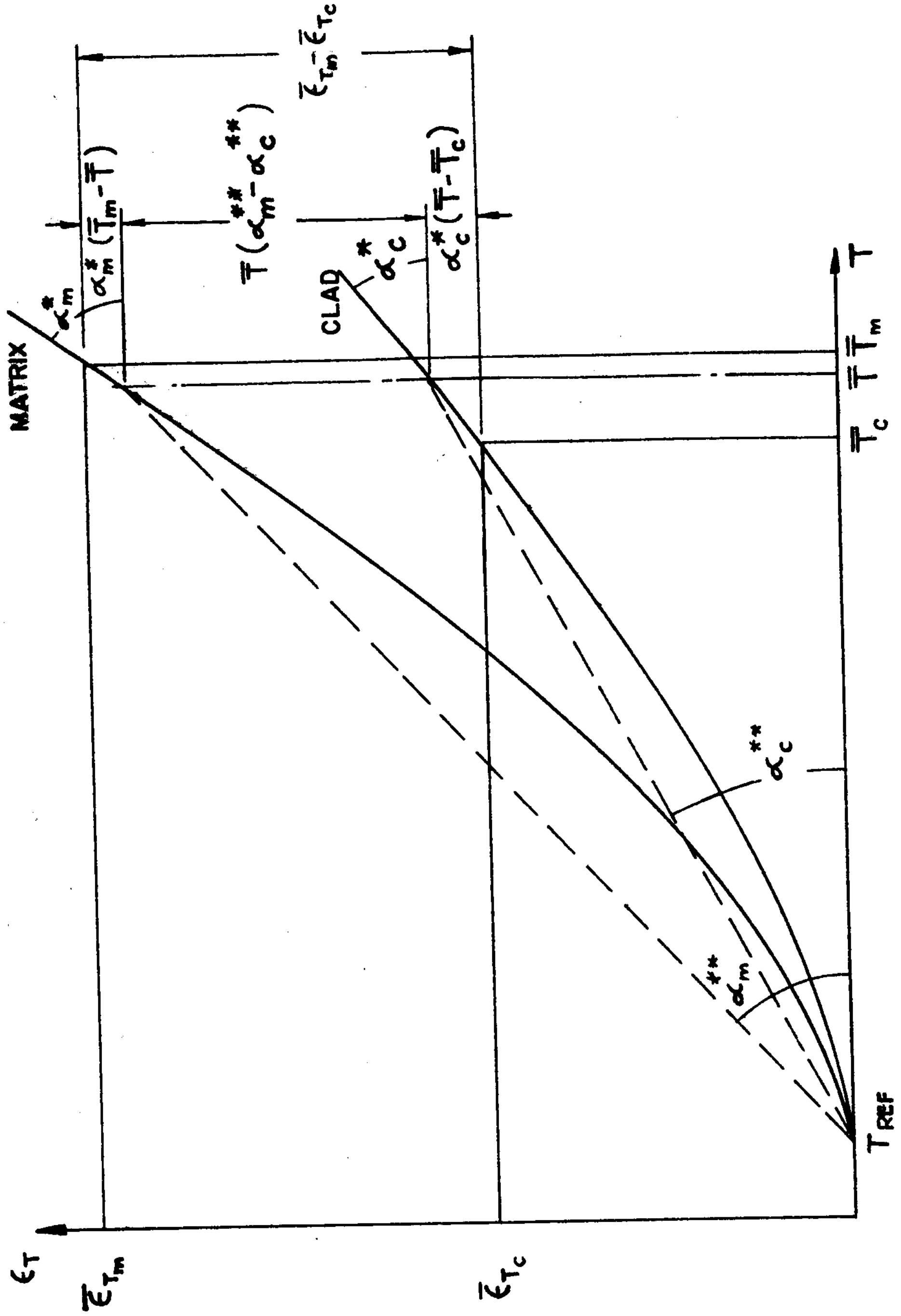
MATRIX
CLAD
α_m^*
α_c^*
α_m^{**}
α_c^{**}
$\alpha_m^*(\bar{T}_m-\bar{T})$
$\bar{T}(\alpha_m^{**}-\alpha_c^{**})$
$\alpha_c^*(\bar{T}-\bar{T}_c)$
$\bar{\epsilon}_{T_m}-\bar{\epsilon}_{T_c}$
$\bar{T}_c$
$\bar{T}$
$\bar{T}_m$
T
T_{REF}
ϵ_T
$\bar{\epsilon}_{T_m}$
$\bar{\epsilon}_{T_c}$

Fig. 23 Differential thermal expansion relationships.

in the mean expansions of the clad and the matrix can be expressed as the sum of three terms (mean values are denoted by a bar over the corresponding quantity).

$$\bar{\epsilon}_{Tm} - \bar{\epsilon}_{Tc} = \bar{T}\,(\alpha_m^{**} - \alpha_c^{**}) + \alpha_m^{*}\,(\bar{T}_m - \bar{T}) + \alpha_c^{*}\,(\bar{T} - \bar{T}_c) \qquad \text{(B-2)}$$

where $\bar{T}_c$ = clad mean temperature

$\bar{T}_m$ = matrix mean temperature

$\bar{T}$ = composite mean temperature

α^{**} = mean coefficient of thermal expansion between T_{REF} and $\bar{T}$

$\alpha^{*} \approx \alpha_i$ = instantaneous coefficient of thermal expansion at $T = \bar{T}$

Equation (B-2) provides the relationship required to permit continued use of a linear approximation to the thermal expansion properties in the thermal stress calculations for a composite tube.

APPENDIX C

VISCOELASTIC BEHAVIOR

Creep tests of BeO reported by Vandervoort and Barmore(1) together with work done under the ANPD program indicate that BeO behaves as a linear Maxwell solid*. This means that the creep strain rate, $\dot{\epsilon}_c$, is directly proportional to the stress i.e.

$$\dot{\epsilon}_c = k \sigma \qquad \text{(C-1)}$$

This has important implications in the development of a viscoelastic stress analysis for a BeO fuel element. It was shown by Boltzman that a generalized principle of super position may be used in the case of linear viscoelastic materials. In addition, for the special case of a Maxwell solid subject to an initial elastic thermal stress distribution, the relaxation due to creep will produce a simple decay of stress amplitudes without any redistribution of stress. The decay is exponential in form so that at any time, t, after the initial application of the elastic thermal stresses, the stress will be

$$\sigma_t = \sigma_o e^{-\beta t} \qquad \text{(C-2)}$$

where σ_o - are the initial elastic stresses

σ_t - are the stresses at any time, t

---

*The use of the linear Maxwell Solid materials model implies identical properties in tension and compression.

$\beta = (\eta/G)$

G = Shear modulus

η = Viscosity

Therefore in this special case, if the initial elastic stresses can be calculated, the viscoelastic stress solution at any time, t, can be obtained directly from the elastic solution by use of equation C-2.

APPENDIX D

SAMPLE PROBLEM

Fuel Element Geometry

$W = 0.300$ in.

$D_i = 0.234$ in.

$a = 0.120$ in.

$b \doteq \frac{1.05\,W}{2} = 0\;1575$

Design Conditions

Reference Temperature $T_{REF} = 70^{o}F$

Bore Temperature, $T_o = 2500^{o}F$

Heat Generation Rates - $q_m''' = 10$ Btu/sec-in^3

$q_c''' = 0.1$ Btu/sec-in^3

Material Properties - Evaluated at $T = T_o$

Modulus of Elasticity $E_m = 15 \times 10^{6}$ psi

Thermal Conductivity $k_m = 18.3 \times 10^{-5}$ Btu/sec-in-^{o}F

Coefficients of thermal expansion $\alpha_m^{*} = 6.8 \times 10^{-6}$ in/in-^{o}F

$\alpha_m^{**} = 6.0 \times 10^{-6}$ in/in-^{o}F

Poisson's ratio $\nu_m = 0.3$

Assume a clad material whose properties in terms of those of the matrix material are:

$(E_c/E_m) = 0.5$; $(k_c/k_m) = 0.2$; $(\alpha_c^*/\alpha_m^*) = 1.01$; $(\alpha_c^*/\alpha_m^*) = 1.015$; $\nu_c/\nu_m = 1.0$

Parameter Calculations

$\rho_1 = \frac{a}{b} = 0.7619$; $\rho_2 = \frac{1}{\rho_1} = 1.313$; $\rho_3 = \frac{D_i}{2a} = 0.975$; $\rho_4 = \frac{1}{\rho_3} = 1.026$

$R_A = \frac{1 - \rho_3^2}{1 - \rho_1^2} = 0.096$; $R_K = \frac{k_c}{k_m} = 0.2$; $R_q = \frac{q_c'''}{q_m'''} = 0.01$

$\frac{q_m''' b^2}{k_m} = 1356$; $\frac{q_m''' a^2}{k_c} = 4390$

$\frac{E_m \alpha_m^*}{1-\nu_m} = 145.5$ psi/°F; $\frac{E_c \alpha_c^*}{1-\nu_c} = 73.0$ psi/°F

Geometry Factors

$G_1(\rho_1) = 0.0205$ $\quad$ $G_1(\rho_3) = 0.00097$ $\quad$ } Ref: Figure 15

$G_2(\rho_1) = 0.0032$ $\quad$ $G_2(\rho_3) = 0.00056$ $\quad$ }

$G_3(\rho_1) = 0.141$ $\quad$ $G_3(\rho_2) = -0.123$ $\quad$ } Ref: Figure 16

$G_3(\rho_3) = 0.013$ $\quad$ $G_3(\rho_4) = -0.013$ $\quad$ }

$G_4 = 0.021$ $\quad$ Ref: Figure 17

$G_5 = 0.048$ $\quad$ Ref: Figure 18

$L(\rho_1) = 3.76$ $\quad$ $L(\rho_3) = 39.8$ $\quad$ Ref: Figure 19

Equivalent Circular Tube Solution

Temperatures: Reference - Table 2

$$\overline{T}_m - T_b = -\frac{q_m''' b^2}{k_m} G_2(\rho_1) = -11.1^\circ F$$

$$\overline{T}_m - T_a = \frac{q_m''' b^2}{k_m} G_1(\rho_1) = 27.8^\circ F$$

$$\overline{T}_c - T_a = \frac{q_m''' a^2}{k_c} \left[-G_2(\rho_3)\, R_q + \frac{1}{2} (\rho_2{}^2 - 1)\, G_3(\rho_4) \right] = -19.8^\circ F$$

$$\overline{T}_c - T_o = \frac{q_m\ a^2}{k_c} \left[G_1(\rho_3)\, R_q + \frac{1}{2} (\rho_2{}^2 - 1)\, G_3(\rho_3) \right] = 19.8^\circ F$$

$$\overline{T}_m - \overline{T}_c = (\overline{T}_m - T_a) - (\overline{T}_c - T_a) = 48^\circ F$$

$$\overline{T} = T_b - (T_b - \overline{T}_m) - \left(\frac{R_a}{1+R_A} \right) (\overline{T}_m - \overline{T}_c) = 2564^\circ F$$

Elastic Stresses Reference Table 3

$$P_1 = E_m \left[\alpha_m^* (\overline{T}_m - \overline{T}) - \alpha_c^* \ (\overline{T} - \overline{T}_c) \right] = 4905 \text{ psi}$$

$$P_2 = E_m \overline{T} (\alpha_m^{**} - \alpha_c^{**}) = -3800 \text{ psi}$$

Location	Stress Component	Matrix σ_T	Matrix σ_{I1}	Matrix σ_{I2}	Clad σ_τ	Clad σ_{I1}	Clad σ_{I2}
Outer Surface	σ_θ	-1615	-284	220	-1445	4099	-3170
	σ_r	0	0	0	0	103	- 69
	σ_z	-1615	-236	183	-1445	2448	-1900
Inner Surface	σ_θ	4045	-387	300	1445	4202	-3240
	σ_r	0	103	-69	0	0	0
	σ_z	4045	-236	183	1445	2448	-1900

Hexagonal Tube and End Correction Factors

From Figure 20, the hexagonal tube correction factors are:

$$H_{A\theta} = 1.51 \qquad H_{B\theta} = 1.43$$

$$H_{AZ} = 1.31 \qquad H_{DZ} = 1.21$$

From Figure 21, the end correction factors are:

$$\text{outer surface} - e_b = 1.53$$

$$\text{inner surface} - e_a = 0.29$$

Summary of The Fuel Element Maximum Initial and Maximum Residual Elastic Stresses

Assume that for both the clad and matrix materials.

$$\left(E_{RT}/E_{\overline{T}}\right) = 3.0$$

Then the following table summarizes the extremes of the fuel element thermal stresses. (Initial elastic values and elastic residual stresses at room temperature assuming complete relaxation.)

Axial Location	Point Ref. Fig. 20	Stress Component	Matrix		Clad	
			Initial	Residual	Initial	Residual
End	B	σ_θ	-3940	11,820	-	-
End	A	σ_θ	1900	-5700	-770	2310
Center	A	σ_θ	5530	-16,590	5290	-15,870
		σ_z	5160	-15,480		
Center	D	σ_z	-2070	6,210	-	-
Center	B	σ_θ	-2500	7,500	-	-

LIST OF SYMBOLS

a	Tube inner radius - inches
A	Area - square inches
b	Tube outer radius - inches
c	Subscript referring to the clad
D_i	Fuel element inner diameter - inches
e	End correction factor - Non-dimensional
E	Modulus of Elasticity - psi
G	Shear modulus - psi
G_1 through G_5	Geometry factors - Non-dimensional
H	Hexagonal tube correction factor - Non-dimensional
k	Conductivity - Btu/sec-in-°F
K	Stiffness factors - Non-dimensional
L	Lamé coefficient - Non-dimensional
m	Subscript referring to the matrix
o	Subscript referring to the fuel element inner surface
p	Pressure - psi
q''	Heat flux - Btu/sec-in^2
q'''	Volumetric heat generation rate - Btu/in^3-sec
r	Radius - inches Radial coordinate Subscript referring to the radial direction
R_r	Radius ratio
R_k	Conductivity ratio
R_q	Heat generation ratio

LIST OF SYMBOLS (Cont'd.)

t	Time - seconds
T	Temperature - ^{o}F
	Subscript referring to temperature
W	Across flats dimension of an hexagonal cross section element
Z	Axial coordinate
	Subscript referring to the axial direction
α	Linear coefficient of thermal expansion, in/in-^{o}F
α_i	Instantaneous coefficient of thermal expansion, in/in-^{o}F
$\alpha^{*} \approx \alpha_i$	(See appendix B)
α^{**}	Mean coefficient of thermal expansion
Δ	Increment in the associated variable
ϵ	Strain - inch/inch
θ	Angular coordinate
	Subscript referring to the θ direction (tangential or circumferential stress)
ν	Poisson's ratio
σ	Stress - psi (a negative value indicates a compressive stress)
η	Viscosity - psi/sec

A bar, ($\bar{\ }$), over a symbol denotes the mean value of the associated quantity.